THE UNIVERSITY OF WARWICK

Exploiting the Extreme Properties of Boron Doped Diamond in Electroanalysis

James Glenn Iacobini

A thesis submitted for the degree of Doctor of Philosophy

Department of Chemistry

September 2013

Table of Contents

Table of Contents I

List of Figures V

List of Tables XIV

Acknowledgements XVI

Declaration XVII

Abstract XVIII

Abbreviations XX

Glossary of Terms XXIII

1 Introduction 1

1.1 Boron Doped Diamond 1

1.1.1 Synthesis and Growth 2

1.1.2 Structure 8

1.1.3 Electrical Characteristics 9

1.2 Spectroscopic Aspects of Boron Doped Diamond 13

1.2.1 Bulk Properties 13

1.2.2 Surface Properties 16

1.3 Electrochemistry 19

1.3.1 Dynamic Electrochemistry 19

1.3.2 Cyclic Voltammetry 21

1.3.3 Electrochemistry of Boron Doped Diamond 23

1.3.4 Fundamental Studies of pBDD Electrochemistry 25

1.4 Applications of pBDD as an Electrode Material 30

1.4.1 Trace Metal Detection 30

1.4.2 Electroanalysis at BDD 31

1.5 Aims and Objectives 33

1.6 References 34

2 Experimental 40

2.1 Materials and Chemicals 40

2.1.1 Chemicals 40

2.1.2 Salt Bridge Preparation 41

2.1.3 Polycrystalline Boron Doped Diamond Samples 41

2.2 Diamond Electrode Fabrication 42

2.2.1 pBDD Disk Preparation 42

2.2.2 Glass Sealed Electrode 43

2.2.3 High Temperature Cell Electrode 44

2.3 Instrumentation and Techniques 46

2.3.1 Field-Emission Scanning Electron Microscopy (FE-SEM) 46

2.3.2 Resistivity Measurements 48

2.3.3 Micro Raman Spectroscopy 48

2.3.4 X-ray Photoelectron Spectroscopy (XPS) 50

2.3.5 Atomic Force Microscopy (AFM) 50

2.3.6 Secondary Ion Mass Spectrometry (SIMS) 51

2.4 Electrochemical Measurements 51

2.5 High Temperature Electrochemistry 52

2.5.1 Continuous Heating 52

2.5.2 Pulsed Laser Heating 52

2.6 References 56

3 Examination of the Factors Affecting the Electrochemical Performance of Oxygen Terminated pBDD Electrodes 57

3.1 Introduction 59
3.2 Results and Discussion 60
3.2.1 BDD Characterisation 60
3.2.2 pBDD Background Electrochemical Processes 65
3.2.3 pBDD Outer-Sphere Redox Processes 70
3.2.4 Finite Element Simulations 72
3.2.5 Hydrogen and Oxygen Termination, Stability and Surface Sensitive Processes 77
3.2.6 pBDD Surface Sensitive Redox Processes 80
3.3 Conclusion 87
3.4 References 89
4 Electrical and Raman Studies of pBDD 93
4.1 Conductivity of BDD 94
4.1.1 Conduction Mechanisms in semiconducting BDD 94
4.1.2 Conduction in Heavily BDD 96
4.1.3 Conductivity Measurements at Variable Temperature 99
4.2 Micro-Raman Spectroscopy 106
4.2.1 Raman Spectroscopy of BDD 106
4.2.2 Mapping the Heterogeneity of pBDD 107
4.3 Conclusion 110
4.4 References 112
5 High Temperature Electrochemistry 114
5.1 Introduction 115
5.1.1 Continuously Heated Voltammetry 117
5.2 Pulsed Voltammetry 119

5.2.1 Pulse Heated Voltammetry 121
5.2.2 Material Considerations 123
5.3 Results and Discussion 125
5.3.1 Continuous Heating 125
5.3.2 Non-Faradaic and Background Processes 133
5.3.3 Experimental Determination of Solution Temperature Close to the Electrode 137
5.3.4 Electrochemical Characterisation of System 140
5.3.5 Outer and Inner Sphere Redox Mediators 151
5.3.6 Finite Element Simulations 155
5.4 Conclusion 161
5.5 References 163
6 Heated Stripping Voltammetry at a pBDD Electrode 165
6.1 Introduction 166
6.2 Room Temperature Studies 169
6.2.1 Glass Sealed pBDD Electrode 169
6.3 Isothermal Studies 172
6.4 Non-Isothermal Studies 174
6.4.1 All-Diamond Macroelectrode Sample Characterisation 174
6.4.2 Pulse Heated Deposition 179
6.4.3 Pulse Heated Stripping 187
6.5 Conclusion 191
6.6 References 193
7 Conclusions 195
7.1 References 201

List of Figures

Figure 1.1 - Schematic depiction of 'NIRIM-type' microwave plasma CVD reactor, adapted from ref [1]. 5

Figure 1.2 – Schematic depiction of polycrystalline diamond growth[40] upwards from the nucleation face and corresponding SEM image[41] a) as-grown and b) after lapping. 6

Figure 1.3 – Depiction of the structure of diamond, atoms that comprise the unit cell are coloured blue. 9

Figure 1.4 – Schematic representation of the position of the boron acceptor level in BDD. 11

Figure 1.5 – Resistivity vs. boron concentration of a series of diamond films, indicating the regions of different conduction mechanisms. 12

Figure 1.6 – Raman spectra of BDD showing the increasing effect of the Fano interference as the boron in the gas phase is increased from 2240 to 14000 ppm.[67] .16

Figure 1.7 – Droplet shapes of water on a) hydrogen-terminated and b) oxygen-terminated diamond displaying different contact angles.[81].....17

Figure 1.8 – Schematic representation of charge accumulation at hydrogen-terminated diamond surface following gas dissociation in surface water, adapted from[105] 19

Figure 1.9 – Schematic showing the processes that occur near to an electrode surface; (1) mass transport from bulk solution, (2) chemical reactions that may happen before or after HET, (3) adsorption/desorption of species at the electrode surface and (4) HET at the interface.[110].....20

Figure 1.10 - Schematic depiction of CV; a) applied waveform and b) resultant voltammogram obtained under quiescent conditions.....22

Figure 1.11 – Potential windows of a) high quality pBDD, b) low quality pBDD, c) platinum and d) HOPG in 0.5 M H_2SO_4.[128] 26

Figure 2.1 – Photograph of glass sealed pBDD electrode used in this thesis. 44

Figure 2.2 - Photograph of custom built cell used for pulsed heating experiments...45

Figure 2.3 - Schematic depiction of diamond disk mounted in Perspex window a) solution facing side and b) irradiation side, the silver electrical contact is omitted for clarity.....45

Figure 2.4 – Schematic illustration of the different signals given off by a sample upon electron irradiation; 1) backscattered electrons, 2) secondary electrons, 3) Auger electrons, 4) x-ray photons and 5) UV-IR photons. 47

Figure 2.5 – Schematic diagram showing the different modes of photon scattering and their associated transitions. 49

Figure 2.6 - Photograph of jacketed glass cell used for continuous heating experiments. The cell is connected to a thermostatted water bath. 52

Figure 2.7 - Schematic description of how an electrochemical experiment is performed whilst pulsed heating is applied to the electrode simultaneously. 54

Figure 2.8 - Expanded schematic for simultaneous application of potential sweep and laser pulses on pBDD electrode during TPV. 54

Figure 3.1 - In-lens FE-SEM images of pBDD electrodes A – G (a – g respectively). 62

Figure 3.2 - Typical Raman spectra for the seven pBDD electrodes A-G (a – g respectively) recorded at room temperature with a 514.5 nm laser. The insets in spectra a, b and c are zoom-ins of the sp^2 (NDC) region, (d) and (e) show Raman spectra for the low doped (red) and higher doped (black) grains. 65

Figure 3.3 - CVs in aerated 0.1 M KNO_3 recorded at a scan rate of 0.1 V s^{-1} over the potential range (a) -2 V to 2V (where CVs have been vertically offset for clarity) and (b) -0.07 V to 0.07 V vs. SCE, for (i) 1 mm diameter electrodes A (black), B (red), C (blue), D (pink) and E (green) and (ii) electrodes F (brown) and G (orange), as-grown (dashed) and acid-cycled (solid). Also shown is the response for platinum (light green)

and glassy carbon (light blue). Note the difference in current density scales between (a) and (b) and also (bi) and (bii). 66

Figure 3.4 - CV in 0.1 M KNO_3 recorded at a scan rate of 0.1 V s^{-1} for electrodes D (blue), E (red), glassy carbon (green) and platinum (purple). The CVs have been plotted on different scales and vertically offset for clarity. 67

Figure 3.5 - CVs performed with 1 mm diameter disc pBDD (a) electrodes A (black), B (red), C (blue), D (pink) and E (green) and (b) electrodes F (brown) and G (orange), with an as-grown (dashed) or oxygen-terminated (solid) surface, at a scan rate of 0.1 V s^{-1} for (i) the oxidation of 1 mM $IrCl_6^{3-}$, (ii) the oxidation of 1 mM $FcTMA^+$ and (iii) the reduction of 1 mM $Ru(NH_3)_6^{3+}$ in 0.1 M KNO_3. 70

Figure 3.6 - Geometry used for simulation of CV at pBDD electrodes.....73

Figure 3.7 - R_2 curve used for electrode A, where $\varphi = 7\times10^{-6}$, $\chi = 1.5$, $\gamma = 10$ and n' = 1.3.....76

Figure 3.8 - The best fit simulated (red) and experimental (black) CVs for (a) oxidation of $FcTMA^+$ ($k^o_{app} = 2 \times 10^{-3}$ cm s^{-1}) and (b) reduction of $Ru(NH_3)_6^{3+}$ ($k^0_{app} = 6 \times 10^{-4}$ cm s^{-1}) respectively at the lowest doped semiconducting electrode A, where R_1 = 52 kΩ and R_2 varies with potential as shown in Figure 3.7. 77

Figure 3.9 - CVs performed with pBDD 1 mm diameter disc electrode B; acid cleaned oxygen-terminated surface (solid black), freshly hydrogen-terminated surface (dashed black) and similarly E; acid cleaned oxygen-terminated surface (solid black), freshly hydrogen-terminated surface (dashed green) at a scan rate of 0.1 V s^{-1} for the electrolysis of 1 mM $Ru(NH_3)_6^{3+}$ in 0.1 M KNO_3. 78

Figure 3.10 – CVs performed with electrode B in a solution of 1 mM $Ru(NH_3)_6^{3+}$ 0.1 M KNO_3 where; (a) the potential has been cycled (5 times) between increasingly extreme potentials of ± 0.6, ± 0.7, ± 0.8, ± 0.9 and ± 1 V between subsequent scans and (b) the potential has been cycled from ± 1.5 V in 0.1 M KNO_3 between subsequent scans. 79

Figure 3.11 - C1s XPS spectra for pBDD electrode E at (a) room temperature and upon heating to (b) 300 ºC and (c) 500 ºC for an (i) alumina polished and (ii) anodically

polarised surface with peak fitting where the grey line is the experimental data, coloured peaks are fittings and the black is the overall fit. 82

Figure 3.12 - Survey XPS spectra for the alumina polished pBDD surface at room temperature.....82

Figure 3.13 - (a) CVs performed with 1 mm diameter disc electrode E after alumina polish (red) and anodic pretreatment (black) for the oxidation of (i) 1 mM $Fe(CN)_6^{4-}$ in 0.1 M KNO_3 and (ii) 1 mM Fe^{2+} in 0.1 M $HClO_4$. (b) CVs for the oxidation of 1 mM Fe^{2+} in 0.1 M $HClO_4$ after 5 s treatment at either -1.5 V (green) or 2 V (blue) for the (i) alumina polished (black) and (ii) anodically polarised electrode (black). 85

Figure 4.1 – Theoretical hole concentration calculated from equation (4.3) as a function of temperature at different compensation ratios. 95

Figure 4.2 – Schematic of the metal-insulator transition in a semiconductor upon p-type doping at 0 K, yellow shading represents states filled with electrons.[13].....97

Figure 4.3 – Theoretical variation of activation energy with boron concentration for diamond calculated from equation (4.7). 98

Figure 4.4 – Resistivity versus reciprocal temperature of sample A, experimentally determined (black symbols) and theoretically calculated values (red line). 101

Figure 4.5 – Resistivity versus reciprocal temperature of sample B, experimentally determined (black symbols) and theoretically calculated values (red line). 102

Figure 4.6 - Resistivity versus reciprocal temperature of sample C, experimentally determined (black symbols) and theoretically calculated values (red line). 102

Figure 4.7 – Resistivity as a function of temperature for samples D (red) and E (blue). Experimental values are plotted as symbols and theoretical values calculated from equation (4.8) are solid lines. 105

Figure 4.8 – Raman spectra of sample D showing a) non-sp^2 carbon containing region and b) region with pronounced sp^2 carbon signature. 107

Figure 4.9 – SEM of heavily doped pBDD recorded with an 'in-lens' secondary electron detector. 107

Figure 4.10 – Raman maps of sample D showing; a) variation in sp^3 region peak area and b) variation in sp^2 region peak area. 108

Figure 4.11 - Raman maps of sample E showing; a) variation in sp^3 region peak area and b) variation in sp^2 region peak area. 109

Figure 5.1 - Schematic of potential waveform applied during a DPV experiment including, current samples are taken at τ' and τ respectively. 120

Figure 5.2 – a) DPV of pBDD in 0.5 mM $FcTMA^+$ 0.1 M KNO_3 at pulse amplitudes from 10 mV (smallest peak) to 100 mV (largest peak) and b) comparison of peak currents from a) (black symbols) and theoretical values (red symbols). 121

Figure 5.3 - CVs of pBDD macroelectrode in 1 mM $FcTMA^+$, 0.1 M KNO_3 from 15^{o}C (black) to 75 ^{o}C (olive) in increments of 10 ^{o}C performed at (a) 10 mV s^{-1}, (b) 25 mV s^{-1}, (c) 50 mV s^{-1} and (d) 100 mV s^{-1}.....126

Figure 5.4 – Theoretical (red symbols) and measured (black symbols) peak currents of pBDD macroelectrode in 1 mM $FcTMA^+$, 0.1 M KNO_3 at different temperatures. Performed at scan rates of (a) 10 mV s^{-1}, (b) 25 mV s^{-1}, (c) 50 mV s^{-1} and (d) 100 mV s^{-1}. 129

Figure 5.5 - CVs of Pt UME in 1 mM $FcTMA^+$, 0.1 M KNO_3 at temperatures of; black 23 ^{o}C, red 32 ^{o}C, green 50 ^{o}C, blue 60 ^{o}C and cyan 72 ^{o}C performed at scan rates of a) 10 mVs^{-1} and b) 100 mVs^{-1}. 132

Figure 5.6 – Comparison of theoretically calculated limiting currents (black line) vs. experimentally determined limiting currents of 1 mM $FcTMA^+$, 0.1 M KNO_3 at 10 mVs^{-1} (red symbols) and 100 mVs^{-1} (blue symbols). 133

Figure 5.7 – a) TPV of pBDD in 0.1 M KNO_3; black line no laser heating, red line 27.5 W with a pulse width of 10 ms, scan rate of 100 mVs^{-1}, b) expanded view…134

Figure 5.8 – TPV of pBDD in 0.1 M KNO_3 at different laser powers of; black joined symbols 0 W, red joined symbols 5 W, green joined symbols 15 W and blue joined symbols 27.5 W.....134

Figure 5.9 – Low sampling rate TPV of 0.1 M KNO_3 at 100 mV s^{-1}, laser powers of; black 0 W, red 5 W and blue 12.5 W. 136

Figure 5.10 – Measured OCP between two 1 mm pBDD electrodes in separate equimolar solutions of 0.5 mM $K_3[Fe(CN)_6]$ + $K_4[Fe(CN)_6]$ in 0.1 M KNO_3 versus temperature difference. 138

Figure 5.11 – Measured OCP between a non-heated and laser-heated pBDD electrode as a function of time at different laser power in an equimolar solution of 0.5 mM $K_3[Fe(CN)_6]$ + $K_4[Fe(CN)_6]$ in 0.1 M KNO_3. The associated temperature rise is shown on the right hand axis using $\beta = 1.62$ mVK^{-1}. 139

Figure 5.12 - Expanded view TPV at 25 W of pBDD in 1 mM $Ru(NH_3)_6^{3+}$ 0.1 M KNO_3 at different laser pulse lengths. 141

Figure 5.13 – TPV of pBDD in 1 mM $Ru(NH_3)_6^{3+}$ 0.1 M KNO_3 black line 0 W, red line 5 W; a) forward scan, b) backward scan, c) full scan and d) full scan (sampled data), all conducted at 100 mV s^{-1}.....142

Figure 5.14 – TPV (sampled data) of pBDD in 1 mM $Ru(NH_3)_6$ 0.1 M KNO_3 at laser powers of; 0 W, 7.5 W, 12.5 W, 17.5 W and 22.5 W. 144

Figure 5.15 – Peak current vs. laser power for $Ru(NH_3)_6^{3+}$ 0.1 M KNO_3 at concentrations of; black 0.2 mM, red 0.5 mM, green 1 mM and blue 5 mM. 144

Figure 5.16 – Shift of peak potential vs. laser power for pBDD in 1 mM $Ru(NH_3)_6^{3+}$ 0.1 M KNO_3. 145

Figure 5.17 – Idealised hot CV (red) compare against an ambient CV (black), the former possesses currents of a higher magnitude and is translated along the potential axis. 148

Figure 5.18 – Results of analytical expression for thermal modulation for different values of σ. 150

Figure 5.19 – Experimental and calculated TPVs of pBDD in 1 mM $Ru(NH_3)_6^{3+}$ 0.1 M KNO_3; a) experiment at 0 W, b) calculated modulation, c) sum of 0 W experiment and calculated modulation and d) experiment at 10 W.....151

Figure 5.20 – TPV (sampled data) of pBDD in 1 mM $IrCl_6$ 0.1 M KNO_3 at laser powers of; 0 W (red curve) and from 5 W, to 22.5 W in increments of 2.5 W.....152

Figure 5.21 - TPV (sampled data) of pBDD in 1 mM $FcTMA^+$ 0.1 M KNO_3 at laser powers of; 0 W (red curve), 2.5 W, 5 W, 7.5 W, 10 W, 12.5 W, 15 W, 17.5 W, 20 W, 22.5 W and 25 W (highest curve at 0.7 V). 153

Figure 5.22 – Expanded TPV transient of 1 mV $FcTMA^+$ 0.1 M KNO_3 at 20 W showing individual samples performed at 100 mV s^{-1}.....154

Figure 5.23 – a) TPV of pBDD (sampled data in 1 mM $FeSO_4$, 0.1 M $HClO_4$ at laser powers of; 0 W (smallest curve), to 22.5 W (largest curve) in increments of 2.5 W, b) expanded view of reduction peak shift at same laser powers increasing in the order; black, red, green, blue, cyan, magenta, yellow, dark yellow and navy.....155

Figure 5.24 – Simulation geometry (not to scale) for a pBDD disk in contact with water; a) different simulation domains and b) different boundary edges. 157

Figure 5.25 – Results of finite element simulations; (a) modelled temperature of centre of pBDD disk at solution interface vs. time and (b) peak temperatures attained at 10 ms; modelled data (black symbols) and experimental data from OCP experiments in section 5.3.3 (red symbols) vs. laser power. 160

Figure 6.1 – CV of glass sealed pBDD electrode in 100 µM Pb^{2+} at a scan rate of 50 mVs^{-1}, forward and return scans are coloured black and red respectively.....169

Figure 6.2 – DPV of 1 mm pBDD (sample E) with varying concentrations of Pb^{2+} in 0.1 M KNO_3. Experimental conditions; pulse width, 50 ms; pulse period, 200 ms; pulse amplitude 50 mV; step size, 2 mV and deposition time 300 s. 171

Figure 6.3 – Measured (a) peak currents and (b) peak areas with associated charges of DPV data from Figure 6.2.....171

Figure 6.4 – DPV stripping of glass sealed electrode in 5 µM Pb^{2+} at various temperatures, heating is performed isothermally with a water bath apparatus. 173

Figure 6.5 – Peak areas and associated charges of DPV in a solution of 5 µM Pb^{2+}at various temperatures. 173

Figure 6.6 – Schematic depiction of all diamond structure (a) side view and (b) top down view; intrinsic and boron doped regions are represented with blue and black respectively. 175

Figure 6.7 – CV of all diamond structure in 0.88 mM $Ru(NH_3)_6$, 0.1 M KNO_3 at 100 mVs^{-1}.....176

Figure 6.8 – Raman spectrum of relatively higher (black line) and lower (red line) boron doped regions of the all diamond structure.....176

Figure 6.9 – In-lens SEM of all diamond structure.....177

Figure 6.10 – Measured OCP between a non-heated and laser-heated pBDD electrode as a function of time at different laser powers in an equimolar solution of 0.5 mM $K_3[Fe(CN)_6]$ + $K_4[Fe(CN)_6]$ in 0.1 M KNO_3. The associated temperature rise is shown on the right hand axis using $\beta = 1.62\ mVK^{-1}$. 178

Figure 6.11 - TPV (sampled data) of all diamond structure in 1 mM $Ru(NH_3)_6^{2+/3+}$ 0.1 M KNO_3 at various laser powers.....179

Figure 6.12 – DPV stripping of all diamond structure in 5 µM Pb^{2+} at ambient (black line) and 10 W heated (red line) deposition conditions. 181

Figure 6.13 - (a) in-lens and (b) secondary electron SEM of all diamond structure after deposition in 5 µM Pb^{2+}at ambient conditions.....183

Figure 6.14 – (a) in-lens and (b) secondary electron SEM of all diamond structure after 10 W heated deposition in 5 µM Pb^{2+}.....183

Figure 6.15 – In-lens SEM of all diamond structure after ambient deposition in 1 mM Ag^{+}. 184

Figure 6.16 - DPV stripping of all diamond structure in 50 µM Pb^{2+} at ambient (black line) and 10 W heated (red line) deposition conditions. 185

Figure 6.17 - (a) in-lens and (b) secondary electron SEM of all diamond structure after deposition in 50 µM Pb^{2+}at ambient temperature. 186

Figure 6.18 - (a) in-lens and (b) secondary electron SEM of all diamond structure after 10 W heated deposition in 50 µM Pb^{2+}.....186

Figure 6.19 - Secondary electron SEM of all diamond structure after 10 W heated deposition in 50 µM Pb^{2+}. 187

Figure 6.20 – Schematic of DPV experiment performed in parallel with pulsed electrode heating. 188

Figure 6.21 - DTPV stripping of all diamond structure in 5 µM Pb^{2+} at ambient (black line) and 10 W heated (red line) stripping conditions.....189

Figure 6.22 - DTPV stripping of all diamond structure in 50 µM Pb^{2+} at ambient (black line), 10 W heated (red line) and 20 W heated (green line) stripping conditions. ...190

List of Tables

Table 2.1 - List of all the chemicals used in this work. 40

Table 2.2 – List of all pBDD samples used in this work from various suppliers. 42

Table 3.1 – Material and electrochemical characteristics of pBDD electrodes from various sources. 61

Table 3.2 - Summary of electrochemical characteristics of the seven different pBDD electrodes, all performed in 0.1 M KNO_3 71

Table 3.3 - Summary of the boundary conditions used for the simulation of the pBDD electrode current. 73

Table 4.1 – Parameters affording the best fit to data for semiconducting pBDD samples; s, N_A and N_D are fixed values for each sample. 103

Table 4.2 – Adjustable parameters of equations (4.9) and (4.10) used to obtain best fit for experimental data of heavily boron doped samples. 105

Table 5.1 - Comparison of theoretical and experimentally determined peak separations of a 1 mm pBDD electrode in 1 mM $FcTMA^+$ 0.1 M KNO_3 at different temperatures. 130

Table 5.2 – Measured OCP values with associated temperature rises after 10 ms of laser heating at different laser powers in an equimolar solution of 0.5 mM $K_3[Fe(CN)_6]$ + $K_4[Fe(CN)_6]$ in 0.1 M KNO_3. 140

Table 5.3 – The observed current rise of TPV in 1 mM $Ru(NH_3)_6^{3+}$, 0.1 M KNO_3 for different laser pulse times. 141

Table 5.4 – Boundary conditions of finite element simulation for a heated pBDD disk in water associated with domains from Figure 5.24 (a). 158

Table 5.5 - Boundary conditions of finite element simulation for a heated pBDD disk in water associated with boundary edges from Figure 5.24 (b). 159

Table 6.1 - Measured OCP values with associated temperature rises after 10 ms of laser heating at different laser powers in an equimolar solution of 0.5 mM $K_3[Fe(CN)_6]$ + $K_4[Fe(CN)_6]$ in 0.1 M KNO_3. 179

Acknowledgements

Firstly I wish to thank my supervisors, Prof. Julie Macpherson and Prof. Mark Newton for their continued assistance and for helping me to maintain enthusiasm for science even when things become difficult. You have both been very helpful throughout the entirety of my studies, which I could not have completed without you. Thank you also to Element Six for providing me with the best specimens of diamond possible.

A very special thank you goes to Dr. Laura Hutton, who has always been there for me, from my first day to the last day over 5 years. I gained so much knowledge and insight from you about all the aspects of diamond and electrochemistry.

And of course thank you to the entire Electrochemistry and Interfaces group at Warwick, many of you have helped throughout the years with various discussions and equipment training. It is nice to have such a large group whose collective knowledge has been invaluable to me.

Finally, I want to thank my family for their continued support and encouragement, thank you to Greg for setting a good example and giving me something to aim for.

Declaration

The work contained within this thesis is entirely original and my own work, except where acknowledged. I confirm that this thesis has not been submitted for a degree at another university. In Chapter 3, experiments were carried out in conjunction with Laura Hutton and Eleni Bitziou; Robert Channon performed the simulations. XPS in this chapter was performed by Marc Walker (Dept. of Physics). The simulations in Chapter 5 were performed in conjunction with Maxim Joseph, experiments in Chapters 5 and 6 were conducted in conjunction with Lingcong Meng.

Parts of this thesis have been published as detailed below:

L. Hutton, J. G. Iacobini, E. Bitzniou, R. B. Channon, M. E. Newton & J. V. Macpherson, *Examination of the Factors Affecting the Electrochemical Performance of Oxygen-Terminated Polycrystalline Boron-Doped Diamond Electrodes*, *Anal. Chem*., **2013**, 85, 7230-7240.

Abstract

The advantages of polycrystalline boron doped diamond (pBDD) are many when compared to other electrode materials in the field of electrochemistry. The superior properties of pBDD has generated substantial interest over the last 10 years, accelerating diamond to the cutting edge of electroanalytical studies, which benefit from lower levels of detection when utilising pBDD. The impressive chemical properties of pBDD allow it to be used in hostile environments where extreme temperature, pressure and pH may exist, affording researchers a means to create devices and sensors that could not be made with other materials. In addition pBDD also possesses extreme physical properties, notably its exceptionally high thermal conductivity which allows rapid transfer of heat energy. Currently, pBDD is widely used as an electrode material by many institutions, the production and employment of this material varies considerably. It is therefore of great importance to understand this material on a fundamental level, utilising experimental procedures that yield reproducible results.

The aims of this thesis are as follows: to suitably characterise a series of pBDD electrodes and elucidate which attributes afford the best performance, to enhance the electrochemical response of pBDD with temperature effects by exploiting its high thermal conductivity. A series of electrochemical, spectroscopic and electrical experiments are performed to assess different pBDD samples, which contain varying amounts of boron and non-diamond carbon impurities. The effect of electrode heating is explored. This is performed with a laser light source that allows rapid heating and cooling of the pBDD electrode, leaving the bulk solution temperature relatively unchanged. Enhancements are seen at elevated temperatures for several redox couples,

showing the feasibility of using laser electrode heating with pBDD. In the final chapter, elevated temperatures through electrode heating of an all diamond structure are used to enhance the deposition and subsequent stripping of lead in solution

Abbreviations

ADT	advanced diamond technologies
AFM	atomic force microscopy
ASTeX	applied science and technology, Inc.
ASV	anodic stripping voltammetry
BDD	boron doped diamond
BEN	bias enhanced nucleation
C-AFM	conducting atomic force microscopy
CL	cathodoluminescence
CV	cyclic voltammetry
CVD	chemical vapour deposition
DP-ASV	differential pulse anodic stripping voltammetry
DPV	differential pulse voltammetry
DTPV	differential temperature pulse voltammetry
fcc	face centred cubic
FE-SEM	field emission scanning electron microscopy
FET	field effect transistor
FWHM	full width half maximum
GC	glassy carbon
HER	hydrogen evolution reaction
HET	heterogeneous electron transfer
HFCVD	hot filament chemical vapour deposition
HOPG	highly oriented pyrolytic graphite
HPHT	high pressure high temperature
IR	infrared

LDOS	local density of states
LSV	linear sweep voltammetry
MPCVD	microwave plasma chemical vapour deposition
NDC	non diamond carbon
NDD	nitrogen doped diamond
NIRIM	national institute for research in inorganic materials
NPs	nanoparticles
NPV	normal pulse voltammetry
NRL	naval research laboratory
NTC	negative temperature coefficient
OCP	open circuit potential
OER	oxygen evolution reaction
pBDD	polycrystalline boron doped diamond
PDD	phosphorous doped diamond
RDE	rotating disc electrode
RF	radio frequency
SC	surface conductivity
scBDD	single crystal boron doped diamond
SCE	saturated calomel electrode
SEIRAS	surface enhanced infrared absorption spectroscopy
SEM	scanning electron microscopy
SIMS	secondary ion mass spectrometry
TPV	temperature pulse voltammetry
TST	transition state theory
UME	ultramicroelectrode
UV	ultraviolet

XPS	x-ray photoelectron spectroscopy

Glossary of Terms

$\Delta G_c^{\ddagger}$	energy barrier for reduction
E_D^{ox}	activation energy for mass transport of oxidised species
E_D^{red}	activation energy for mass transport of reduced species
$\Delta G_a^{\ddagger}$	energy barrier for oxidation
μ	mobility
μ_{300}	mobility at 300 K
μ_e	chemical potential of electrons in solution
μ_n	electron mobility
μ_p	hole mobility
A	electrode area
a	electrode radius
A_b	pre-exponential factor for backward rate constant
A_f	pre-exponential factor for forward rate constant
$A_{geometric}$	geometric electrode area
a_o	lattice parameter length
C	capacitance
C^*	bulk concentration of a species
c_b	bulk concentration of electroactive species (simulation)
c_i	concentration of species i
C_p	specific heat capacity
D	diffusion coefficient
D_i	diffusion coefficient of species i
E	potential

$E^{0'}$	formal potential
$E_{1/2}$	half wave potential
E_A	activation energy
E_{eq}	equilibrium potential
E_f	fermi level
E_{fb}	flat band potential
E_p	peak potential
F	Faraday's constant
G	Gibb's free energy
g_a	degenerescence level of acceptor state
H	enthalpy
h	Planck's constant
i	current
$i_{l,ox}$	limiting current for oxidation process
$i_{l,red}$	limiting current for reduction process
i_{lim}	limiting current
i_p	peak current
j	flux
k^0	standard heterogeneous rate constant
k^0_{app}	apparent heterogeneous rate constant
k_b	backward rate constant for electron transfer
k_B	Boltzmann's constant
k_{exc}	self-exchange rate constant
k_f	forward rate constant for electron transfer
K_p	precursor equilibrium constant
k_t	mass transfer coefficient

l	length
m^*	effective mass
n	number of electrons transferred per molecule
n'	model parameter
N_A	acceptor concentration
N_D	donor concentration
N_V	density of states of valence band
p	number of holes in the valence band
q	elementary charge
r	hydrodynamic radius of diffusing species (chapter 5)
r	radial distance from electrode centre (chapter 3)
R	molar gas constant
R_1	bulk electrode resistance
R_2	interfacial resistance
R_{int}	intrinsic material resistance
S	entropy
s	model parameter
T	absolute temperature
t	time
z	distance normal to electrode centre
α	transfer coefficient
β	temperature coefficient
γ	mass diffusivity ratio
γ	model parameter
ΔE_p	peak to peak separation
η	dynamic viscosity (chapter 5)

η	overpotential (chapter 3)
κ	thermal conductivity
κ_{el}	electronic transmission coefficient
ν_n	frequency factor
ρ	density (chapter 5)
ρ	resistivity (chapter 3, 4)
σ	conductivity
σ	DPV parameter (chapter 5)
τ	sample taken after each pulse in DPV
τ'	sample taken before each pulse in DPV
υ	potential scan rate
ϕ	dimensionless potential
φ	model parameter
χ	model parameter

1 Introduction

1.1 Boron Doped Diamond

Diamond is a well-known material, perhaps best known historically for its beauty and rarity, bestowing upon it incredible value as a gemstone. Besides this rather superficial property however, diamond possesses many incredible properties that can be exploited in a variety of disciplines. Perhaps best known is the hardness of diamond, with a resistance to applied pressure of 90 GPa making it very useful as a drilling tool and industrial abrasive. Other impressive properties include; very high thermal conductivity (2000 $Wm^{-1}K^{-1}$ at 298 K), transmission of light over a wide range of frequencies from deep ultraviolet (UV) to far infrared (IR) and very high electrical resistivity (10^{13} Ωcm).[1] With such excellent properties it is unsurprising that there has been a desire to create diamond artificially due to the lack of abundance of natural material, making diamond prohibitively expensive. Methods to produce diamond include; high pressure high temperature (HPHT) synthesis, use of detonation and chemical vapour deposition (CVD). The last of these becoming the most economically viable process for producing large amounts of high quality films, drastically increasing the opportunities for diamond in applications such as radiation detectors,[2] field effect transistors (FETs)[3] and heat sinks.[4] An important advantage of CVD over other methods of diamond production is the ability to introduce dopants into the lattice during growth, allowing precise control over the electrical characteristics of grown films. This creation of electrical conductivity upon the introduction of dopants (most importantly boron), coupled with the unique qualities of diamond has led to boron doped diamond (BDD) becoming an increasing useful tool for electrochemists.[5] Electrochemically, BDD possesses substantial advantages over traditional metal and

carbon electrodes including; high chemical stability,[6] resistance to fouling,[7] wide potential window and low capacitive currents.[8] These impressive qualities, however, are subject to the quality of BDD samples grown. Poorly grown samples (containing non-diamond phases) are unlikely to possess properties which make them superior to traditional electrodes such as platinum and glassy carbon (GC). As a result of different growth conditions, times and parameters etc. a diverse range of BDD materials have been grown which vary in boron dopant density, sp^2 carbon content and surface termination. Unfortunately in some cases in the literature the BDD is not properly characterised leading to sometimes conflicting experimental interpretations of the data when BDD is employed as an electrode material.[9, 10]

1.1.1 Synthesis and Growth

Natural diamond is produced within the earth's crust over the course of billions of years, where conditions of extremely high pressure and high temperature exist. The HPHT process, as the name suggests, somewhat mimics this natural process by applying high temperatures and pressures to graphite in order to convert it into diamond.[11] Typical conditions may range from pressures of 55×10^3 to 100×10^3 atm (5.6 to 10.1 GPa) and temperatures of 1200 to 2400 ^{o}C to produce thermodynamically stable diamond.[12] Although this method has been used successfully for many years, the main restriction of HPHT is the ability to only produce diamonds on the millimetre to nanometre scale,[1] limiting the applications of diamonds grown in this way.

An alternative method for producing diamond is the CVD method,[13] which in recent years has become the main commercially viable way in which to produce large high quality diamond films. All samples used in this work are grown in this way unless otherwise indicated, either as free-standing films or thin films on a growth substrate.

A somewhat more elegant alternative to HPHT synthesis, which aims to produce diamond at thermodynamically stable conditions, CVD is based on the supposition that diamond may be grown upwards from a substrate, one layer of carbon at a time. The obvious advantage of this is that if diamond could be produced at thermodynamically metastable conditions, less energy and less specialised equipment would be required for growth. Preliminary efforts in the use of CVD for diamond production began with Eversole[14] and Derjaguin *et al*,[15] where carbonaceous gases were flowed under reduced pressure onto a heated natural diamond substrate. Unfortunately this process produced impure mixtures of diamond with graphitic carbon. As a result slow growth rates were reported. In 1968, Angus *et al*[16] discovered that growth could be improved by the presence of atomic hydrogen, which preferentially etched graphite over diamond, this led to improved rates of deposition. Further investigations showed that growth could occur on non-diamond substrates such as tungsten.[17] Research carried out in Japan led to construction of the first hot filament[18] and microwave reactors, which produced high quality films at substantial rates of approximately 3 μm hr^{-1}.

Diamond growth via the CVD method encompasses different experimental conditions and operational parameters such as gas flow rates, pressures, temperatures and substrate choice. Carbon containing gases are only present in small concentrations, diluted by a vast excess of hydrogen in the reaction chamber, where temperatures may exceed 2000 ^{o}C. Activation of gas phase molecules is required for all types of CVD, with the two most common methods[1] utilising filament heating or microwave generation, leading to hot filament CVD (HFCVD)[19-21] and microwave plasma CVD (MPCVD)[22-24] respectively. The former makes use of an unreactive metal filament that can withstand temperatures around 2200 ^{o}C, typically tungsten or tantalum, this

is electrically heated which in turn leads to gas phase activation.[1] Dissociation of the gaseous molecules occurs leading to the creation of active species that form diamond on the substrate. This method produces diamond films of reasonable quality and is relatively inexpensive. The main disadvantages of HFCVD however are contamination of the diamond film with the filament material, and degradation of the filament.[19] The sensitivity of the filament severely limits the gas mixtures that may be used for this type of CVD growth.

MPCVD, despite its expense, has become the most widely used CVD method[1] by which high quality[25] diamond films are grown. Though similar to HFCVD, MPCVD utilises microwave energy as an activation method. Microwaves are generated at 2.45 GHz and directed into the reactor chamber with a waveguide, energy is then delivered to electrons present in the gas phase and by a process of collisions this energy is transferred to the gas phase molecules. The two most common variations of the MPCVD process are the NIRIM-type (National Institute for Research in Inorganic Materials),[26] shown in Figure 1.1, and the ASTeX-type (Applied Science and Technology Inc.)

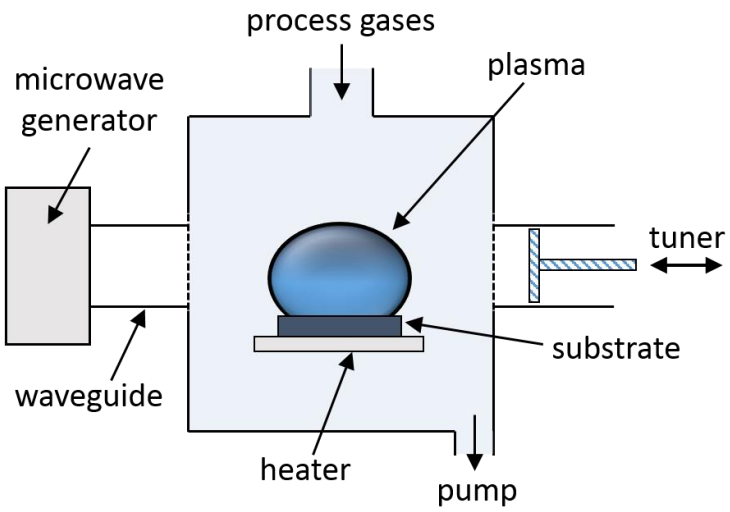

Figure 1.1 - Schematic depiction of 'NIRIM-type' microwave plasma CVD reactor, adapted from ref [1].

MPCVD boasts a faster rate of growth than HFCVD (> 10 μm h^{-1}), very high rates of 150 μm h^{-1} have even been reported for single crystal diamond.[27] The diversity of carbon sources gases is far less restrictive allowing many mixtures to be used; in MPCVD there is no metal filament that can interfere with reactive gases. Perhaps most importantly however, MPCVD produces films of unrivalled purity, due to less pollution of the growth material with foreign contaminants.[19, 28]

Both single crystal and polycrystalline forms of diamond may be grown with CVD,[29] the former is grown homoepitaxially on single crystal substrates which may be natural,[30, 31] or produced via the HPHT process.[32, 33] The orientation of the substrate diamond dictates the orientation of the CVD grown crystal, with (100), (110) and (111) being possible.[34] Polycrystalline diamond films are grown heteroepitaxially on a variety of different substrates,[35] where individual crystallites emerge from nucleation sites on the substrate and grow outwards in three dimensions. Coalescence occurs when the particles meet and a polycrystalline film is formed growing upwards,[36] Figure 1.2. There is a correlation between (growth face) grain size and film thickness,

allowing routine production of ultrananocrystalline,[37] nanocrystalline[38] and microcrystalline diamond films. Polycrystalline boron doped diamond (pBDD) is produced when a boron source is incorporated during CVD growth. The distribution of boron in polycrystalline diamond is not uniform; uptake occurs approximately ten times faster in the (111) face than the (100) face.[39] As polycrystalline diamond can be grown on non-diamond substrates, large films can be produced as opposed to single crystal diamond which is limited to the size of natural or HPHT crystals. Polycrystalline diamond is therefore more readily available and widely used in electrochemistry; this thesis will focus on polycrystalline BDD as this was used in all experiments.

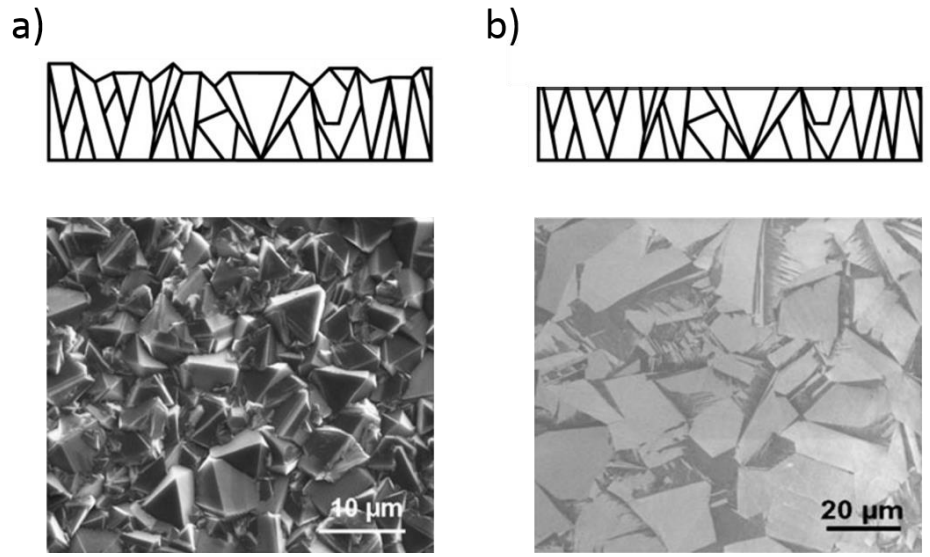

Figure 1.2 – Schematic depiction of polycrystalline diamond growth[40] upwards from the nucleation face and corresponding SEM image[41] a) as-grown and b) after lapping.

Ever since realisation of metastable diamond growth with CVD methods, researchers have sought to understand the complicated chemical processes governing deposition of films. Despite its complexity, diamond film growth may be envisaged as two steps; nucleation and growth. For the former, reactant gases consisting of sources of carbon, boron and hydrogen are flowed into the chamber at reduced pressure. Activation of

these molecules occurs producing extremely reactive species such as radicals, electrons and ions which rapidly undergo chemical reactions, being further broken down as the entire mixture becomes increasingly hot. Occasionally, a reactive species will approach and make contact with the surface of the substrate, whereupon it may simply desorb back into the mixture it came from or adsorb to the surface in order to react. Diffusion along the substrate surface may also occur until the reactive species locates a suitable reaction site.

Despite the lattice parameter mismatch of 52% due to different inter atomic spacing, diamond may be grown on silicon.[42, 43] Metallic substrates with a lattice parameter similar to that of diamond such as iridium have also been found to be suitable for CVD growth,[44] though it would be preferential to utilise silicon due to its high availability created in no small part by the semiconductor industry. It was discovered that the nucleation density could be vastly increased[45] by scratching the substrate with an abrasive powder, typically diamond, allowing nucleation densities between 10^7-10^8 cm^{-2} for silicon.[46] Unfortunately the act of producing nucleation sites by scratching the substrate leads to damaged surfaces and does not permit the growth of epitaxial films on non-diamond substrates. Bias enhanced nucleation (BEN),[22] where a suitably negative potential bias is applied to the substrate, has instead been utilised as means to induce high nucleation densities on smooth, unscratched non-diamond surfaces.[47, 48]

Butler *et al*[49, 50] have performed computer simulations, modelling the growth and morphologies of diamond films in CVD on the atomic and molecular scale.[51] It is now known that hydrogen must be present in a vast excess within the gas mixtures; once broken down into atomic hydrogen by the activation method, it is essential for several processes that occur. (1) Hydrogen will preferentially etch graphitic and sp^2 carbon

functionalities;[16] etching of sp^3 (diamond) carbon does still occur albeit at a much slower rate. Due to this there is a faster deposition of diamond than graphitic carbon, as the latter is removed from the growing material and returned back into the gas mixture far more frequently than the former. (2) Any long-chained hydrocarbons are easily and quickly broken down by the highly reactive hydrogen atoms in the gas phase, replenishing supplies of low weight carbonaceous molecules and maintaining cleanliness of the reaction chamber from the accumulation of unwanted deposits. It should be noted that CVD is possible with many carbon containing sources,[52] as mentioned above the aggressive nature of the hydrogen breaks down hydrocarbons into smaller fragments eventually into CH_3•, regardless of the starting molecule. (3) Diamond possesses dangling bonds at its surface under conditions of low pressure and high temperature; these are present on atoms whose valence electrons are not all participating in a chemical bond. At standard conditions, the surface of diamond is typically terminated with monovalent atoms such as hydrogen or various oxygen functionalities, as discussed in section 1.2.2. During the growth phase, a temporary terminus must exist to avoid the cross linking of adjacent carbon atoms to one another. Hydrogen, which is by far the most probable arrival at the growing surface, provides this termination during growth helping prevent graphitisation.

1.1.2 Structure

Composed entirely of carbon, diamond is a purely covalent solid, with strong σ-bonds connecting adjacent atoms in a tetrahedral configuration. Each bond is formed when one s-orbital and three p-orbitals hybridise to form four sp^3, pointing to the four corners of a tetrahedron. The Bravais lattice of diamond is that of a face centred cubic (fcc) type, with a lattice constant of 3.567 Å for natural diamond.[53] This is shown in Figure 1.3, where the lattice parameter is the length a_o. The unit cell may be considered

as two interpenetrating fcc structures, translated relative to each other by ¼ of the diagonal length of the Bravais lattice.

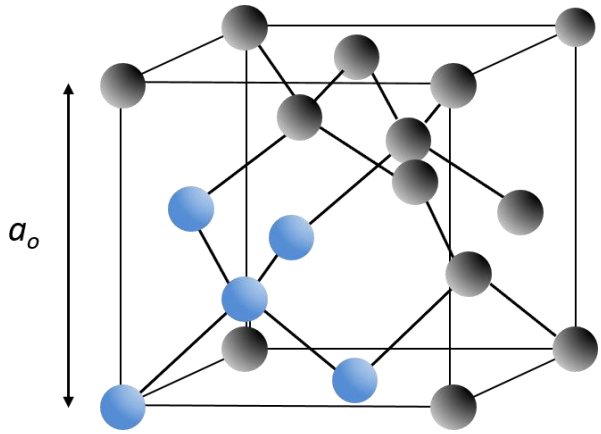

Figure 1.3 – Depiction of the structure of diamond, atoms that comprise the unit cell are coloured blue.

The band structure of intrinsic diamond is a result of a splitting in energy of bonding (σ) and anti-bonding (σ*) orbitals, created when many atoms are present and molecular orbitals are formed from the overlap of hybridised atomic orbitals. Each of the four sp^3 atomic orbitals interacts with a neighbouring sp^3 atomic orbital, producing a bonding orbital and an anti-bonding orbital, σ and σ* respectively. When a pair of electrons (with opposite spins) occupy the bonding orbital a bond is formed, an anti-bond is formed when electrons occupy an anti-bonding orbital. The anti-bonding orbital is much higher in energy than the bonding orbital, therefore the two electrons available per bond occupy the latter, forming a covalent bond. These two orbitals may be considered as two energy levels, separated by an energy gap; when many atoms participate in bonding, many energy levels are formed leading to the creation of two bands separated by a band gap.

1.1.3 Electrical Characteristics

Intrinsic diamond is often regarded as an electrical insulator, though strictly it should be considered as a wide band gap (ca. 5.5 eV) semiconductor. This large separation

between valence and conduction bands is responsible for the very high electrical resistivity of diamond. Surface conductivity may be induced by a hydrogen terminated surface,[54] however this does not affect bulk resistivity. The most routinely used method of producing conducting diamond is the introduction of dopants into the lattice during growth, creating an extrinsic semiconductor. The most widely used element for the doping of diamond is boron, producing a shallow acceptor level 0.37 eV above the top of the valence band[55] as shown schematically in Figure 1.4. Boron contains one less electron than carbon and therefore doping with this element leads to creation of a p-type semiconductor, where an electron deficiency (or hole surplus) exists. The comparable size of boron to carbon also ensures that boron is easily substituted for carbon into the diamond lattice. At room temperature, approximately 10^{-3} cm^{-3} boron atoms are ionised assuming very low doping levels;[56] electrons must be thermally promoted across the 0.37 eV gap to the acceptor level. Relatively high concentrations of boron ([B] > 10^{18} cm^{-3}) must therefore be present for BDD to possess appreciable conductivity at room temperature. Secondary ion mass spectrometry is a common method by which to obtain the boron concentration in diamond films.[57, 58] For inhomogeneous polycrystalline samples, an average [B] is measured depending on the crystallite size, although large crystallites can be probed individually if spatial resolution is required.

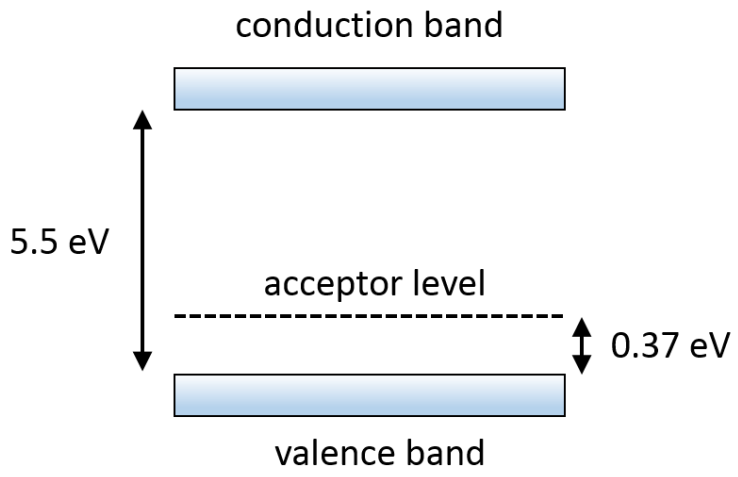

Figure 1.4 – Schematic representation of the position of the boron acceptor level in BDD.

Diamond may also be n-type, indeed diamonds produced by the HPHT method contain large amounts of nitrogen and are coloured yellow. The ability to produce both p-type and n-type diamond is of great importance, as semiconductor devices such as transistors and by extension integrated circuits rely on both p-type and n-type materials to function. The obvious dopants for n-type doping are group IV elements, particularly nitrogen, however this produces a deep donor level approximately 1.7 eV below the conduction band.[59] This large energy gap ensures that nitrogen doped diamond (NDD) exhibits very low conductivity at room temperature.[46] Phosphorous is another dopant that has shown promise to produce n-type diamond, MPCVD has been used to produce phosphorous doped diamond (PDD).[60]

A source of boron is used during CVD growth to produce BDD, typically diborane or trimethylboron[61] are used. Upon introduction of boron into diamond, an acceptor level is created in the band structure,[62] as depicted in Figure 1.4. As more boron is incorporated, an acceptor band is formed that may accommodate electrons or holes.

Much research has been dedicated to understanding electrical conduction in BDD, the vast majority of which has focused on scBDD. High quality pBDD films display

similar characteristics, despite a decreased carrier mobility due to scattering at grain boundaries. At room temperature, the conductivity of BDD films is strongly affected by the boron concentration present, and progresses through three distinct regimes as [B] is increased. At relatively low levels, [B] < 10^{19} cm^{-3}, conduction occurs mainly via the movement of free holes present in the valence band transporting charge. Between approximately 10^{19} and 3×10^{20} cm^{-3} nearest neighbour hopping dominates conduction, where charge carriers 'hop' between an ionised (electron deficient) and a neutral boron atom, and above 3×10^{20} cm^{-3} metallic type conduction takes place, since sufficient overlap of bonding orbitals occurs. A graph of resistivity, ρ, plotted against [B] is shown in Figure 1.5, indicating the regions of the three types of conduction mechanism.[63]

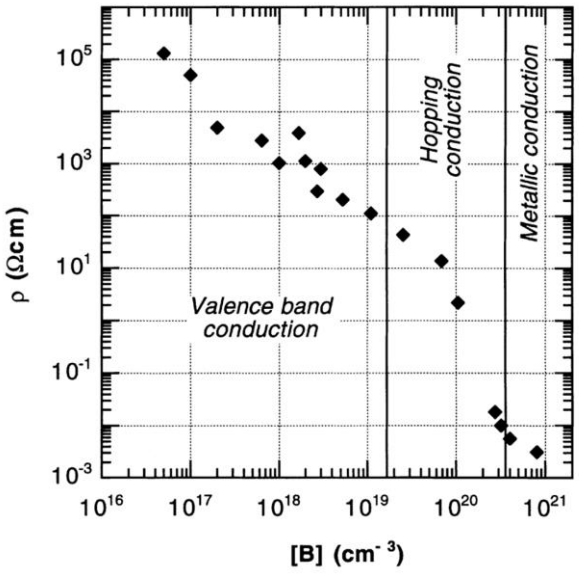

Figure 1.5 – Resistivity vs. boron concentration of a series of diamond films, indicating the regions of different conduction mechanisms.

The value of 10^{19} cm^{-3} for the onset of nearest-neighbour hopping is predicted by Werner *et al.*[64] In the metallic conduction regime, [B] > 2.7×10^{20} cm^{-3} according to Lagrange *et al,*[63] conductivity decreases with increasing temperature, similar to a

metal where lattice vibrations increase scattering of charge carriers. This is consistent with the Mott transition[65] predicted at approximately 2×10^{20} cm^{-3}. Lagrange *et al* found the metal-insulator transition to be slightly higher at 3×10^{20} cm^{-3}, the activation energy at this doping level is zero, indicative of an overlap of the boron impurity band with the valence band.[66] The onset of metallic type conductivity in pBDD can also be inferred with Raman spectroscopy,[67] where a change in the shape of the zone centre optical phonon peak occurs with doping past the metallic threshold.

1.2 Spectroscopic Aspects of Boron Doped Diamond

The electrical attributes of BDD are most influenced by the concentration of boron present as discussed above. Attention must be paid however to the quality of diamond films produced as this is also very important to the electrical properties of BDD. The bulk and surface properties of BDD must both be considered.

1.2.1 Bulk Properties

The term ‘quality’ in this context refers to aspects of the bulk of diamond such as: presence of non-diamond carbon; contamination with elements other than carbon or boron and structural defects. Non-diamond carbon may be formed during CVD growth; graphitic carbon and sp^2 bonding may accumulate and if present in large amounts will undermine the impressive qualities of BDD in some applications. Presence of impurities such as metals can be detrimental to the structural growth of BDD, whereas nitrogen will act to compensate boron atoms by donating an electron. The exclusion of nitrogen is very important when growing BDD, as films doped with large quantities of boron may not possess sufficient electrical conductivity if a comparable amount of nitrogen is present. Boron is useful as a dopant because of the ease with which it is accepted into the diamond lattice, replacing carbon atoms, due to

its similar size to carbon. Interestingly though, it has been shown[68] that incorporation of boron actually increases the crystalline quality of polycrystalline diamond up to approximately 10^{19}-10^{20} cm^{-3}. Careful control of the film thickness of CVD grown pBDD is also a means by which to improve crystalline quality, where thicker films produce larger grains (section 1.1.1) which rival the quality on single crystal specimens as shown by IR transmission studies.[69]

Raman spectroscopy is a very useful diagnostic tool for assessing the crystalline quality of diamond and for qualitative, analysis of impurity concentrations. Little surface preparation is required and the technique is non-destructive, making it ideal for sample analysis. Graphitic carbon is easily detected in Raman spectroscopy, as it is approximately 50 times more sensitive to sp^2 than sp^3 bonded carbon.[70] Features attributed to sp^2 bonded carbon such as graphite and amorphous carbon occur at around 1580 cm^{-1} and 1500 cm^{-1} respectively, enabling easy detection of non-diamond carbon.[56] To facilitate this, different laser wavelengths may be used, where longer wavelengths (lower energies) are more sensitive to non-diamond carbon (NDC).[71] For example, the 632.8 nm line of a He-Ne laser is more sensitive to non-diamond carbon and parasitic phases, whereas the 514.5 nm of an Ar^+ laser is better suited to looking at crystalline quality.

The characteristic ‘diamond peak’ present in Raman spectra is the zone centre optical phonon peak, and is situated at 1332 cm^{-1}. The properties of this peak yield information about crystalline quality and dopant concentration of BDD. Most importantly for crystalline quality is the full width at half maximum (FWHM), where lower values are indicative of fewer defects and hence better quality. The FWHM of the zone centre optical phonon peak is seen to decrease with incorporation of boron up to about 3×10^{20} cm^{-3}, around the onset of metallic conductivity.[72] At very high

concentrations of boron the FWHM begins to increase, however this is not due to deterioration of crystalline quality. At the threshold for metallic conductivity a change in line shape is observed for the peak at 1332 cm^{-1}, and is attributed to a coupling between the zone centre optical phonon and a continuum of states present in a degenerately doped (metallic) semiconductor.[73] This is called a Fano-type interference and has been observed in heavily doped silicon also.[74] The Fano effect of BDD is shown in Figure 1.6, where the concentration of boron in the gas phase is increased from 2240 to 14000 ppm. Additionally, the position of the peak originally at 1332 cm^{-1} begins to shift to lower wavenumbers as the boron concentration is increased. At extremely high boron concentrations, a complete loss of the zone centre optical phonon peak occurs, instead two broad features at around 1340 cm^{-1} and 1600 cm^{-1} are seen, Figure 1.6. The peak seen at 500 cm^{-1} in Figure 1.6 was fitted with the sum of a Lorentizian and Gaussian function by Denueville et al,[67] the position of the former function was found to vary with boron concentration. Due to the heterogeneity of pBDD different regions will display different Raman spectra as the local boron concentration varies, Szunerits *et al*[75] mapped the surface of pBDD by analysing the changes in Raman spectra.

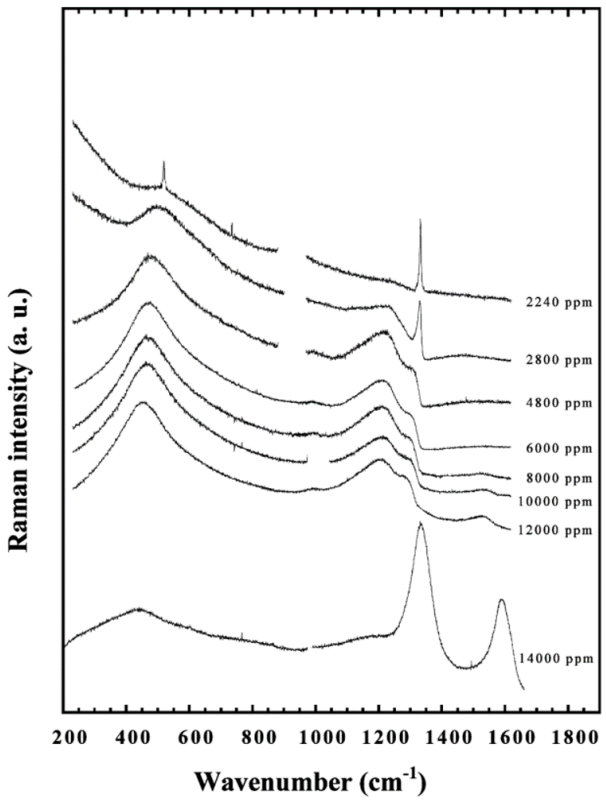

Figure 1.6 – Raman spectra of BDD showing the increasing effect of the Fano interference as the boron in the gas phase is increased from 2240 to 14000 ppm.[67]

1.2.2 Surface Properties

Although the bulk of diamond consists of carbon atoms bound to each other in a tetrahedral arrangement, a termination at the surface must exist to ensure complete occupancy of the carbon valence orbitals. The form of this termination strongly influences the surface electrical characteristics of diamond films. CVD grown diamond films are hydrogen-terminated when removed from the growth chamber due to the vast excess of hydrogen present in the high temperature plasma.[76] The hydrogen-terminated surface has been found to be stable in air for months at a time,[77] however oxidation may occur after only modest electrochemical experiments are performed.[78] Diamond surfaces can be deliberately oxygen-terminated through a variety of methods including; boiling in acid,[79, 80] anodic polarisation,[81, 82] oxygenation by photochemical

means[83] and contact with an oxygen plasma.[84] Oxygen and hydrogen-terminated surfaces have different affinities for water, with the former displaying hydrophilicity and the latter hydrophobicity. Contact angle measurements therefore are an adequate way to quickly assess the termination of diamond, the contact angle of hydrogen-terminated diamond is greater than that of oxygen-terminated diamond, Figure 1.7. Contact angles may vary based on the method of termination, and hence the extent of the respective termination, this is typically around 90° for hydrogen-termination[85, 86] and between 0.6° and 65° for oxygen-termination.[86-88]

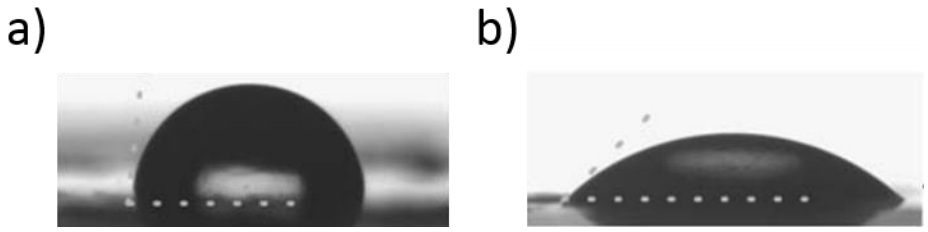

Figure 1.7 – Droplet shapes of water on a) hydrogen-terminated and b) oxygen-terminated diamond displaying different contact angles.[81]

More detailed analysis of the surface termination of diamond can be achieved with x-ray photoelectron spectroscopy (XPS), where a sample is subject to x-ray radiation resulting in the ejection of electrons which carry information about core orbitals.[89] On the single crystal (111) face, the C 1s peak appears at ca. 284 eV,[90] which is the convolution of many peaks representing carbon bonding to different groups. The surface chemistry of oxygen-terminated diamond is complex, as it may possess many different oxygen containing functional groups such; as carbonyl (C=O), ether (C-O-C) and hydroxyl (C-OH) groups.[91] The former two of these are prominent on the (100) crystal face,[92] whereas the hydroxyl group is the main constituent of the (111) crystal face.[93] The population of these groups relative to each other have been found to change with different surface treatments.[94-96] Wang *et al* found that electrochemical, oxygen

plasma and UV photochemical oxidation all produced small amounts C=O groups, approximately 5%.[94] The UV photochemical treatment was found to give the largest proportion (29%) of C-O bonds, comprised of both O-C-O and C-OH groups.[94]

Oxygen and hydrogen-terminated diamond differ in their band structures considerably, the presence of hydrogen even provides diamond with a negative electron affinity as the conduction band resides above the vacuum level.[97, 98] The surface termination strongly affects the electronic structure of diamond by accumulating or depleting charge carriers in a channel near to the surface. Intrinsic diamond, due to its large band gap, resists the flow of current very effectively, however it was observed by Landstrass *et al* in 1989 that intrinsic diamond terminated by hydrogen displayed surface conductivity (SC),[99] this was later confirmed by other groups.[100, 101] Experiments investigating the Hall effect confirmed that SC was caused by an accumulation of positive charge carriers, creating a p-type semiconductor,[102] allowing production of FETs.[103] Initial speculations ascribed this SC to subsurface hydrogen interacting with carbon dangling bonds creating acceptors, providing holes for conduction.[104]

In 2000 Maier *et al* proposed a mechanism in which adsorbates interacting with the hydrogen-terminated surface produced an accumulation of holes on diamond.[105] At ambient pressure, humidity and temperature, all surfaces are coated in a thin layer of water, where electron exchange between water and diamond can occur. Dissociation of CO_2 in water produces CO_3^- and H_3O^+ ions (Figure 1.8), which creates a chemical potential, μ_e, in water lower than that of the Fermi level, E_f, in hydrogen-terminated diamond. Equilibration takes place to minimise differences between energy levels once diamond is immersed in water, where electrons migrate from the hydrogen-terminated diamond into water, leaving holes behind. This accumulation of holes in

diamond and electrons in water creates a separation of charge between the water and diamond, promoting surface conductivity on the order of 10^{-5} Ω^{-1} at room temperature.[105, 106] This model is corroborated by the disappearance of appreciable SC upon surface oxidation or removal of the adsorbed water layer.[107]

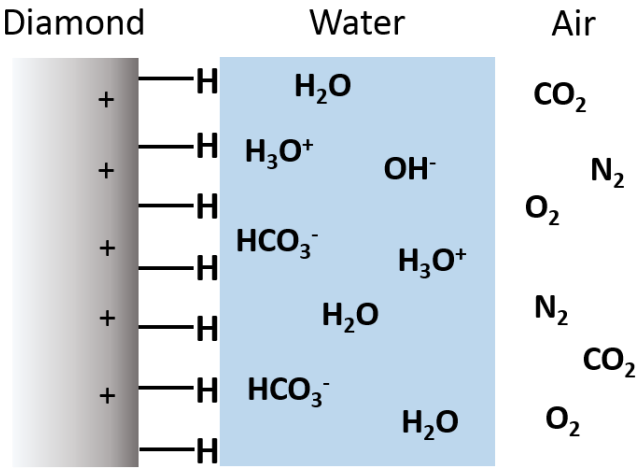

Figure 1.8 – Schematic representation of charge accumulation at hydrogen-terminated diamond surface following gas dissociation in surface water, adapted from[105]

1.3 Electrochemistry

1.3.1 Dynamic Electrochemistry

The study of electrochemical processes that occur at non-equilibrium conditions is termed dynamic electrochemistry.[108] A potentiostat is used to supply an electrical signal that perturbs the system and the response is measured as the experiment is run, for example, typically an electrical current is recorded as a voltage is applied. Electrical currents that are observed during electrochemical measurements comprise of two discrete components, faradaic and non-faradaic.[109] The former is manifested from charge carriers (electrons or holes) crossing the electrode/electrolyte interface and moving through an electrical circuit, this causes the oxidation or reduction of

electroactive species known as heterogeneous electron transfer (HET). The non-faradaic component occurs due to capacitance at the electrode/electrolyte interface created from a build-up of charge across the double layer. Metal and even GC electrodes suffer from direct reduction/oxidation of the electrode surface itself, causing an additional faradic component that is not due to the analyte species. The rate at which faradaic processes take place is subject to several phenomena that occur near to the electrode, as shown in Figure 1.9.

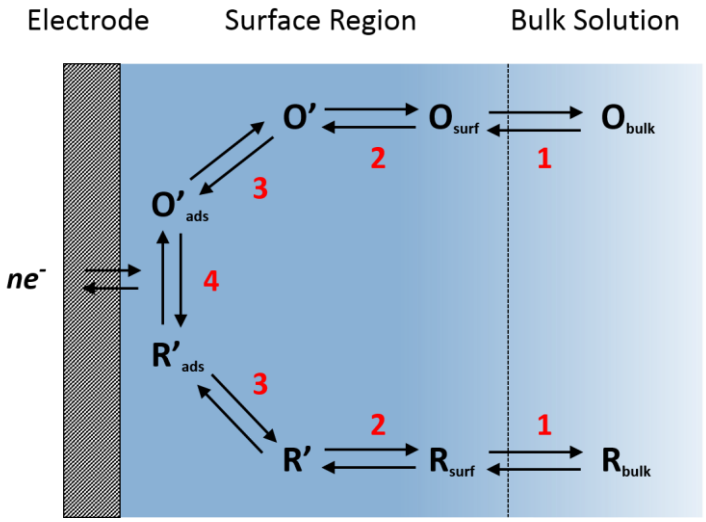

Figure 1.9 – Schematic showing the processes that occur near to an electrode surface; (1) mass transport from bulk solution, (2) chemical reactions that may happen before or after HET, (3) adsorption/desorption of species at the electrode surface and (4) HET at the interface.[110]

For large electrodes in stationary solution mass transport of reactive species is often the slowest and therefore rate determining step, process 1 in Figure 1.9. Mass transport is due to the movement of species due to a variety of gradients, which is comprised of three distinct processes; migration, diffusion and convection:

Migration is the movement of species in solution due to an applied electric field. This can be negated experimentally if an excess (ca. 100 times compared to the analyte species) of an inert salt,[111] such as KNO_3, is added to the solution. The addition of an

inert salt has the effect of screening the analyte from the electric field produced between electrodes, as well as increasing the conductivity of solution to reduce ohmic drop effects.[112]

Convection is the movement of species in solution due to thermal gradients, and also mechanically influenced processes such as stirring.[113, 114] For most electrochemical measurements, the influence on mass transport from convection may also be considered negligible, as long as the electrochemical cell is left at ambient temperature and is not deliberately agitated.

Diffusion is the movement of species in solution due to concentration gradients, i.e. the movement of a species from an area of high concentration to an area of low concentration and will always operate when the electrode is biased at a potential to electrochemically remove species from solution at the electrode/electrolyte interface.[115] This is the most significant mode of mass transport and can be studied by a variety of electrochemical means.

1.3.2 Cyclic Voltammetry

Dynamic electrochemical techniques are used to drive electrochemical reactions by supplying energy to a system, oxidation and reduction of species may occur as shown in equations (1.1) and (1.2) below;

$$R \rightarrow O + e^- \quad (1.1)$$

$$O + e^- \rightarrow R \quad (1.2)$$

In equation (1.1) the species R loses an electron and is itself oxidised, conversely in equation (1.2) the species O gains an electron and is reduced. The current passed in any electrochemical experiment, *i*, is be given by;[110]

$$i = nAFj \tag{1.3}$$

where n is the number of electrons transferred per molecule, A is the electrode area in cm^{-2}, F is Faraday's constant (96485 $Cmol^{-1}$) and j is the flux of redox active species towards the electrode in mol cm^{-2} s^{-1}.

Undoubtedly the most widely used technique in electrochemistry is cyclic voltammetry (CV), where a linearly changing potential, E, is applied to an electrochemical cell and the resultant current measured. When the potential reaches a predefined value its direction is reversed and the potential sweep continues in the opposite direction. This reversal of scan direction distinguishes CV from linear sweep voltammetry (LSV), where only a single scan direction is used. A typical applied waveform (potential vs. time) used and the resulting voltammogram for a large electrode under quiescent conditions are shown in Figure 1.10 a) and Figure 1.10 b) respectively.

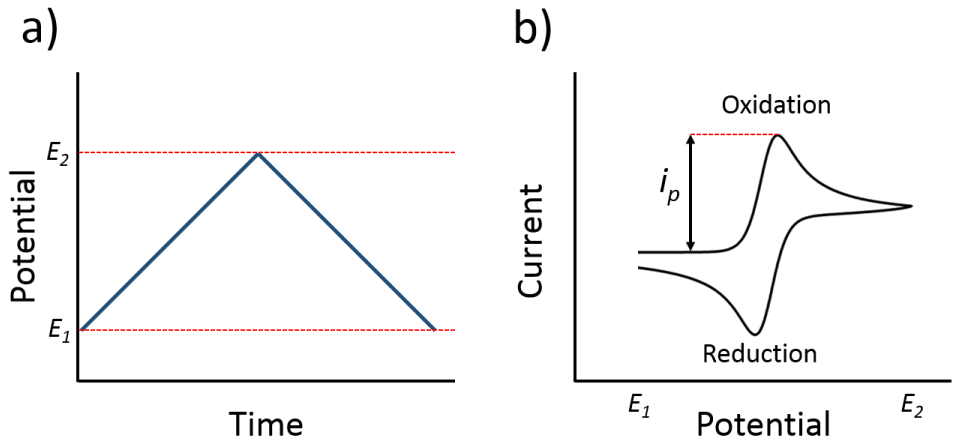

Figure 1.10 - Schematic depiction of CV; a) applied waveform and b) resultant voltammogram obtained under quiescent conditions.

The experiment begins at E_1 and the potential is increased towards E_2. The starting potential is chosen specifically to be in a region where no appreciable reaction occurs

for the examined species. No (faradaic) current due to oxidation is observed near to E_1, as the potential is increased towards E_2 however an increase in faradaic current is seen indicating oxidation of the redox mediator, equation (1.1). A current maximum (peak) is achieved which subsequently falls as the potential is increased further towards E_2. The potential direction is then reversed and the reduction of the mediator occurs in a similar manner, also producing a current peak which is offset from the first peak by a value of 59/n mV for a reversible reaction at 298 K as described by the Nernst equation.[115] For a large electrode under quiescent conditions, a peak in the current response is expected due to the relative rates of electrolysis and mass transport. The latter is significantly slower than the former for a reaction displaying fast HET under such conditions; mass transport cannot effectively replenish the electrode with fresh redox species to replace those which have already reacted. The value of this peak current, i_p, for a diffusion controlled process displaying planar diffusion is given by the following relation;[110]

$$i_p = 0.4463\left(\frac{F^3}{RT}\right)^{1/2} n^{3/2} A D^{1/2} C^* \upsilon^{1/2} \qquad (1.4)$$

where R is the molar gas constant (8.314 m^2 kg s^{-2} K^{-1} mol^{-1}), T is the absolute temperature in K, D is the diffusion coefficient of species in cm^2s^{-1}, C^* is the bulk concentration of redox species in mol cm^{-3}, υ is the potential scan rate in V s^{-1} and all other symbols have their usual meanings.

1.3.3 Electrochemistry of Boron Doped Diamond

Diamond is a relative newcomer to the field of electrochemistry, possibly due to its electrically insulating nature, making it not an obvious choice of material with which to conduct electrochemical studies. Initial experiments were performed on diamond

made to conduct using of ion implantation. It was found that diamond implanted with zinc possessed three advantages over GC; lower background currents, a wider potential window and higher reversibility in the presence of a redox mediator (faster kinetics).[116] Further investigations of diamond electrodes were undertaken by Pleskov *et al*,[117] semiconducting diamond was produced synthetically using CVD and was subjected to light illumination during electrochemical measurements. The act of illuminating semiconducting diamond was found to enhance its activity, even at wavelengths of light corresponding to energies lower than that of the band gap. Fujishima *et al* also conducted extensive research in the area of diamond photoelectrochemistry,[118] it was later found that 193 nm (6.4 eV) radiation from an ArF laser was sufficient to excite electrons into the conduction band[119] and that different surface terminations of diamond are responsible for different values of the flat band potential.[120] It was also found that nitrate in solution may be reduced into ammonia on a diamond by electrochemical means.[121]

Swain *et al* comprehensively studied high quality pBDD films, making note of their singular qualities for use in electroanalysis, qualities such as low background currents (due to low double layer capacitances), chemical stability and wide potential windows.[122, 123] Aside from analytical applications, diamond electrodes have also proved to be useful for industrial treatments of waste water[124] and organics,[125] where films need not be of the highest quality in order to anodically break down contaminants. These initial studies prompted more and more work into the field, as researchers endeavoured to fully exploit the unique properties of BDD.

1.3.4 Fundamental Studies of pBDD Electrochemistry

It has already been mentioned that initial studies of pBDD revealed its potential uses and significant advantages over other electrodes, however, the electrochemistry of pBDD is complex and subject to a number of factors. Growth conditions are undeniably important when attempting to produce films of high quality and purity; nitrogen is abundant in the atmosphere and is therefore hard to exclude from the growth chamber. The concentration of dopants such as boron has a pronounced effect on the electrical properties of diamond, in turn affecting its electrochemical performance. A perfect diamond crystal should be comprised of entirely sp^3 hybridised carbon, though other forms of carbon bonding (sp^2) can occur which changes the electrochemical response. The surface termination of pBDD may also affect electrochemical response, different chemical terminations may be realised by specific treatments with oxygen and hydrogen termination being the most common.

It was quickly discovered that as-grown (hydrogen terminated) CVD diamond possessed an unusually wide potential window,[126] greater than that of HOPG and platinum. BDD therefore permits the study of processes that occur outside the potential windows of other electrodes, for example the Ce^{3+}/Ce^{4+} couple.[127] When poor quality pBDD was tested however, water electrolysis was observed to occur much faster, resulting in a narrower potential window as shown in Figure 1.11. This lower grade of pBDD contained appreciable amounts of sp^2 carbon, as evidenced by Raman spectroscopy, representing a surface somewhat akin to a GC electrode.

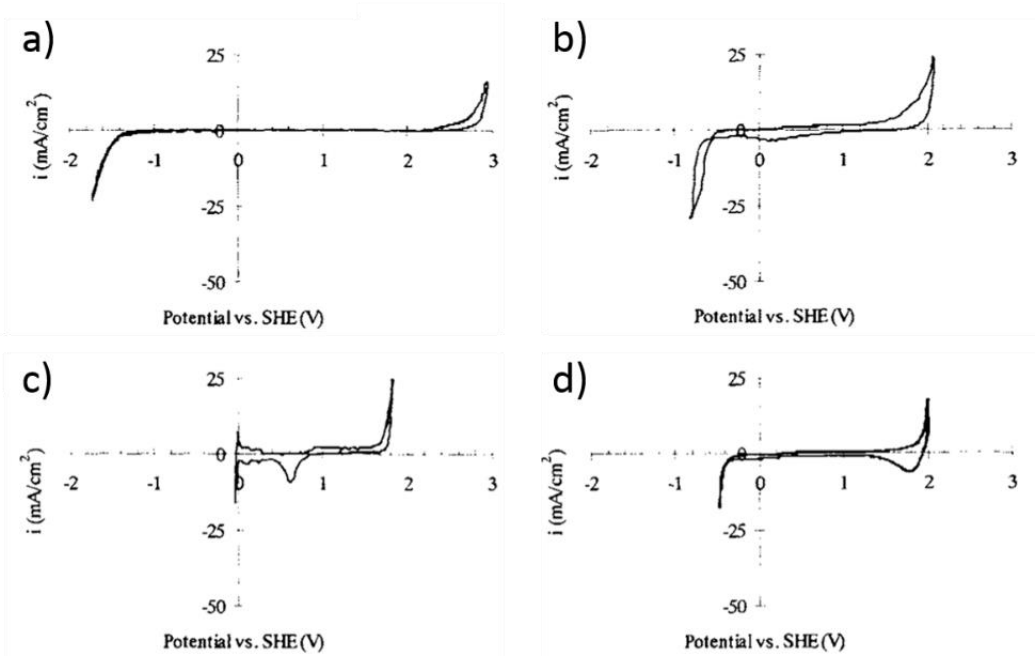

Figure 1.11 – Potential windows of a) high quality pBDD, b) low quality pBDD, c) platinum and d) HOPG in 0.5 M H_2SO_4.[128]

A correlation exists between sp^2 carbon content and overpotential for some electrochemical reactions, Bennett *et al*[129] found that the presence of this non-diamond impurity reduced the kinetic overpotential for water electrolysis but had little effect on reversible outer-sphere mediators.

It was thought that the hydrogen terminated surface was responsible for the slow kinetics of water electrolysis, as the hydrophobic nature of this surface renders reactions that require adsorption unfavourable.[128] However, oxygen terminated pBDD was found to give only a slightly better result in aqueous media than hydrogen terminated pBDD,[130] indicating that the wide solvent window of pBDD was not due to the hydrogen terminated surface present on as-grown films. Slow reaction kinetics for the hydrogen and oxygen evolution reactions (OER, HER) are responsible for the wide potential window of BDD, requiring large overpotentials to drive them. Water reduction and oxidation are inner sphere processes, adsorption to the electrode is therefore required and the diamond surface structure is important. It can be concluded

then that neither the oxygen nor hydrogen terminated diamond surface is favourable for water adsorption in comparison to Pt or GC. Suffredini *et al*[131] investigated the decomposition of water at both extremes of the potential window of BDD, calculating activation energies for the OER and HER as 106 and 150 $KJmol^{-1}$ respectively.

As previously mentioned, hydrogen termination increases the surface conductivity of diamond by introducing charge carriers and surface electronic states. This added conductivity is superfluous when the boron concentration is sufficiently high ($> 2 \times 10^{20}$ cm^{-3}), but may allow better than expected electrochemistry (faster electron transfer) for semiconducting diamond with lower doping levels. At lower boron concentrations for oxygen-terminated diamond, resistance effects hinder the kinetics of water electrolysis widening the potential window.

Another impressive quality of BDD that may be exploited electrochemically is its lack of reactivity to many different species, rendering diamond very chemically stable in a wide variety of media. For example, for the oxidation of cyanide ions, electrodes such as RuO_2 and IrO_2 are not stable and show low current efficiencies, however this is not the case using pBDD. [132] Li *et al*[133] proved BDD to be suitable for the deposition of lithium from a polymeric electrolyte; during deposition no alloys were formed on the BDD surface indicating that it does not promote underpotential deposition. Various studies in corrosive (acidic and alkaline) media have been performed demonstrating the ability of BDD to withstand harsh conditions. In 1989 Natishan and Morrish[134] showed that undoped diamond grown on a molybdenum film protected the metal from corrosion and oxidation, the diamond was found not to degrade during anodic polarisation. Chen *et al*[135] compared thin film BDD electrodes against traditional carbon electrodes for the generation of chlorine in solution of 1 M HNO_3 and 2 M NaCl, experiencing current densities and times of up to 0.5 Acm^{-2} and 20 h

respectively. No significant changes in morphology of the sp^3 bonded carbon were observed in the BDD films, although surface oxidation and etching of non-diamond carbon was observed. Swain[136] performed a series of analyses of carbon electrodes after potential cycling for 2 h in a solution of 1 M HNO_3 and 0.1 M NaF at 50 ^oC, observing again that the morphological structure of BDD is relatively unchanged whereas HOPG and GC suffered corrosion from pitting, oxidation and cavitation. A subsequent study by DeClements and Swain[137] comparing both high and low quality BDD showed that preferential etching of non-diamond carbon at the grain boundaries occurred upon anodic polarisation in KOH for the low quality films. Conversely, no structural damage was seen for the high quality films, the authors ascribe this to the lack of non-diamond carbon present in these films.

Of particular importance in analytical electrochemistry are low background currents,[122] which are manifested due to capacitance of the electrode/electrolyte interface and reduction/oxidation of the electrode itself. BDD possesses very low background currents, approximately one order of magnitude lower than that of GC.[119, 138] This property allows improvement of signal-to-noise[139] and hence lower (better) detection limits by utilising BDD as an analytical tool.[140, 141] The low background currents of BDD may be attributed to its low double layer capacitance. Highly ordered pyrolytic graphite (HOPG) is another form of carbon consisting of stacked layers of graphite (sp^2 bonded carbon atoms), which possesses an even lower capacitance of approximately 2 µF cm^{-2},[142] provided that no electrode degradation occurs.

It must not be forgotten that BDD is an extrinsic semiconductor, and at doping levels beneath that of metallic conductivity there is a low concentration of electronic states at the Fermi level. A space charge layer exists at the electrode/solution interface due to depletion of charge carriers at potentials less positive than E_{fb} for p-type

semiconductors. Any potential drop occurs over the space charge layer resulting in a small potential gradient and hence small double layer capacitance. Even at BDD doped above the metallic threshold, the number of charge carriers is approximately 3 orders of magnitude less than that at a metal electrode.

1.4 Applications of pBDD as an Electrode Material

The use of electrochemistry is very attractive for use in the environmental and biological fields for a variety of reasons; low cost, long term reproducibility, portability of instrumentation and sensitivity.[142] Electrodes employing mercury have long been utilised in the field of electrochemistry,[143] although mercury is toxic and is undesirable for environmental and biological applications.[144] With its outstanding electrochemical properties of low background currents, wide potential window, chemical stability and biocompatibility it is unsurprising that pBDD has found extensive use as an electrode material.

1.4.1 Trace Metal Detection

The detection and analysis of heavy metals in various media has become increasingly important in recent years, metals such as cadmium, lead, selenium and arsenic are toxic and threaten organisms. Electrochemistry is well suited for environmental monitoring of toxic species,[145] typically a form of stripping voltammetry[146] is used. In this technique metal ions are deposited onto the working electrode by holding or sweeping at a reducing potential during a preconditioning step. The potential of the working electrode is then swept in the opposite direction to remove the deposits and the measured current may be used to infer concentrations of the metal species present. Variations of stripping voltammetry exist that improve the sensitivity and detection limits such as differential pulse voltammetry (DPV)[147] and normal pulse voltammetry (NPV). In the past electrodes employing a mercury droplet have been used,[148, 149] this is advantageous as metals in solution form an amalgam with the mercury droplet providing uncomplicated stripping. Mercury though, as mentioned previously, is not suitable for use in many scenarios due to its toxicity. pBDD is an obvious candidate

for stripping voltammetry, with its wide potential window, low background currents, and extreme stability allowing detection of toxic metals with more versatility than mercury can provide. In 1999 Ramehsam *et al*[150] and Manivannan *et al*[151] proved that trace metal analysis could be performed with pBDD as the working electrode, with no mercury present. The low background currents displayed by pBDD allow high sensitivity, low detection limits at the ppb level have been reported for different metals at pBDD electrodes using stripping voltammetry,[152, 153] surpassing the sensitivity and longevity of GC electrodes.[154] The wide potential window of pBDD allows detection of a variety of different metals, perhaps not available to other electrodes displaying a more narrow range.

1.4.2 Electroanalysis at BDD

Diamond electrodes have shown promise in electroanalysis due to their advantages over metal and GC electrodes, such as a greater chemical stability and higher sensitivity.[141, 155-157] Other qualities that make BDD a worthy electroanlytical tool are its inertness to the adsorption of species[158] and its insensitivity towards dissolved oxygen.[130, 159] The termination of BDD has been found to change its properties and electrochemical behaviour towards different compounds,[87, 126] where hydrogen terminated BDD shows electrochemical activity towards a broad range of different chemical compounds such as the protonated form of nicotinamide adenine dinucleotide (NADH),[6] azides,[141] caffeine[160] and DNA[161] where diamond has been shown to outperform metal and GC electrodes. Accurate detection of DNA has become of increasing importance in medicine as knowledge of genetic disorders continues to grow. The current due to oxygen evolution makes electrochemical detection of DNA difficult with conventional electrodes, due to the high oxidation potentials of the pyrimidine and purine bases. This problem can be avoided, however,

by use of a hydrogen terminated BDD electrode, which possesses a high overpotential for oxygen evolution.

Oxygen terminated BDD appears to be more stable, and more selective than hydrogen terminated BDD, the former can be exploited for the detection of certain compounds. Uric acid is difficult to detect in the presence of ascorbic acid due to both having a similar potential for oxidation of approximately 0.9 V vs. SCE. By anodically treating (oxidising) BDD electrodes, it has been shown that uric acid can be successfully detected in ascorbic acid.[162] By anodically polarising a BDD electrode the authors found that separation of the peaks could be achieved, with the oxygen terminated surface displaying different selectivity for the two acids.

Chlorophenols are known to be carcinogenic[163] and are present in large quantities in industrial waste, though typical methods to remove these pollutants such as precipitation, filtration and coagulation are not always adequate for the removal of these species.[164] Chlorophenols can be detected with many traditional solid electrodes, when oxidised however, radicals are formed that couple to form a polymeric coating that fouls the electrode. Anodically treated BDD has been tested against GC for the detection of 2, 4-dichlorophenol during flow injection analysis.[165] The authors found that oxygen terminated BDD displayed much better stability than that of GC, where the former only suffered a 10 % reduction in signal and the latter a 70 % reduction. This is thought to be due to the repulsion of phenoxy radicals from the electrode surface by polar oxygen containing functional groups present on oxygen terminated BDD.

1.5 Aims and Objectives

As outlined above, the characteristics of BDD produced in different reactors with different growth conditions vary substantially across the literature. It is of great importance therefore that BDD is thoroughly characterised and understood before embarking on electroanalytical studies. Chapter 3 discusses in detail the differences between several pBDD films procured from various sources. Spectroscopic and electrochemical techniques are used to study the pBDD films and establish which aspects are desirable for electroanalysis. Further characterisation of some of these samples is discussed in Chapter 4. Electrical measurements are made at different temperatures in order to study the semiconducting or metallic nature of pBDD films. Raman mapping was also performed on two samples displaying similar boron concentrations to assess doping heterogeneity and the presence of non-diamond phases.

In Chapter 5 pBDD is utilised in high temperature experiments, an isothermal system was first employed to observe the effects of performing electrochemistry in solution above room temperature. Pulse heated voltammetry was then performed with a custom made diamond electrode cell, exploiting the high thermal conductivity of diamond. A laser was used to apply heat to the system in a controlled way, heating parameters were optimised to influence the electrochemical response without heating the bulk solution. Pulsed electrode heating is applied to lead stripping voltammetry in Chapter 6, high temperatures are used as a means to increase the analytical signal indicating an improved removal of deposited lead. The morphology and density of lead deposits are investigated with AFM for ambient and heated deposition conditions, conclusions are discussed in Chapter 7.

1.6 References

1. P. W. May, *Philosophical Transactions of the Royal Society of London. Series A: Mathematical, Physical and Engineering Sciences*, 2000, **358**, 473-495.
2. D. R. Kania, M. I. Landstrass, M. A. Plano, L. S. Pan and S. Han, *Diamond Relat. Mater.*, 1993, **2**, 1012-1019.
3. M. Kasu, K. Ueda, Y. Yamauchi, A. Tallaire and T. Makimoto, *Diamond Relat. Mater.*, 2007, **16**, 1010-1015.
4. T. Ackemann, M. Alduraibi, S. Campbell, S. Keatings, P. L. Sam, H. Fraser, A. S. Arnold, E. Riis and M. Missous, *J. Appl. Phys.*, 2012, **112**, 123109-123106.
5. T. N. Rao and A. Fujishima, *Diamond Relat. Mater.*, 2000, **9**, 384-389.
6. T. N. Rao, I. Yagi, T. Miwa, D. A. Tryk and A. Fujishima, *Anal. Chem.*, 1999, **71**, 2506-2511.
7. M. Hupert, A. Muck, J. Wang, J. Stotter, Z. Cvackova, S. Haymond, Y. Show and G. M. Swain, *Diamond Relat. Mater.*, 2003, **12**, 1940-1949.
8. M. Panizza and G. Cerisola, *Electrochim. Acta*, 2005, **51**, 191-199.
9. J. P. McEvoy and J. S. Foord, *Electrochim. Acta*, 2005, **50**, 2933-2941.
10. M. C. Granger and G. M. Swain, *J. Electrochem. Soc.*, 1999, **146**, 4551-4558.
11. F. P. Bundy, H. T. Hall, H. M. Strong and R. H. Wentorf, *Nature*, 1955, **176**, 51.
12. H. P. Bovenkerk, F. P. Bundy, H. T. Hall, H. M. Strong and R. H. Wentorf, *Nature*, 1959, **184**, 1094.
13. C. P. Klages, *Appl. Phys. A*, 1993, **56**, 513-526.
14. W. G. Eversole and N. Y. Kenmore, 1958, **Vol. US Patent 3030187**.
15. B. V. Derjaguin, D. V. Fedoseev, V. M. Lukyanovich, B. V. Spitzin, V. A. Ryabov and A. V. Lavrentyev, *J. Cryst. Growth*, 1968, **2**, 380-384.
16. J. C. Angus, H. A. Will and W. S. Stanko, *J. Appl. Phys.*, 1968, **39**, 2915-2922.
17. B. V. Spitsyn, L. L. Bouilov and B. V. Derjaguin, *J. Cryst. Growth*, 1981, **52, Part 1**, 219-226.
18. S. Matsumoto, Y. Sato, M. Tsutsumi and N. Setaka, *J Mater Sci*, 1982, **17**, 3106-3112.
19. R. Haubner and B. Lux, *Diamond Relat. Mater.*, 1993, **2**, 1277-1294.
20. Q. Chen, J. Yang and Z. Lin, *Appl. Phys. Lett.*, 1995, **67**, 1853-1855.
21. S. Bohr, R. Haubner and B. Lux, *Appl. Phys. Lett.*, 1996, **68**, 1075-1077.
22. S. Yugo, T. Kanai, T. Kimura and T. Muto, *Appl. Phys. Lett.*, 1991, **58**, 1036-1038.
23. R. Haubner, A. Lindlbauer and B. Lux, *Diamond Relat. Mater.*, 1993, **2**, 1505-1515.
24. F. J. G. Silva, A. P. M. Baptista, E. Pereira, V. Teixeira, Q. H. Fan, A. J. S. Fernandes and F. M. Costa, *Diamond Relat. Mater.*, 2002, **11**, 1617-1622.
25. T. Teraji and T. Ito, *J. Cryst. Growth*, 2004, **271**, 409-419.
26. M. Kamo, Y. Sato, S. Matsumoto and N. Setaka, *J. Cryst. Growth*, 1983, **62**, 642-644.
27. C.-s. Yan, Y. K. Vohra, H.-k. Mao and R. J. Hemley, *Proceedings of the National Academy of Sciences*, 2002, **99**, 12523-12525.

28. P. Mehta Menon, A. Edwards, C. S. Feigerle, R. W. Shaw, D. W. Coffey, L. Heatherly, R. E. Clausing, L. Robinson and D. C. Glasgow, *Diamond Relat. Mater.*, 1999, **8**, 101-109.
29. C. Wild, R. Kohl, N. Herres, W. Müller-Sebert and P. Koidl, *Diamond Relat. Mater.*, 1994, **3**, 373-381.
30. G. Janssen, W. J. P. van Enckevort, W. Vollenberg and L. J. Giling, *Diamond Relat. Mater.*, 1992, **1**, 789-800.
31. C. J. Chu, R. H. Hauge, J. L. Margrave and M. P. D'Evelyn, *Appl. Phys. Lett.*, 1992, **61**, 1393-1395.
32. A. Tallaire, J. Achard, F. Silva, R. S. Sussmann and A. Gicquel, *Diamond Relat. Mater.*, 2005, **14**, 249-254.
33. P. Djemia, A. Tallaire, J. Achard, F. Silva and A. Gicquel, *Diamond Relat. Mater.*, 2007, **16**, 962-965.
34. L. F. Sutcu, C. J. Chu, M. S. Thompson, R. H. Hauge, J. L. Margrave and M. P. D'Evelyn, *J. Appl. Phys.*, 1992, **71**, 5930-5940.
35. R. Ramesham, T. Roppel, R. W. Johnson and J. M. Chang, *Thin Solid Films*, 1992, **212**, 96-103.
36. F. G. Celii and J. E. Butler, *Annu. Rev. Phys. Chem.*, 1991, **42**, 643-684.
37. X. Xiao, J. Birrell, J. E. Gerbi, O. Auciello and J. A. Carlisle, *J. Appl. Phys.*, 2004, **96**, 2232-2239.
38. D. Zhou, T. G. McCauley, L. C. Qin, A. R. Krauss and D. M. Gruen, *J. Appl. Phys.*, 1998, **83**, 540-543.
39. P. Wurzinger, P. Pongratz, P. Hartmann, R. Haubner and B. Lux, *Diamond Relat. Mater.*, 1997, **6**, 763-768.
40. N. R. Wilson, S. L. Clewes, M. E. Newton, P. R. Unwin and J. V. Macpherson, *J. Phys. Chem. B.*, 2006, **110**, 5639-5646.
41. P. Actis, M. Manesse, C. Nunes-Kirchner, G. Wittstock, Y. Coffinier, R. Boukherroub and S. Szunerits, *PCCP*, 2006, **8**, 4924-4931.
42. X. Jiang, C. P. Klages, R. Zachai, M. Hartweg and H. J. Fusser, *Appl. Phys. Lett.*, 1993, **62**, 3438-3440.
43. C. L. Jia, K. Urban and X. Jiang, *Phys. Rev. B.*, 1995, **52**, 5164-5171.
44. K. Ohtsuka, K. Suzuki, A. Sawabe and T. Inuzuka, *Jpn. J. Appl. Phys.*, 1996, **35**, L1072-L1074.
45. Y. Mitsuda, Y. Kojima, T. Yoshida and K. Akashi, *J Mater Sci*, 1987, **22**, 1557-1562.
46. C. E. Nebel and J. Ristein, *Thin-Film Diamond I*, Elsevier Academic Press, 2003.
47. X. Jiang, K. Schiffmann and C. P. Klages, *Phys. Rev. B.*, 1994, **50**, 8402-8410.
48. X. Jiang, C. P. Klages, M. Rösler, R. Zachai, M. Hartweg and H. J. Füsser, *Appl. Phys. A*, 1993, **57**, 483-489.
49. C. C. Battaile, D. J. Srolovitz and J. E. Butler, *J. Appl. Phys.*, 1997, **82**, 6293-6300.
50. C. C. Battaile, D. J. Srolovitz and J. E. Butler, *Diamond Relat. Mater.*, 1997, **6**, 1198-1206.
51. C. C. Battaile, D. J. Srolovitz and J. E. Butler, *J. Electron. Mater.*, 1997, **26**, 960-965.
52. J. E. Butler, Y. A. Mankelevich, A. Cheesman, M. Jie and M. N. R. Ashfold, *J. Phys.: Condens. Matter*, 2009, **21**, 364201.
53. K. Suzuki, A. Sawabe, H. Yasuda and T. Inuzuka, *Appl. Phys. Lett.*, 1987, **50**, 728-729.

54. M. Szameitat, X. Jiang and W. Beyer, *Appl. Phys. Lett.*, 2000, **77**, 1554-1556.
55. J. F. Prins, *Phys. Rev. B.*, 1988, **38**, 5576-5584.
56. A. Fujishima, Y. Einaga, T. N. Rao and D. A. Tryk, *Diamond Electrochemistry*, Elsevier, 2005.
57. T. Kolber, K. Piplits, R. Haubner and H. Hutter, *Fresenius J. Anal. Chem.*, 1999, **365**, 636-641.
58. E. Gheeraert, A. Deneuville and J. Mambou, *Diamond Relat. Mater.*, 1998, **7**, 1509-1512.
59. R. G. Farrer, *Solid State Commun.*, 1969, **7**, 685-688.
60. S. Koizumi, T. Teraji and H. Kanda, *Diamond Relat. Mater.*, 2000, **9**, 935-940.
61. D. Gandini, E. Mahé, P. A. Michaud, W. Haenni, A. Perret and C. Comninellis, *J. Appl. Electrochem.*, 2000, **30**, 1345-1350.
62. A. T. Collins and A. W. S. Williams, *J. Phys. C: Sol. St. Phys.*, 1971, **4**, 1789.
63. J. P. Lagrange, A. Deneuville and E. Gheeraert, *Diamond Relat. Mater.*, 1998, **7**, 1390-1393.
64. M. Werner, R. Locher, W. Kohly, D. S. Holmes, S. Klose and H. J. Fecht, *Diamond Relat. Mater.*, 1997, **6**, 308-313.
65. A. W. S. Williams, E. C. Lightowlers and A. T. Collins, *J. Phys. C: Sol. St. Phys.*, 1970, **3**, 1727.
66. M. Werner, O. Dorsch, H. U. Baerwind, E. Obermeier, L. Haase, W. Seifert, A. Ringhandt, C. Johnston, S. Romani, H. Bishop and P. R. Chalker, *Appl. Phys. Lett.*, 1994, **64**, 595-597.
67. M. Bernard, A. Deneuville and P. Muret, *Diamond Relat. Mater.*, 2004, **13**, 282-286.
68. E. Colineau, E. Gheeraert, A. Deneuville, J. Mambou, F. Brunet and J. P. Lagrange, *Diamond Relat. Mater.*, 1997, **6**, 778-782.
69. S. E. Coe and R. S. Sussmann, *Diamond Relat. Mater.*, 2000, **9**, 1726-1729.
70. D. S. Knight and W. B. White, *J. Mater. Res.*, 1989, **4**, 385-393.
71. S. M. Leeds, T. J. Davis, P. W. May, C. D. O. Pickard and M. N. R. Ashfold, *Diamond Relat. Mater.*, 1998, **7**, 233-237.
72. K. Nishimura, K. Das and J. T. Glass, *J. Appl. Phys.*, 1991, **69**, 3142-3148.
73. J. W. Ager Iii, W. Walukiewicz, M. McCluskey, M. A. Plano and M. I. Landstrass, *Appl. Phys. Lett.*, 1995, **66**, 616-618.
74. N. H. Nickel, P. Lengsfeld and I. Sieber, *Phys. Rev. B.*, 2000, **61**, 15558-15561.
75. S. Szunerits, M. Mermoux, A. Crisci, B. Marcus, P. Bouvier, D. Delabouglise, J.-P. Petit, S. Janel, R. Boukherroub and L. Tay, *J. Phys. Chem. B*, 2006, **110**, 23888-23897.
76. H. Kawarada, *Surf. Sci. Rep.*, 1996, **26**, 205-259.
77. G. R. Salazar-Banda, L. S. Andrade, P. A. P. Nascente, P. S. Pizani, R. C. Rocha-Filho and L. A. Avaca, *Electrochim. Acta*, 2006, **51**, 4612-4619.
78. H. B. Martin, A. Argoitia, J. C. Angus and U. Landau, *J. Electrochem. Soc.*, 1999, **146**, 2959-2964.
79. B. D. Thoms, M. S. Owens, J. E. Butler and C. Spiro, *Appl. Phys. Lett.*, 1994, **65**, 2957-2959.
80. P. K. Baumann and R. J. Nemanich, *Surf. Sci.*, 1998, **409**, 320-335.
81. H. A. Girard, E. de La Rochefoucauld, D. Ballutaud, A. Etcheberry and N. Simon, *Electrochem. Solid-State Lett.*, 2007, **10**, F34-F37.
82. H. A. Girard, N. Simon, D. Ballutaud, E. de La Rochefoucauld and A. Etcheberry, *Diamond Relat. Mater.*, 2007, **16**, 888-891.

83. R. Boukherroub, X. Wallart, S. Szunerits, B. Marcus, P. Bouvier and M. Mermoux, *Electrochem. Commun.*, 2005, **7**, 937-940.
84. J. Shirafuji and T. Sugino, *Diamond Relat. Mater.*, 1996, **5**, 706-713.
85. L. Ostrovskaya, V. Perevertailo, V. Ralchenko, A. Dementjev and O. Loginova, *Diamond Relat. Mater.*, 2002, **11**, 845-850.
86. F. B. Liu, J. D. Wang, B. Liu, X. M. Li and D. R. Chen, *Diamond Relat. Mater.*, 2007, **16**, 454-460.
87. I. Yagi, H. Notsu, T. Kondo, D. A. Tryk and A. Fujishima, *J. Electroanal. Chem.*, 1999, **473**, 173-178.
88. Y. Kaibara, K. Sugata, M. Tachiki, H. Umezawa and H. Kawarada, *Diamond Relat. Mater.*, 2003, **12**, 560-564.
89. D. A. Shirley, *J. Vac. Sci. Technol.*, 1975, **12**, 280-285.
90. S. Ghodbane, D. Ballutaud, F. Omnes and C. Agnes, *Diamond Relat. Mater.*, 2010, **19**, 630-636.
91. D. A. Tryk, H. Tachibana, H. Inoue and A. Fujishima, *Diamond Relat. Mater.*, 2007, **16**, 881-887.
92. P. E. Pehrsson and T. W. Mercer, *Surf. Sci.*, 2000, **460**, 49-66.
93. K. P. Loh, X. N. Xie, S. W. Yang and J. C. Zheng, *J. Phys. Chem. B*, 2002, **106**, 5230-5240.
94. M. Wang, N. Simon, C. Decorse-Pascanut, M. Bouttemy, A. Etcheberry, M. Li, R. Boukherroub and S. Szunerits, *Electrochim. Acta*, 2009, **54**, 5818-5824.
95. T. Kondo, K. Honda, D. A. Tryk and A. Fujishima, *J. Electrochem. Soc.*, 2005, **152**, E18-E23.
96. C. H. Goeting, F. Marken, A. Gutiérrez-Sosa, R. G. Compton and J. S. Foord, *Diamond Relat. Mater.*, 2000, **9**, 390-396.
97. D. Takeuchi, H. Kato, G. S. Ri, T. Yamada, P. R. Vinod, D. Hwang, C. E. Nebel, H. Okushi and S. Yamasaki, *Appl. Phys. Lett.*, 2005, **86**, 152103-152103.
98. J. van der Weide, Z. Zhang, P. K. Baumann, M. G. Wensell, J. Bernholc and R. J. Nemanich, *Phys. Rev. B.*, 1994, **50**, 5803-5806.
99. M. I. Landstrass and K. V. Ravi, *Appl. Phys. Lett.*, 1989, **55**, 1391-1393.
100. T. Maki, S. Shikama, M. Komori, Y. Sakaguchi, K. Sakuta and T. Kobayashi, *Jpn. J. Appl. Phys.*, 1992, **31**, L1446-L1449.
101. S. Albin and L. Watkins, *Appl. Phys. Lett.*, 1990, **56**, 1454-1456.
102. K. Hayashi, S. Yamanaka, H. Okushi and K. Kajimura, *Appl. Phys. Lett.*, 1996, **68**, 376-378.
103. K. Tsugawa, K. Kitatani, H. Noda, A. Hokazono, K. Hirose, M. Tajima and H. Kawarada, *Diamond Relat. Mater.*, 1999, **8**, 927-933.
104. N. Jiang and T. Ito, *J. Appl. Phys.*, 1999, **85**, 8267-8273.
105. F. Maier, M. Riedel, B. Mantel, J. Ristein and L. Ley, *Phys. Rev. Lett.*, 2000, **85**, 3472-3475.
106. J. Ristein, M. Riedel and L. Ley *J. Electrochem. Soc.*, 2004, **151**, E315-E321.
107. M. Riedel, J. Ristein and L. Ley, *Phys. Rev. B.*, 2004, **69**, 125338.
108. R. S. Schrebler Guzmán, J. R. Vilche and A. J. Arvía, *J. Appl. Electrochem.*, 1979, **9**, 321-327.
109. J. J. O'Dea, A. Ribes and J. G. Osteryoung, *J. Electroanal. Chem.*, 1993, **345**, 287-301.
110. A. J. Bard and L. R. Faulkner, *Electrochemical Methods: Fundamentals and Applications*, Wiley, New York, 1980.

111. E. J. F. Dickinson, J. G. Limon-Petersen, N. V. Rees and R. G. Compton, *J. Phys. Chem. C*, 2009, **113**, 11157-11171.
112. M. Ciszkowska and Z. Stojek, *J. Electroanal. Chem.*, 1999, **466**, 129-143.
113. J. Wang and L. D. Hutchins-Kumar, *Anal. Chem.*, 1986, **58**, 402-407.
114. G. Weber and J. Messerschmidt, *Anal. Chim. Acta*, 2005, **545**, 166-172.
115. C. M. A. Brett and A. M. O. Brett, *Electrochemistry: Principles, Methods, and Applications*, Oxford University Press, Oxford, 2000.
116. M. Iwaki, S. Sato, K. Takahashi and H. Sakairi, *Nucl. Instrum. Methods Phys. Res.* , **209–210, Part 2**, 1129-1133.
117. Y. V. Pelskov, A. Y. Sakharova, M. D. Krotova, L. L. Bouilov and B. V. Spitsyn, *J. Electroanal. Chem. Inter. Electrochem.*, 1987, **228**, 19-27.
118. K. Patel, K. Hashimoto and A. Fujishima, *Denki Kagaku*, 1992, **60**, 659.
119. L. Boonma, T. Yano, D. A. Tryk, K. Hashimoto and A. Fujishima, *J. Electrochem. Soc.*, 1997, **144**, L142-L145.
120. T. N. Rao, D. A. Tryk, K. Hashimoto and A. Fujishima, *J. Electrochem. Soc.*, 1999, **146**, 680-684.
121. R. Tenne, K. Patel, K. Hashimoto and A. Fujishima, *J. Electroanal. Chem.*, 1993, **347**, 409-415.
122. G. M. Swain and R. Ramesham, *Anal. Chem.*, 1993, **65**, 345-351.
123. G. M. Swain, *Adv. Mater.*, 1994, **6**, 388-392.
124. R. Ramesham, R. F. Askew, M. F. Rose and B. H. Loo, *J. Electrochem. Soc.*, 1993, **140**, 3018-3020.
125. J. J. Carey, C. S. Christ and S. N. Lowery, *US Patent 5399*, 1995, 247.
126. H. B. Martin, A. Argoitia, U. Landau, A. B. Anderson and J. C. Angus, *J. Electrochem. Soc.*, 1996, **143**, L133-L136.
127. Y. Maeda, K. Sato, R. Ramaraj, T. N. Rao, D. A. Tryk and A. Fujishima, *Electrochim. Acta*, 1999, **44**, 3441-3449.
128. C. E. Nebel and J. Ristein, *Thin-Film Diamond II*, Elsevier Academic Press, 2004.
129. J. A. Bennett, J. Wang, Y. Show and G. M. Swain, *J. Electrochem. Soc.*, 2004, **151**, E306-E313.
130. T. Yano, D. A. Tryk, K. Hashimoto and A. Fujishima, *J. Electrochem. Soc.*, 1998, **145**, 1870-1876.
131. H. B. Suffredini, S. A. S. Machado and L. A. Avaca, *J. Braz. Chem. Soc.*, 2004, **15**, 16-21.
132. A. Perret, W. Haenni, N. Skinner, X. M. Tang, D. Gandini, C. Comninellis, B. Correa and G. Foti, *Diamond Relat. Mater.*, 1999, **8**, 820-823.
133. L.-F. Li, D. Totir, B. Miller, G. Chottiner, A. Argoitia, J. C. Angus and D. Scherson, *J. Am. Chem. Soc.*, 1997, **119**, 7875-7876.
134. P. M. Natishan and A. Morrish, *Mater. Lett.*, 1989, **8**, 269-272.
135. Q. Chen, M. C. Granger, T. E. Lister and G. M. Swain, *J. Electrochem. Soc.*, 1997, **144**, 3806-3812.
136. G. M. Swain, *J. Electrochem. Soc.*, 1994, **141**, 3382-3393.
137. R. DeClements and G. M. Swain, *J. Electrochem. Soc.*, 1997, **144**, 856-866.
138. S. Alehashem, F. Chambers, J. W. Strojek, G. M. Swain and R. Ramesham, *Anal. Chem.*, 1995, **67**, 2812-2821.
139. J. W. Strojek, M. C. Granger, G. M. Swain, T. Dallas and M. W. Holtz, *Anal. Chem.*, 1996, **68**, 2031-2037.
140. T. A. Ivandini, B. V. Sarada, C. Terashima, T. N. Rao, D. A. Tryk, H. Ishiguro, Y. Kubota and A. Fujishima, *J. Electroanal. Chem.*, 2002, **521**, 117-126.

141. J. Xu and G. M. Swain, *Anal. Chem.*, 1998, **70**, 1502-1510.
142. A. N. Patel, M. G. Collignon, M. A. O'Connell, W. O. Y. Hung, K. McKelvey, J. V. Macpherson and P. R. Unwin, *J. Am. Chem. Soc.,* 2012, **134**, 20117-20130.
143. J. L. Anderson, L. A. Coury and J. Leddy, *Anal. Chem.*, 1998, **70**, 519-590.
144. G. Kahan, *Indust. Eng. Chem. Anal. Ed.*, 1942, **14**, 549-549.
145. K. Rajeshwar, J. G. Ibanez and G. M. Swain, *J. Appl. Electrochem.*, 1994, **24**, 1077-1091.
146. D. Desmond, B. Lane, J. Alderman, M. Hill, D. W. M. Arrigan and J. D. Glennon, *Sens. Actuators, B*, 1998, **48**, 409-414.
147. W. D. Ellis, *J. Chem. Educ.*, 1973, **50**, A131.
148. H. W. Nürnberg, *Anal. Chim. Acta*, 1984, **164**, 1-21.
149. K. R. Wehmeyer and R. M. Wightman, *Anal. Chem.*, 1985, **57**, 1989-1993.
150. G. Gillain, G. Duyckaerts and A. Disteche, *Anal. Chim. Acta*, 1979, **106**, 23-37.
151. R. Ramesham, *J Mater Sci*, 1999, **34**, 1439-1445.
152. A. Manivannan, D. A. Tryk and A. Fujishima, *Electrochem. Solid-State Lett.*, 1999, **2**, 455-456.
153. A. Manivannan, M. S. Seehra and A. Fujishima, *Fuel Process. Technol.*, 2004, **85**, 513-519.
154. E. A. McGaw and G. M. Swain, *Anal. Chim. Acta*, 2006, **575**, 180-189.
155. O. El Tall, N. Jaffrezic-Renault, M. Sigaud and O. Vittori, *Electroanalysis*, 2007, **19**, 1152-1159.
156. E. Popa, H. Notsu, T. Miwa, D. A. Tryk and A. Fujishima, *Electrochem. Solid-State Lett*, 1999, **2**, 49.
157. B. V. Sarada, T. N. Rao, D. A. Tryk and A. Fujishima, *J. Electrochem. Soc.* 1999, **146**, 1469.
158. S. Jolley, M. Koppang, T. Jackson and G. M. Swain, *Anal. Chem.*, 1997, **69**, 4099.
159. J. Xu, Q. Chen an G. M. Swain, *Anal. Chem.*, 1998, **70**, 3146.
160. T. Yano, E. Popa, D. A. Tryk, K. Hashimoto and A. Fujishima, *J. Electrochem. Soc.*, 1999, **146**, 1081.
161. N. Spataru, B. V. Sarada, D. A. Tryk and A. Fujishima, *Electroanal.*, 2002, **14**, 721.
162. T. N. Rao, T. A. Ivandini, C. Tershima, B. V. Sarada and A. Fujishima, *New Diamond Front. Carbon Technoly.*, 2003, **13**, 79.
163. E. Popa, Y. Kubota, D. A. Tryk and A. Fujishima, *Anal. Chem.*, 2002, **72**, 1724.
164. V. K. Gupta, I. Ali and V. K. Saini, *Environ. Sci. Technol..*, 2004, **38**, 4012-4018.
165. C. Saez, M. Panizza, M. A. Rodrigo and G. Cerisola, *J. Chem. Technol. Biotechnol.*, 2007, **82**, 575-581.
166. C.Terashima, T. N. Rao, B. V. Sarada, D. A. Tryk and A. Fujishima, *Anal. Chem.*, 2002, **74**, 895.
167. V. Uberoi and S. K. Bhattacharya, *Water Environ. Res..*, 1997, **692**, 146.

2 Experimental

2.1 Materials and Chemicals

2.1.1 Chemicals

Ultrapure water with a resistivity of 18.2 Ωcm at 25 ºC (Milli-Q, Millipore Corp.) was used to make all solutions used in this work. The chemicals used in this thesis are listed below in Table 2.1.

Chemical	Formula	Purity	Supplier
Ferrocenyltrimethylammonium Hexafluorophosphate	$FcTMA.PF_6$	N/A	Made in-house
Ruthenium (III) Hexamine Chloride	$Ru(NH_3)_6Cl_3$	98%	Acros Organics
Potassium Ferricyanide	$K_3Fe(CN)_6$	99%	Sigma-Aldrich
Potassium Ferrocyanide	$K_4Fe(CN)_6$		Sigma-Aldrich
Potassium Hexacyanoferrate (II) trihydrate	$K_4Fe(CN)_6•3H_2O$	> 99.99%	Sigma-Aldrich
Iron (II) Sulphate Heptahydrate	$FeSO_4•7H_2O$	≥ 99%	Sigma-Aldrich
Potassium Hexachloroiridate (III)	K_3IrCl_6	98%	Sigma-Aldrich
Lead Nitrate	$PbNO_3$	≥ 99.99%	Sigma-Aldrich
Potassium Nitrate	KNO_3	≥ 99.99%	Sigma-Aldrich
Potassium Nitrate	KNO_3	≥ 99%	Sigma-Aldrich
Sulphuric Acid	H_2SO_4	≥ 95%	Sigma-Aldrich
Sulphuric Acid	H_2SO_4	99.999%	Sigma-Aldrich
Perchloric Acid	$HClO_4$	Reagent grade	Sigma-Aldrich
Agarose	N/A	N/A	Sigma-Aldrich
Silver Nitrate	$AgNO_3$	99.9%	Sigma-Aldrich

Table 2.1 - List of all the chemicals used in this work.

2.1.2 Salt Bridge Preparation

A piece of PVC tubing was cut into a 30 cm length, each end was cut diagonally to leave a sharp interface. A solution of 2% agarose in ultrapure water was prepared, boiling while vigorously stirring was necessary to dissolve all of the solid without burning. To this solution was added 40 g of KNO_3 which was allowed to dissolve, the hot solution was then poured into the PVC tube and allowed to cool.

2.1.3 Polycrystalline Boron Doped Diamond Samples

pBDD materials from four different sources, with dopant densities in the range $9.2 \times 10^{16} – 1.6 \times 10^{21}$ boron atoms cm^{-3}, were utilised in this thesis and are listed in with the relevant results chapters. They include the Naval Research Laboratory (Naval Research Laboratory (NRL), Washington DC, US, electrodes A and C; Element Six (Element Six Ltd (E6), Harwell, UK, electrodes B, D, E and H; Condias (Condias GmbH, Itzehoe, Germany) electrode F and; Advanced Diamond Technologies (Advanced Diamond Technologies (ADT), Inc., Illinois, USA) electrode G. Electrodes D - G are commercially available. Electrodes A-E and H are thick enough ($\geq$ 200 μm) to be freestanding, whilst electrodes F and G are thin film (7 μm and 2 μm thick respectively) and attached to a niobium substrate. Contact angle measurements revealed electrode F was predominantly hydrogen-terminated prior to use, whilst as-grown electrode G had suffered partial air oxidation. These samples and some details of their properties are listed below in Table 2.2, values denoted with * were estimated.

Electrode	Structure	Source	[B] (boron atoms cm^{-3})	Chapter Reference
A	Freestanding, microcrystalline	NRL	9.2×10^{16}	3, 4
B	Freestanding, microcrystalline	E6	2.0×10^{18}	3, 4
C	Freestanding, microcrystalline	NRL	Mid 10^{19}	3, 4
D	Freestanding, microcrystalline	E6	1.9×10^{20}	3, 4
E	Freestanding, microcrystalline	E6	3.0×10^{20}	3, 4
E (all diamond structure)	Freestanding, microcrystalline	E6	3.0×10^{20}	6
F	Nb substrate microcrystalline	Condias	1.9×10^{20}	3
G	Nb substrate microcrystalline	ADT	1.6×10^{21}	3
H	Freestanding, microcrystalline	E6	3.0×10^{20}	5

Table 2.2 – List of all pBDD samples used in this work from various suppliers.

2.2 Diamond Electrode Fabrication

2.2.1 pBDD Disk Preparation

A laser micromachiner (E-355H-3-ATHI-O system, Oxford Lasers) was used to cut pBDD samples of the desired diameter from a large wafer of material. Diamond is a difficult material to cut and requires many passes of the laser, acquisition of a precise cut is realised by using a kerfing procedure. This procedure involves using the laser to make a series of cuts in the pBDD wafer either side of a specified axis.

During the laser cutting process amorphous carbon is formed, this is removed with acid cleaning. Concentrated H_2SO_4 ($\geq$ 95 %, Sigma-Aldrich) was supersaturated with KNO_3, diamond samples were transferred into the acid solution in a Pyrex beaker

which was then placed onto a hotplate stirrer. The beaker and its contents were heated until the solution began to boil, which continued until the brown fumes (NO_2) being given off had changed to white indicating exhaustion of the KNO_3. This step was repeated without adding KNO_3 to ensure that no salt crystals remained. Acid cleaning also serves to yield a reproducible, oxygen-terminated surface that can be recovered with subsequent acid cleaning.[1]

An electrical contact was made to pBDD by sputtering (Edwards E606 sputter/evaporator) a layer of Ti followed by a layer of Au of thickness 20 nm and 400 nm respectively. Annealing then takes place in a tube furnace for 4.5 h at 450 ^{o}C, allowing a carbide to form to the Ti metal which yields a robust ohmic contact.[2]

2.2.2 Glass Sealed Electrode

The majority of electrochemical experiments at ambient conditions were performed with a glass sealed pBDD electrode, allowing precise definition of a 1 mm disk geometry, prepared as described in section 2.2.1. The pBDD was sealed in borosilicate glass (i.d. 1.16 mm, o.d. 2 mm, Harvard Apparatus Ltd, UK) using the heating coil of a capillary puller; sealing was performed under a mild vacuum. A protruding electrical contact was made with copper wire, connected to the back of the pBDD disk with silver loaded epoxy (RS Components Ltd, Northants, UK) which was allowed to set for 24 hours. The end of the glass capillary was then polished on carbimet grit paper disks of decreasing roughness, revealing the sealed pBDD surface from the glass, this type of electrode is shown below in Figure 2.1

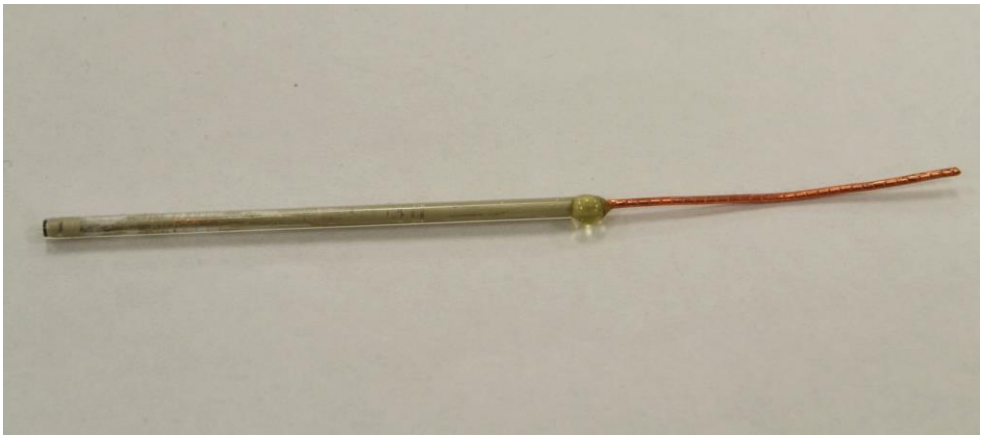

Figure 2.1 – Photograph of glass sealed pBDD electrode used in this thesis.

2.2.3 High Temperature Cell Electrode

A 9 mm diameter disk of pBDD (sample was prepared as described in section 2.2.1, the centre of the back surface of the disk was then deliberately laser etched at low power (ca. 0.5 W) in a grid like pattern of dimensions 3 × 3 mm, in order to produce a rough, matt finish. This helps reduce reflections from the incident laser irradiation (during pulsed heating experiments) and therefore increases total energy absorption in the form of heat.

In order to perform electrochemical measurements during pulsed heating of the BDD electrode, section 5.4, a custom-built electrochemical cell was designed and fabricated in-house. The cell comprised two separate parts, a Teflon vessel and a Perspex window, which were held together with Teflon screws as can be seen in Figure 2.2. The Perspex window has a hole in the centre across which the pBDD disk was mounted and held in place with adhesive Kapton tape (60 µm thickness, 250 – 1000 ^{o}C, R.S. Components Ltd.). Adhesive Kapton tape was also used to mask off the pBDD surface from the solution; a 1 mm disk geometry was formed by using the laser micromachiner to cut a hole in the Kapton film, this is depicted in Figure 2.3. A conductive track was made from the annealed Ti/Au contact on the back face of the

pBDD disk using silver conductive paint (R.S. Components Ltd.) to the top of the Perspex window, allowing an electrical connection to be made to the electrode with a crocodile clip.

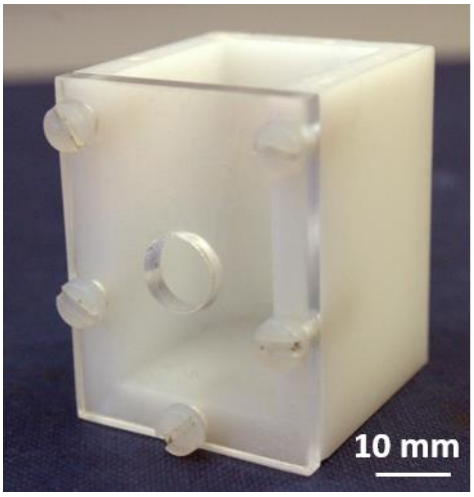

Figure 2.2 - Photograph of custom built cell used for pulsed heating experiments.

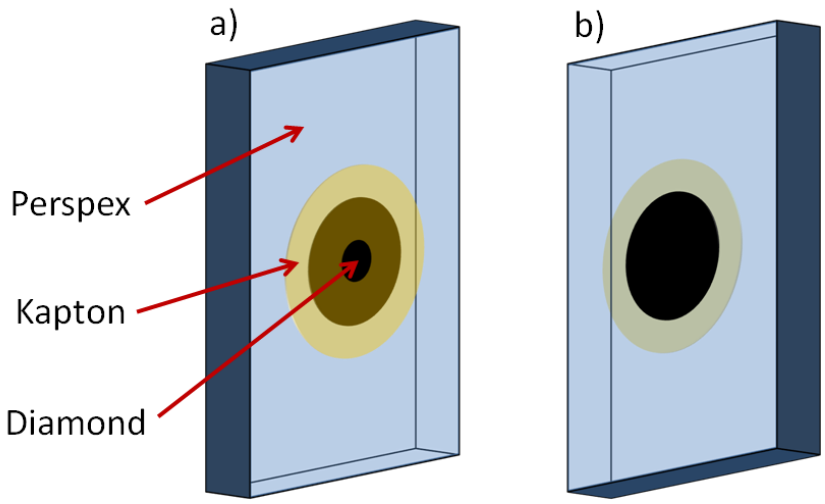

Figure 2.3 - Schematic depiction of diamond disk mounted in Perspex window a) solution facing side and b) irradiation side, the silver electrical contact is omitted for clarity.

2.3 Instrumentation and Techniques

2.3.1 Field-Emission Scanning Electron Microscopy (FE-SEM)

In SEM a focussed beam of electrons is fired at a sample, the interactions between incident electron radiation and the sample produce several types of signal that provide information about the sample composition and topography.[3] Two distinct types of radiation emanate from a sample during irradiation, electrons (beta radiation) and photons (electromagnetic radiation). Beta radiation may manifest from backscattered, secondary or Auger electrons. Backscattering of electrons occurs due to elastic scattering of incident electrons, these electrons possess high energy. When inelastic scattering occurs secondary electrons are emitted that possess low energies (< 50 eV), this type of signal depends on the topography of the sample.[4]

A secondary electron detector mounted in the same orientation of the electron gun may be called an 'in-lens' detector; high resolution imaging of BDD microelectrode arrays was performed by Macpherson *et al*,[5] where this detector allows simultaneous imaging of silver nanoparticles and BDD grain structure. Electromagnetic radiation may range from x-rays to IR with the lower energies (UV-IR) being studied in the technique of cathodoluminescence (CL).[6] Incident electrons may also be absorbed as current as they flow to ground or may be transmitted through the sample. The various types of emission upon electron irradiation of a sample are depicted in Figure 2.4.

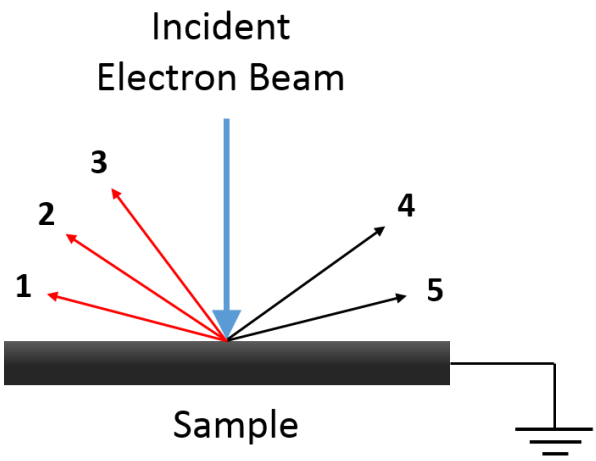

Figure 2.4 – Schematic illustration of the different signals given off by a sample upon electron irradiation; 1) backscattered electrons, 2) secondary electrons, 3) Auger electrons, 4) x-ray photons and 5) UV-IR photons.

An electron gun is used to accelerate electrons under vacuum towards the sample, a series of lenses and apertures are used to focus and condense the beam. In traditional SEM a hot filament generates the electron source relying on thermionic emission. The electron gun in field emission-scanning electron microscopy (FE-SEM) consists of a very sharp metal tip (~ 100 nm), which serves as a cold cathode, held at a potential of typically between 0.1 to 30 kV measured relative to some anode. Electron guns of this type have two main advantages over filament guns; a much higher intensity and smaller spot radius which allows increased resolution.[7]

In this work a high resolution Zeiss Supra 55 VP FE-SEM was used to examine pBDD samples. The wide range of available magnification enables the study of large areas such as the grain structure of microcrystalline diamond and also small features such as deposited metal nanoparticles. An in-lens detector was used for viewing grain structures at a working distance of 4 mm and at accelerating voltages between 1 and 15 kV.

2.3.2 Resistivity Measurements

The resistivity of pBDD was measured with a source meter (Keithley Instruments Inc, Cleaveland, USA) by applying a constant current of 10 μA and recording the resulting voltage/resistance at an ambient temperature of ~ 23 ºC. A four point Van Der Pauw probe configuration was employed using annealed Ti/Au contacts, to negate possible contact resistance effects. The material to be measured is cut into a square geometry and ohmic contacts placed onto each corner, resistance is then systematically measured between adjacent contacts. Repeat measurements are conducted with the source polarity reversed, this helps negate any contact resistance effects. Electrical contact to the diamond was made with micro-positioning probes (Quater Research and Development, Bend, Oregon) positioned on annealed Ti/Au pads, enabling ohmic connection to the pBDD. Measurements conducted at different temperatures employed the use of a temperature controlled stage (THMS600, Linkam Scientific Instruments, Surrey, U.K.). Samples were mounted onto the stage and allowed to reach the target temperature before any electrical measurements were made.

2.3.3 Micro Raman Spectroscopy

Upon photoexcitation a material may re-emit photons either elastically or inelastically; the former is termed Rayleigh scattering and the latter Raman scattering.[8] The term inelastic refers to the change in energy (frequency) of photons upon emission which may experience an energy loss or gain, a Stokes and anti-Stokes shift respectively. A high intensity monochromatic light source such as a laser is used to excite molecules from a ground state to a virtual excited state.[9] When the molecule relaxes to a discrete energy state, which may be higher or lower than its initial state, a photon is emitted of a different energy to that of the excitation energy. Excitation wavelengths used in

Raman spectroscopy may range from UV to IR,[10] the different forms of photon scattering are shown schematically in Figure 2.5.

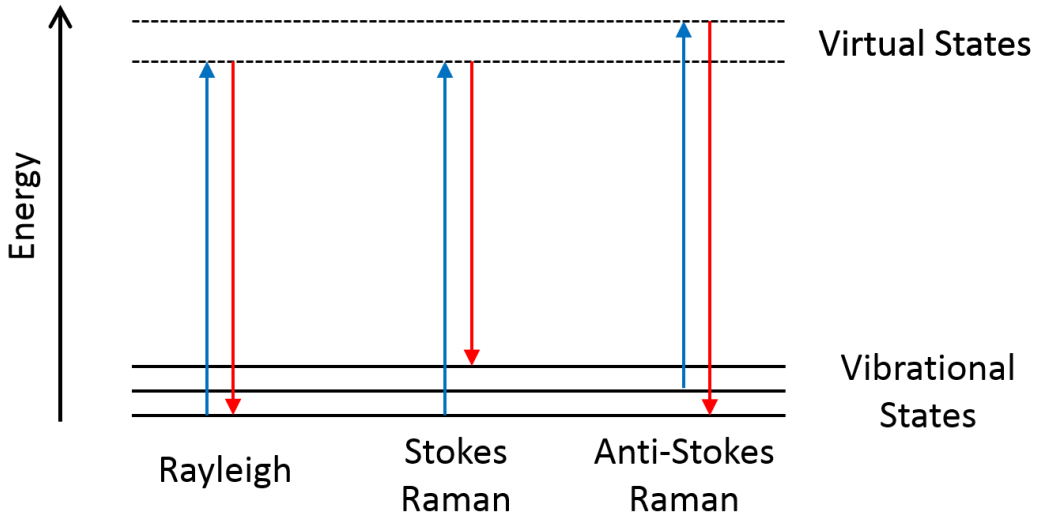

Figure 2.5 – Schematic diagram showing the different modes of photon scattering and their associated transitions.

Diamond is Raman active and observation of spectra yields important information about samples, such as crystalline quality,[11] sp^2 content[12] and boron concentration.[13] Raman spectroscopy in this work was performed with a Renishaw inVia spectrometer connected to an optical microscope, all experiments were conducted at room temperature. Single spot measurements were performed with the 514.5 nm line of an Ar^+ laser running at an optical power of 10 mW, a 50× objective lens was used giving a laser spot size of approximately 2 µm. Mapping experiments[14] (section 4.2.2) that required the collection of many spectra made used of an automated x-y stage; a 100× objective lens allowing better spatial resolution was used in these experiments (~ 1 µm spot size).

2.3.4 X-ray Photoelectron Spectroscopy (XPS)

High energy electromagnetic radiation causes ejection of electrons from an atom, this phenomenon is known as the photoelectric effect.[15] Monochromatic x-rays are fired at the sample to be analysed, these high frequency photons transfer their energy to core electrons allowing them to escape from the atom. If an electron is ejected from an atom near to the sample surface (~ 10 nm),[16] then it may escape into vacuum and be collected and analysed. Measurement of the energy of ejected electrons provides information on the atomic/molecular environment from which the electron originated, whereas the amount of electrons ejected allows quantitative elemental analysis.[17] XPS provides information on different elements which display characteristic binding energies for different core atomic orbitals.

XPS measurements were performed with an Omicron Sphera analyser, an Omicron XM1000 was used providing the monochromated Al K(alpha) x-ray source at an energy of 1486.6 eV, 30^{o} take-off angle giving an approximate 1.1 mm sampling size.

2.3.5 Atomic Force Microscopy (AFM)

AFM is technique useful for the precise study of surface topographies of samples on the nanoscale.[18] A cantilever possessing a very sharp tip is scanned over the sample and topographical information is gained from the interaction forces between the tip and surface features. A laser is shone onto the back of the cantilever which reflects onto a photosensitive diode, this allows precise tracking of the tip deflection. Two common modes of AFM operation are contact mode and tapping mode; in the former a feedback mechanism (oscillation amplitude) is used to maintain a constant force between the tip and sample. In tapping mode AFM, the cantilever is made to oscillate very close to its natural resonant frequency as the tip is scanned across the surface.

AFM was used to assess the surface roughness of samples in Chapter 3, these studies were performed in air on a Veeco EnviroScope AFM with NanoScope IV controller.

2.3.6 Secondary Ion Mass Spectrometry (SIMS)

Quantification of boron dopant levels for some of the CVD grown BDD films in this thesis was achieved with SIMS. For measuring the average [B] of a pBDD film, a relatively large spot size (~ 0.16 mm^2) was used which spans many regions of differing [B]. Grain dependant SIMS was also used employing a smaller spot size (~ 0.05 mm^2) allowing individual grains to be assessed. Ion implantation was used to calibrate the SIMS measurements by introducing an estimated amount of boron (1×10^{19} atoms cm^{-3} at a depth of 1 μm) into a single crystal control sample, the signal due to boron was assumed to be linear in the range 1×10^{14} to 7×10^{21} atoms cm^{-3}. SIMS was performed at the Loughborough Surface Analysis Centre, UK, with a Cameca ims 4f system.

2.4 Electrochemical Measurements

All electrochemical experiments utilised a three electrode setup controlled by a potentiostat; (CompactStat, Ivium Technologies, The Netherlands) or (CHI730A, CH Instruments Inc. TX) connected to a laptop computer. A thick coiled platinum wire was used as the counter electrode and either a commercial SCE (CHI150, CH Instruments Inc. TX) or silver-silver chloride wire (Ag/AgCl) served as the reference electrode.

2.5 High Temperature Electrochemistry

2.5.1 Continuous Heating

Isothermal experiments were carried out by heating the entire electrochemical cell including all electrodes; CV experiments were then performed in the usual manner. A heated water bath apparatus attached to a jacketed glass cell, Figure 2.6, was used to change the temperature of the electrochemical system in a controlled way. Some experiments required measurements in two separate solutions, one held at ambient conditions and the other heated. The solution to be heated was placed into the water bath, with the other solution being kept sufficiently far away to maintain ambient conditions, the two solutions were connected with a saturated KNO_3 salt bridge prepared as described in section 2.1.2.

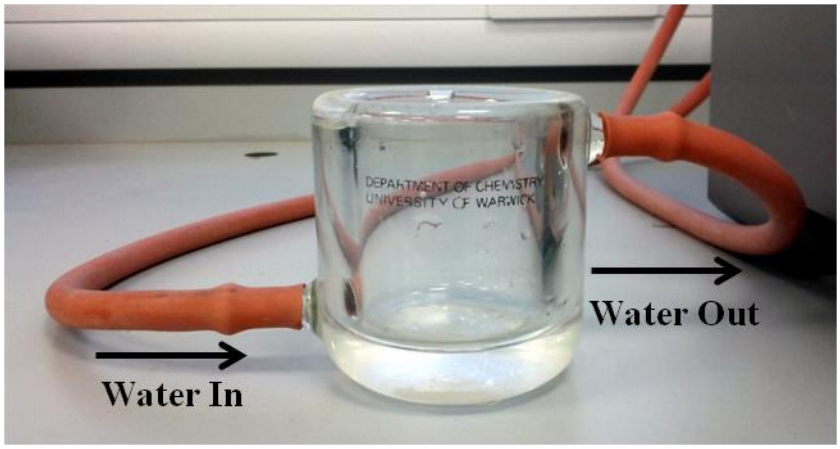

Figure 2.6 - Photograph of jacketed glass cell used for continuous heating experiments. The cell is connected to a thermostatted water bath.

2.5.2 Pulsed Laser Heating

To perform CV with pulsed laser heating, hereafter named temperature pulse voltammetry (TPV), a potentiostat was used in a three electrode configuration. During standard CV a varying potential is applied to the working electrode as a function of

time, the applied potential is measured against a reference electrode that is in contact with the same solution. The computer controlled potentiostat produces a 'potential staircase'. For general electrochemical studies this is not normally problematic, provided that the potential steps of the staircase are sufficiently small, typically 1 mV. The data sampling rate is controlled by the nature of the potential sweep, smaller potential steps result in a higher sampling rate. For TPV in this work a sampling rate of 400 samples/s was used, which allows 4 current samples to be recorded for the duration of a 10 ms heat pulse.

A dual-channel arbitrary function generator (AFG3022B, Tektronix) was used as a master controller for TPV experiments to ensure that all instruments and events were synchronised. When manually triggered, the function generator sends a signal to trigger a potentiostat whilst simultaneously sending a pulse-type square waveform to a laser diode controller (LDC1000, Laser Electronics Ltd Lincolnshire, England). This is shown schematically in Figure 2.7; an expanded view of the simultaneous energy perturbation applied to the working electrode is shown in Figure 2.8. A diode laser (LM-D0296, LIMO) was used for all pulsed temperature experiments: 914.7 nm, 30 W, ~ 1 mm spot size.

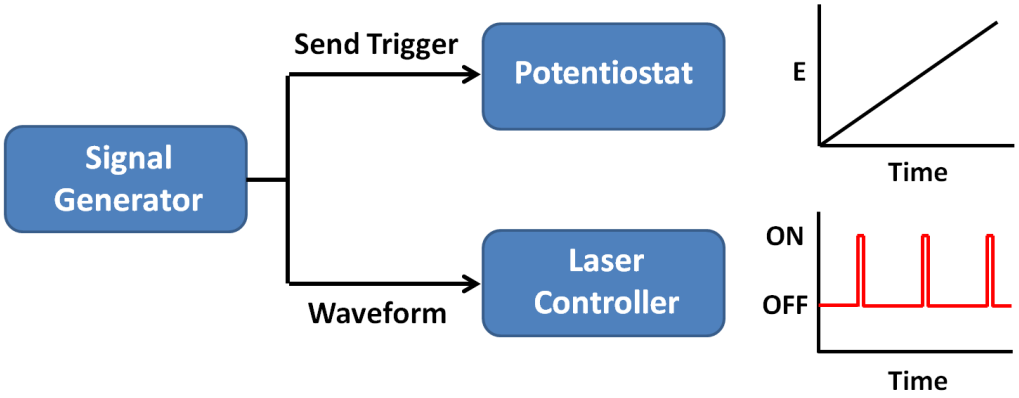

Figure 2.7 - Schematic description of how an electrochemical experiment is performed whilst pulsed heating is applied to the electrode simultaneously.

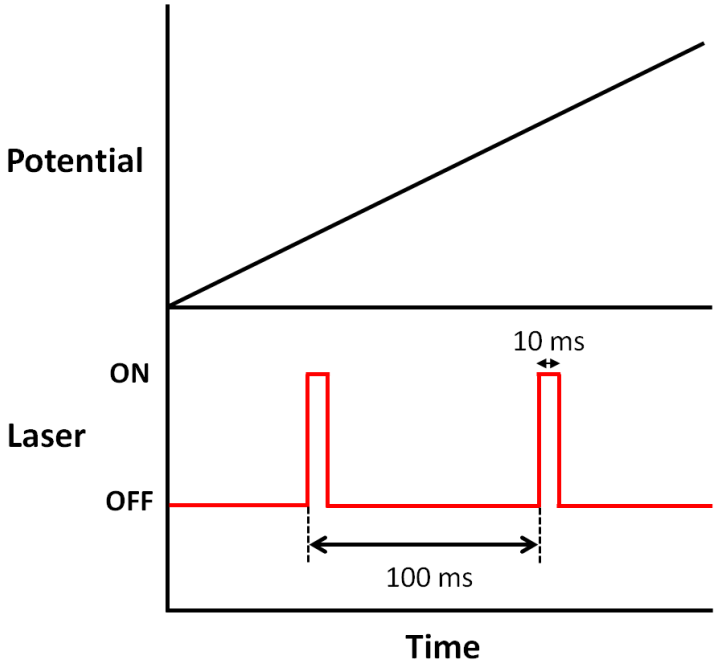

Figure 2.8 - Expanded schematic for simultaneous application of potential sweep and laser pulses on pBDD electrode during TPV.

After the function generator is manually triggered, the potentiostat imposes a potential staircase on the electrochemical cell described above in section 2.2.3, this would result in an ordinary CV experiment if no laser heating occurred. However, during TPV, the power of the diode laser is set to the desired value (0 – 30 W) and is also triggered by the function generator. A pulse type waveform, with a controllable period and pulse width, is fed to the laser diode controller which produces a pulsed laser beam that is

focused onto the rear face of the diamond electrode (sample H). The outcome is data being collected by the potentiostat whilst the working electrode is struck by a pulsed laser beam, producing observable peaks in current as the electrode rapidly heats and cools, corresponding to the applied laser pulses. The raw data collected comprises the entire experiment; data is collected throughout, resulting in both heated and ambient states of the electrode, including any transition between the two. The treatment and analysis of this raw data is described later in section 5.3.4.

For typical TPV experiments involving redox mediators, the pulse period and pulse width were set to 100 ms and 10 ms respectively, giving an effective duty cycle (ratio of 'off time' to 'on time') of 10:1. It must be noted that a compromise exists between varying the relative durations of the laser being on or off. Larger ratios (> 10:1) result in a longer time to cool between pulses but fewer 'hot' data points collected for a given scan rate, whereas smaller ratios (< 10:1) produce more hot data points but more TPV distortion at higher laser powers. A compromise also exists when setting the scan rate for a TPV experiment; slower scan rates allow longer cooling times between pulses though fewer data points are collected by the potentiostat. A scan rate of 100 mV s^{-1} was chosen for TPV experiments, as when combined with a duty cycle of 10:1 (100:10 ms) was found to give a reasonable balance.

2.6 References

1. I. Yagi, H. Notsu, T. Kondo, D. A. Tryk and A. Fujishima, *J. Electroanal. Chem.*, 1999, **473**, 173-178.
2. T. Tachibana, B. E. Williams and J. T. Glass, *Phys. Rev. B.*, 1992, **45**, 11975-11981.
3. P. W. Hawkes and J. C. H. Spence, *Science of Microscopy*, Springer, 2007.
4. H. Seiler, *J. Appl. Phys.*, 1983, **54**, R1-R18.
5. A. L. Colley, C. G. Williams, U. D'Haenens Johansson, M. E. Newton, P. R. Unwin, N. R. Wilson and J. V. Macpherson, *Anal. Chem.*, 2006, **78**, 2539-2548.
6. B. G. Yacobi and D. B. Holt, *J. Appl. Phys.*, 1986, **59**, R1-R24.
7. A. V. Crewe, D. N. Eggenberger, J. Wall and L. M. Welter, *Rev. Sci. Instrum.*, 1968, **39**, 576-583.
8. R. J. Nemanich, J. T. Glass, G. Lucovsky and R. E. Shroder, *J. Vac. Sci. Technol., A*, 1988, **6**, 1783-1787.
9. R. L. McCreery, *Raman Spectroscopy for Chemical Analysis*, John Wliey & Sons, 2000.
10. S. M. Leeds, T. J. Davis, P. W. May, C. D. O. Pickard and M. N. R. Ashfold, *Diamond Relat. Mater.*, 1998, **7**, 233-237.
11. J. Asmussen, J. Mossbrucker, S. Khatami, W. S. Huang, B. Wright and V. Ayres, *Diamond Relat. Mater.*, 1999, **8**, 220-225.
12. K. W. R. Gilkes, S. Prawer, K. W. Nugent, J. Robertson, H. S. Sands, Y. Lifshitz and X. Shi, *J. Appl. Phys.*, 2000, **87**, 7283-7289.
13. M. Bernard, A. Deneuville and P. Muret, *Diamond Relat. Mater.*, 2004, **13**, 282-286.
14. M. Mermoux, B. Marcus, G. M. Swain and J. E. Butler, *J. Phys. Chem. B.*, 2002, **106**, 10816-10827.
15. N. Paik, *Surf. Coat. Technol.*, 2005, **200**, 2170-2174.
16. J. M. Hollander and W. L. Jolly, *Acc. Chem. Res.*, 1970, **3**, 193-200.
17. J. C. Vickerman and I. S. Gilmore, *Surface Analysis The Principal Techniques*, Wiley, 2009.
18. G. Binnig, C. F. Quate and C. Gerber, *Phys. Rev. Lett.*, 1986, **56**, 930-933.

3 Examination of the Factors Affecting the Electrochemical Performance of Oxygen Terminated pBDD Electrodes

In order to produce polycrystalline oxygen-terminated boron doped diamond (BDD) electrodes suitable for electroanalysis, *i.e.* widest solvent window, lowest capacitive currents, stable and reproducible current responses and capable of demonstrating fast electron transfer, for outer sphere redox couples, the following factors must be considered. The material must contain enough boron that the electrode shows metal-like conductivity. Electrical measurements demonstrate this is achieved at [B] > 10^{20} B atoms cm^{-3}. Even though BDD contains a lower density of states than a metal it is not necessary to use extreme doping levels to achieve fast HET. An average [B] ~ 3 × 10^{20} B atoms cm^{-3} was found to be optimal; increasing [B] results in higher capacitative values and increases the likelihood of NDC incorporation. Hydrogen-termination also causes a semi-conducting BDD electrode to behave ~ metal-like due to the additional surface conductivity hydrogen-termination brings. Thus, unless [B] of the material is known the electrochemical properties of the electrode may be incorrectly interpreted. It is essential during growth that NDC is minimized as it acts to increase capacitive currents and decrease the solvent window. We found complete removal of NDC after growth using aggressive acid cleans, acid cycling and diamond polishing impossible. Although hydrogen-termination can mask the NDC signature in the solvent window and lower capacitive currents, this is not a practical procedure for improving sensitivity in electroanalysis. For the optimal pBDD electrode, cleaning with alumina polishing was found to be an effective way to produce well-defined,

stable and reproducible surfaces, which support fast (reversible) HET for $Fe(CN)_6^{4-/3-}$ electrolysis. This is the first time this has been reported at an NDC-free oxygen-terminated surface. Finally, the hydrogen terminated surface at lapped (polished) electrodes was shown to be electrochemically unstable, an effect which was exacerbated at extreme potentials.

3.1 Introduction

Carbon electrodes continue to be the subject of intensive investigation, given their importance in many fields ranging from sensors,[1, 2] to fuel cell catalyst supports.[3-5] A significant body of research is dedicated to understanding how material properties control electrochemical characteristics, for both inner and outer sphere redox couples, in order to optimise electrode performance.[6-9] BDD is an important member of the carbon electrode family, which is being employed increasingly in electrochemical applications.[2, 10-12] In contrast to the vast majority of all other carbon electrodes, BDD is the only carbon electrode, in its purest form, which does not contain sp^2 carbon. This leads to extremely interesting electrochemical properties,[13, 14] such as the widest potential window of all carbon electrodes, low background currents and an increased resistance to electrochemical fouling,[2, 15-17] making it particularly attractive for use in electroanalysis.

Depending on the growth conditions employed, both thin and thick films can be grown, where the grain size of the growth face typically increases with film thickness. During growth it is also possible to vary the boron dopant density [B] of the material, and hence electrical properties, by controlling the concentration of boron in the gas phase.[18-23] At high [B], it is easier to synthesise poly- (or nano-) crystalline material than single crystal BDD.[24] Hence the vast majority of electrochemical applications focus on this material, which is typically synthesised using the CVD method.

As crystallographic orientation influences the amount of boron taken up,[25] poly- (or nano) crystalline material has a boron content which varies heterogeneously. As for other carbon materials, such as carbon nanotubes, the growth conditions also determine the quality of the resulting material, in terms of the sp^2-sp^3 ratio.[26-28] For

BDD, sp^2 carbon, residing either at grain boundaries or within the grain itself, can affect electrochemical performance.

As CVD growth occurs in a hydrogen rich atmosphere, the majority of studies tend to focus on hydrophobic hydrogen-terminated BDD electrodes, often referred to as, "as grown".[29-31] However, the hydrogen-terminated layer on intrinsic diamond, in the presence of water, is now known to support surface conductance.[32,33] Furthermore, although the hydrogen-terminated surface is stable over many months in air, the surface can gradually oxidise.[31, 34, 35] In contrast, oxygen-termination (as described in section 1.2.2) does not result in a measurable surface conductivity.

In this paper we explore the effect of [B], sp^2 carbon content, and different pre-treatment processes on the electrochemical response of both inner and outer sphere electron transfer mediators at oxygen terminated pBDD electrodes. In this way we provide a benchmark for other researchers wishing to work with oxygen-terminated pBDD electrodes with material properties which show fast heterogeneous electron transfer (for outer sphere redox couples over a wide potential range) whilst maintaining as low as possible background signals with the widest extended solvent window characteristics. We also investigate and compare the electrochemical stability of lapped (~ nm roughness) oxygen and hydrogen-terminated pBDD electrodes over different electrochemical potential ranges.

3.2 Results and Discussion

3.2.1 BDD Characterisation

In order to explore the factors which affect the electrochemical response and stability of oxygen-terminated pBDD, seven different electrodes, of defined area (1 mm diameter) from various sources spanning a range of diamond morphologies, boron

content and quality were investigated. Studies initially focused on freshly cleaned surfaces. Prior to electrochemical analysis, the material structure, electrical properties and NDC carbon content of samples used in this study were characterised using SIMS, resistivity measurements, FE-SEM and micro-Raman, and are summarised in below in Table 3.1. Quoted capacitances are calculated from measured geometric areas.

Electrode	**Source**	**[B] (boron atoms cm^{-3})**	**Resistivity (Ωcm)**	**sp^2 signature**	**Solvent Window (V)**	**Capacitance (μFcm^{-2})**
A	NRL	9.2×10^{16}	40700	No	4.11	2.9 (± 0.1)
B	E6	2.0×10^{18}	87.9	Yes	3.89	8.5 (± 0.5)
C	NRL	Mid 10^{19}	41.55	No	3.67	3.3 (± 0.3)
D	E6	1.9×10^{20}	0.061	Yes	3.53	11 (± 0.5)
E	E6	3.0×10^{20} (av) 1.9×10^{20} (lo) 4.7×10^{20} (hi)	0.053	No	3.60	6.5 (± 0.4)
F as-received O-term	Condias	1.9×10^{20}	-	Yes	2.30 1.43	3.9 (± 0.4) 23 (± 0.5)
G as-received O-term	ADT	1.6×10^{21}	-	Yes	1.38 -	153 (± 3) 381 (± 8)

Table 3.1 – Material and electrochemical characteristics of pBDD electrodes from various sources.

The electrodes fall into two main categories where the designations low, med, high and very high in parentheses refer to the relative boron concentration, freestanding microcrystalline pBDD films, electrodes A (low) – E (high) increasing in average [B] from 9.2×10^{16} (electrode A) - 3×10^{20} (electrode E) all > 200 μm thick) and thin film microcrystalline pBDD on niobium substrates, the latter denoted by (thin). Figure 3.1 shows the grain structure revealed by in-lens secondary electron FE-SEM images for the seven pBDD electrodes. Electrodes A (low) –E (high) have all been lapped,[36] to reveal a surface roughness of < 5 ± 0.5 nm rms, as determined by AFM (data not

shown). The thinness of electrodes F (high, thin) and G (very high, thin) means they cannot be polished; they have as-grown surface rms roughnesses of 1.9 ± 0.4 μm and 9.3 ± 0.4 nm respectively, determined by white light interferometry (data not shown).

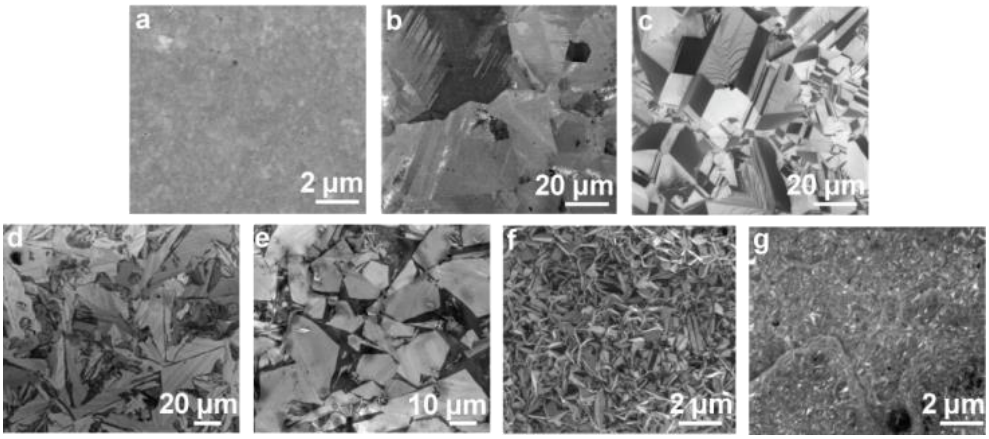

Figure 3.1 - In-lens FE-SEM images of pBDD electrodes A – G (a – g respectively).

Of the freestanding electrodes, A (low) is the thinnest at 210 μm and thus has the smallest grain size ranging from 100 nm to 1 μm. In contrast, B (low-mid) is the thickest at 880 μm with grain size from 7 to 100 μm, whilst C (mid) is 380 μm thick with grain size in the range 2 to 25 μm. While the thickness of electrodes D (high) and E (high) are similar at ca. 635 μm and contain similar [B] (Table 3.1), the randomly orientated grain structure is different (Figure 3.1 (d) and (e)). This is due to differences in the pressure, power density and source carbon concentrations of the growth plasma as well as the deposition temperature of the substrate.[37] Previous FE-SEM work on pBDD material of a similar boron dopant density to electrodes D (high) and E (high) showed that the dark regions correlated with more highly boron doped regions. By inference this is also most likely true for electrodes B (low-mid) and C (mid).[38]

Average [B] was determined by SIMS for each electrode, apart from C (mid) which was previously reported to have an average [B] of mid 10^{19} boron atoms cm^{-3}.[29] For

sample E (high) the grain size meant it was also possible to take SIMS measurements in both the high and lower doped grains, showing a greater than ×2 difference in [B] (Table 3.1). Electrical sheet resistivity measurements were only possible for the freestanding electrodes, as the thin film electrodes reside on a conducting support. Importantly, a clear trend of decreasing resistivity with increasing average [B] is observed (Table 3.1).[22] The resistivity and SIMS data indicate that electrodes D - F are just above the metallic threshold (D (high) and F (high, thin) have the same doping level),[18, 39] whilst A (low) – C (mid) are in the semiconducting region.[20, 40] G (very high) is doped (1.6×10^{21} boron atoms cm^{-3}) strongly into the metallic regime.

Micro-Raman spectroscopy was used to investigate the sp^3-sp^2 content of the seven electrodes and also provide further qualitative information on [B]. Figure 3.2 shows typical micro-Raman spectra taken at a wavelength of 514.5 nm for electrodes A–G, (a-g) respectively. All spectra are representative of many (n = 7) recorded in different locations. Figure 3.2 (d) and (e) contain two spectra as it was possible to interrogate both the high (black line) and low (red line) doped grains of electrodes D (high) and E (high). The diamond zone centre optical phonon peak, attributed to sp^3 carbon bonding, is obvious in all spectra, occurring at ~ 1332 cm^{-1} for electrodes A (low) – C (mid), whereas a shift to lower wavenumbers is observed for electrodes D (high) – G (very high, thin), especially in the darker (FE-SEM) grains, consistent with higher [B].[41] Asymmetric deformation and attenuation of the sp^3 peak, is also observed for electrodes D(high) – G(very high), a feature attributed to a Fano-type interference between the discrete zone centre optical phonon and a continuum of electronic excitations, typically seen at [B] > 10^{20} boron atoms cm^{-3}.[42-44] Broad features at ca. 500 cm^{-1} and 1220 cm^{-1} are seen only for electrodes D (high) – G (very high), and are more prominent in the higher doped grains (D (high) and E (high)). These peaks have

also been reported in the literature for other BDD materials when [B] is in the range $10^{20} – 10^{22}$ atoms cm^{-3}.[39]

NDC such as graphite and amorphous carbon, is typically seen in polycrystalline BDD between 1400 to 1600 cm^{-1}.[45] Within the resolution of micro-Raman, electrodes C (mid) and E (high) show no evidence of NDC, whereas electrodes B(low-mid), D (high), F (high, thin) and G(very high, thin) all show NDC features, as highlighted in the higher resolution inset of Figure 3.2 (b) and Figure 3.2 (d), (f) and (g). NDC features are easier to see in spectra associated with the metallic electrodes D (high), F (high, thin) and G (very high, thin) due to the attenuation of the sp^3 peak as a result of high boron uptake. The least doped electrode A (low) shows a high background, most likely due to luminescence, which can mask the presence of NDC.[46, 47] Note, for electrodes A (low), B (low-mid) and D (high) even after diamond polishing and stringent acid cleaning, NDC is still present. Interestingly, the NDC signal in electrode D (high) appears only to be prominent in the higher doped grains, as shown in Figure 3.2 (d) and in Raman maps, reported in section 4.2.2, where it is also clear the NDC is prominent within the grain and not just at boundaries. These higher doped, lower quality grains constitute less than half the surface (as determined from FE-SEM). In contrast, single point Raman measurements and Raman mapping of electrode E (high) shows no evidence of sp^2 content within any grain.

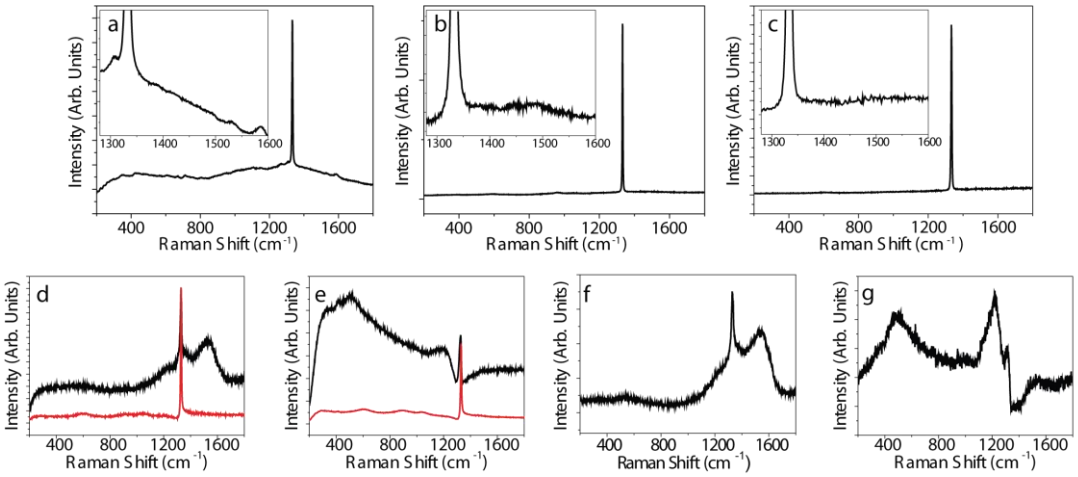

Figure 3.2 - Typical Raman spectra for the seven pBDD electrodes A-G (a – g respectively) recorded at room temperature with a 514.5 nm laser. The insets in spectra a, b and c are zoom-ins of the sp^2 (NDC) region, (d) and (e) show Raman spectra for the low doped (red) and higher doped (black) grains.

3.2.2 pBDD Background Electrochemical Processes

Solvent windows for electrodes A (low) - G (very high) were recorded in 0.1 M KNO_3 (pH = 6.5) at a scan rate of 100 mV s^{-1} and compared against a commercially available 2 mm diameter disk Pt and 3 mm diameter disk GC electrode, as shown in Figure 3.3, where the CVs have been vertically offset for clarity. This is further emphasised in Figure 3.4, where CVs of electrodes D (high) and E (high), along with Pt and GC, are plotted on the same graph. The electrochemical process of water decomposition (for a given pH) defines the solvent window, where hydrogen and oxygen evolution takes place at cathodic and anodic extremes, respectively. Here we define the anodic and cathodic potential limits as the potential at which a current of 0.4 mA cm^{-2} is passed for water electrolysis, as documented in Table 3.1. For Pt and GC due to the high background processes (> 0.4 mA cm^{-2}) it was not possible to quote a solvent window using this definition.

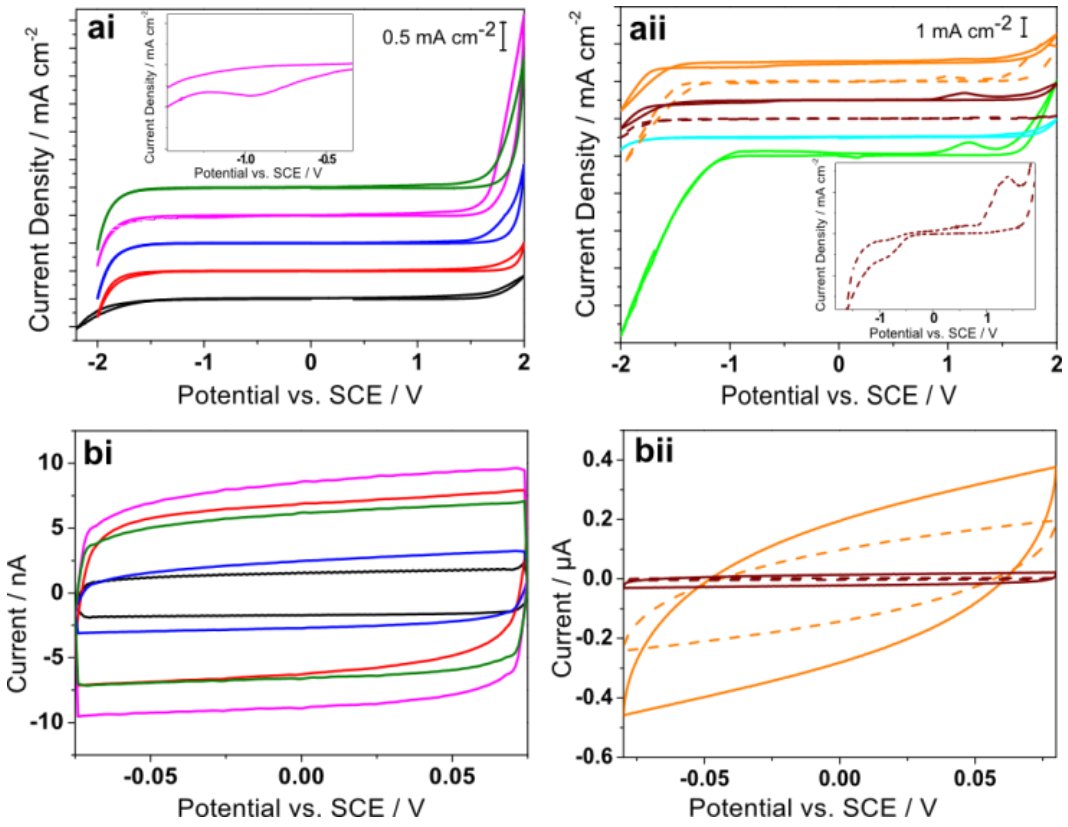

Figure 3.3 - CVs in aerated 0.1 M KNO_3 recorded at a scan rate of 0.1 V s^{-1} over the potential range (a) -2 V to 2V (where CVs have been vertically offset for clarity) and (b) -0.07 V to 0.07 V vs. SCE, for (i) 1 mm diameter electrodes A (black), B (red), C (blue), D (pink) and E (green) and (ii) electrodes F (brown) and G (orange), as-grown (dashed) and acid-cycled (solid). Also shown is the response for platinum (light green) and glassy carbon (light blue). Note the difference in current density scales between (a) and (b) and also (bi) and (bii).

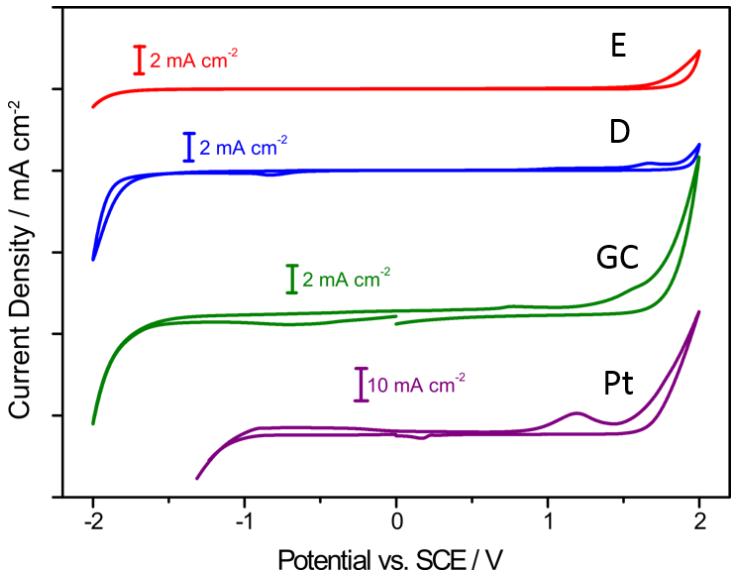

Figure 3.4 - CV in 0.1 M KNO_3 recorded at a scan rate of 0.1 V s^{-1} for electrodes D (blue), E (red), glassy carbon (green) and platinum (purple). The CVs have been plotted on different scales and vertically offset for clarity.

For freestanding pBDD electrodes A (low) – E (high), two trends are apparent; firstly all show wider potential windows than Pt and GC (Figure 3.3 (ai) and (aii), Table 3.1 and Figure 3.4). Secondly, as [B] increases, the solvent window can be seen to decrease slightly (Table 3.1 and Figure 3.3 (ai)).[45] Electrode A (low), which contains the lowest [B], and has the highest resistivity, exhibits the widest solvent window, especially in the cathodic region, due to the limited number of charge carriers, especially at negative potentials. To be efficient, water electrolysis requires the presence of catalytic sites on the electrode surface (inner sphere electron transfer).[48, 49] Water electrolysis is hindered at metallic pBDD electrodes, D (high) and E (high), compared to GC and Pt, most likely due to a lack of available binding sites on the oxygen-terminated surface to mediate HET.[50] On Pt and GC, both unfilled d-orbitals and reactive quinine-like groups are present, respectively, enabling more efficient (better binding) water-electrode interactions.[51, 52] Interestingly, the presence of NDC in electrode D (high) is not sufficient to significantly affect the width of the solvent

window, as it shows a similar solvent window to negligible NDC electrode, E (high). However, while the CVs for electrodes A (low) – C (mid) and E (high) appear featureless between -1.5 V and +1.5 V, electrode D (high) does show evidence of a reduction peak between -0.7 and -0.95 V (Figure 3.3 (ai) inset), most likely due to NDC impurities providing catalytic sites for oxygen reduction. Similar responses have been reported for pBDD electrodes which contain sp^2 carbon.[29, 53]

For the thin film electrodes, as-grown electrode F (high, thin) shows a wider solvent window than G (very high, thin). Features are evident in the CV for electrode F at +1.4 V and -0.95 V (Figure 3.3 (aii) inset) which increase significantly in magnitude and shift to more kinetically facile potentials of +1.15 V and -0.91 V, after potential cycling in acid, due to the increased presence of oxygen containing redox active NDC impurities.[28, 54] This is also observed to a greater extent for electrode G. These processes were greater in magnitude for the first acid cycle, decreasing with subsequent cycles (data not shown) until a constant response was observed (data in Figure 3.3 (aii)), indicative of a decrease in NDC content.[29, 55] However not all NDC was removed. Acid cycling was found to decrease the solvent window of both electrodes (Table 3.1).

From Raman, although the NDC content of electrode F (high, thin) appears similar to that of the highly doped grains in electrode D (high), the currents associated with NDC-driven electrochemical processes are almost a factor of ten greater at electrode F. Although electrode F is rougher than D (roughness factor ~ 3.5) this is unlikely to account for the order of magnitude increase. Instead, we attribute the difference to the fact that over half the surface of electrode D contains lower doped and importantly, negligible NDC containing grains. In contrast, no area of electrode F was found to be NDC free on the scale of the micro-Raman measurement. Finally, for the highest

doped electrode (G), both as-received and oxygen terminated, the solvent window is not as wide as that for glassy carbon (Table 3.1).

Capacitance values, *C*, of 2.9 (± 0.1) μF cm^{-2}, 8.5 (± 0.5) μF cm^{-2}, 3.3 (± 0.3) μF cm^{-2}, 11 (± 0.5) μF cm^{-2} and 6.5 (± 0.4) μF cm^{-2} were determined from the CV data presented in Figure 3.3 (bi) for the pBDD electrodes A-E respectively at 0 V vs. SCE in 0.1 M KNO_3 using, $C = i/2vA_{geometric}$,where *i* is the current, *v* is the scan rate and $A_{geometric}$ the geometric electrode area. The measured values are all lower than that measured at the GC and Pt electrodes, 24 (± 2) μF cm^{-2} and 35 (± 3) μF cm^{-2}, respectively. This is likely to originate from the lower local density of states for pBDD compared to classical electrode materials,[56] and a significant reduction in surface driven redox processes, especially in the case of negligible NDC content. By comparing the capacitance values measured at the three NDC-free pBDD electrodes, A (low), C (mid) and E (high), it can be seen that increasing boron content acts to increase the measured capacitance, most likely due to an increasing LDOS. Based on boron content alone, electrodes B (low-mid) and D (high) have higher capacitance values than expected. We attribute this to the presence of NDC.

Thin film electrode F (high, thin) gave significantly higher capacitance values after oxidation (23 (± 0.5) μF cm^{-2}) via acid cycling, as opposed to when as-grown (H-terminated: 3.9 (± 0.4) μF cm^{-2}), again most likely due to revealing a significant number of oxygen containing redox active surface groups. Although a similar affect was seen with the highest doped electrode G (very high, thin) the capacitance values are abnormally high for both as-received and acid cycled; 153 (± 3) μF cm^{-2} to 381 (± 8) μF cm^{-2}. Very large capacitances at heavily doped BDD has been previously observed and attributed to NDC content,[57] however, as the Raman spectrum for electrode G does not indicate significantly high sp^2 content we speculate that the

material may contain cracks and pinholes not visible in FE-SEM,[58] or boron carbide phases which adversely affect the electrochemical response.[59] Unfortunately the Raman signature of boron carbide is likely to be masked by features associated with BDD.[60]

3.2.3 pBDD Outer-Sphere Redox Processes

To assess the performance of the seven pBDD electrodes, the electrochemical CV characteristics were recorded for three outer-sphere redox active species, whose formal potentials, $E^{0'}$ cover a wide potential range, all reported with respect to a SCE reference electrode. These include $IrCl_6^{2-/3-}$ ($E^{0'}$ = 0.67 V), $FeCp_2CH_2N(CH_3)_3^{+/2+}$ hereafter referred to as $FcTMA^{+/2+}$ ($E^{0'}$ = 0.35 V) and $Ru(NH_3)_6^{3+/2+}$ ($E^{0'}$ = -0.16 V) as shown in Figure 3.5 (a) (freestanding pBDD) and Figure 3.5 (b) (thin film pBDD). The peak to peak separations, ΔE_p, for each pBDD electrode are shown in Table 3.2.

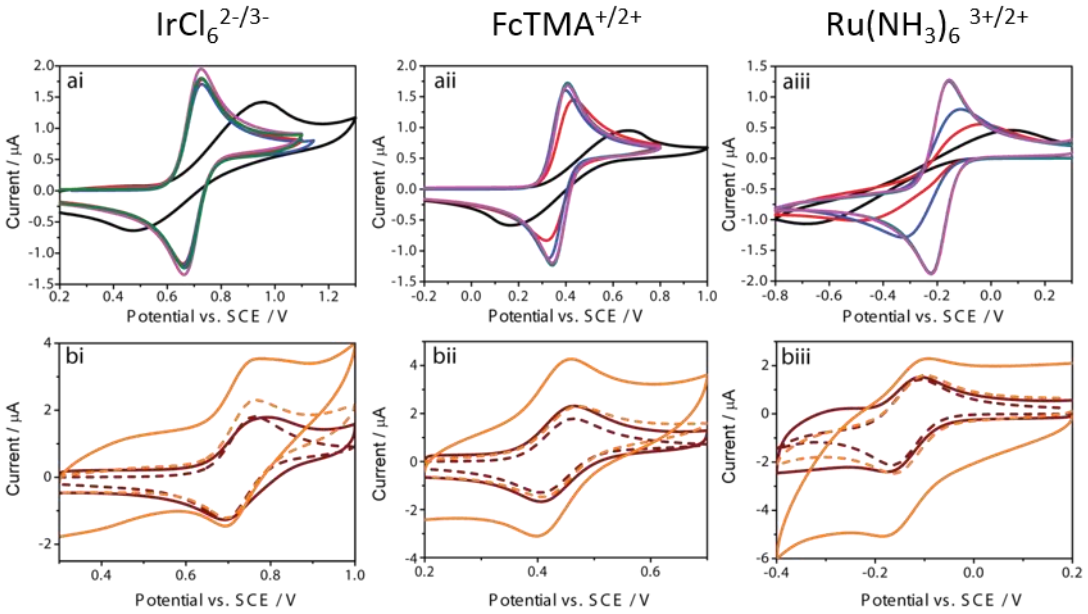

Figure 3.5 - CVs performed with 1 mm diameter disc pBDD (a) electrodes A (black), B (red), C (blue), D (pink) and E (green) and (b) electrodes F (brown) and G (orange), with an as-grown (dashed) or oxygen-terminated (solid) surface, at a scan rate of 0.1 V s^{-1} for (i) the oxidation of 1 mM $IrCl_6^{3-}$, (ii) the oxidation of 1 mM $FcTMA^+$ and (iii) the reduction of 1 mM $Ru(NH_3)_6^{3+}$ in 0.1 M KNO_3.

pBDD Electrode	1 mM $IrCl_6^{2-/3-}$ ΔE_p (mV)	1 mM $FcTMA^+$ ΔE_p (mV)	1 mM $Ru(NH_3)_6^{3+/2+}$ ΔE_p (mV)
A (R = 51.8 kΩ)	554 (±9)	589 (±7)	642 (±6)
B (R = 1119 Ω)	80 (±6)	105 (±6)	615 (±8)
C (R = 180 Ω)	69 (±3)	72 (±9)	212 (±9)
D (R = 0.48 Ω)	62 (±2) $k^0_{app} \geq 0.1$	62 (±3) $k^0_{app} \geq 0.1$	68 (±4) $k^0_{app} = 0.04$
E (R = 0.43 Ω)	61 (±2) $k^0_{app} \geq 0.1$	61 (±2) $k^0_{app} \geq 0.1$	65 (±2) $k^0_{app} = 0.06$
F; As-received O-term	76(±2) 84.5	64 (±3) 60.5	66.5(±4) 55.5
G; As-received O-term	67.5 (±2) 72.5	63.5 (±2) 60.5	66 (±2) 95

Table 3.2 - Summary of electrochemical characteristics of the seven different pBDD electrodes, all performed in 0.1 M KNO_3

For electrodes A (low) –E (high), for the mediators $IrCl_6^{3-}$, $FcTMA^+$ and $Ru(NH_3)_6^{3+}$, the lowest doped electrode A shows the largest ΔE_p (and smallest peak currents, i_p) which increases in value, with a corresponding decrease in i_p, as the formal potential of the redox species becomes more negative. This is further exacerbated by increasing the concentration of the redox species (data not shown), reflective of the p-type semiconducting nature of electrode A. A similar trend is seen for the higher doped semiconducting electrodes B (low-mid) and C (mid), except the observed ΔE_p values are smaller.

For electrodes D (high) and E (high), the ΔE_p values are very close to reversible for all three redox mediators investigated, irrespective of the potential range. This indicates that these electrodes are doped sufficiently to behave as metal-like electrodes, as even in the negative potential window, where charge depletion effects

dominate for semiconducting electrodes there are a sufficient number of charge carriers available to maintain efficient HET.

3.2.4 Finite Element Simulations

A finite element model to simulate CVs at a 1 mm diameter disk pBDD electrode as a function of k^0 and electrode resistances using Butler-Volmer kinetics was constructed using COMSOL Multiphysics 4.3 (COMSOL AB, Sweden). Typically, triangular mesh elements were used in each simulation with the greatest mesh resolution at the pBDD boundaries. The following equation was solved to describe diffusion within the 2D-axisymmetric geometry:

$$\frac{\partial c_i}{\partial t} = D_i \left(\frac{\partial^2 c_i}{\partial r^2} + \frac{1}{r}\frac{\partial c_i}{\partial r} + \frac{\partial^2 c_i}{\partial z^2} \right) \tag{3.1}$$

where c_i (mol cm^{-3}) and D_i represent the concentration and the diffusion coefficient of species i ($FcTMA^+$, $Ru(NH_3)_6^{3+}$, $IrCl_6^{3-}$), t is the time, r is the radial distance from the center of the electrode and z is the distance normal to it. D_i was assumed to be identical for both oxidation states of the redox species. The model was used to simulate the current at the pBDD electrode by solving the diffusion equation for the geometry depicted in Figure 3.6 subject to the boundary conditions summarised in Table 3.3.

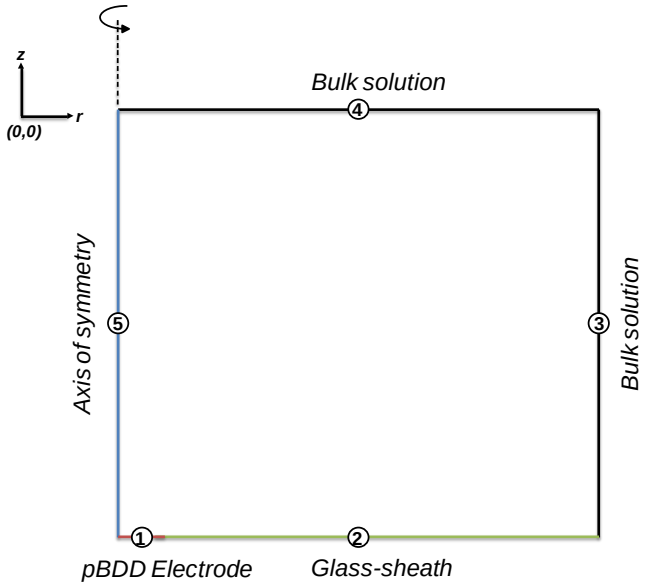

Figure 3.6 - Geometry used for simulation of CV at pBDD electrodes

Label	Boundary Type	Co-ordinates (R,Z) / mm	Equation	
1	Electrode	(0,0) – (0.5,0)	$D\frac{\partial c}{\partial z} = k_f\left(c_b - c\right) - k_b \times c$ $D\frac{\partial c}{\partial z} = k_b\left(c_b - c\right) - k_f \times c$	$Ru(NH_3)_6^{3+}$ $IrCl_6^{3-}$ and $FcTMA^+$
2	Glass-sheath	(0.5,0) – (30,0)	$0 = \nabla c.\underline{n}$	
3	Bulk solution	(30,0) – (30,30)	$c = c_b$	
4	Bulk solution	(30,30) – (0,30)	$c = c_b$	
5	Axis of symmetry	(0,30) – (0,0)	$0 = \nabla c.\underline{n}$	

Table 3.3 - Summary of the boundary conditions used for the simulation of the pBDD electrode current.

In Table 3.3, c_b represents the concentration of the electroactive species in bulk solution and R and Z are the co-ordinates parallel to the electrode and normal to the electrode respectively. Butler-Volmer kinetics (equations (3.2) and (3.3)) were used to describe HET kinetics at the pBDD electrode/solution interface as follows:

$$k_f = k^0 \exp\left[\frac{-\alpha nF\left(\eta - iR_{\text{int}}\right)}{RT}\right] \tag{3.2}$$

$$k_b = k^0 \exp\left[\frac{(1-\alpha)nF\left(\eta - iR_{\text{int}}\right)}{RT}\right] \tag{3.3}$$

where k_f is the forward and k_b is the back rate constant for the electron transfer process, k^0 is the standard rate constant, α is the transfer coefficient (which is assumed as 0.5 in these experiments), n is the number of electrons involved in the reaction, F is Faraday's constant and η is the overpotential. The overpotential is the applied potential – the half wave potential, where the half wave potential is given as $IrCl_6^{2-/3-}$ = +0.67 V, $FcTMA^{+/2+}$ = +0.35 V and $Ru(NH_3)_6^{3+/2+}$ = -0.16 V, experimentally determined against a SCE. i is the current and R_{int} is the intrinsic material resistance. For metal-like pBDD electrodes, R_{int} represents the intrinsic resistance of the material (R_1) calculated from electrical resistivity measurements. For the semiconducting pBDD electrodes, R_{int} is the sum of the bulk electrode resistance R_1 (measured in air) and the potential dependent interfacial resistance due to charge depletion/accumulation effects (R_2).

A range of apparent HET rate constants, k^0_{app}, were simulated and fitted against the experimental CVs. For the metallic electrodes D (high) –G (very high, thin), an ohmic drop term due to the resistance of the diamond material, R_1, was incorporated into the model, calculated as $R_1 = \rho\, l/A$, where ρ = diamond sheet resistivity, l = diamond thickness and A = electrode cross sectional area. Table 3.2 shows the best fit k^0_{app} values for the different redox mediators for electrodes D and E.

From the simulations k^0_{app} values are estimated to be > 0.1 cm s^{-1} for $IrCl_6^{3-}$ and $FcTMA^+$, with slightly lower values of 0.04 (± 0.002) cm s^{-1} (D) and 0.06 (± 0.002)

cm s^{-1} (E) for $Ru(NH_3)_6^{3+}$, which may be due to its lower self-exchange rate constant, k_{exc}, of 4×10^3 M^{-1} s^{-1}. These values compare favourably to HET reported rate constants on GC electrodes[7, 8] and demonstrate it is possible to produce sufficiently doped diamond electrodes, which although have a lower LDOS than a metal electrode, can support fast HET. Moreover, this data shows it is not necessary to employ very high doping levels, *i.e.* > 10^{21} B atoms cm^{-3} (> 1 in 100 C atoms replaced with B), or incorporate NDC, to achieve fast HET rates with BDD.[61] Note that in the literature, higher doped boron electrodes have been shown to demonstrate higher catalytic activity than lower doped electrodes, however Raman indicates a significantly higher NDC content, which is most likely the cause of the increased electroactivity.[62]

The CV data for the thin film metallic electrodes F (high, thin) and G (very high, thin) for both as-received and oxygen-terminated surfaces are shown in Figure 3.5 (b). While comparable ΔE_p values to electrodes D (high) and E (high) are recorded, the effect of the larger background currents (Figure 3.3) on the faradaic response is clearly seen, especially after oxygen-termination. Hence we did not attempt to quantify k^0_{app} for electrodes F and G.

For semiconducting electrodes, charge depletion/accumulation is dependent on the electrode potential which will affect the CV response.[63] This was modelled using a potential dependent resistance term, R_2 given by equation (3.4):

$$R_2 = \frac{1}{\varphi\left[1+\frac{n'\left(E+\chi\right)^{n'-1}}{\gamma^{n'-1}}\right]} \tag{3.4}$$

E is the applied potential (restricted to the range ± 1.5 V). φ has dimensions Ω^{-1}, χ and γ have dimensions of V and n' (≥ 1) is dimensionless. Note if $n' \rightarrow 1$, $R_2 \rightarrow (1/\varphi)$

and is potential independent. Unlike metals, the amount of available charge carriers at the semiconductor-electrolyte interface is dependent upon applied potential. For a p-type semiconductor the majority charge carriers (holes) are depleted upon the imposition of a negative potential, forming a gradient from the interface into the bulk semiconductor, the space charge region. Equation (3.4) allowed the use of a working curve that could be adjusted to model this phenomenon. A typical potential dependent resistance curve is shown in Figure 3.7 for the lowest boron doped electrode, A, depicting how resistance is assumed to increase at more negative potentials.

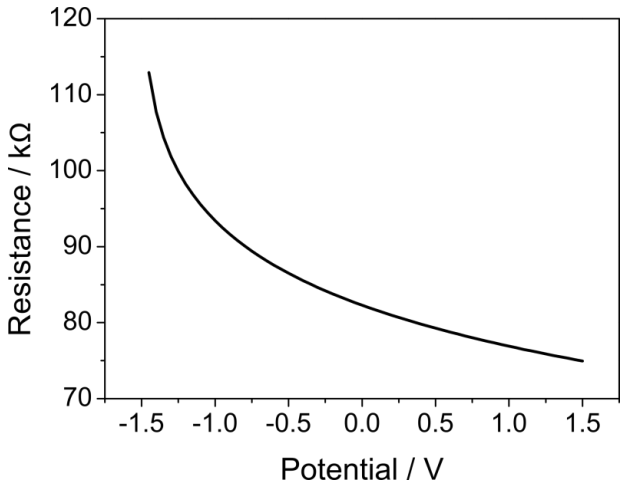

Figure 3.7 - R_2 curve used for electrode A, where $\varphi = 7\times10^{-6}$, $\chi = 1.5$, $\gamma = 10$ and $n' = 1.3$.

Figure 3.8 (a) and (b) show, as an example, the best fit of simulated (red) and experimental (black) CVs for the oxidation of 1 mM $FcTMA^+$ ($k^0_{app} = 2 \times 10^{-3}$ cm s^{-1}) and reduction of 1 mM $Ru(NH_3)_6^{3+}$ ($k^0_{app} = 6 \times 10^{-4}$ cm s^{-1}) respectively at electrode A, recorded at a scan rate of 100 mV s^{-1}.

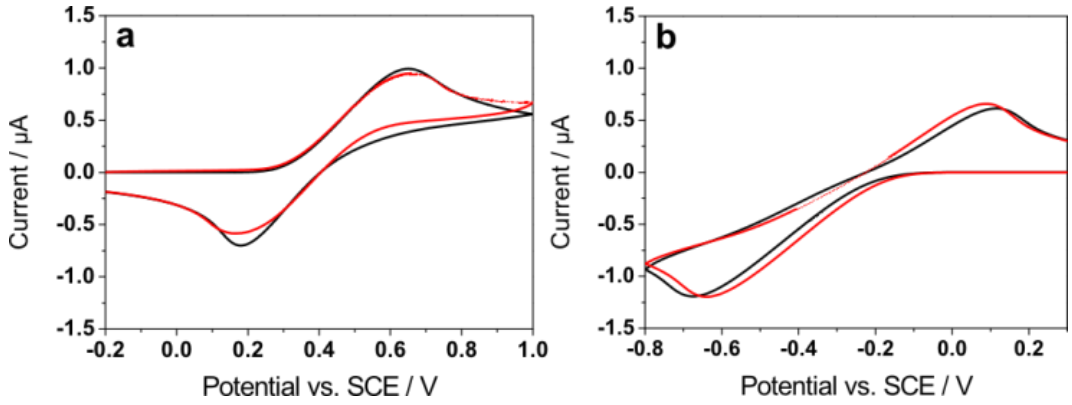

Figure 3.8 - The best fit simulated (red) and experimental (black) CVs for (a) oxidation of $FcTMA^+$ (k^o_{app} = 2 × 10^{-3} cm s^{-1}) and (b) reduction of $Ru(NH_3)_6^{3+}$ (k^0_{app} = 6 × 10^{-4} cm s^{-1}) respectively at the lowest doped semiconducting electrode A, where R_1 = 52 kΩ and R_2 varies with potential as shown in Figure 3.7.

3.2.5 Hydrogen and Oxygen Termination, Stability and Surface Sensitive Processes

To explore the electrochemical response and more importantly stability of hydrogen- versus oxygen-terminated surfaces, CV measurements were recorded using both lapped semiconducting pBDD electrode B (dopant density 2 × 10^{18} B atoms cm^{-3}) and metallic pBDD electrode (E). The outer sphere redox couple $Ru(NH_3)_6^{3+}$ was employed as its formal potential is sufficiently in the band gap region, see above, to show very different electrochemical characteristics for the two differently doped electrodes (Figure 3.5). Electrode E (high) was chosen for these studies as E shows the optimal characteristics of all "metal-like" electrodes investigated in terms of minimal NDC, widest solvent window and lowest capacitive currents.

Figure 3.9 (a) shows CVs recorded at hydrogen- (dashed) and oxygen- (alumina polished; solid line) terminated electrodes B (black line) and E (red line). For electrode E (high), ΔE_p is independent of whether the surface is hydrogen- or oxygen-terminated, however hydrogen-termination of electrode B (low-mid) results in a

significant decrease in ΔE_p from 615 mV to 140 mV, suggesting a significant increase in the rate of HET. Although hydrogen-termination does not alter the intrinsic bulk resistance of the diamond, it does cause the density of charge carriers to increase, as holes form in an accumulation layer at the diamond surface, decreasing the potential drop across the depletion layer, resulting in the observed increase in HET.[64-66]

It has been shown that the application of very positive potentials (a few volts vs. SCE) in acidic media is sufficient to almost completely convert from a hydrogen- to an oxygen-terminated surface.[67] However, it was of interest here to investigate the electrochemical stability of the hydrogen-terminated layer under potential conditions and less extreme pH conditions more akin to conventional electrochemical measurements, in order to verify whether hydrogen-termination of semiconducting electrodes was a viable route for increasing HET. In order to do this, electrochemical studies focused on hydrogen-terminated semiconducting electrode B with $Ru(NH_3)_6^{3+}$ in 0.1 M KNO_3 (pH = 6).

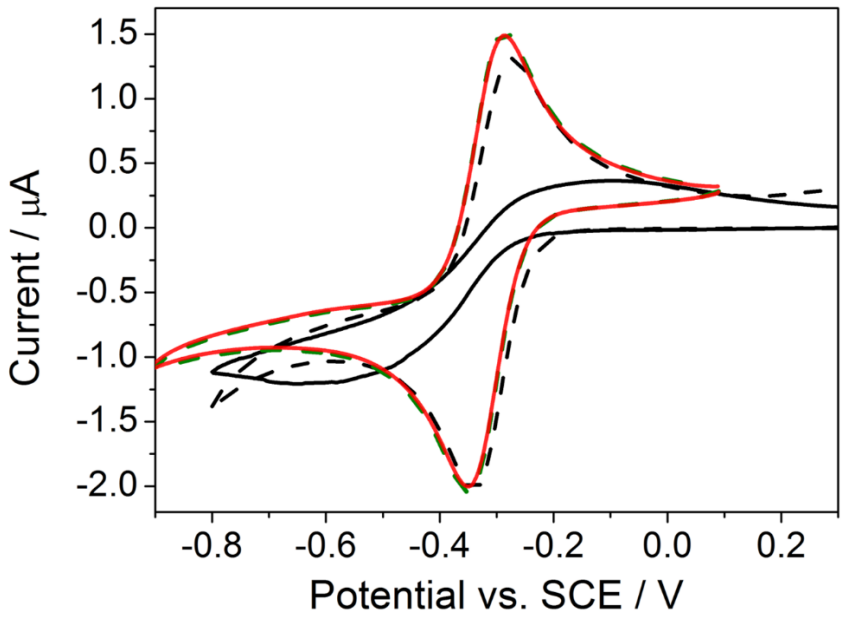

Figure 3.9 - CVs performed with pBDD 1 mm diameter disc electrode B; acid cleaned oxygen-terminated surface (solid black), freshly hydrogen-terminated surface (dashed black) and similarly E;

acid cleaned oxygen-terminated surface (solid black), freshly hydrogen-terminated surface (dashed green) at a scan rate of 0.1 V s^{-1} for the electrolysis of 1 mM $Ru(NH_3)_6^{3+}$ in 0.1 M KNO_3.

Figure 3.10 (a) shows the redox behaviour of 1 mM $Ru(NH_3)_6^{3+}$ over the potential ranges ± 0.6 V, ± 0.7 V, ± 0.9 V and ± 1 V versus SCE, where the first CV of five, for each potential range is shown. The first CV recorded is in agreement with the CV data shown in Figure 3.9, however after just five potential cycles, the second CV shown displays a slight decrease in i_p and increase in ΔE_p (154 mV), which is exacerbated with repeated scanning especially as the potential range is slowly increased by 100 mV each five cycles. This effect was not seen for the oxygen-terminated surface.

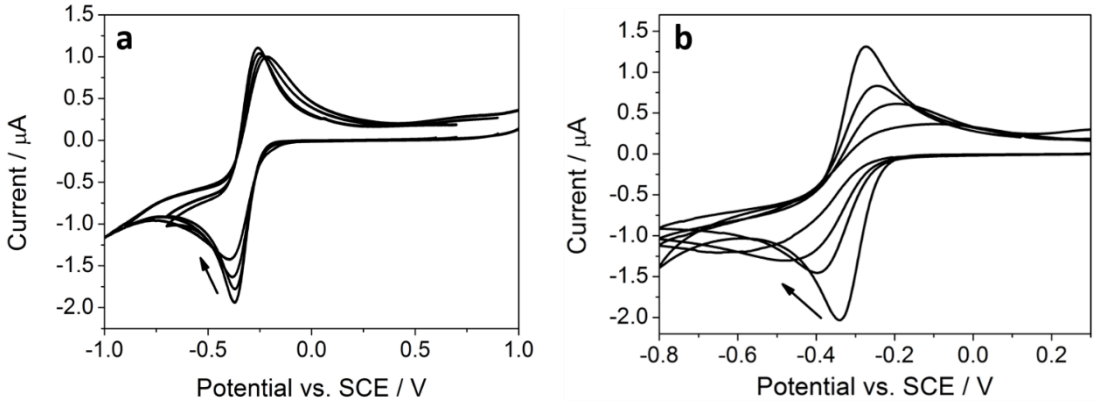

Figure 3.10 – CVs performed with electrode B in a solution of 1 mM $Ru(NH_3)_6^{3+}$ 0.1 M KNO_3 where; (a) the potential has been cycled (5 times) between increasingly extreme potentials of ± 0.6, ± 0.7, ± 0.8, ± 0.9 and ± 1 V between subsequent scans and (b) the potential has been cycled from ± 1.5 V in 0.1 M KNO_3 between subsequent scans.

These data indicate that the surface termination is slowly being converted from hydrogen to oxygen; an effect which is exacerbated as the potential is increased. Importantly, we show conversion occurs at even relatively mild applied potentials in close to neutral pH conditions, which can lead to possible mis-interpretation in HET data, if not accounted for. Figure 3.10 (b) shows the effect of potential scanning

between ± 1.5 V in 0.1 M KNO_3 on a freshly hydrogen-terminated electrode B (low-mid). After just three potential cycles the resulting CV now closely resembles that of the oxygen-terminated surface. Hence, although hydrogen-termination can significantly improve the HET capabilities of a semiconducting BDD electrode it is not an electrochemically stable surface and even the application of mild potentials will cause deterioration. Unfortunately, re-hydrogen-terminating the surface is non-trivial and can only be done reliably through exposure to hydrogen plasma or through hydrogen dosing.[64] This data, and the CV data presented in Figure 3.5, also highlight that the redox couple $Ru(NH_3)_6^{3+}$ is the most appropriate to use when assessing the HET properties of an unknown [B] BDD oxygen-terminated electrode. This is due to its high sensitivity to the electrical properties of pBDD and outer sphere characteristics.

3.2.6 pBDD Surface Sensitive Redox Processes

Surface sensitive HET processes will also be strongly influenced by the surface termination of the electrode. Studies focused on differently oxygen-terminated metal-like lapped electrode, E with two different redox couples thought to be surface sensitive $Fe(CN)_6^{4-/3-}$ [68, 69] and $Fe^{2+/3+}$.[70] For highly doped pBDD, HET kinetics of $Fe(CN)_6^{3-/4-}$ are reported to be slower at oxygen- than hydrogen-terminated pBDD surfaces.[30, 71-73] It has been suggested that oxygen functional groups inhibit HET of $Fe(CN)_6^{3-/4-}$ due to blocking of adsorption sites.[30, 74] Alternative theories[75] consider it is the negative charge on oxygen containing groups which repel the negatively charged redox species. In contrast, studies by McEvoy have shown mechanical cleaning to mildly improve the kinetics for $Fe(CN)_6^{3-/4-}$, thought to be due to hydrocarbon contaminant removal.[76] Some forms of anodic pre-treatment have also been shown to improve HET kinetics.[74, 77] The differences in the BDD literature also highlight the

fact it is vitally important when measuring HET to carefully assess the material and surface properties so comparative assessments between different group's measurements can be made.

Several methods exist for oxygen-termination including boiling in acid,[33, 78] alumina polishing, exposure to oxygen plasma,[79] photochemical oxidation,[73] reaction with oxygen at high temperatures,[80] and probably the most common anodic polarisation.[81] Here we use two contrasting procedures, alumina polishing, commonly used by researchers as the electrode cleaning step prior to electrochemical measurement and anodic polarisation in acid. Figure 3.13 (ai) shows CVs for 1 mM $Fe(CN)_6^{3-/4-}$ in 0.1 M KNO_3 with electrode E, at a scan rate of 0.1 V s^{-1} oxygen terminated via (red) alumina polishing and (black) anodic polarisation for 60 s at 3 V vs. SCE in 0.1 M H_2SO_4. These are representative of at least n = 20 measurements on freshly prepared electrodes.

Alumina polishing electrode E results in a near reversible response for $Fe(CN)_6^{3-/4-}$ electrolysis (ΔE_p of 65 mV), although this was not tested at higher scan rates. Taking into account electrode size, and comparing all studies in the literature, this represents the fastest reported HET kinetics for this couple at an oxygen-terminated pBDD electrode. In contrast, after anodic polarisation, the effect on the CV behaviour is dramatic, with ΔE_p increasing in value from near reversible to 500 mV, and the currents falling in magnitude, indicative of significantly reduced HET.

To investigate further, XPS was performed on the two oxygen-terminated surfaces. Figure 3.11 shows typical C1s XPS spectra for alumina polished (i) and anodically polarised (ii) pBDD electrodes recorded at (a) room temperature and after elevation to (b) 300 ^{o}C and (c) 500 ^{o}C. A wide XPS survey scan, Figure 3.12, showed no aluminium, indicating the surface had been cleaned of all alumina particles. The data

for all spectra was fitted using Lorentzian-Gaussian peaks after a Shirley background subtraction to investigate the chemical environments in which carbon is present at the surface.

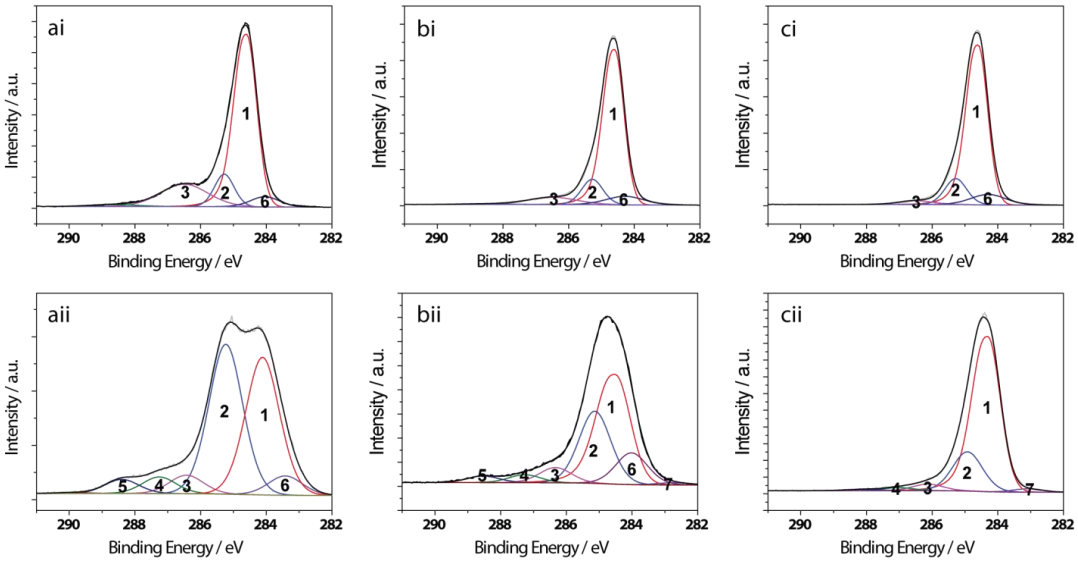

Figure 3.11 - C1s XPS spectra for pBDD electrode E at (a) room temperature and upon heating to (b) 300 °C and (c) 500 °C for an (i) alumina polished and (ii) anodically polarised surface with peak fitting where the grey line is the experimental data, coloured peaks are fittings and the black is the overall fit.

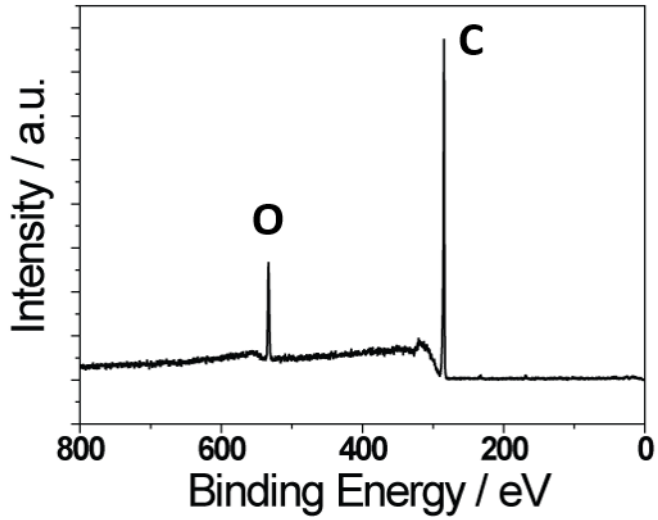

Figure 3.12 - Survey XPS spectra for the alumina polished pBDD surface at room temperature.

For the room temperature alumina polished surface, Figure 3.11 (ai), the largest component (peak 1) found at 284.6 eV can be attributed to sp^3 C-C present in the

diamond bulk; all other component peaks are given relative to this one. Higher binding energies have been associated with carbon in the form of adsorbed hydrocarbons (+0.6 to +0.9 eV) and different forms of oxidation e.g. alcohol C-OH and ether C-O-C (+1 to 2 eV), carbonyl C=O (+2.9 to 3.8 eV) and carboxyl COOH (+3.7 to 4.3 eV).[76, 82-85] These assignments suggest the presence of C-OH and C-O-C groups (peak 2), as well as C=O groups (peak 3). Peak 6 at lower energies (-1 to -2.1 eV) can be assigned to sp^2 C-C, where reconstruction of the diamond surface, especially at the polycrystalline grain boundaries, may give rise to π bonding. Although no evidence of sp^2 was seen in the Raman spectra, XPS is a much more sensitive surface technique.

To gain further insight, XPS was also performed after heating to elevated temperatures, as shown in Figure 3.11 (bi) and (ci) respectively. Peak 3, associated with ketonic (C=O) functional groups, decreases significantly after heating to 300 ^{o}C (7% of peak 1) and is almost completely removed after heating to 500 ^{o}C (3% of peak 1). In contrast peak 2 (ethers and alcohols) appears stable at these temperatures. This is in agreement with reports which show that C=O groups are more weakly bound to the surface than C-O-C groups and are thus more easily removed at lower temperatures (100-400 ^{o}C).[86] Importantly, the XPS spectra after heating to 500 ^{o}C, resembles that of an *in-situ* annealed single crystal,[87] indicating the high quality of this electrode material.

These peak assignments can also be applied to the anodically polarised XPS spectra in Figure 3.11 (ii), which at room temperature are dramatically different to the alumina polished surface. The main sp^3 C-C peak 1 has shifted slightly to a lower binding energy of 284.2 eV, indicating charging effects or a change in the valence band position. Peak 2 is a much larger component of the C1s spectra (107% of peak 1) compared to the alumina polished surface. Increases in peak 2 have previously been

observed after anodic treatment, but to varying degrees.[87, 88] A significant tail at the higher binding energies (peaks 3 – 5, spanning +2.2 to +5.4 eV) indicates the presence of highly oxidised carbon functional groups such as COOH and even polycarbonate groups (41% of peak 1).[84, 89] Upon heating to 300 ^{o}C, a decrease in peaks 3-5 (26% of peak 1) is observed, and also peak 2 (64% of peak 1), with further decreases after heating to 500 ^{o}C. For this surface, the data suggests that many of the carbon-oxygen groups are only weakly adsorbed to the surface, and may even be present in an adsorbed layer. At 500 ^{o}C, the surfaces of the two differently prepared electrodes give similar XPS spectra.

Given that we obtain reversible HET for $Fe(CN)_6^{4-/3-}$ at our alumina polished surface, the concentration of ketonic, ether and alcohol groups on this surface are not sufficient to hinder HET of this mediator. However, as soon as more oxidised groups are introduced *e.g.* COOH (which are also likely to be present for electrodes containing non negligible NDC) and the concentration of ether and alcohol groups significantly increase, the effect on HET is dramatic, resulting in $Fe(CN)_6^{4-}$ - surface interactions which slow down HET. Note that we can rule out any possible electronic factors associated with not the material not being sufficiently doped. This data also re-emphasises that the $Fe(CN)_6^{4-}$ couple should be treated with caution when being used to assess the HET properties of an electrode.[90] Finally, simply alumina polishing an anodically treated surface, resulted in the attainment of reversible HET for $Fe(CN)_6^{4-}$.

Further investigations employed the classic inner-sphere redox couple $Fe^{2+/3+}$. Figure 3.13 (aii) shows CVs for the oxidation of 1 mM Fe^{2+} in 0.1 M $HClO_4$ at a scan rate of 0.1 V s^{-1} for (red) alumina polished and (black) anodically polarised, electrode E. ΔE_p at the alumina polished electrode was 803 mV, which decreased to 472 mV upon anodic pretreatment. This increase in HET is likely to be due to the increased presence

of functional groups such as carbonyls (including COOH), which favourably mediate HET for this couple.[7, 68] Also visible in Figure 3.13 (aii) is the presence of a small peak which is unresolved on top of the main CV, for both surfaces, at 0.47 V (red line) and 0.46 V (black line). Tentatively we attribute this feature to different rates of HET at different facets (see Figure 3.1 (e)) on electrode E.

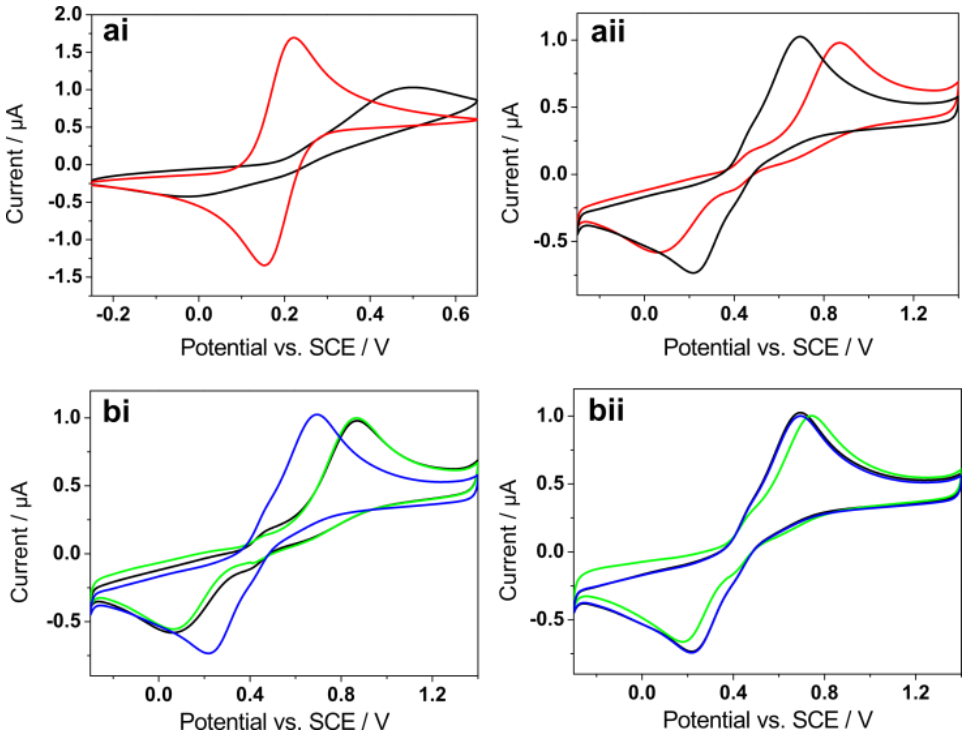

Figure 3.13 - (a) CVs performed with 1 mm diameter disc electrode E after alumina polish (red) and anodic pretreatment (black) for the oxidation of (i) 1 mM $Fe(CN)_6^{4-}$ in 0.1 M KNO_3 and (ii) 1 mM Fe^{2+} in 0.1 M $HClO_4$. (b) CVs for the oxidation of 1 mM Fe^{2+} in 0.1 M $HClO_4$ after 5 s treatment at either -1.5 V (green) or 2 V (blue) for the (i) alumina polished (black) and (ii) anodically polarised electrode (black).

For both surface treatments it was essential to verify the electrochemical stability of the lapped oxygen terminated surface as this is a key requirement in electroanalysis. This was achieved by repeatedly scanning (10 cycles per day) the electrode, in 1 mM Fe^{2+} in 0.1 M $HClO_4$, over the potential range -0.3 V - +1.4 V versus SCE for a week. Both electrodes were found to give very stable responses (ΔE_p values deviated by no

greater than ± 12 mV). We found that only by applying more extreme anodic/cathodic potentials was it possible to affect the CV response. For example, as shown in Figure 3.13 (bi), when starting with an alumina polished surface, applying cathodic potentials, -1.5 V for 5 s in 0.1 M $HClO_4$ (ca. 15 µC passed), had no effect on the CV (ΔE_p of 802 mV), however, 2 V for 5 s in 0.1 M $HClO_4$ (ca. 15 µC passed), caused ΔE_p to decrease from 803 mV to 475 mV, as the surface approaches a surface functionality more akin to that obtained with the anodic treatment.

In the case of the anodically polarised surface as shown in Figure 3.13 (bii) further anodic polarisation, 2 V for 5 s in 0.1 M $HClO_4$, gives no change in the response, as to be expected, however, cathodic polarisation, -1.5 V for 5 s in 0.1 M $HClO_4$ results in a small increase in ΔE_p from 472 mV to 564 mV. Importantly, for both surfaces, provided the applied potential is not run out too far negative or positive, both forms of surface termination are stable.

3.3 Conclusion

In order to produce pBDD oxygen-terminated electrodes suitable for electroanalysis, and exploiting attributes such as low background currents, wide solvent window, high stability and reproducibility, it is essential the material properties of the electrode are carefully optimised. Firstly, the material must demonstrate metal-like conductivity. Electrical measurements demonstrated this was achieved at average [B] > 10^{20} boron atoms cm^{-3}. Although lower [B] results in larger solvent windows and lower capacitances, the smaller number of charge carriers available at more negative potentials, due to the p-type semi-conducting nature of the electrode, result in sluggish HET kinetics for redox couples with formal potentials in the band gap (e.g. $Ru(NH_3)_6^{3+}$), which is undesirable. Significantly faster HET for $Ru(NH_3)_6^{3+}$ electrolysis at semi-conducting electrodes can be obtained by hydrogen-terminating the surface. However, as HET was shown to decrease as the electrode was subjected to successive potential cycles, exacerbated as the potential was increased; the hydrogen-terminated lapped surface appears to be electrochemically unstable

Second, it is essential no evidence of NDC in either the Raman spectra or the solvent window is observed. In the latter, NDC content is confirmed due to the presence of NDC oxidative currents and/or an oxygen reduction signal, in near neutral pH aqueous solutions. In general, the more NDC present, the smaller the solvent window and higher the NDC driven surface currents. As hydrogen-termination can significantly mask NDC-like features in the solvent window, as well as decreasing capacitive currents, it is important to consider this affect when using CV to assess NDC content of as-grown *i.e.* H-terminated electrodes. Note as we found it impossible to remove NDC completely, post-growth, by either diamond polishing or cycling (or boiling) in acid, growth must be carefully controlled to minimise NDC.

Thirdly, it is essential [B] content is optimised. Even though BDD contains a lower density of states than a metal it is not necessary to use extreme doping levels e.g. > 1 $\times 10^{21}$ B atoms cm^{-3}, as increased [B] results in slightly narrower solvent windows, higher capacitance and can increase the likelihood of NDC incorporation. We found oxygen-terminated pBDD electrodes with an average [B] ~ 3×10^{20} boron atoms cm^{-3} (negligible NDC content), recorded the lowest capacitive currents (~ 6 $\mu F\ cm^{-2}$), widest solvent windows and achieved fast (reversible) HET for a wide range of outer sphere redox couples, on the experimental timescale provided by a 1 mm diameter electrode scanned at 100 mV s^{-1}.

For the surface sensitive redox couples, $Fe(CN)_6^{3-/4-}$ and $Fe^{2+/3+}$, it is possible to drastically influence HET simply by changing the method of oxygen-termination. In particular, for the optimal electrode material employed, alumina polishing of the lapped surface promoted near reversible HET for $Fe(CN)_6^{3-/4-}$, the fastest reported HET for this couple to-date at an oxygen-terminated pBDD electrode. In contrast anodic polarisation resulted in a significant reduction in HET. Less dramatic effects were seen with the redox couple $Fe^{2+/3+}$, although oxidation of Fe^{2+} was favoured on the anodically polarised surface. XPS analysis suggested a higher prevalence of oxygen functional groups such as carbonyl and carboxyl groups on the anodically polarised surface, and increased levels of ether and alcohol groups, thought to be responsible for the significant decrease in HET for $Fe(CN)_6^{4-}$ and slightly increased HET for Fe^{2+}. Temperature dependant XPS studies revealed the alumina cleaned XPS surface to be high quality, containing only monolayer oxygen functionalities. Most importantly, for both methods of oxygen termination, the CV responses for e.g. $Fe^{3+/2+}$ were found to be stable over repetitive cycles, over a week of testing.

3.4 References

1. M. A. T. Gilmartin and J. P. Hart, *Analyst*, 1995, **120**, 1029-1045.
2. R. G. Compton, J. S. Foord and F. Marken, *Electroanalysis*, 2003, **15**, 1349-1363.
3. X. Huang, Z. Zeng, Z. Fan, J. Liu and H. Zhang, *Adv. Mater. (Weinheim, Germany)*, 2012, **24**, 5979-6004.
4. D. A. C. Brownson, D. K. Kampouris and C. E. Banks, *Chem. Soc. Revs.*, 2012, **41**, 6944-6976.
5. S. Sharma and B. G. Pollet, *J. Power Sources*, 2012, **208**, 96-119.
6. R. C. Engstrom, *Anal. Chem.*, 1982, **54**, 2310-2314.
7. P. H. Chen, M. A. Fryling and R. L. McCreery, *Anal. Chem.*, 1995, **67**, 3115-3122.
8. K. K. Cline, M. T. McDermott and R. L. McCreery, *J. Phys. Chem.*, 1994, **98**, 5314-5319.
9. I. Dumitrescu, P. R. Unwin and J. V. Macpherson, *Chem. Comm. (Cambridge, United Kingdom)*, 2009, 6886-6901.
10. A. Kraft, *Int. J. Electrochem. Sci.*, 2007, **2**, 355-385.
11. J. H. T. Luong, K. B. Male and J. D. Glennon, *Analyst*, 2010, **135**, 3008-3008.
12. Y. Liu, D. O. Wipf and C. S. Henry, *Analyst*, 2001, **126**, 1248-1251.
13. S. Alehashem, F. Chambers, J. W. Strojek, G. M. Swain and R. Ramesham, *Anal. Chem.*, 1995, **67**, 2812-2821.
14. N. Vinokur, B. Miller, Y. Avyigal and R. Kalish, *J. Electrochem. Soc.*, 1996, **143**, L238-L240.
15. Y. V. Pleskov, *Russ. J. Electrochem.*, 2002, **38**, 1275-1291.
16. J. S. Xu, M. C. Granger, Q. Y. Chen, J. W. Strojek, T. E. Lister and G. M. Swain, *Anal. Chem.*, 1997, **69**, A591-A597.
17. G. M. Swain, *Adv. Mater.*, 1994, **6**, 388-392.
18. J. P. Lagrange, A. Deneuville and E. Gheeraert, *Diamond Relat. Mater.*, 1998, **7**, 1390-1393.
19. E. Gheeraert, A. Deneuville and J. Mambou, *Diamond Relat. Mater.*, 1998, **7**, 1509-1512.
20. T. Inushima, T. Matsushita, S. Ohya and H. Shiomi, *Diamond Relat. Mater.*, 2000, **9**, 1066-1070.
21. H. Shiomi, Y. Nishibayashi and N. Fujimori, *Jpn. J. Appl. Phys. Part 1 - Regul. Pap. Short Notes Rev. Pap.*, 1991, **30**, 1363-1366.
22. K. Nishimura, K. Das and J. T. Glass, *J. Appl. Phys.*, 1991, **69**, 3142-3148.
23. R. Tenne, K. Patel, K. Hashimoto and A. Fujishima, *J. Electroanal. Chem.*, 1993, **347**, 409-415.
24. R. Issaoui, J. Achard, F. Silva, A. Tallaire, A. Tardieu, A. Gicquel, M. A. Pinault and F. Jomard, *Appl. Phys. Lett.*, 2010, **97**, 182101-182103.
25. S. J. Charles, J. W. Steeds, D. J. F. Evans and J. E. Butler, *Mater. Lett.*, 2003, **57**, 3690-3693.
26. H. B. Martin, A. Argoitia, U. Landau, A. B. Anderson and J. C. Angus, *J. Electrochem. Soc.*, 1996, **143**, L133-L136.
27. R. Trouillon and D. O'Hare, *Electrochim. Acta*, 2010, **55**, 6586-6595.
28. J. A. Bennett, J. A. Wang, Y. Show and G. M. Swain, *J. Electrochem. Soc.*, 2004, **151**, E306-E313.

29. M. C. Granger, M. Witek, J. S. Xu, J. Wang, M. Hupert, A. Hanks, M. D. Koppang, J. E. Butler, G. Lucazeau, M. Mermoux, J. W. Strojek and G. M. Swain, *Anal. Chem.*, 2000, **72**, 3793-3804.
30. M. C. Granger and G. M. Swain, *J. Electrochem. Soc.*, 1999, **146**, 4551-4558.
31. A. E. Fischer, Y. Show and G. M. Swain, *Anal. Chem.*, 2004, **76**, 2553-2560.
32. H. J. Schäfer and R. Schneider, *Tetrahedron*, 1991, **47**, 715-724.
33. F. B. Liu, J. D. Wang, B. Liu, X. M. Li and D. R. Chen, *Diamond Relat. Mater.*, 2007, **16**, 454-460.
34. G. R. Salazar-Banda, L. S. Andrade, P. A. P. Nascente, P. S. Pizani, R. C. Rocha and L. A. Avaca, *Electrochim. Acta*, 2006, **51**, 4612-4619.
35. H. P. Godfried, S. E. Coe, C. E. Hall, C. S. J. Pickles, R. S. Sussmann, X. Tang and W. K. L. van der Voorden, in *Use of CVD diamond in high-power CO2 lasers and laser diode arrays*, SPIE, Bellingham, 2000.
36. S. S. Zuo, M. K. Yaran, T. A. Grotjohn, D. K. Reinhard and J. Asmussen, *Diamond Relat. Mater.*, 2008, **17**, 300-305.
37. R. S. Balmer, J. R. Brandon, S. L. Clewes, H. K. Dhillon, J. M. Dodson, I. Friel, P. N. Inglis, T. D. Madgwick, M. L. Markham, T. P. Mollart, N. Perkins, G. A. Scarsbrook, D. J. Twitchen, A. J. Whitehead, J. J. Wilman and S. M. Woollard, *J. Phys.: Condens. Matter*, 2009, **21**, 364221.
38. N. R. Wilson, S. L. Clewes, M. E. Newton, P. R. Unwin and J. V. Macpherson, *J. Phys. Chem. B.*, 2006, **110**, 5639-5646.
39. M. Bernard, *Diamond Relat. Mater.*, 2004, **13**, 282-286.
40. R. Locher, J. Wagner, F. Fuchs, M. Maier, P. Gonon and P. Koidl, *Diamond Relat. Mater.*, 1995, **4**, 678-683.
41. C. Levy-Clement, N. A. Ndao, A. Katty, M. Bernard, A. Deneuville, C. Comninellis and A. Fujishima, *Diamond Relat. Mater.*, 2003, **12**, 606-612.
42. R. Locher, J. Wagner, F. Fuchs, C. Wild, P. Hiesinger, P. Gonon and P. Koidl, *Mater. Sci. Eng. B-Solid State Mater. Adv. Technol.*, 1995, **29**, 211-215.
43. K. Ushizawa, K. Watanabe, T. Ando, I. Sakaguchi, M. Nishitani-Gamo, Y. Sato and H. Kanda, *Diamond Relat. Mater.*, 1998, **7**, 1719-1722.
44. E. Gheeraert, A. Deneuville and J. Mambou, *Carbon*, 1999, **37**, 107-111.
45. C. Levy-Clement, F. Zenia, N. A. Ndao and A. Deneuville, *New Diam. Front. Carbon Technol.*, 1999, **9**, 189-206.
46. M. Mermoux, B. Marcus, G. M. Swain and J. E. Butler, *J. Phys. Chem. B.*, 2002, **106**, 10816-10827.
47. S. Prawer and R. J. Nemanich, *Philos. T. Roy. Soc. A.*, 2004, **362**, 2537-2565.
48. A. N. Correia and S. A. S. Machado, *Electrochim. Acta*, 1998, **43**, 367-373.
49. A. Damjanovic, A. Dey and J. O. M. Bockris, *Electrochim. Acta*, 1966, **11**, 791-814.
50. R. E. Thomas, R. A. Rudder and R. J. Markunas, *J. Vac. Sci. Technol. A-Vac. Surf. Films*, 1992, **10**, 2451-2457.
51. E. Yeager, *Electrochim. Acta*, 1984, **29**, 1527-1537.
52. M. S. Hossain, D. Tryk and E. Yeager, *Electrochim. Acta*, 1989, **34**, 1733-1737.
53. H. B. Martin, A. Argoitia, J. C. Angus and U. Landau, *J. Electrochem. Soc.*, 1999, **146**, 2959-2964.
54. T. Yano, D. A. Tryk, K. Hashimoto and A. Fujishima, *J. Electrochem. Soc.*, 1998, **145**, 1870-1876.
55. Z. V. Živcová, O. Frank, V. Petrák, H. Tarábková, J. Vacík, M. Nesládek and L. Kavan, *Electrochim. Acta*, 2013, **87**, 518-525.

56. H. V. Patten, K. E. Meadows, L. A. Hutton, J. G. Iacobini, D. Battistel, K. McKelvey, A. W. Colburn, M. E. Newton, J. V. Macpherson and P. R. Unwin, *Angew. Chem. Int. Ed.*, 2012, **51**, 7002-7006.
57. T. Watanabe, T. K. Shimizu, Y. Tateyama, Y. Kim, M. Kawai and Y. Einaga, *Diamond Relat. Mater.*, 2010, **19**, 772-777.
58. B. P. Chaplin, D. K. Hubler and J. Farrell, *Electrochim. Acta*, 2013, **89**, 122-131.
59. A. M. Hartley and H. D. Axelrod, *J. Electroanal. Chem. Interfac. Eelectrochem.*, 1968, **18**, 115-121.
60. D. R. Tallant, T. L. Aselage, A. N. Campbell and D. Emin, *Phys. Rev. B.*, 1989, **40**, 5649-5656.
61. S. Fierro, K. Abe, C. Comninellis and Y. Einaga, *J. Electrochem. Soc.*, 2011, **158**, F183-F189.
62. Y. Feng, J. Lv, J. Liu, N. Gao, H. Peng and Y. Chen, *Appl. Surf. Sci.*, 2011, **257**, 7-7.
63. H. Gerischer, *Physical Chemistry, An Advanced Treatise*, 1970.
64. H. Kawarada, *Surf. Sci. Rep.*, 1996, **26**, 205-259.
65. N. Vassal, E. Salmon and J. F. Fauvarque, *J. Electrochem. Soc.*, 1999, **146**, 20-26.
66. J. Ristein, *Appl. Phys. A-Mater. Sci. Process.*, 2006, **82**, 377-384.
67. R. Hoffmann, H. Obloh, N. Tokuda, N. Yang and C. E. Nebel, *Langmuir*, 2011, **28**, 47-50.
68. P. Shakkthivel and S.-M. Chen, *Biosens. Bioelectron.*, 2007, **22**, 1680-1687.
69. K. Pihel, Q. D. Walker and R. M. Wightman, *Anal. Chem.*, 1996, **68**, 2084-2089.
70. K. Ohnishi, Y. Einaga, H. Notsu, C. Terashima, T. N. Rao, S. G. Park and A. Fujishima, *Electrochem. Solid State Lett.*, 2002, **5**, D1-D3.
71. F. Marken, C. A. Paddon and D. Asogan, *Electrochem. Commun.*, 2002, **4**, 62-66.
72. P. Actis, A. Denoyelle, R. Boukherroub and S. Szunerits, *Electrochem. Commun.*, 2008, **10**, 402-406.
73. R. Boukherroub, X. Wallart, S. Szunerits, B. Marcus, P. Bouvier and M. Mermoux, *Electrochem. Commun.*, 2005, **7**, 937-940.
74. O. El Tall, N. Jaffrezic-Renault, M. Sigaud and O. Vittori, *Electroanalysis*, 2007, **19**, 1152-1159.
75. T. N. Rao, I. Yagi, T. Miwa, D. A. Tryk and A. Fujishima, *Anal. Chem.*, 1999, **71**, 2506-2511.
76. J. P. McEvoy and J. S. Foord, *Electrochim. Acta*, 2005, **50**, 2933-2941.
77. C. Prado, S. J. Wilkins, F. Marken and R. G. Compton, *Electroanalysis*, 2002, **14**, 262-272.
78. P. K. Bachmann, D. Leers and H. Lydtin, *Diamond Relat. Mater.*, 1991, **1**, 1-12.
79. H. S. H. a. B. B. Owen, *The Physical Chemistry of Electrolytic Solutions*, Reinhold, New York, 1958.
80. L. Ostrovskaya, V. Perevertailo, V. Ralchenko, A. Dementjev and O. Loginova, *Diamond Relat. Mater.*, 2002, **11**, 845-850.
81. M. Werner, R. Job, A. Zaitzev, W. R. Fahrner, W. Seifert, C. Johnston and P. R. Chalker, *Phys. Status Solidi A-Appl. Res.*, 1996, **154**, 385-393.
82. H. A. Girard, N. Simon, D. Ballutaud, E. de La Rochefoucauld and A. Etcheberry, *Diamond Relat. Mater.*, 2007, **16**, 888-891.

83. S. Ghodbane, D. Ballutaud, F. Omnes and C. Agnes, *Diamond Relat. Mater.*, 2010, **19**, 630-636.
84. D. Ballutaud, N. Simon, H. Girard, E. Rzepka and B. Bouchet-Fabre, *Diamond Relat. Mater.*, 2006, **15**, 716-719.
85. R. Graupner, F. Maier, J. Ristein, L. Ley and C. Jung, *Phys. Rev. B.*, 1998, **57**, 12397-12409.
86. J. E. Field, *The Properties of Natural and Synthetic Diamond*, Academic Press Limited: London, 1992.
87. A. Denisenko, C. Pietzka, A. Romanyuk, H. El-Hajj and E. Kohn, *J. Appl. Phys.*, 2008, **103**, 014904-014908.
88. C. H. Goeting, F. Marken, A. Gutiérrez-Sosa, R. G. Compton and J. S. Foord, *Diamond Relat. Mater.*, 2000, **9**, 390-396.
89. H. A. Girard, N. Simon, D. Ballutaud and A. Etcheberry, *C. R. Chim.*, 2008, **11**, 1010-1015.
90. A. N. Patel, M. G. Collignon, M. A. O'Connell, W. O. Y. Hung, K. McKelvey, J. V. Macpherson and P. R. Unwin, *J. Am. Chem. Soc.*, 2012, **134**, 20117-20130.

4 Electrical and Raman Studies of pBDD

Further characterisation of samples A – E was performed in this chapter with Raman mapping and electrical measurements. Samples A – C are moderately doped (9.2×10^{16} – 6×10^{19} cm^{-3}) and displayed large changes in resistivity at different temperatures, whereas samples D and E ($2 – 3 \times 10^{20}$ cm^{-3}) showed only small changes. Theoretical data showed a satisfactory fit to experimental plots of resistivity vs. reciprocal temperature for all samples, validating the obtained values of boron concentration. The heavily doped samples (D and E) showed small activation energies of around 0.03 – 0.04 eV, and were deemed effectively metallic at room temperature.

Raman mapping was performed on samples D and E to assess the heterogeneity of boron concentration and the presence of NDC. The zone centre optical phonon peak occurring at ~ 1332 cm^{-1} diminishes with increasing amounts of boron and a broad feature at 1500 cm^{-1} becomes larger with more NDC. Maps were constructed from many spectra across the pBDD surface by recording the areas of these two features, a similar structure to that seen in FE-SEM was observed when assessing boron concentration for both D and E. Sample D showed evidence of NDC, which correlated well with areas of higher boron, this was not seen in sample E indicating negligible amounts of NDC.

4.1 Conductivity of BDD

Intrinsic diamond is a semiconductor that possesses a very large band gap of 5.5 eV,[1] this large separation between electrons in the valence band and holes in the conduction band renders diamond insulating at room temperature. Doping with impurity atoms allows the creation of an extrinsic semiconductor which may display appreciable conductivity at room temperature.[2] The conductivity processes in pBDD are somewhat complex and are dependent upon factors such as; acceptor concentration (N_A in cm^{-3}), donor concentration (N_D in cm^{-3}), temperature and the presence of traps and scattering sites such as grain boundaries.

4.1.1 Conduction Mechanisms in semiconducting BDD

The conductivity of a semiconductor is given by the following relation;

$$\sigma = nq\mu_n + pq\mu_p \tag{4.1}$$

where σ is conductivity in $\Omega^{-1}cm^{-1}$, n is the number of electrons in the conduction band in (cm^{-3}), p is the number of holes in the valence band in (cm^{-3}), q is the elementary charge in C, μ_n and μ_p are the respective mobilities of electrons and holes in $cm^2V^{-1}s^{-1}$. For a boron-doped semiconductor $N_A >> N_D$; $p >> n$ (at temperatures where electrons can be permanently excited to acceptors) therefore;

$$\sigma \approx pq\mu_p \tag{4.2}$$

The concentration of holes available in the valence band, p, in a partially compensated p-type semiconductor may be calculated with the following idealised equation;[3]

$$\frac{p\left(N_D + p\right)}{N_A - N_D - p} = \frac{2}{g_a}\left(\frac{2\pi m^* k_B T}{h^2}\right)^{3/2} \exp\left(\frac{-E_A}{k_B T}\right) \tag{4.3}$$

where N_D and N_A are the concentrations of donors and acceptors in cm^{-3} respectively, g_a is the degenerescence level of the acceptor state, m^* is the effective mass of a hole in kg, and all other symbols have their usual meanings. As temperature increases the number of available 'holes' in the valence band increases, this is caused by thermal promotion of electrons into bound acceptor states leaving behind holes in the valence band. At sufficiently high temperatures the concentration of holes in the valence band will reach saturation such that;[3]

$$p = N_A - N_D \tag{4.4}$$

This is illustrated in Figure 4.1 where p is calculated from equation (4.3); values for N_A, m^* and E_A were 1×10^{19} cm^{-3}, 6.83×10^{-31} kg and 0.37 eV respectively, N_D is varied to produce different compensation ratios.

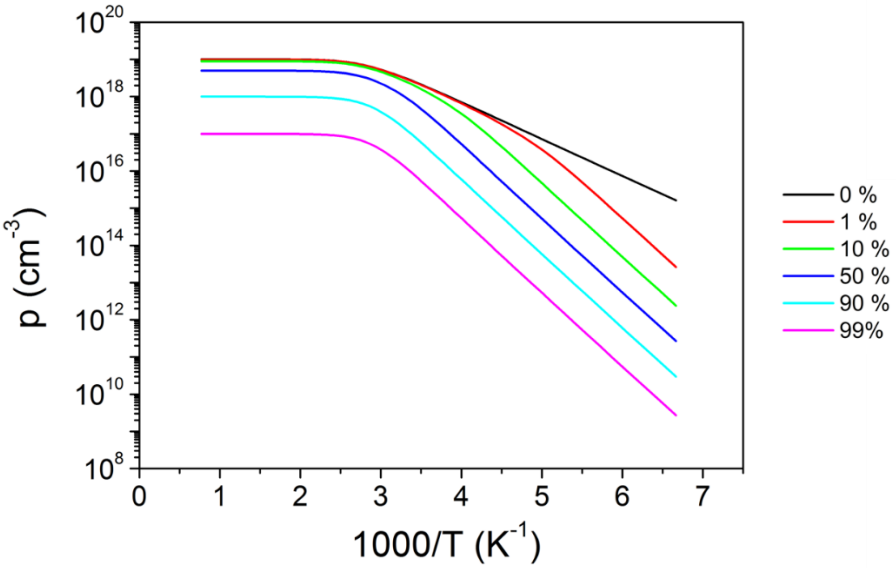

Figure 4.1 – Theoretical hole concentration calculated from equation (4.3) as a function of temperature at different compensation ratios.

The mobility of charge carriers in a semiconductor will also vary with temperature, with increased temperatures causing more carrier scattering due to lattice vibrations,

therefore reducing mobility.[4] The variation of mobility with temperature for a semiconductor is given by;[5]

$$\mu_{phonon} = \mu_{300}\left(\frac{T}{300}\right)^{-s} \tag{4.5}$$

where μ_{300} is the mobility at 300 K in $cm^2V^{-1}s^{-1}$ and s is a dimensionless parameter that describes the variation of μ_{phonon} with T. At low temperature impurity scattering becomes significant and limits mobility.

4.1.2 Conduction in Heavily BDD

The aforementioned description of conductivity only describes the movement of holes in the valence band and is not satisfactory for higher levels of boron doping, where it has been shown that other conductivity mechanisms contribute.[6] Studies by Fritzsche *et al*[7-9] have suggested that there are three main conductivity mechanisms in doped germanium that operate at different temperatures and doping levels. These conductivities may be combined to yield the total conduction, which is given by;[10]

$$\sigma = \sigma_1 \exp\left(\frac{-E_1}{k_B T}\right) + \sigma_2 \exp\left(\frac{-E_2}{k_B T}\right) + \sigma_3 \exp\left(\frac{-E_3}{k_B T}\right) \tag{4.6}$$

where the subscripts of σ and E denote the conductivities and the activation energies of the three conduction mechanisms respectively. The same type of conduction mechanisms have been proposed for BDD, equation (4.6) has been used by Collins,[6] Inushima[11] and Visser[12] to explain variable temperature resistivity measurements. The first conductivity term, σ_1, is due to the movement of holes in the valence band, σ_2 is thought to arise from conduction in an acceptor band, although there is discussion into the existence of this mechanism.[11] The third conductivity term, σ_3, is due to hopping

between ionised and neutral boron atoms, finally at boron dopant levels above the metallic threshold (3×10^{20} cm^{-3}) metallic type conduction occurs.[11] The band structure of semiconductor undergoing a metal-insulator transition is shown schematically in Figure 4.2.[13] Impurity energy levels in an extrinsic semiconductor begin to coalesce at high doping levels, forming an impurity band when these impurities are close enough such that their wavefunctions overlap. This half-filled impurity band splits into two separate bands forming an 'effective' band gap, (c). Upon further doping these two bands begin to merge and a metal-insulator transition occurs, (d).[13]

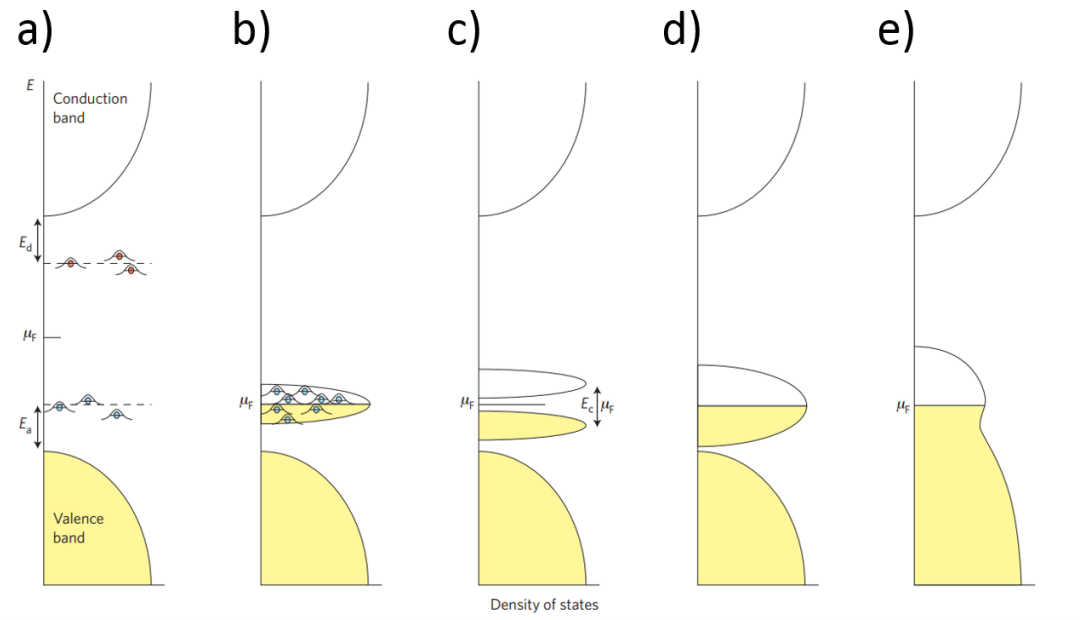

Figure 4.2 – Schematic of the metal-insulator transition in a semiconductor upon p-type doping at 0 K, yellow shading represents states filled with electrons.[13]

The effect of dopants on the activation energy of silicon have been studied by Pearson and Bardeen,[14] with adjustment this relation may be applied to BDD. The activation energy at a given boron concentration (where [B] ~ N_A-N_D) may be approximated with the following equation;[15]

$$E_A = 0.37 - 6.7 \times 10^{-8} N_A^{1/3} \tag{4.7}$$

where the value 0.37 corresponds to the ionisation energy of boron in diamond in eV and the coefficient of N_A is a collection of other terms. This is shown graphically in Figure 4.3, where E_A is observed to sharply drop around a boron concentration of ~ 2 × 10^{20} cm^{-3}.

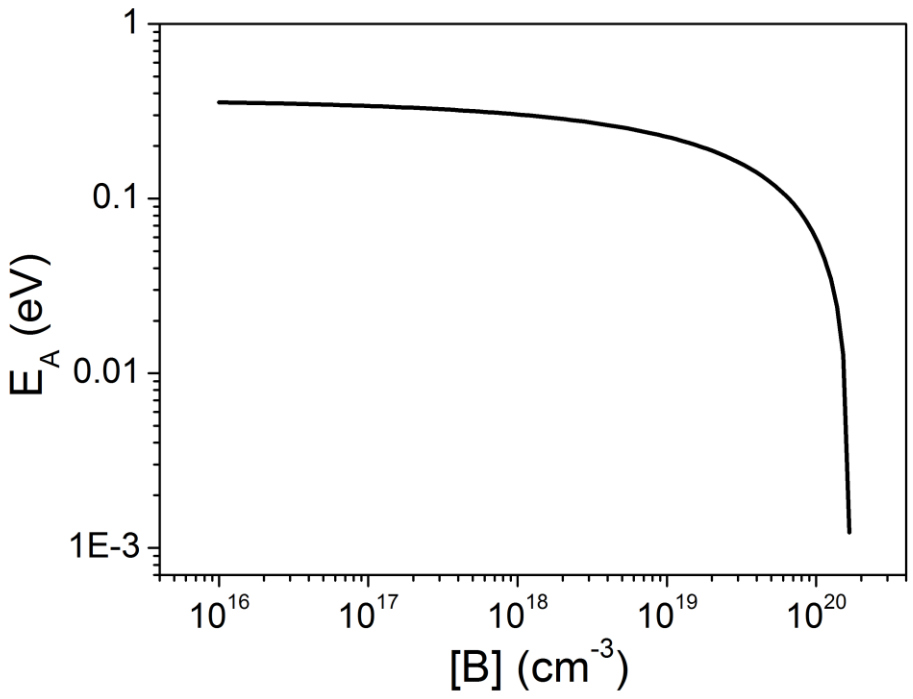

Figure 4.3 – Theoretical variation of activation energy with boron concentration for diamond calculated from equation (4.7).

4.1.3 Conductivity Measurements at Variable Temperature

Lagrange *et al*[5] suggested a method of obtaining information about scBDD samples, such as μ and N_D, by measuring the resistivity of a sample at various temperatures, without the need for Hall mobility measurements. The second conductivity term (σ_2) described above in section 4.1.1 is not considered for this calculation, the total conductivity can therefore be expressed as;[5]

$$\frac{1}{\sigma} = \frac{1}{\sigma_1} + \frac{1}{\sigma_3} \tag{4.8}$$

$$\sigma_1 = q\mu \frac{N_V}{g_a} \frac{\left(N_A - N_D\right)}{N_D} \exp\left(\frac{-E_A}{kT}\right) \tag{4.9}$$

$$\sigma_3 = q\mu \left[\frac{N_V}{g_a}\left(N_A - N_D\right)\right]^{1/2} \exp\left(\frac{-E_A}{2kT}\right) \tag{4.10}$$

$$N_V = N_0 T^{3/2} \tag{4.11}$$

where N_V is the density of states of the valence band in cm^{-3}, and N_0 is a collection of other terms in $cm^{-3}K^{-3/2}$.

The resistivities ($\rho = 1/\sigma$) of semiconducting samples used in this thesis were measured at various temperatures as described in section 2.3.2, these samples are; A, B and C. Experimental data were fit with equation (4.8), yielding a curve whose shape is dictated by the various parameters in equations (4.9), (4.10) and (4.11). The solver function in Microsoft Excel was used as a means to optimise these parameters so that a good fit to experimental data was obtained. Due to the large number of parameters

however, certain constraints were required in order to avoid seemingly good graphical solutions providing unrealistic parameters.

The degenerescence level of the acceptor state, g_a, was set at 4 and the N_0 term was set to 3.4×10^{15} cm^{-3}, both of these parameters are non-adjustable for the purposes of this fit, values for N_A were supplied by SIMS. Values calculated from equation (4.7) were used as starting values for E_A, though many authors[12, 15, 16] have reported a wide range of values that deviate from the curve presented in Figure 4.3. The *s* parameter was initially set to 1.5, though this is reduced to 0 for samples with high concentrations of boron, N_D was set at a value of 1×10^{16} cm^{-3} unless otherwise stated. This was chosen as a reasonable value of the donor concentration as Element Six Ltd. have demonstrated the ability to grow intrinsic diamond with $N_D << 10^{16}$ cm^{-3}.

For the purposes of this data, equation (4.5) was used to calculate mobility as a function of temperature, however mobility may be considered to comprise two different components based on two different scattering mechanisms; scattering from phonons and also from impurity atoms. The following general relation therefore may be considered;[17]

$$\frac{1}{\mu} = \frac{1}{\mu_{phonon}} + \frac{1}{\mu_{impurity}} \tag{4.12}$$

where μ is some general mobility and the subscripts denote scattering due to phonons and impurity atoms respectively. The term μ_{phonon} will decrease with increasing temperature, at high impurity concentrations however mobility becomes temperature independent.[18] The value of the *s* parameter in equation (4.5) therefore describes the sensitivity of temperature dependent scattering, a value of 0 dictates that scattering is temperature independent.

The experimentally determined resistivities of samples A, B and C are plotted against reciprocal temperature in Figure 4.4, Figure 4.5 and Figure 4.6 respectively, model curves from equation (4.8) are also plotted, error bars lie within data symbols. The results of fitting equation (4.8) to experimental values for these samples are summarised in Table 4.1

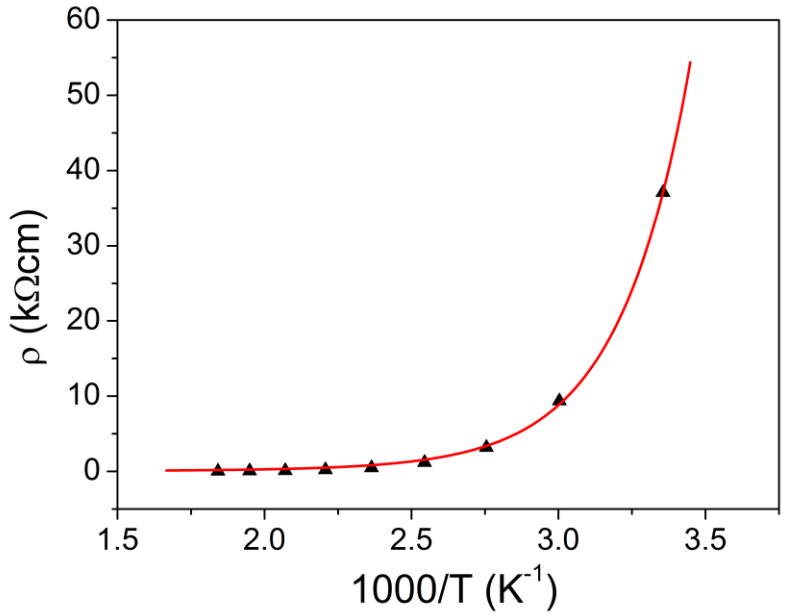

Figure 4.4 – Resistivity versus reciprocal temperature of sample A, experimentally determined (black symbols) and theoretically calculated values (red line).

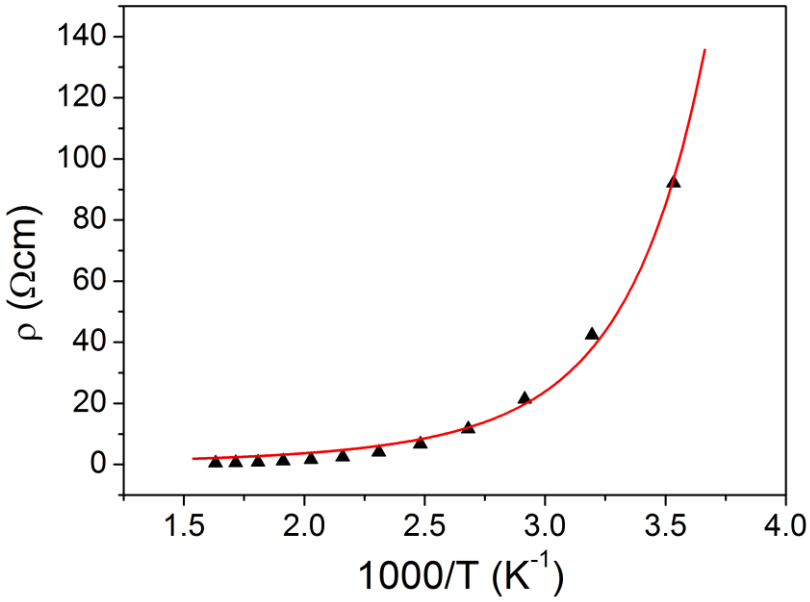

Figure 4.5 – Resistivity versus reciprocal temperature of sample B, experimentally determined (black symbols) and theoretically calculated values (red line).

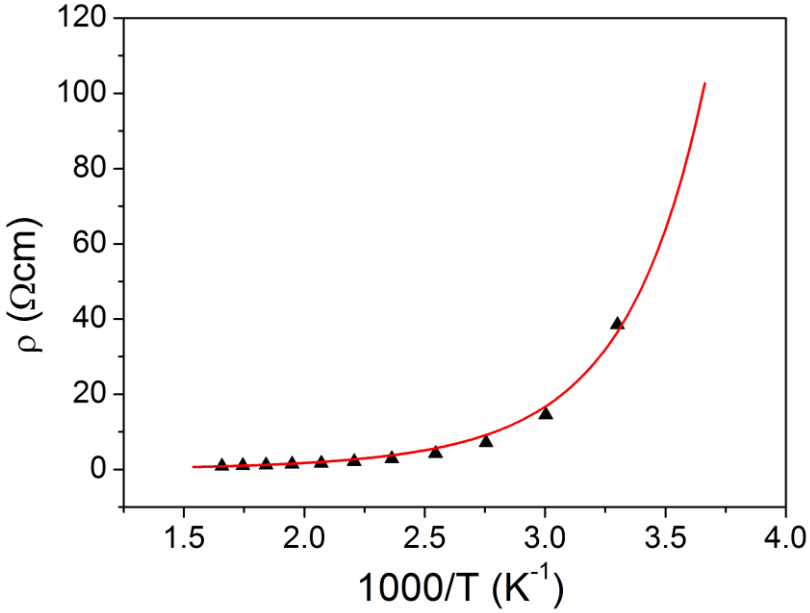

Figure 4.6 - Resistivity versus reciprocal temperature of sample C, experimentally determined (black symbols) and theoretically calculated values (red line).

Sample	μ_{300} ($cm^2V^{-1}s^{-1}$)	E_A (eV)	s	N_A (cm^{-3})	N_D (cm^{-3})
A	~ 7	~ 0.36	1.5	9×10^{16}	1×10^{16}
B	~ 31	~ 0.30	1.5	2×10^{18}	1×10^{16}
C	~ 4	~ 0.27	0	6×10^{19}	1×10^{17}

Table 4.1 – Parameters affording the best fit to data for semiconducting pBDD samples; s, N_A and N_D are fixed values for each sample.

Mobilities at 300 K are in the range from 4 – 31 $cm^2V^{-1}s^{-1}$, with the highest value belonging to sample B. These mobilities are considerably lower than values for intrinsic single crystal CVD diamond, which have been reported to range from 2000 – 2250 $cm^2V^{-1}s^{-1}$ and up to 3800 $cm^2V^{-1}s^{-1}$.[19, 20] These values drop substantially with increasing boron content.[21, 22] Hole mobilities in pBDD are lower than scBDD due to carrier scattering at grain boundaries,[23] the highest reported (room temperature) carrier mobility for pBDD doped with a boron concentration of approximately 5×10^{17} cm^{-3} is ~ 70 $cm^2V^{-1}s^{-1}$.[24] The mobilities presented here are as expected lower than this value. They are similar to values reported by Zhang *et al*[25] of between 9.7 – 2.8 $cm^2V^{-1}s^{-1}$. It is interesting to note that the sample with the highest mobility (B) does not have the lowest concentration of boron, which would be unexpected if only scattering due to impurity atoms was operating. Scattering due to grain boundaries also occurs and boron doping is not uniform across all polycrystalline diamond. This will vary with average grain size, where films with larger grains (less boundaries) are expected to have less grain boundary scattering.[26] Sample B is the thickest film (860 μm) and contains grains far larger than those of A and C, this causes less scattering due to grain boundaries and increases the overall mobility.

Sample A, Figure 4.4, displays very high resistivity which is strongly dependent on temperature (note the units of the scale). This is due to its low boron concentration, as

temperature is increased more holes are thermally excited into the valence band thereby increasing conductivity. The activation energy of ~ 0.36 eV is close to that of the boron acceptor ionisation energy (0.37 eV).

Data for samples B and C, Figure 4.5 and Figure 4.6 respectively, show a similar trend of decreasing resistivity with increasing temperature as was observed in sample A. The resistivities of B and C are similar in the measured temperature range despite there being more than order of magnitude difference in boron doping, this could be explained by the fact that sample B has a higher mobility. The activation energies for these samples are lower than that of A, reflecting the increase in [B] and movement of the bottom of the acceptor band towards the top of the valence band. A reasonable fit to data for sample C could only be achieved by increasing N_D to 1×10^{17} cm^{-3} and changing s to 0. The latter suggests that the mobility of carriers in this sample is temperature independent over the range studied.

The resistivities of samples D and E, which contain high concentrations of boron, were also assessed at various temperatures and are plotted in Figure 4.7. Experimental resistivity data was fit with equation (4.8) as before, using the solver function in Microsoft Excel to modify the adjustable parameters in order to obtain the best fit, these values are listed below in Table 4.2. The s parameter was set to 0 due the high concentration of boron in these films.

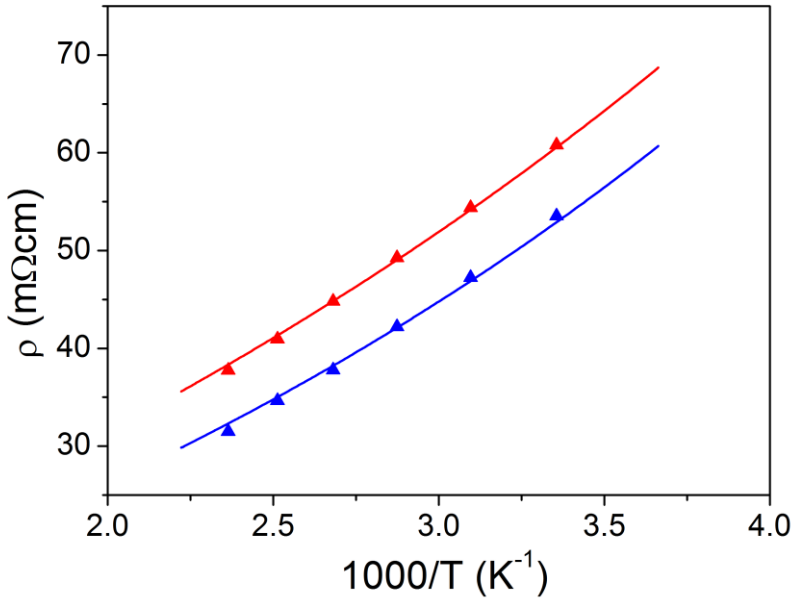

Figure 4.7 – Resistivity as a function of temperature for samples D (red) and E (blue). Experimental values are plotted as symbols and theoretical values calculated from equation (4.8) are solid lines.

Sample	μ_{300} ($cm^2V^{-1}s^{-1}$)	E_A (eV)	s	N_A (cm^{-3})	N_D (cm^{-3})
D	~ 7	~ 0.03	0	2×10^{20}	1×10^{16}
E	~ 7	~ 0.04	0	3×10^{20}	1×10^{16}

Table 4.2 – Adjustable parameters of equations (4.9) and (4.10) used to obtain best fit for experimental data of heavily boron doped samples.

Around the metallic threshold of 2 - 3 × 10^{20} cm^{-3}, only a weak dependence of resistivity with temperature is expected, above this value conductivity is expected to decrease with increasing temperature.[5] It can be seen in Figure 4.7 that both samples display a temperature dependent resistivity, with higher temperatures reducing resistivity. This temperature dependence is very small however, and at 300 K $K_BT \approx$ 26 meV which is similar to the activation energies presented here, these samples are therefore deemed to be effectively metallic. Due to their polycrystalline nature a range of different boron concentrations are present throughout each sample, N_A values noted

in Table 4.2 represent an average over several grains. Experimentally derived activation energies therefore may represent an E_A maximum attributed to the lower doped grains. It is surprising however that sample D seems to display a slightly smaller activation energy than sample E, despite the latter containing a higher boron concentration. It is known from Raman spectroscopy that sample D contains non-negligible amounts of sp^2 carbon, which may contribute to a decrease in the overall resistivity and possibly skew data derived from resistivity measurements as the material in not exclusively BDD.

4.2 Micro-Raman Spectroscopy

4.2.1 Raman Spectroscopy of BDD

Raman spectroscopy is a useful tool for studying BDD, as it yields information about crystalline quality, boron concentration and the presence of sp^2 bonded carbon. The latter is of particular importance in electrochemistry as it has detrimental effects on electrode response such as; increased capacitance, narrower solvent window and sensitivity to species such as dissolved oxygen. The presence of sp^2 bonded carbon is easily identified with Raman spectroscopy, appearing as a broad feature around 1500 cm^{-1}. Raman is also useful for qualitatively assessing the extent of local boron doping by observing the zone centre optical phonon (sp^3) peak at 1332 cm^{-1}; the features arising from sp^2 incorporation and boron doping are shown in Figure 4.8 (a) and (b). The spectrum in (a) shows an area of sample D that contains a relatively low boron concentration and no detectable sp^2 bonded carbon, whereas in (b) a large peak due to the presence of sp^2 carbon has appeared and the peak at 1332 cm^{-1} has been attenuated indicating a relatively high boron concentration.

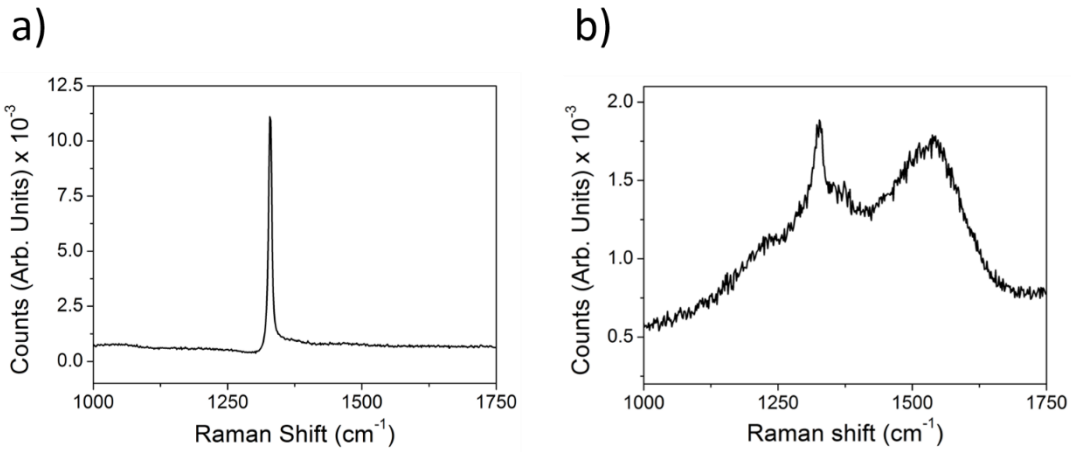

Figure 4.8 – Raman spectra of sample D showing a) non-sp^2 carbon containing region and b) region with pronounced sp^2 carbon signature.

4.2.2 Mapping the Heterogeneity of pBDD

A Raman study was undertaken to assess the heterogeneity and sp^2 content of two heavily doped pBDD samples, D and E. pBDD will incorporate boron at different rates for different crystal faces during growth, such that (111) > (110) > (100).[27] This can easily be seen as contrast between grains in SEM using an in-lens secondary electron detector, where areas of higher boron content appear as dark regions and vice versa. Figure 4.9 is a typical SEM image of a heavily doped pBDD sample, the heterogeneity across the sample is clearly observed.

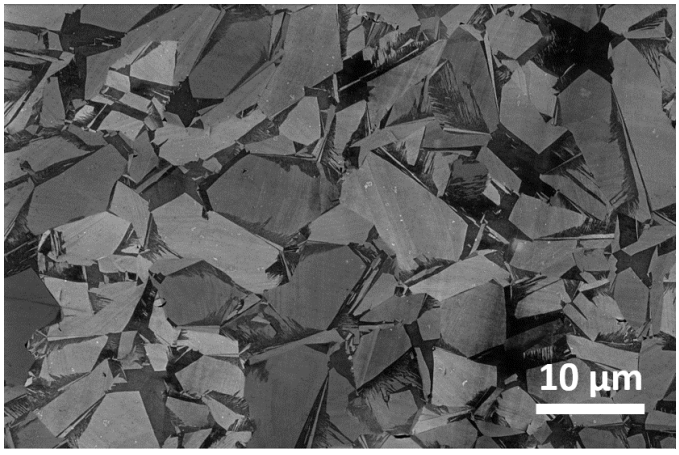

Figure 4.9 – SEM of heavily doped pBDD recorded with an 'in-lens' secondary electron detector.

It is known that boron doping has a profound impact on the Raman spectra of diamond. The zone centre optical phonon peak in intrinsic diamond is situated at a Raman shift of 1332 cm^{-1}, its shape is described by a Lorentizian function.[28] Upon heavy boron doping however several changes to this peak occur; a shift to lower wavenumbers, an attenuation of peak height/area and a change in lineshape. These changes in Raman spectra may be used to map a surface.[29] Additionally, a feature at ~ 600 cm^{-1} appears which also shifts to lower wavenumbers with increased boron doping,[30] analysis of this feature was only shown to be quantitative for $2 \times 10^{20} < [B] < 10^{22}$ cm^{-3}.[31]

Raman spectroscopy was performed over a 20 µm × 20 µm area (400 μm^2) for samples D and E, a spectrum was recorded for every 1 μm^2. The areas of the peaks at 1332 and ~ 1500 cm^{-1} were recorded for sample D and are plotted in Figure 4.10 as an image. Peak area is plotted on a colour scale, with the highest values represented with red and the lowest values with blue.

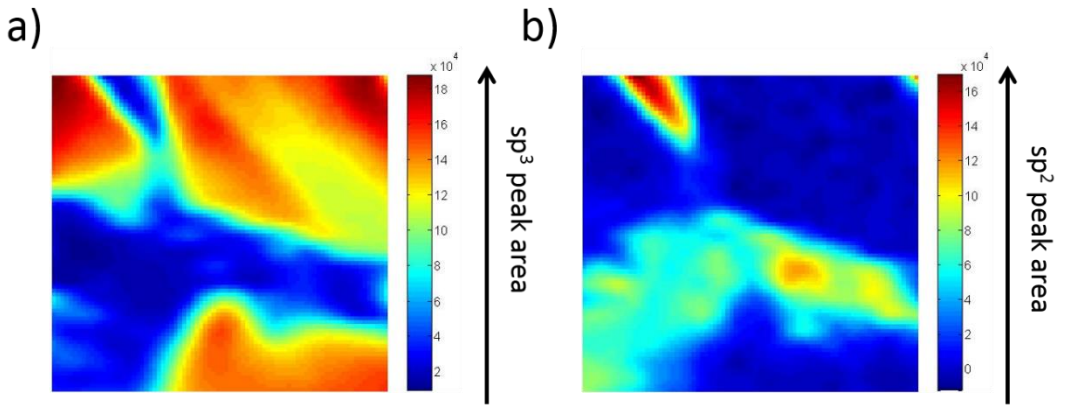

Figure 4.10 – Raman maps of sample D showing; a) variation in sp^3 region peak area and b) variation in sp^2 region peak area.

It can be seen that the boron concentration is not uniform and varies between different grains, as is seen in SEM. Interestingly in sample D, there appears to be a correlation between boron concentration and sp^2 carbon, indicating that the diamond quality

suffers (more sp^2) at higher boron concentrations. The blue areas in Figure 4.10 correspond with the non-blue areas in Figure 4.10 (b), whereas areas of relatively low boron concentration seem to contain no detectable sp^2 carbon.

Raman maps of sample E were recorded and are plotted in Figure 4.11, the same procedure was used as described above for sample D.

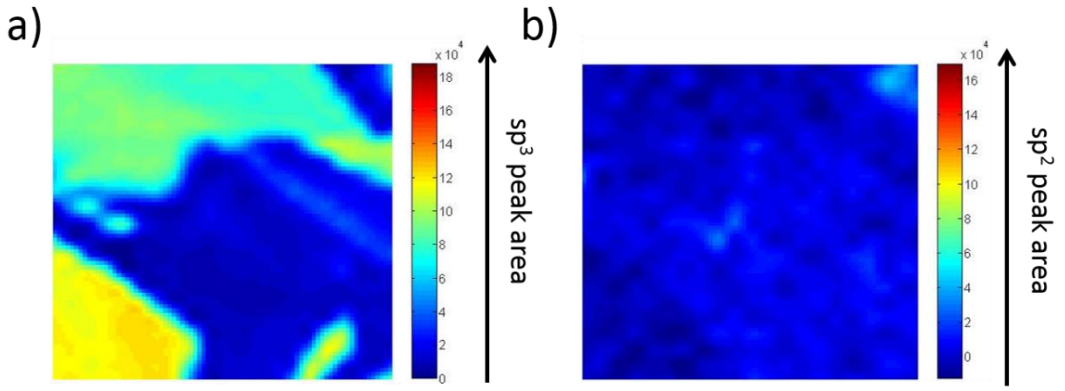

Figure 4.11 - Raman maps of sample E showing; a) variation in sp^3 region peak area and b) variation in sp^2 region peak area.

A variation in boron content was again seen across the region studied, though for this sample there seems to be less variation within grains on the same colour scale. However, in contrast to sample D no correlation between areas of relatively high boron content and sp^2 carbon is observed. The map in Figure 4.11 b) appears to be very uniform, this is because of the negligible amounts of sp^2 carbon present which are not detectable by Raman in this study.

4.3 Conclusion

Further characterisation of pBDD has been performed by electrical resistivity measurements and Raman spectroscopy. The resistivities of semiconducting samples showed a strong temperature dependence, resistivity decreases as temperature increases due to an increased number of available charge carriers. Heavily doped samples doped with $2 – 3 \times 10^{20}$ atoms cm^{-3} of boron were also assessed in this way; resistivity was found to be weakly temperature dependent. Calculated curves were successfully simulated, the fit to experimental data showing validity of the theoretical models used. It is known that carrier mobility is dependent upon factors such as impurity atom concentration, grain size and sample thickness; at high boron concentrations, hole mobility was assumed to be temperature independent.

More information could be gleaned by performing resistivity measurements over a larger temperature range and by performing Hall measurements to extract hole mobilities. The results presented here though do confirm the semiconducting or metallic nature of the samples used and the electrical properties are consistent with literature values.

The heterogeneity of boron incorporation and sp^2 content of samples D and E were assessed with Raman spectroscopy. At high boron concentrations the peak located at 1332 cm^{-1} is attenuated and its area diminishes, the area of the feature at around 1500 cm^{-1} is indicative of non-diamond carbon content. By plotting these areas as contrast in an image the variation of boron doping and sp^2 content can be seen. Both samples displayed a heterogeneous distribution of boron which is expected for polycrystalline diamond films. In sample D a correlation of high boron concentration and sp^2 carbon

was observed, no such correlation was seen in sample E indicating that the latter is of higher quality and more suitable for electrochemical analysis.

4.4 References

1. C. E. Nebel, *Semicond. Sci. Technol.*, 2003, **18**, S1.
2. R. Kalish, *Carbon*, 1999, **37**, 781-785.
3. A. T. Collins and A. W. S. Williams, *J. Phys. C: Sol. St. Phys.*, 1971, **4**, 1789.
4. C. E. Nebel and J. Ristein, *Thin-Film Diamond I*, Elsevier Academic Press, 2003.
5. J. P. Lagrange, A. Deneuville and E. Gheeraert, *Diamond Relat. Mater.*, 1998, **7**, 1390-1393.
6. A. W. S. Williams, E. C. Lightowlers and A. T. Collins, *J. Phys. C: Sol. St. Phys.*, 1970, **3**, 1727.
7. H. Fritzsche, *Phys. Rev.*, 1955, **99**, 406-419.
8. H. Fritzsche and K. Lark-Horovitz, *Phys. Rev.*, 1959, **113**, 999-1001.
9. H. Fritzsche, *J. Phys. Chem. Solids*, 1958, **6**, 69-80.
10. E. A. Davis and W. D. Compton, *Phys. Rev.*, 1965, **140**, A2183-A2194.
11. T. Inushima, T. Matsushita, S. Ohya and H. Shiomi, *Diamond Relat. Mater.*, 2000, **9**, 1066-1070.
12. E. P. Visser, G. J. Bauhuis, G. Janssen, W. Vollenberg, J. P. v. Enckevort and L. J. Giling, *J. Phys.: Condens. Matter*, 1992, **4**, 7365.
13. X. Blase, E. Bustarret, C. Chapelier, T. Klein and C. Marcenat, *Nat Mater*, 2009, **8**, 375-382.
14. G. L. Pearson and J. Bardeen, *Phys. Rev.*, 1949, **75**, 865-883.
15. T. H. Borst and O. Weis, *Diamond Relat. Mater.*, 1995, **4**, 948-953.
16. J. C. Bourgoin, J. Krynicki and B. Blanchard, *physica status solidi (a)*, 1979, **52**, 293-298.
17. H. Kiyota, E. Matsushima, K. Sato, H. Okushi, T. Ando, J. Tanaka, M. Kamo and Y. Sato, *Diamond Relat. Mater.*, 1997, **6**, 1753-1758.
18. J. Seymour, *Electronic Devices and Components*, Pitman, London, 1981.
19. M. Nesladek, A. Bogdan, W. Deferme, N. Tranchant and P. Bergonzo, *Diamond Relat. Mater.*, 2008, **17**, 1235-1240.
20. J. Isberg, J. Hammersberg, E. Johansson, T. Wikström, D. J. Twitchen, A. J. Whitehead, S. E. Coe and G. A. Scarsbrook, *Science*, 2002, **297**, 1670-1672.
21. J. Pernot, P. N. Volpe, F. Omnès, P. Muret, V. Mortet, K. Haenen and T. Teraji, *Phys. Rev. B.*, 2010, **81**, 205203.
22. M. Werner, R. Locher, W. Kohly, D. S. Holmes, S. Klose and H. J. Fecht, *Diamond Relat. Mater.*, 1997, **6**, 308-313.
23. A. Masood, M. Aslam, M. A. Tamor and T. J. Potter, *Appl. Phys. Lett.*, 1992, **61**, 1832-1834.
24. H. J. Looi, R. B. Jackman and J. S. Foord, *Appl. Phys. Lett.*, 1998, **72**, 353-355.
25. R. J. Zhang, S. T. Lee and Y. W. Lam, *Diamond Relat. Mater.*, 1996, **5**, 1288-1294.
26. D. M. Malta, J. A. von Windheim and B. A. Fox, *Appl. Phys. Lett.*, 1993, **62**, 2926-2928.
27. P. Wurzinger, P. Pongratz, P. Hartmann, R. Haubner and B. Lux, *Diamond Relat. Mater.*, 1997, **6**, 763-768.
28. L. Bergman and R. J. Nemanich, *J. Appl. Phys.*, 1995, **78**, 6709-6719.

29. S. Szunerits, M. Mermoux, A. Crisci, B. Marcus, P. Bouvier, D. Delabouglise, J.-P. Petit, S. Janel, R. Boukherroub and L. Tay, *J. Phys. Chem. B*, 2006, **110**, 23888-23897.
30. A. N. Ndao, F. Zenia, A. Deneuville, M. Bernard and C. Lévy-Clément, *Diamond Relat. Mater.*, 2000, **9**, 1175-1180.
31. M. Bernard, A. Deneuville and P. Muret, *Diamond Relat. Mater.*, 2004, **13**, 282-286.

5 High Temperature Electrochemistry

The effects of temperature on the electrochemical response of pBDD are investigated in this chapter, under isothermal and non-isothermal conditions. A glass sealed pBDD electrode was employed in the former, where a water bath apparatus was used to control the temperature of the solution. A thin (200 μm) pBDD sample mounted in a custom made cell was utilised in non-isothermal experiments, a laser was used to apply heat pulses to this electrode during voltammetric experiments.

Bulk solution heating in isothermal experiments introduced appreciable convection into the system. CVs displayed steady state-like shapes under these conditions in addition to increased peak currents that could not be reproduced with calculated values. These effects were more pronounced at higher temperatures and slower scan rates. A Pt UME was tested in the same manner, however it was shown that limiting currents could be predicted suggesting that the increased rate of convection under this regime is still not significant compared to diffusion for a small (25 μm) electrode.

Pulsed laser heating was used to rapidly heat a thin pBDD electrode in synchronous with voltammetric experiments. The $Ru(NH_3)_6^{2+/3+}$, $FcTMA^{+/2+}$, $IrCl_6^{2-/3-}$ and $Fe^{2+/3+}$ couples were examined with this technique, all showed a response under pulse heated conditions. $Ru(NH_3)_6^{2+/3+}$ showed a large current enhancement in the cathodic direction, whereas the effects of heating diminished the recorded current in the anodic direction for $FcTMA^{+/2+}$.

5.1 Introduction

The effect of temperature in electrochemistry is of great importance[1, 2] yet most electrochemical experiments are performed at, or very near to, room temperature (ca. 25 ^{o}C). This is surprising since temperature, *T*, is a key variable in many thermodynamic equations that describe various processes in electrochemistry such as entropy, enthalpy and Gibbs free energy (*S*, *H* and *G* respectively).[3] Temperature can also be used to drive many chemical and physical processes at faster rates, due to energetic barriers becoming more easily overcome or reaction mechanisms changing.[4] Being able to arbitrarily vary temperature as an independent variable in an experiment gives rise to the technique known as thermoelectrochemistry, which spans a broad range of experimental conditions.

Electrochemistry involves the study of many different processes and mechanisms, many with their own temperature dependence.[5] At the simplest level, the situation can be broken down into a two-step process; mass transport of species towards the electrode followed by electron transfer. The former describes the movement of electrochemically active molecules in solution; whilst the latter describes processes that occur at the electrode/electrolyte interface, in particular charge transfer. Whichever is the slowest step governs the overall reaction rate, hence the rates of electron transfer and mass transport, relative to one another, must be carefully considered in an electrochemical experiment. Importantly, both will be affected by temperature.[6] Concerning mass transport, an increased temperature will act to increase the rates of both convective and diffusive flux; the former through induced thermal gradients[7] and the latter due to a decreased solvent viscosity.[8]

Temperature also has an impact upon the HET rate for an electrochemical reaction. If this electron transfer is considered using transition state theory (TST), it is assumed that an energy barrier must be overcome and a transition state achieved in order for the (forward or backward) reaction to proceed. The rate constants that describe the forward and backward reactions, k_f and k_b respectively, are assumed to take an Arrhenius form, equations (5.1) and (5.2);

$$k_f = A_f \exp\left(-\frac{\Delta G_c^{\ddagger}}{RT}\right) \tag{5.1}$$

$$k_b = A_b \exp\left(-\frac{\Delta G_a^{\ddagger}}{RT}\right) \tag{5.2}$$

where A_f and A_b are the pre-exponential factors for k_f and k_b respectively, $\Delta G_c^{\ddagger}$ and $\Delta G_a^{\ddagger}$ are the energy barriers for reduction and oxidation and all other symbols have their usual meanings.

At equilibrium, k_f and k_b are equal to each other; this is called the HET standard rate constant k^0. At other potentials the rate constants may be stated relative to k^0, from which the Butler-Volmer equation may be derived, equation (5.3).[9]

$$i = FAk^0\left[C_O(0,t)e^{-\alpha f\left(E-E^{0'}\right)} - C_R(0,t)e^{(1-\alpha) f\left(E-E^{0'}\right)}\right] \tag{5.3}$$

where i is the current, F is the Faraday constant, $f = F/RT$, A is the electrode area in cm, $C_O(0,t)$ and $C_R(0,t)$ are the surface concentrations of the oxidised and reduced forms of the redox couple at time t respectively, α is the transfer coefficient (often assumed to be 0.5, unless known explicitly), and $E^{0'}$ is the formal electrode potential.

A relation between the rate of HET and temperature may also be drawn by considering Marcus theory, where k^0 varies exponentially with reciprocal temperature; as temperature increases so does k^0, equation (5.4)[10].

$$k^0 = K_p \kappa_{el} \nu_n \exp\left(-\frac{\Delta G^{\ddagger}}{RT}\right) \tag{5.4}$$

where K_p is the precursor equilibrium constant, κ_{el} is the electronic transmission coefficient and ν_n is the frequency factor, though for the purposes of this discussion these terms may be collected into a single constant.

Equations (5.1) (5.2) and (5.4) are all of a similar form, that of an Arrhenius expression, a more general form of this equation may be given as;

$$k = A\exp\left(-\frac{\Delta E_A}{RT}\right) \tag{5.5}$$

where k is the rate constant of some general reaction, A is a pre-exponential factor and ΔE_A is the activation energy for the reaction. Examination of this equation reveals that as the absolute temperature increases, the entire bracketed term becomes smaller and therefore less negative. Taking the exponential function of a decreasingly negative number (as T increases) results in a larger value of k. Thus it is expected that the rate of HET of an electrochemical reaction will increase with temperature, assuming no other appreciable conflicting factors are present such as an appreciable increase in electrode resistance.

5.1.1 Continuously Heated Voltammetry

An obvious way to perform high temperature electrochemical measurements is to heat the entire solution of interest isothermally and conduct experiments in the usual manner. The advantages of this method are that it is experimentally simple to set up

and perform, as well as mimicking processes that may occur at elevated temperatures, such as chemical reactions inside a nuclear reactor[11] or fuel cell technology[12, 13]. If a high pressure system is used in conjunction with high temperature then the temperature of water (for example) can be raised above 100 ^{o}C, enabling solution based experiments to be undertaken in aqueous solution under conditions that exceed the boiling point of water.[14, 15]

Continuous heating of the entire solution however, may lead to unintentional time-dependant thermal gradients, resulting in the movement of species due to convection. This is undesirable as mass transport in the system can then be difficult to predict quantitatively. It is also important to consider possible thermal degradation of the electroanalyte molecule of interest, as some species may be thermally unstable[16] for prolonged periods. Experiments performed under these conditions may last several hours as heating using a water bath containing a large volume of water (greater than 1 dm^3) is relatively slow.

Isothermal experiments are useful for initial studies of a given system, as the cell temperature (including that of all electrodes) can be controlled and known to be constant throughout the experiment. Data gathered can then be used in situations where the system temperature is not known. Isothermal studies have been used to perform electrochemical experiments at a variety of temperatures to elucidate thermodynamic quantities such as ΔH, ΔS and ΔG of a system. Fundamental equations relating thermodynamic state functions and temperature are given in equations (5.6) and (5.7):[17]

$$\Delta G^{o} = -nFE^{o} \qquad (5.6)$$

$$\left(\frac{\partial E^o}{\partial T}\right)_P = -\Delta S^o \qquad (5.7)$$

From which equation (5.8) may be obtained, since E^o and ΔG^o are both independent of pressure:

$$\left(\frac{dE^o}{dT}\right)_P = \frac{\Delta S^o}{nF} \qquad (5.8)$$

Examination of equation (5.8) reveals a close relationship between potential, temperature and entropy; the change in potential of an electrochemical cell due to a change in temperature is proportional to the entropy of the reaction in question. The potential of an electrode versus a given reference will shift with a change in temperature, this 'temperature coefficient', β, of an electrode is intimately connected with the thermodynamic state functions; values typically have been found to range from ± 2.4 mVK^{-1}.[18] Examples of experiments carried out in an isothermal system include; calculation of diffusion coefficients,[19] investigation of methanol electrochemistry in fuel cell technology[20] and determining the temperature coefficient of the calomel electrode potential.[21]

5.2 Pulsed Voltammetry

CV is certainly the most significant and widely used technique in the field of electrochemistry, whereby a potential varying linearly with time is applied to an electrode and the resulting current flowing through it is recorded. More insight into a particular electrochemical system can be gained however, by the implementation of techniques involving more sophisticated excitation potential waveforms where the free energy of the reaction is perturbed abruptly. DPV is an electrochemical technique

that employs the use of potential pulses superimposed onto a potential staircase. The resulting waveform is depicted in Figure 5.1; where labels A, W and S denote the pulse amplitude, pulse width and step size respectively. Two current samples are taken, the first occurring just before the start of each pulse, τ', and the second just before the end of each pulse, τ. The difference between the two is taken and plotted against potential to construct a voltammogram. This subtraction leads to a cancelling out the non-faradaic (capacitive) currents (in the main) as the capacitive currents at τ' and τ are very similar. DPV can be used analytically to achieve better limits of detection than CV, typically going down to approximately 10^{-7} M.[5]

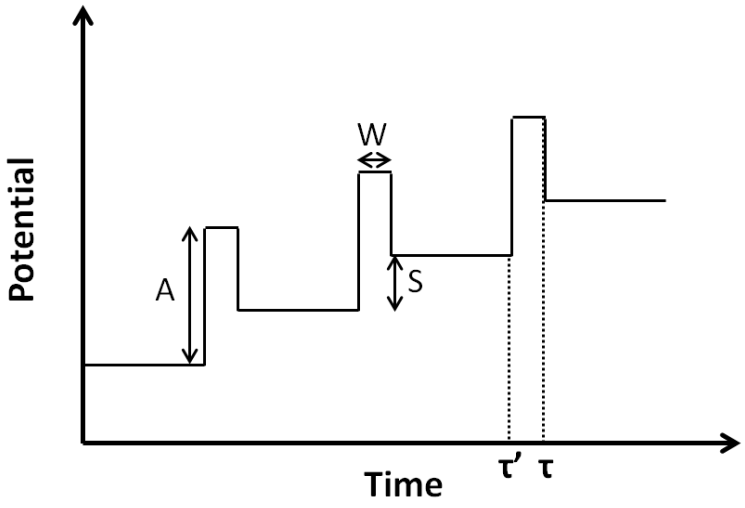

Figure 5.1 - Schematic of potential waveform applied during a DPV experiment including, current samples are taken at τ' and τ respectively.

Assuming that only the oxidised or reduced form of redox mediator is present initially, *O* and *R* respectively, then the peak potential, E_p, and peak current, i_p, may be calculated from equations (5.9) and (5.10):[22, 23]

$$E_p = E_{1/2} \pm \frac{\Delta E}{2} \tag{5.9}$$

$$i_p = \frac{nFAD^{1/2}C^*}{\pi^{1/2}(\tau - \tau')^{1/2}}\left(\frac{1-\sigma_{DPV}}{1+\sigma_{DPV}}\right) \tag{5.10}$$

where ΔE is the pulse amplitude (A in Figure 5.1 and σ_{DPV} is a parameter given by equation (5.11):

$$\sigma_{DPV} = \exp\left(\frac{nF}{RT}\frac{\Delta E}{2}\right) \tag{5.11}$$

Experimental data is plotted against theoretical data in order to test the validity of equation (5.11) at different pulse amplitudes, Figure 5.2. It can be seen that there is good agreement between experiment and theory at lower values of pulse amplitude, however these data appear to begin to diverge at increasingly large values of ΔE_p.

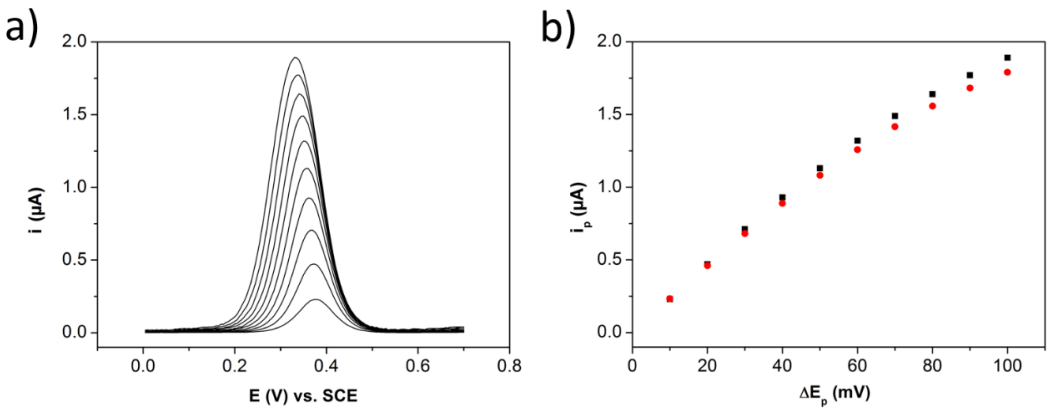

Figure 5.2 – a) DPV of pBDD in 0.5 mM $FcTMA^+$ 0.1 M KNO_3 at pulse amplitudes from 10 mV (smallest peak) to 100 mV (largest peak) and b) comparison of peak currents from a) (black symbols) and theoretical values (red symbols).

5.2.1 Pulse Heated Voltammetry

By combining pulsed voltammetry with heated voltammetry, pulsed thermoelectrochemistry can be conducted. During the pulsed heating method, the temperature of an electrode (typically working) is changed with an external stimulus as a function of time. As a result the bulk temperature of the solution is unchanged,

only the working electrode experiences any change. This leads to the creation of a non-isothermal system where a temperature gradient is present. In contrast to isothermal heating, this methodology allows direct investigation of a single electrode without the need for two half cells and a salt bridge. Any thermodynamic information gathered corresponds only to the electrode heated.

A requirement of this method is that the electrode and solution near the interface can be heated and cooled sufficiently quickly. Typical pulse times range from ca. 5-50 ms, although very short laser pulses (10^{-12} s) have been used for electrical double layer studies.[24] The use of pulsed heating is beneficial in several ways: it helps avoid thermal decomposition of the redox mediator as the bulk solution is not heated, convection can be avoided provided the timescale is fast enough and temperatures can be achieved that exceed the boiling point of the solvent. As the temperature sits at these values for only brief periods of time bubbling due to boiling is avoided.[25]

Pulsed high temperature voltammetry requires two separate perturbations, electrical and thermal, the former as in typical voltammetry and the latter to administer the temperature change. The electrical perturbation can be applied easily, and arbitrarily quickly, with the use of a commercially available potentiostat. The heating may be applied indirectly by using an external heater or directly by using the working electrode itself as the heater. Methods to achieve pulsed heating have included: (i) utilising a Pt working electrode as a resistive heating element,[25] (ii) microwave radiation to deliver energy to a small volume of solution adjacent to the electrode,[26] (iii) radio frequency (RF) radiation to induce heating eddy currents in metal electrodes[27] and laser irradiation.[28, 29]. Induced thermal gradients render theoretical treatment of transport processes difficult at large stationary electrodes, due to the relatively slow rate of diffusion to the electrode. However, effects of convection can

be avoided, or rather accounted for, by moving to a system with increased and defined mass transport; e.g. electrodes with small dimensions such as micro-wires[25] and the rotating disk electrode (RDE).[30] A planar sensor type construction has also been successfully used,[31] the unusual geometry of this electrode is that of a circular-arc shape.

A specific type of thermoelectrochemistry utilising pulsed heating, known as Temperature Pulse Voltammetry (TPV), has been described by Gründler.[31] TPV is analogous to DPV, described in section 3.1.2, except that the former uses temperature to perturb the free energy of an electrochemical system, whereas the latter uses potential. This technique will hereafter be referred to as *differential* temperature pulse voltammetry (DTPV), as this includes a description of the subtractive nature of this technique, and TPV when no current subtraction is applied. For TPV the peak current of each transient is plotted against potential to construct a voltammogram.

5.2.2 Material Considerations

The majority of high temperature studies have been performed on metal electrodes such as platinum and gold. Metals are an obvious choice as they have been routinely used in electrochemical studies for many years and are well understood, metals also have high electrical and thermal conductivities. However, metal electrodes may not always be suitable for electroanalysis at high temperatures due to the formation of oxides,[27] and have been found to become more labile.[25] Glassy carbon fibres are not robust enough for high temperature electrochemistry, as they have been found to fail with simultaneous heating and electrical polarisation.[32] A suitable material for performing high temperature electrochemistry therefore must possess high electrical

and thermal conductivity, and perform well electrochemically at elevated temperatures.

pBDD has emerged as an important material in the field of electrochemistry due to its truly unique properties such as; wide potential window, extreme chemical stability, and low background currents. In addition, pBDD also possesses a very high thermal conductivity, ca. 600 $Wm^{-1}K^{-1}$ at 300 K[33] for comparison the thermal conductivity of copper is ca. 400 $Wm^{-1}K^{-1}$.[34] This property makes pBDD an excellent choice for high temperature electrochemistry, utilising the electrode itself as a thermal conductor to direct thermal energy towards the electrode/solution interface. In the current method, heat is applied to the non-solution face of pBDD disk and must propagate through the sample to reach the electrochemical interface, therefore a higher thermal conductivity is favourable. Additionally, the potential window of a solvent is found to decrease at elevated temperatures possible due to an increase in the rate of solvent electrolysis,[25] making the wide potential window of pBDD even more desirable.

5.3 Results and Discussion

5.3.1 Continuous Heating

CVs at a pBDD disk electrode (sample H, Element Six Ltd) of diameter 1 mm fabricated as described in section 2.2.1 were recorded in a solution of 1 mM $FcTMA^+$ in 0.1 M KNO_3 at different temperatures ranging from 15 ºC to 75 ºC (as described in section 2.5.1 at scan rates of 10, 25, 50 and 100 mV s^{-1} as shown in Figure 5.3 (a), (b), (c) and (d) respectively. It is immediately apparent that changing the solution temperature has an effect on the recorded CVs, at all scan rates. However, the extent of the change depends on the scan rate employed, with the largest changes seen for the slowest scan rate, as shown in Figure 5.3 (a). Firstly, the current increases with increasing temperature, secondly the shape of the CVs move from peak shape, to steady state and finally, the CVs in the limiting current region show fluctuations, especially at the higher temperatures.

An increase in current (i) at higher temperatures is due to an increase in mass transport or flux (j) of species to the working electrode, as described by equation (5.12)[9].

$$i = nAFj \tag{5.12}$$

Where n is the number of electrons transferred, A is the electrode area in cm^2 and F is the Faraday constant (96485 C mol^{-1}). The mass transfer coefficient, k_t, which describes the rate of mass transport for a diffusion limited process is given in equation (5.13):

$$k_t = \frac{i}{nAFC^*} \tag{5.13}$$

Note, by increasing the voltage scan rate the diffusion layer thickness is decreased, leading to a steeper concentration gradient and therefore an increase in flux. A faster scan rate therefore leads to a larger peak current and also a larger value of k_t.

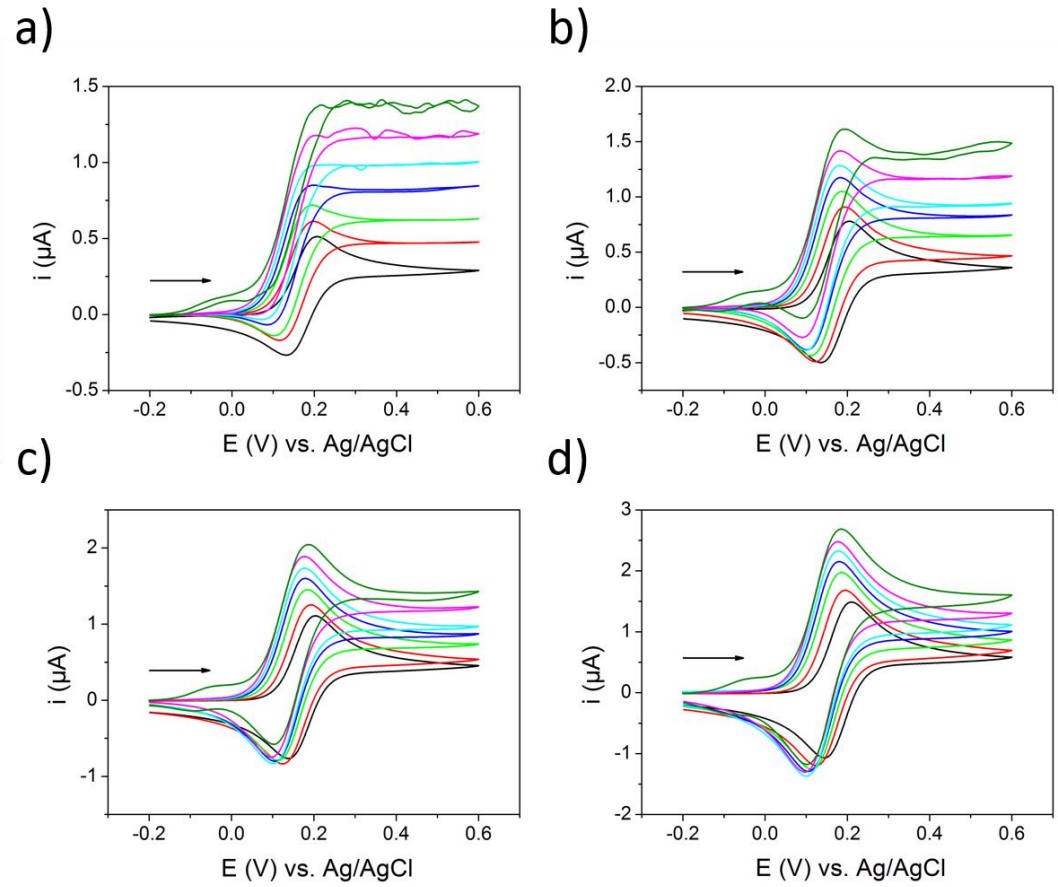

Figure 5.3 - CVs of pBDD macroelectrode in 1 mM $FcTMA^+$, 0.1 M KNO_3 from 15°C (black) to 75 °C (olive) in increments of 10 °C performed at (a) 10 mV s^{-1}, (b) 25 mV s^{-1}, (c) 50 mV s^{-1} and (d) 100 mV s^{-1}.

At the slower scan rates and higher temperatures, the shape of the CV changes from peak-shaped to steady state. Under quiescent conditions, a diffusion-only controlled peak shaped CV is expected for this size electrode coupled with the use of a fast electron transfer redox couple i.e. $FcTMA^+$,[35] with a limiting current given by the Randles-Sevcik equation.[9]

$$i_p = 0.4463\left(\frac{F^3}{RT}\right)^{1/2} n^{3/2} A D^{1/2} C^* \upsilon^{1/2} \qquad (5.14)$$

Where i_p is the peak current, R is the molar gas constant (8.314 m^2 kg s^{-2} K^{-1} mol^{-1}), D is the diffusion coefficient of analyte, C^* is the bulk concentration of analyte, υ is the scan rate and all others symbols have their usual meanings.

Solvent viscosity and diffusion of analyte species are both affected by temperature, with increasing temperatures leading to a decrease in viscosity[36] and an increase in the rate of diffusion. The relationship between D, and T, is given by equation (5.15), the Stokes-Einstein equation.[37]

$$D = \left(k_b T\right) / 6\pi\eta r \qquad (5.15)$$

Where k_b is the Boltzmann constant, η the dynamic viscosity of solution and r is the hydrodynamic radius of diffusing species. By substituting equation (5.15) into equation (5.14) the T terms cancel, though i_p is still dependent upon η which is a function of temperature.

By using equation (5.15) to theoretically determine D for $FcTMA^+$ at the seven different temperatures, it is possible to predict the expected increase in i_p from equation (5.14) based on D changes alone. Values of dynamic viscosity were calculated using an equation derived from a large set of data values.[36] To determine r, for $FcTMA^+$ a literature value[38] of 7.6 x 10^{-6} cm^2 s^{-1} was used for D at 22 ºC, allowing rearrangement of equation (5.15) to determine r. The calculated value of r (0.3 nm) was assumed to be temperature independent for the temperature range used. The Stokes-Einstein relationship has been used successfully by Bard *et al*[15] in comparing experimentally determined and theoretically calculated diffusion coefficients for hydroquinone and iodide in aqueous solution. However, Trevani *et al*[39] found that r

decreases with increasing temperature for $FeSO_4$, the authors ascribe this to speciation; the concentration of $FeSO_4$(aq) increases relative to the concentration of Fe^{2+}(aq). Experimental data taken from Figure 5.3 are examined in Figure 5.4, where measured peak current (i_p) values are compared against theoretical values. It is apparent that as the solution temperature is increased the theoretical and measured peak current values become increasingly divergent, this divergence is exacerbated at the lowest scan rates. This divergence is attributed to thermal convection (introduced by non-uniform heating causing turbulence) in the system which is unaccounted for in equations (5.14) and (5.15). This represents the limitations of using a hot water bath to heat bulk solution; heat cannot be applied perfectly uniformly.

At the slower scan rates and the higher temperatures the CVs in Figure 5.3 approach a steady-state due to the sufficiently high mass transport rates generated in the system due to convection; the timescale is now appropriate for these effects to become evident. However as the data in Figure 5.3 (a) shows (pink and dark green lines) mass transport is uncontrolled as evidenced by the fluctuations in the limiting current.

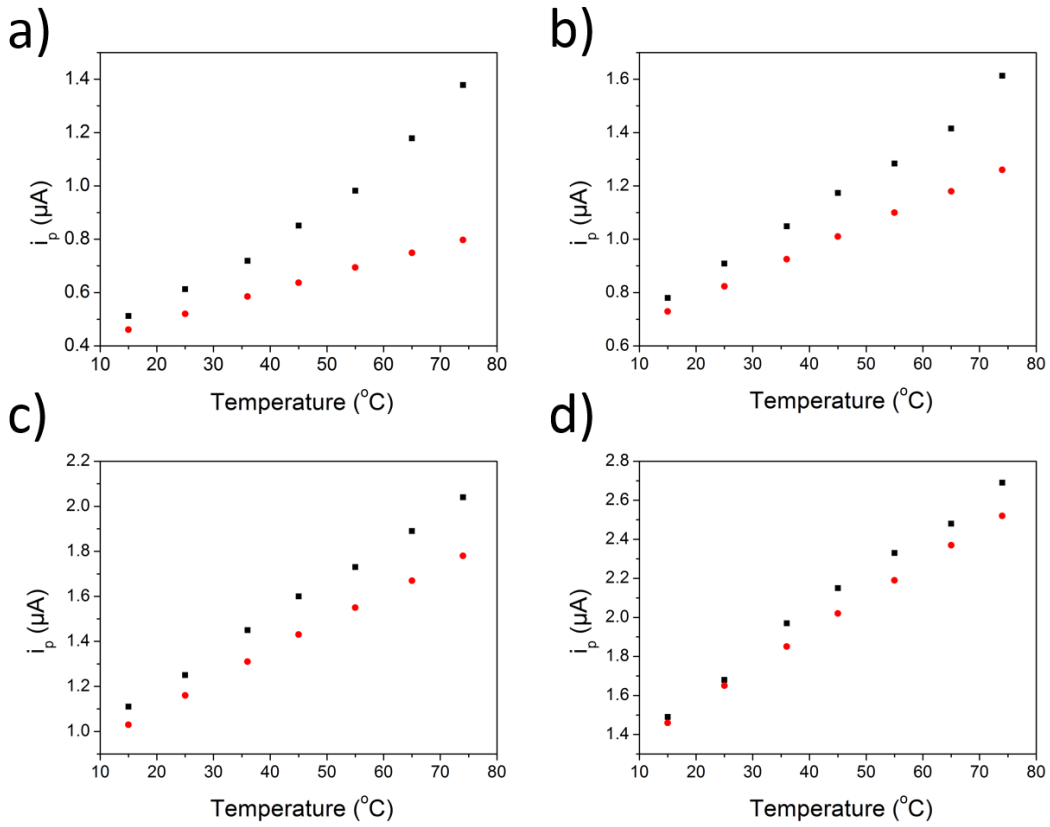

Figure 5.4 – Theoretical (red symbols) and measured (black symbols) peak currents of pBDD macroelectrode in 1 mM $FcTMA^+$, 0.1 M KNO_3 at different temperatures. Performed at scan rates of (a) 10 mV s^{-1}, (b) 25 mV s^{-1}, (c) 50 mV s^{-1} and (d) 100 mV s^{-1}.

At the fastest scan rates of 50 mV s^{-1} and 100 mV s^{-1}, the peak potentials at which oxidation and reduction of $FcTMA^{+/2+}$ occur, shift with temperature. At 50 mVs^{-1} and 100 mV s^{-1}, both oxidation and reduction potentials shift to less positive values with increasing temperature and then start to shift back to more positive potentials as the temperature is increased further. As has been discussed earlier, a shift in peak potential is expected at elevated temperatures due to a change in entropy. Quantitatively assessing this peak shift becomes complicated however as all three electrodes in solution will be affected to a different extent, shifting by different amounts as they each have a different temperature coefficient. The peak to peak separations, ΔE_p, are also seen to change with temperature. For a perfectly reversible system, ΔE_p is equal

to 2.303*RT/nF* (59 mV at 298 K); therefore ΔE_p will increase by approximately 2 mV for every increase in system temperature of 10 °C. Values of ΔE_p from Figure 5.3 are compared against theoretical values and are tabulated in Table 5.1.

Temperature (°C)	Theoretical *ΔEp* (mV)	100 mVs^{-1} *ΔEp* (mV)	Difference (mV)
15	57	66	9
25	59	68	9
35	61	72	11
45	63	74	11
55	65	77	12
65	67	79	12
75	69	82	13

Table 5.1 - Comparison of theoretical and experimentally determined peak separations of a 1 mm pBDD electrode in 1 mM $FcTMA^+$ 0.1 M KNO_3 at different temperatures.

At 25 °C the system displays a ΔE_p of 68 mV, which is indicative of a fairly reversible reaction; values of 59 mV have never been observed on this grade BDD employed herein. As the system temperature is increased however, the disparity between experimental and theoretical ΔE_p increases, possibly suggesting that the reaction is becoming less reversible. It must be considered, however, that the measurement of peak positions and separations is reliant upon the CV being under purely diffusive control. This is certainly not the case for scan rates of 10, 25 and 50 mV s^{-1} and not strictly true for 100 mV s^{-1} at higher temperatures as evidenced by Figure 5.4. Observation of peak potentials therefore may not be a robust method for assessing reversibility under isothermal heating conditions.

Experiments utilising the same setup were performed with a platinum disk ultramicroelectrode (UME) of diameter 25 μm, results are shown in Figure 5.5. Rates of diffusional mass transport are much higher at disk UMEs (larger value of k_t)

compared to disk macroelectrodes due to hemi-spherical diffusion.[40] The diffusion-limited current, i_{lim}, for a disk UME is given by:[22]

$$i_{\lim} = 4nFaDC^* \tag{5.16}$$

Where a is the electrode radius in cm and all other symbols have their usual meanings.

Theoretically predicted diffusion limited currents, equation (5.16), are plotted vs. experimental values at different temperatures (22 ºC, 55 ºC and 65 ºC) for two different scan rates; 10 mV s^{-1} and 100 mV s^{-1}, Figure 5.6. Very good agreement can be seen between theoretical calculations and experimental data collected at 10 mV s^{-1}, with increasing solution temperature, in contrast to the data presented in Figure 5.3 for the macroelectrode. This is due to the fact that the diffusional flux is almost an order of magnitude higher for the microdisk than the macroelectrode, k_t = 7.5 ×10^{-3} cm s^{-1} for the former and 8 x 10^{-4} cm s^{-1} for the latter at 100 mV s^{-1}. Despite the presence of thermal convection the diffusional flux (small diffusion layer) is high enough not to show a significant effect. Experimental data collected at 100 mV s^{-1} also follows the same theoretical trend fairly well, although there is a slight deviation. Investigation of Figure 5.5 (b) though reveals hysteresis in the CVs performed at 100 mV s^{-1}, making accurate quantitative analysis slightly more unreliable. The half wave potential, $E_{1/2}$, is seen to shift in the negative direction with increasing temperature, indicating that this redox couple with a platinum electrode possesses a negative temperature coefficient, this effect is discussed in more detail in section 5.3.4.

In summary, the data indicates that over a long timescale (160 s for a 10 mV s^{-1} scan) continuous solution heating introduces an appreciable amount of convection into the system. Its effect on the resulting electrochemical response depends on the diffusional mass transport coefficient for the electrode/redox couple system under investigation.

For electrodes with high diffusional flux, i.e. UMEs, the effects of thermally induced convection can be significantly minimised and the experimentally observed currents are in good agreement with those predicted using equations (5.14) and (5.16). As the temperature increases $E_{1/2}$ moves to less positive potentials due to the respective temperature coefficients of the working, reference and counter electrodes. For larger electrodes the deviation from the predicted currents is more significant, especially at the slower scan rates where the diffusional flux is smaller and the experimental timescale is longer.

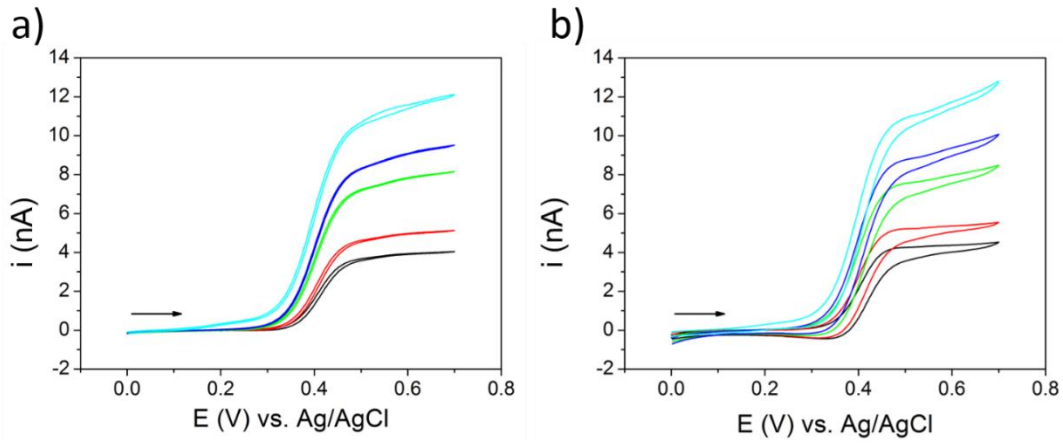

Figure 5.5 - CVs of Pt UME in 1 mM $FcTMA^+$, 0.1 M KNO_3 at temperatures of; black 23 ^oC, red 32 ^oC, green 50 ^oC, blue 60 ^oC and cyan 72 ^oC performed at scan rates of a) 10 mVs^{-1} and b) 100 mVs^{-1}.

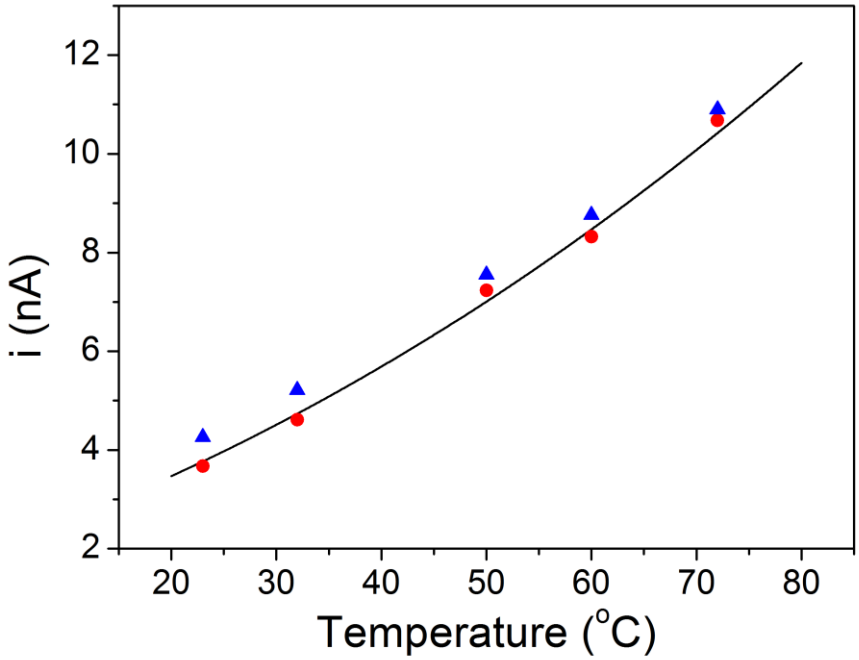

Figure 5.6 – Comparison of theoretically calculated limiting currents (black line) vs. experimentally determined limiting currents of 1 mM $FcTMA^+$, 0.1 M KNO_3 at 10 mVs^{-1} (red symbols) and 100 mVs^{-1} (blue symbols).

5.3.2 Non-Faradaic and Background Processes

TPV was initially performed in the absence of a redox mediator in order to observe the effects of temperature on an electrochemical system where no faradaic processes take place. Observed currents in this regime are due to capacitive charging of the electrode/solution interface as no faradaic charge transfer takes place. A solution of 0.1 M KNO_3 (Sigma-Aldrich) prepared from Milli-Q water (Millipore Corp) was used. TPV was performed on the pBDD cell electrode at different laser powers; this is shown in Figure 5.7 and Figure 5.8. Experimental parameters were as follows: scan rate, 100 mVs^{-1}; laser pulse width, 10 ms; potential step, 0.25 mV and sampling rate, 400 s^{-1}. The interval between each sample is 2.5 ms, with one 10 ms laser pulse corresponding to 4 data points as seen in Figure 5.8.

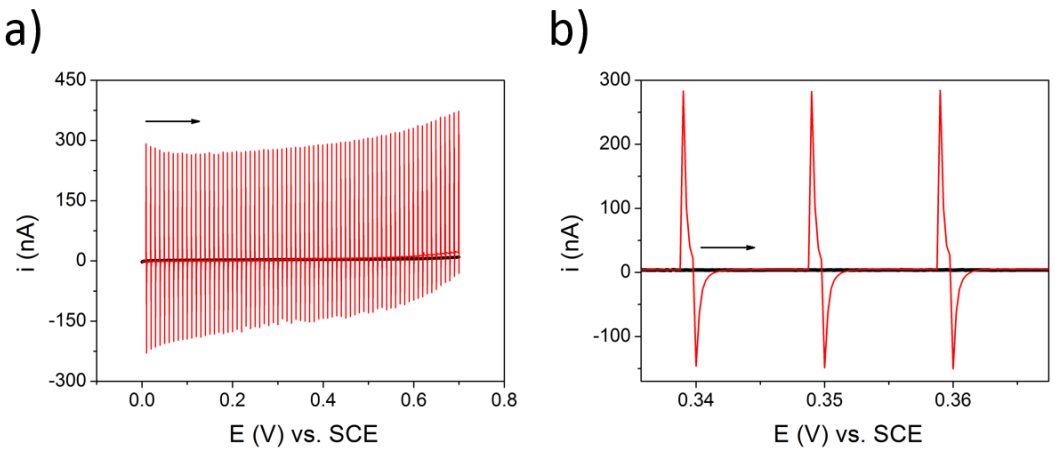

Figure 5.7 – a) TPV of pBDD in 0.1 M KNO_3; black line no laser heating, red line 27.5 W with a pulse width of 10 ms, scan rate of 100 mVs^{-1}, b) expanded view.

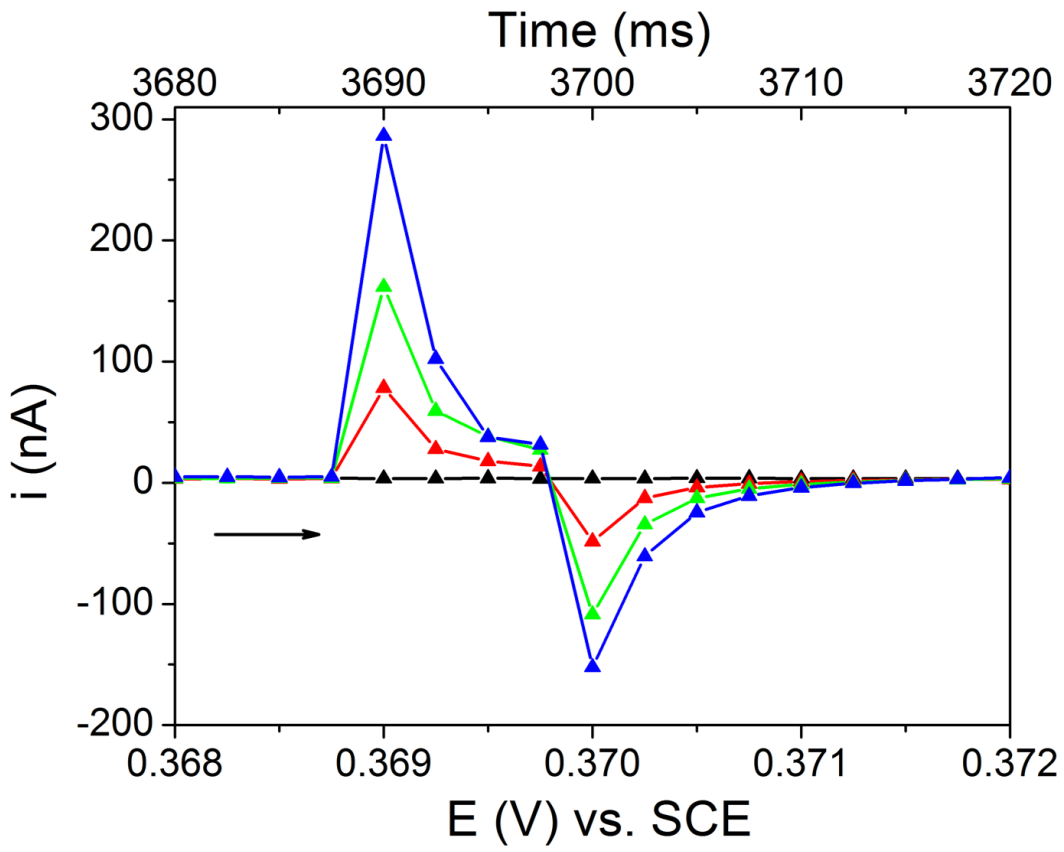

Figure 5.8 – TPV of pBDD in 0.1 M KNO_3 at different laser powers of; black joined symbols 0 W, red joined symbols 5 W, green joined symbols 15 W and blue joined symbols 27.5 W.

It is immediately apparent that heating the electrode influences its electrochemical response, even in the absence of a redox mediator. An expanded view of a single

transient displaying individual samples is shown in Figure 5.8. Upon inspection large current transients can be seen that correspond with a single laser pulse; the current rapidly rises to a value greater than zero and then begins to fall. It is worth noting that the largest change in current is observed during the first 2.5 ms of the laser being on. This is indicative of a very fast event, possibly much faster than the potentiostat can resolve, i.e. less than 2.5 ms. For the remaining 7.5 ms the current is seen to decay back towards its starting value. After the laser pulse is switched off however, a negative current transient is observed that appears to follow the same trend as the previous transient, albeit at a lower magnitude and opposite polarity. Higher laser powers and hence larger temperature changes produce bigger current transients, Figure 5.8.

These non-faradaic current transients occur due to a disruption of the electrical double layer with a sudden change in temperature, requiring a certain relaxation time for the system to reach equilibrium. Picosecond time-resolved surface-enhanced infrared absorption spectroscopy (SEIRAS) has been used to investigate the potential jump at a laser heated electrochemical interface.[24] A rapid laser induced potential jump was observed, occurring only ca. 200 ps after a 35 ps laser pulse ascribed to the rapid heating of a water layer near to the electrode surface (< 10 nm), which changes the orientation, and hence dipole moment of the water molecules. Laser induced temperature jump experiments have also been performed on a Pt foil electrode.[41, 42] The sudden change in open cell potential is described as a consequence of three processes; a junction potential created between the hot electrode and cold connecting wire, the change in the potential drop across the electrical double layer caused by changing dipole moments of water molecules and a change in potential due to the Soret effect. It is thought that this sudden change in potential creates a charging current

due to a change in capacitance of the electrical double layer, producing a current transient.

TPV with large potential steps (10 mV) and low sampling rates (10 samples s^{-1}) was also performed with the same experimental setup, Figure 5.9; current transients are not seen at low sampling rates. It can be seen that heating the working electrode has a pronounced effect on the solvent window, with increased heating reducing the solvent window. At higher laser powers both water oxidation (anodic currents) and water reduction (cathodic currents) are seen to occur at lower overpotentials, indicating that these reactions occur more easily at elevated temperatures.

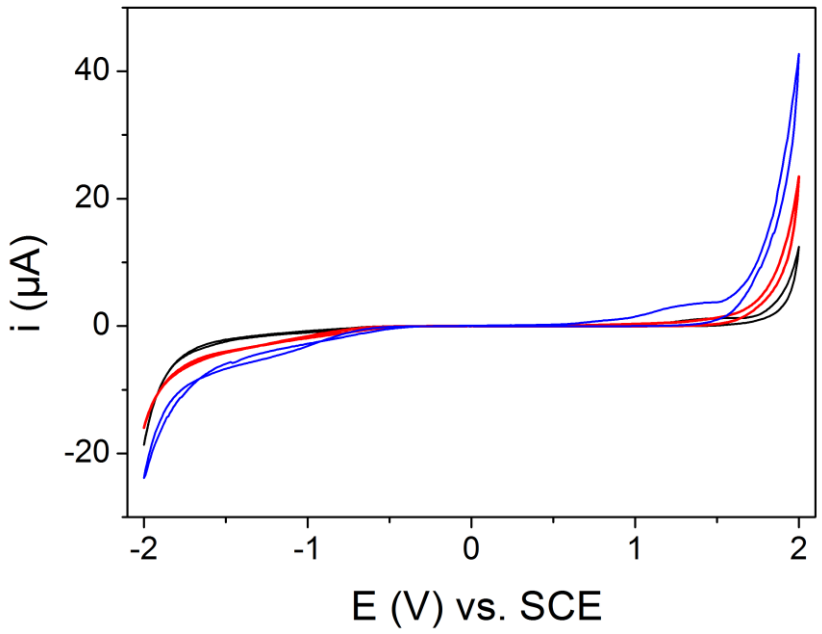

Figure 5.9 – Low sampling rate TPV of 0.1 M KNO_3 at 100 mV s^{-1}, laser powers of; black 0 W, red 5 W and blue 12.5 W.

5.3.3 Experimental Determination of Solution Temperature Close to the Electrode

The temperature of the electrode surface cannot accurately be measured explicitly due to the relatively short time scale of the applied heat pulses (10-50 ms). However, the temperature of the region near to the electrode can be found implicitly by measurement of the open circuit potential (OCP) of the cell, as this will change according to the temperature coefficient of the cell. Continuous heating experiments were first conducted to determine the temperature dependence of the OCP of a redox couple with a pBDD electrode; this experiment is described in detail in section 2.5.1. OCP is measured and plotted as a function of the temperature difference between the two electrochemical cells, Figure 5.10. The data is fitted with a linear trend and the gradient of this line is equal to the temperature coefficient of the redox couple being studied, for the case of the $Fe(CN)_6^{2+/3+}$couple with a pBDD electrode β = - 1.62 mV K^{-1}. This value is in excellent agreement with the literature value of -1.6 mV K^{-1}.[43]

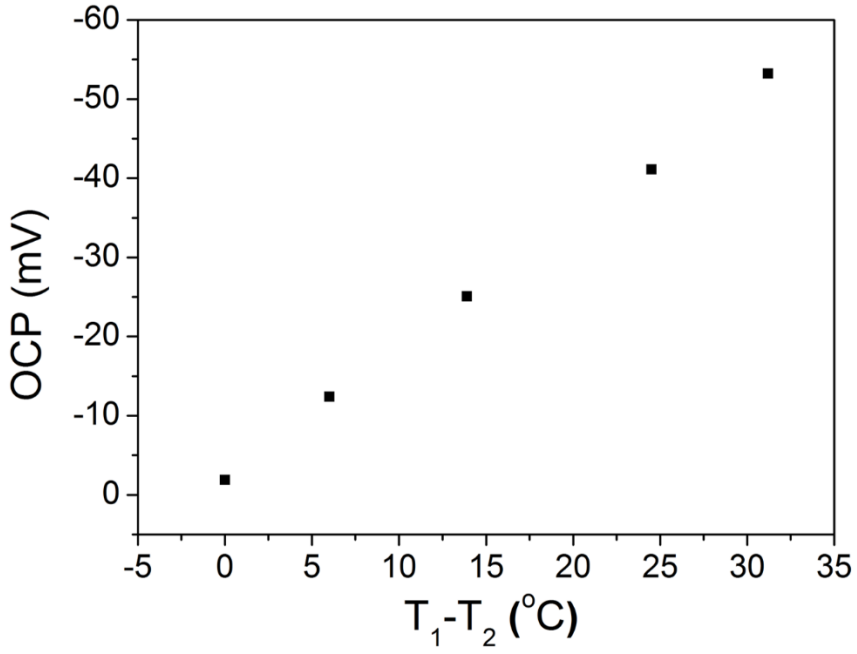

Figure 5.10 – Measured OCP between two 1 mm pBDD electrodes in separate equimolar solutions of 0.5 mM $K_3[Fe(CN)_6]$ + $K_4[Fe(CN)_6]$ in 0.1 M KNO_3 versus temperature difference.

Knowledge of the temperature coefficient of a redox couple allows determination of the temperature change experienced by the electrode/solution interface during heating, as the OCP between two pBDD electrodes will vary when a difference in temperature is present. Non-isothermal experiments with laser heating were performed and are detailed in section 2.5.2. Data are plotted in Figure 5.11 that show how the OCP between two pBDD electrodes of the same dimensions varies as one of the electrodes is selectively heated. Before the laser pulse occurs, both electrodes remain at the bulk solution temperature, T_{bulk}, therefore the temperature difference between electrodes is zero (ΔT = 0 °C). As the laser pulse strikes, the measured OCP rapidly increases in magnitude (becomes more negative for this couple), and continues to do so for the duration of the heat pulse (10 ms). The OCP attains a maximum at 10 ms and then quickly falls as the laser is turned off, relaxing back towards its initial value. By using the temperature coefficient calculated previously, these OCP values can be converted into interfacial temperature rises, which are shown on the right hand axis of Figure

5.11. Higher laser powers result in larger temperature changes, data for all laser powers are tabulated in

Table 5.2.

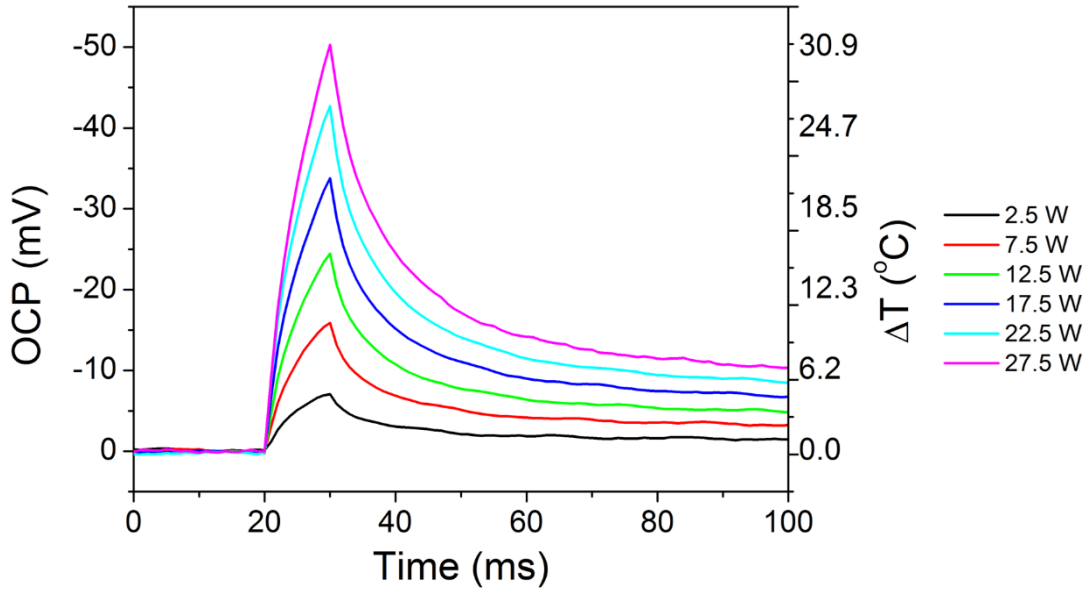

Figure 5.11 – Measured OCP between a non-heated and laser-heated pBDD electrode as a function of time at different laser power in an equimolar solution of 0.5 mM $K_3[Fe(CN)_6]$ + $K_4[Fe(CN)_6]$ in 0.1 M KNO_3. The associated temperature rise is shown on the right hand axis using β = 1.62 mVK^{-1}.

Laser Power (W)	OCP (mV)	Energy Input (mJ)	ΔT (ºC)
2.5	-6.9	25	4.3
5	-11.5	50	7.1
7.5	-15.8	75	9.8
10	-20.0	100	12.3
12.5	-24.7	125	15.2
15	-28.8	150	17.8
17.5	-33.9	175	20.9
20	-38.7	200	23.9
22.5	-42.8	225	26.4
25	-47.4	250	29.3
27.5	-50.3	275	31
30	-54.8	300	33.8

Table 5.2 – Measured OCP values with associated temperature rises after 10 ms of laser heating at different laser powers in an equimolar solution of 0.5 mM $K_3[Fe(CN)_6]$ + $K_4[Fe(CN)_6]$ in 0.1 M KNO_3.

5.3.4 Electrochemical Characterisation of System

TPV experiments investigating faradaic processes were performed with a well-known outer-sphere redox couple,[44] $Ru(NH_3)_6^{3+/2+}$, in order to understand the nature of TPV and how various parameters affect the electrochemical response. The effects of mass transport become important as in order to take part in electron transfer, the mediator must first move towards the working electrode. An expanded view of a single TPV current transient acquired at different pulse times at a laser power of 25 W is shown in Figure 5.12, where individual samples are displayed. Data for this plot were taken from the potential which gave the largest TPV peak, which is different for each pulse time, and are plotted against time with an arbitrarily chosen starting point.

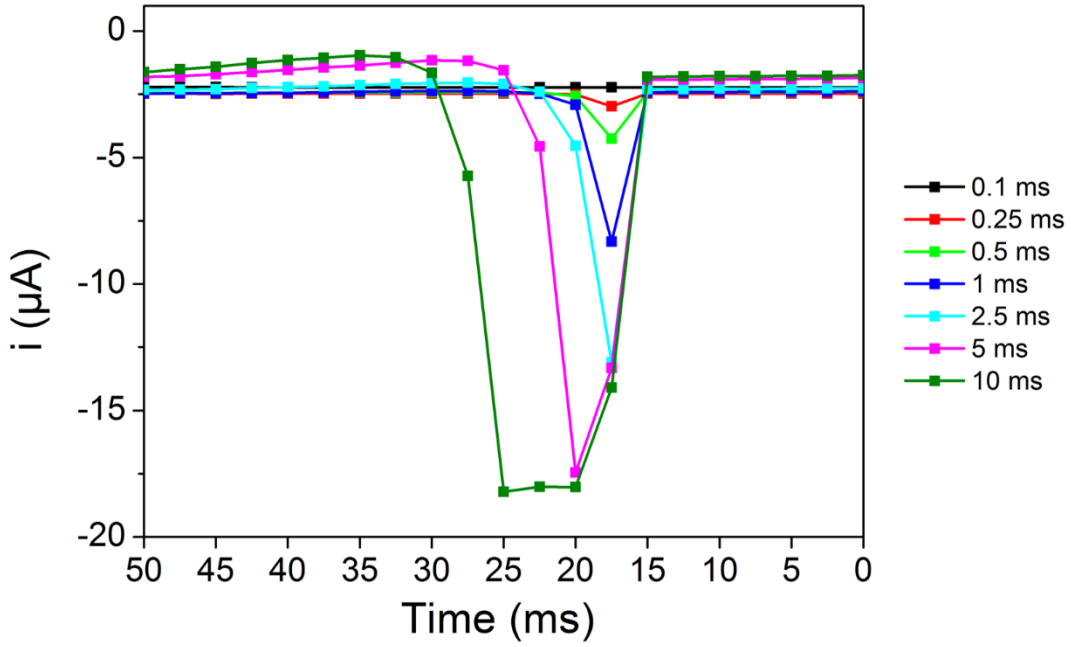

Figure 5.12 - Expanded view TPV at 25 W of pBDD in 1 mM $Ru(NH_3)_6^{3+}$ 0.1 M KNO_3 at different laser pulse lengths.

The largest current transient is seen for the longest heating pulse of 10 ms, transients at shorter pulse times reach a lower value as the electrode is heated for less time; these data are presented in Table 5.3. It can be concluded then that higher temperatures result in a larger current rise during TPV.

Pulse Time (ms)	Energy Input (mJ)	Current Rise (μA)
0	0	0
0.25	6.25	0.50
0.5	12.5	1.84
1	25	5.91
2.5	62.5	10.81
5	125	15.54
10	250	16.40

Table 5.3 – The observed current rise of TPV in 1 mM $Ru(NH_3)_6^{3+}$, 0.1 M KNO_3 for different laser pulse times.

The way in which a sampled TPV is constructed is shown in Figure 5.13, the experiment is performed as an entire sweep but is shown here as two separate sections of different starting directions for clarity, Figure 5.13 (a) and (b). A scan rate of 100 mVs^{-1} was used with a potential step of 0.25 mV, which provides a sampling rate of 400 samples per second. Raw data is collected by the potentiostat and is later sampled by taking every 40^{th} point, which corresponds to the last sample taken at the end of each 10 ms laser pulse, Figure 5.13 (c) and (d) respectively.

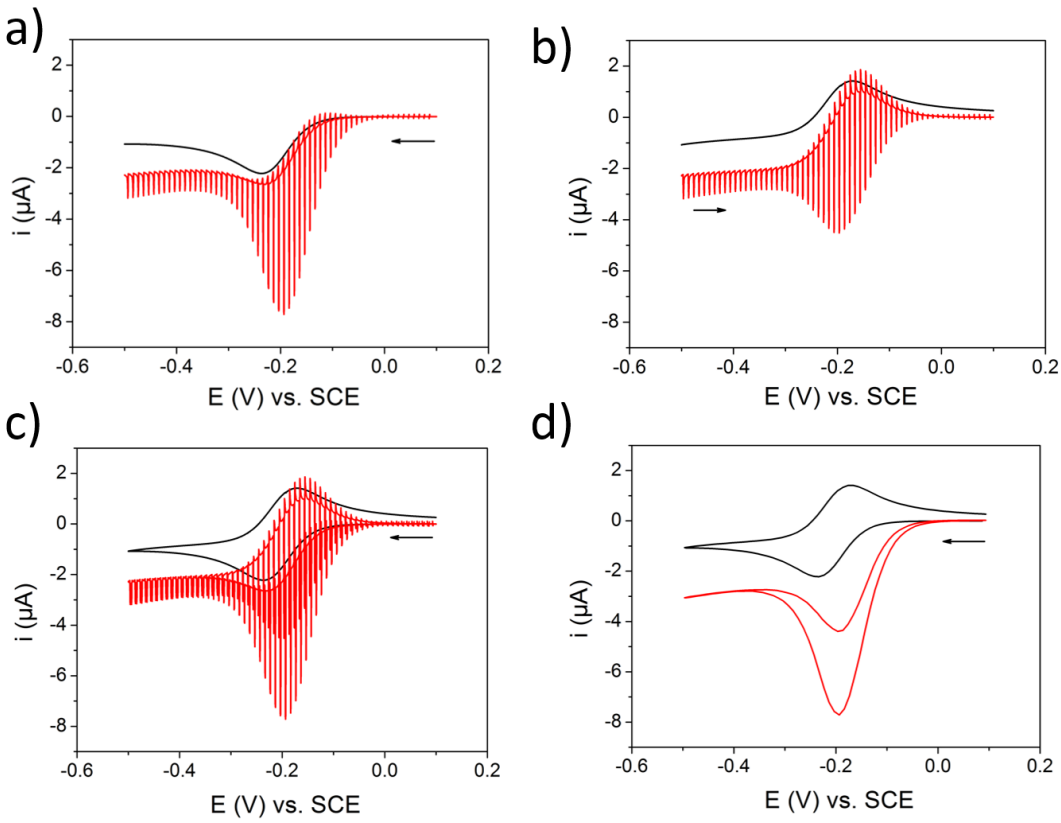

Figure 5.13 – TPV of pBDD in 1 mM $Ru(NH_3)_6^{3+}$ 0.1 M KNO_3 black line 0 W, red line 5 W; a) forward scan, b) backward scan, c) full scan and d) full scan (sampled data), all conducted at 100 $mV\ s^{-1}$.

There is an obvious difference in electrochemical response when the working electrode is heated as opposed to operating at ambient temperature conditions. For the reduction of $Ru(NH_3)_6^{3+}$, Figure 5.13 (a), a clear increase in cathodic current is observed with maximum values being achieved at the end of each pulse, when the

working electrode is at its maximum temperature. This observation could be explained by an increase in mass transport of analyte species from the bulk solution towards the electrode at an elevated temperature, which produces a larger current flow. However, the change in mass transport properties due to diffusion with increasing temperature is not enough to explain the resultant pulse heated CV with a redox mediator present. Calculations as performed in section 5.3.1 do not predict the magnitude of the current enhancement. The reverse scan is somewhat surprising; after sampling the data at the end of each laser pulse, the resultant reverse scan is produced that again produces a cathodic current. This is in contrast to a normal CV of a large electrode, where the opposite process occurs for a reversible redox couple, in this case the oxidation of $Ru(NH_3)_6^{2+}$ which should produce anodic currents.

Sampled TPV data at various laser powers are shown in Figure 5.14 where three effects can be seen; there is an increase in cathodic current, the peak potentials shift towards more positive values and finally the wave becomes distorted at the highest laser power at large overpotentials. TPVs at laser powers higher than 22.5 W have been recorded but are omitted from Figure 5.14 as large amounts of distortion occur, possibly due to the high temperatures attained coupled with relatively large potentials causing bubbles to form of the electrode surface. This is thought to be a limitation of the construction of the electrode, as the edge of the Kapton mask that defines the electrode area provides nucleation points for bubbles to form. The peak currents of TPVs at different concentrations and peak potentials are both plotted against temperature in Figure 5.15 and Figure 5.16 respectively.

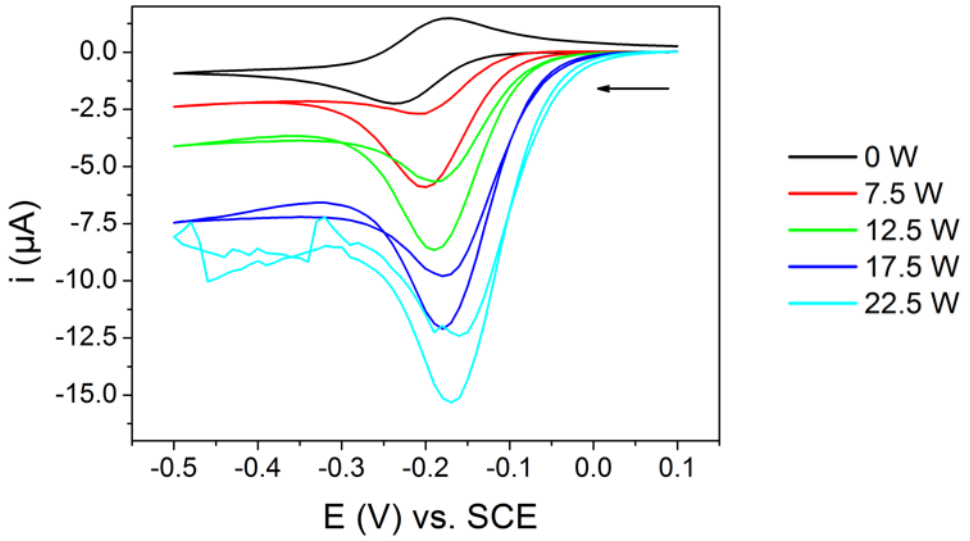

Figure 5.14 – TPV (sampled data) of pBDD in 1 mM $Ru(NH_3)_6$ 0.1 M KNO_3 at laser powers of; 0 W, 7.5 W, 12.5 W, 17.5 W and 22.5 W.

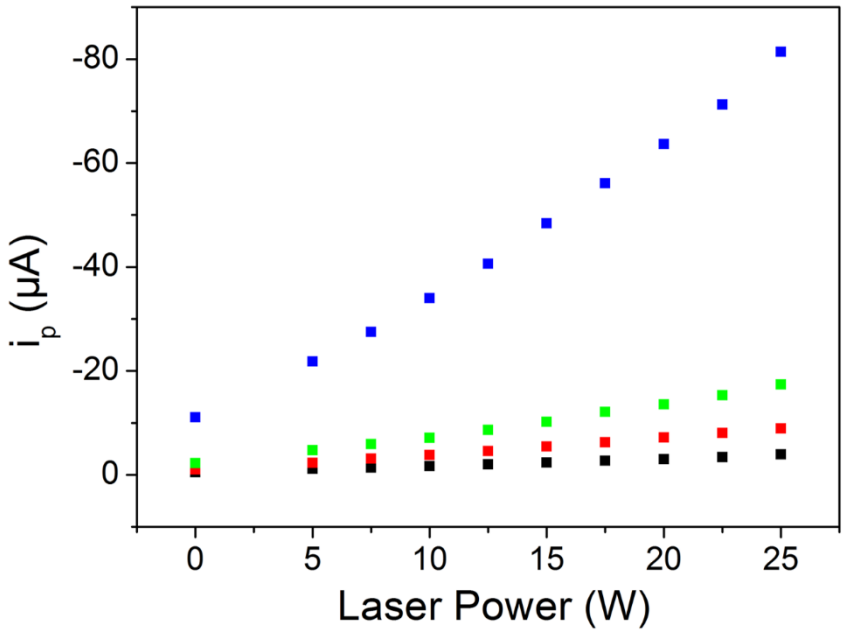

Figure 5.15 – Peak current vs. laser power for $Ru(NH_3)_6^{3+}$ 0.1 M KNO_3 at concentrations of; black 0.2 mM, red 0.5 mM, green 1 mM and blue 5 mM.

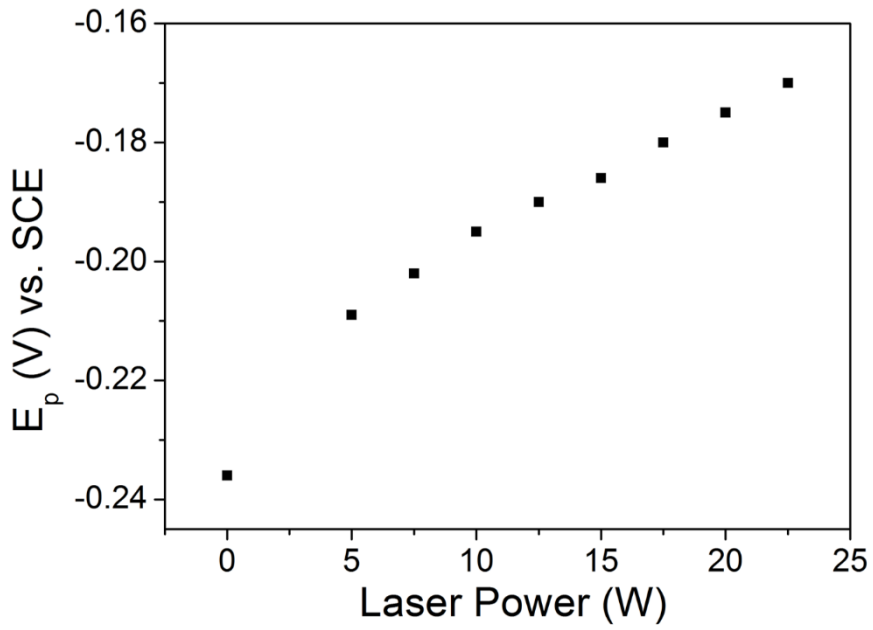

Figure 5.16 – Shift of peak potential vs. laser power for pBDD in 1 mM $Ru(NH_3)_6^{3+}$ 0.1 M KNO_3.

Investigation of Figure 5.15 reveals an expected trend; measured peak currents increase with temperature and also increase linearly with concentration. The trend of increasing peak current with temperature as yet has not been found to comply with theoretical considerations, though use of a 2nd order polynomial produces a reasonable, if empirical fit to data. A clear shift in peak potential with increasing temperature is seen, the direction of the shift is positive. Data are fitted linearly and give a value of the temperature coefficient (β) for $Ru(NH_3)_6^{3+}$ as + 0.75 mVK^{-1}. The first data point in Figure 5.16 is omitted during fitting as this is acquired with no laser heating and therefore is not a TPV but rather a CV derived value. Isothermal experiments conducted with a water bath provide a similar value of β of + 0.83 mVK^{-1} for $Ru(NH_3)_6^{3+}$.

In order to explain the observed effects of heating, consideration must be given to the entropy of the redox system. As discussed previously in section 5.1, a temperature coefficient exists for a given electrode and redox mediator; a shift in potential occurs when there is a change in temperature. By rearrangement of equation (5.8) the entropy,

S, of a redox process can be calculated after a value of β has been obtained. *S* for $Ru(NH_3)_6^{3+}$ is + 72.4 $JK^{-1}mol^{-1}$ (from TPV), the positive nature of this quantity indicates that when $\Delta T > 0$ the obtained TPV shifts along the potential axis in a positive direction. This is indeed observed experimentally as can be seen in Figure 5.14 and Figure 5.16.

The effect of temperature on the current response of an electrode is greatly influenced by the potential at which the temperature pulse occurs relative to the equilibrium potential, E_{eq}, of the reaction. At values sufficiently far from the equilibrium potential (at the beginning or end of a TPV) any increase in current is due to the increase in diffusion coefficient as described previously in section 5.2.1. Near to the equilibrium potential however, the current response of an electrode to a temperature perturbation is much more dramatic. Near to E_{eq} TPV may be considered analogous to DPV; for the former the potential is changed indirectly through the temperature coefficient whereas for the latter the potential is deliberately varied. More specifically, DTPV is analogous to DPV as both techniques involve recording the difference in current sampled before and after each pulse, be it temperature or potential. The amount by which the potential shifts in (D)TPV is governed though by the temperature coefficient/entropy of the redox couple of interest.

For the discussion of temperature effects on the middle portion of a TPV near to E_{eq}, it is convenient to define the case for heated and non-heated peak currents that result, $i_{p,hot}$ and $i_{p,cold}$ respectively. For the forward scan (reduction) of the $Ru(NH_3)_6^{3+/2+}$ couple, $i_{p,hot}$ increases in magnitude with laser power as it becomes increasingly negative. A somewhat naïve analysis of the reverse process indicates that $i_{p,hot}$ decreases in magnitude with laser power as a positive current is expected for an oxidation process, Figure 5.14. Upon closer inspection, it is clear that $i_{p,hot}$ follows the

same trend with increasing laser power for both the forward and reverse processes; the peaks become increasingly cathodic. This is also due to the temperature coefficient for the redox couple, the value of which is +0.46 mVK^{-1} for $Ru(NH_3)_6^{3+/2+}$. The positive sign for this value indicates that the 'polarity' of any current change will be cathodic. If the studied process is already cathodic in nature, then the application of temperature pulses interferes constructively, acting to reinforce the current signal and make it larger. If however the studied process is anodic in nature, then a temperature pulse will actually diminish the observed current signal, the peak may even reverse in polarity if the thermodynamic influence is substantial enough. This is precisely what is seen in Figure 5.14, the reduction of $Ru(NH_3)_6^{3+}$ is enhanced by temperature pulsing whereas the oxidation of $Ru(NH_3)_6^{2+}$ is diminished so much that it becomes cathodic. The reverse is also true for temperature coefficients that contain a negative sign, where anodic processes are favoured.

It is useful to envisage a theoretical, 'ideal hot CV' when considering the observed TPV response; supposing that measured currents are larger due to faster diffusion (lower solvent viscosity) and E_{eq} is shifted along the potential axis, it is assumed that effects due to convection are negligible. This CV cannot be obtained with this technique but is used here to illustrate what would be observed if the diffusion coefficient and E_{eq} of analyte species could be increased arbitrarily without any other consequences. An example of this ideal hot curve is plotted in Figure 5.17 and compared to a CV that would be obtained under ambient conditions. The resulting TPV then may be understood as a convolution of these two curves, where current magnitudes of the ideal hot curve are plotted on the potential scale of the ambient curve.

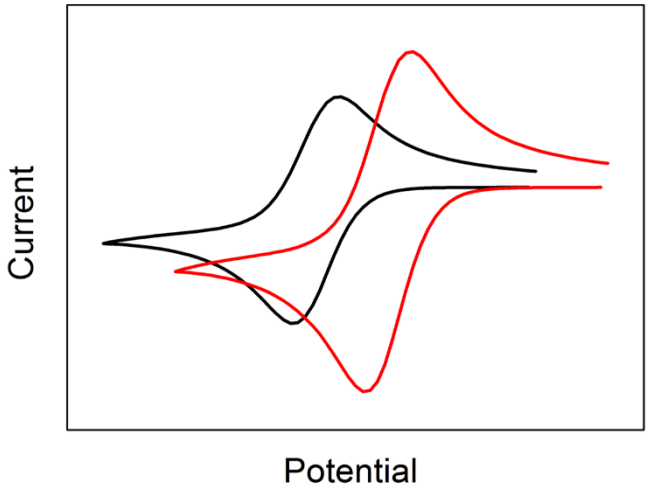

Figure 5.17 – Idealised hot CV (red) compare against an ambient CV (black), the former possesses currents of a higher magnitude and is translated along the potential axis.

Quantitative analysis of TPV has proven very difficult, and no satisfactory method has been found that correctly predicts the observed heated peak currents, although a qualitative assessment is still informative as it shows how the shape of a CV changes when heat is supplied to the system as a series of pulses, the resulting TPV. Valdes and Miller[30] performed studies with a pulsed laser heated gold RDE, and derived expressions for the modulation current, Δi, and associated quantities;

$$\left(\frac{\Delta i}{\Delta i_{l,red}}\right)=\frac{\left[1-\epsilon\exp\left(-\phi\right)\right]}{\left[1+\gamma\exp\left(-\phi\right)\right]}-\frac{\left[\sigma\left(1+\gamma\right)\exp\left(-\phi\right)\right]}{\left[1+\gamma\exp\left(-\phi\right)\right]^{2}} \tag{5.17}$$

$$\sigma=\frac{T\Delta S^{o}}{E_{D}^{red}} \tag{5.18}$$

$$\epsilon=\frac{E_{D}^{ox}}{E_{D}^{red}} \tag{5.19}$$

$$\phi\equiv\left(\frac{nF\left(U-U^{o}\right)}{RT}\right) \tag{5.20}$$

$$\gamma \equiv \left(\frac{D_{red}}{D_{ox}} \right)^{2/3} \tag{5.21}$$

Where $\Delta i_{l,red}$ is the change in limiting reduction current for an RDE, σ and ϵ are dimensionless quantities defined in equations (5.18) and (5.19) respectively, ϕ is a dimensionless potential defined in equation (5.20) and γ is the mass diffusivity ratio parameter as defined in equation (5.21). E_D^{ox} and E_D^{red} are the activation energies associated with mass transport for the oxidised and reduced forms of analyte species respectively, D_{ox} and D_{red} are the corresponding diffusion coefficients.

The authors found that the extent of the thermal modulation was governed by the quantity σ, which is the ratio of entropic energy to activation energy for a mass transport limited process. By substituting typical numbers into equation (5.17) the effect of σ is clearly observed, Figure 5.18. The sign of σ is important, as a positive value leads to a negative modulation whereas a negative value leads to a positive modulation, with larger values causing more modulation. The sign of σ is controlled by the entropy of reaction, there is no effect of thermal modulation if σ is equal to 0.

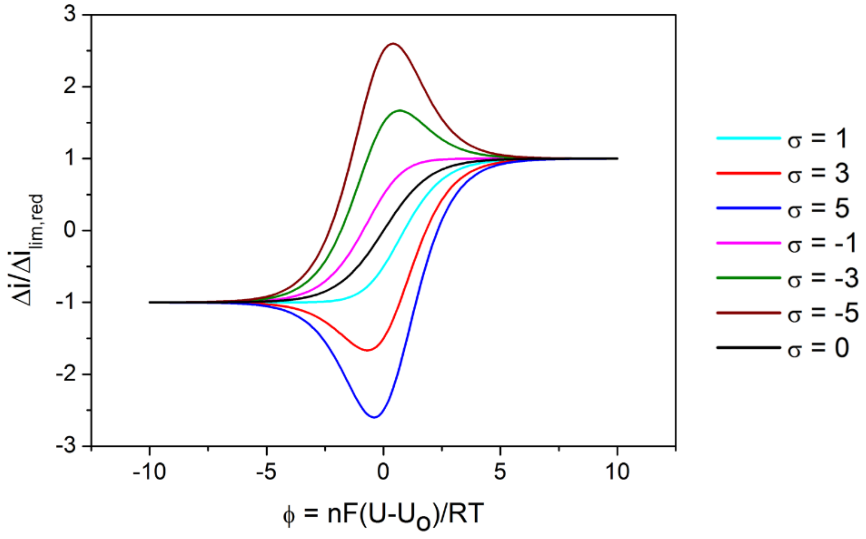

Figure 5.18 – Results of analytical expression for thermal modulation for different values of σ.

The above applies to the case of forced convection, where an RDE is used to enhance mass transport to the electrode. Some modification is therefore needed to make it applicable to a large stationary electrode, where peak type CVs are observed. Firstly, $i_{p,red}$ and $i_{p,ox}$ are used rather than $i_{l,red}$ and $i_{l,ox}$ and are calculated using the Randles-Sevcik relationship. Secondly, equation (5.17) is used to calculate a normalised value of the modulation current, multiplication by $\Delta i_{p,red}$ negates this normalisation. A function for Δi can therefore be obtained, when this function is combined additively with experimental CV data, and plotted on a real potential scale, an approximate TPV is produced, Figure 5.19. Data obtained with no laser heating are combined with the modulation function calculated from equation (5.17) to produce an approximate TPV as shown in Figure 5.19 (c). Whilst not ideal compared to real TPV data obtained at 10 W, the approximate TPV nevertheless displays the same attributes; increased cathodic peak current for the forward process and an inversion of peak current for the backward process leading to a 'double cathodic' peak.

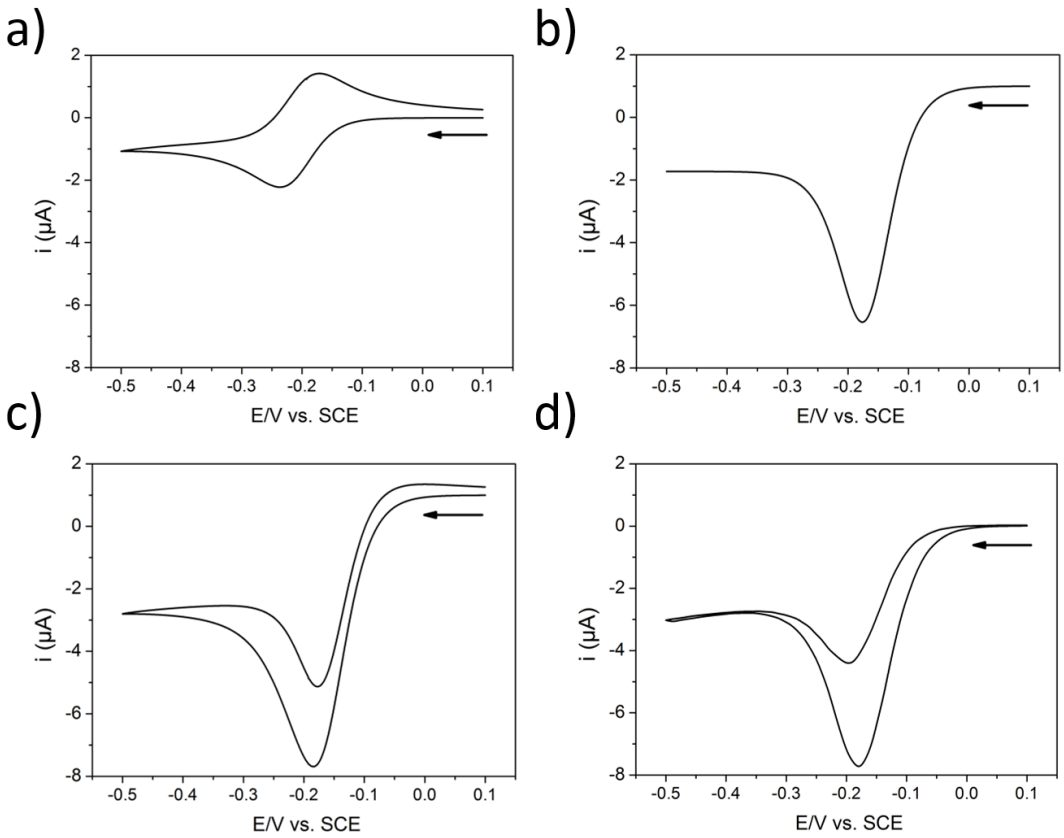

Figure 5.19 – Experimental and calculated TPVs of pBDD in 1 mM $Ru(NH_3)_6^{3+}$ 0.1 M KNO_3; a) experiment at 0 W, b) calculated modulation, c) sum of 0 W experiment and calculated modulation and d) experiment at 10 W.

5.3.5 Outer and Inner Sphere Redox Mediators

Identical experiments to those above have also been performed with different outer-sphere redox mediators, $IrCl_6^{3-/2-}$ and $FcTMA^{+/2+}$, Figure 5.20 and Figure 5.21 respectively. Upon inspection of the $IrCl_6$ TPV, Figure 5.20, it can be seen that the peak current magnitude increases with increasing laser power, though this effect is not to the same extent as $Ru(NH_3)_6^{2+/3+}$; rather than the emergence of a 'double anodic' peak, the shape of the TCV changes to almost resemble that of a sigmoidal CV at higher laser powers. This marked contrast to results obtained with $Ru(NH_3)_6^{2+/3+}$ is thought to be due to $IrCl_6$ possessing a rather small value of β; isothermal experiments could not distinguish a value of β as the potential shifts were too small. A very small

temperature coefficient explains why little peak potential shift is seen in Figure 5.20, and also why peak current enhancements are far smaller than those of $Ru(NH_3)_6^{2+/3+}$. If β were equal to 0, then any enhancement in current, even near to E_{eq}, would only be due to increases in the diffusion coefficient of the mediator (assuming no convection).

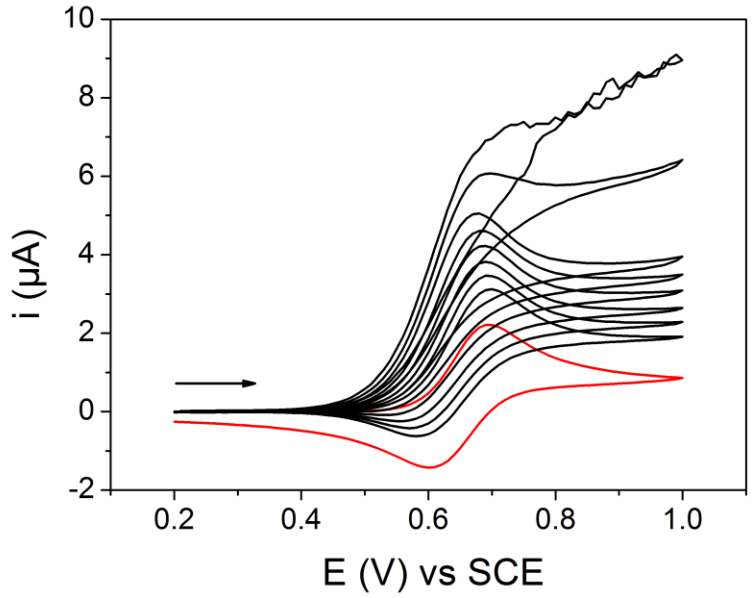

Figure 5.20 – TPV (sampled data) of pBDD in 1 mM $IrCl_6$ 0.1 M KNO_3 at laser powers of; 0 W (red curve) and from 5 W, to 22.5 W in increments of 2.5 W.

TPV data for 1 mM $FcTMA^+$ at different laser powers is shown in Figure 5.21, it is immediately apparent that a different response again to temperature, when compared to the previous redox mediators, is occurring. At potentials well beyond E_{eq}, a limiting current is attained that increases with increasing laser power, but near to E_{eq} the increased temperature serves to reduce the oxidation current of the forward scan. This can be seen in more detail in Figure 5.22; as the laser is turned on the current subsequently drops (becomes more cathodic) and remains low for the duration of the heat pulse (10 ms in total). In Figure 5.21 the curve with no laser heating is shown in red for clarity. For the case of $FcTMA^{+/2+}$, at potentials near to E_{eq}, each heat pulse

acts to diminish the measured oxidation current. This type of response is expected for a mediator with a positive temperature coefficient; as Δi becomes increasingly negative (since σ becomes more negative, equation 5.18) any anodic current near to E_{eq} is diminished. This effect is more pronounced at higher laser powers, as evidenced by the complete loss of the forward (anodic) peak in Figure 5.21. This result suggests that $FcTMA^+$ possesses a positive temperature coefficient, providing a current enhancement in the cathodic direction for both forward and backward peaks as is seen. Isothermal experiments to determine the value of β strangely revealed a negative shift with temperature and hence a negative temperature coefficient, although a value of + 0.8 mVK^{-1} has been reported[45] with a platinum UME for ferrocene.

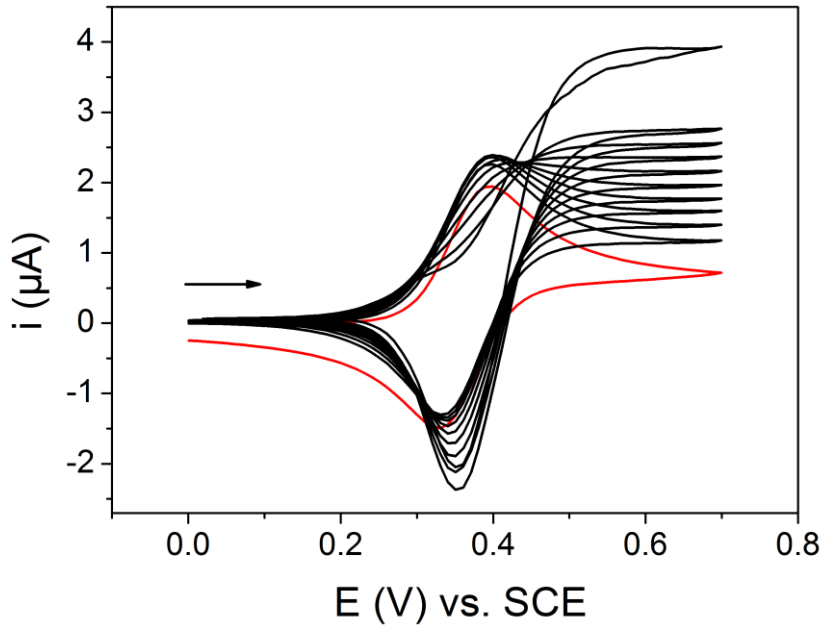

Figure 5.21 - TPV (sampled data) of pBDD in 1 mM $FcTMA^+$ 0.1 M KNO_3 at laser powers of; 0 W (red curve), 2.5 W, 5 W, 7.5 W, 10 W, 12.5 W, 15 W, 17.5 W, 20 W, 22.5 W and 25 W (highest curve at 0.7 V).

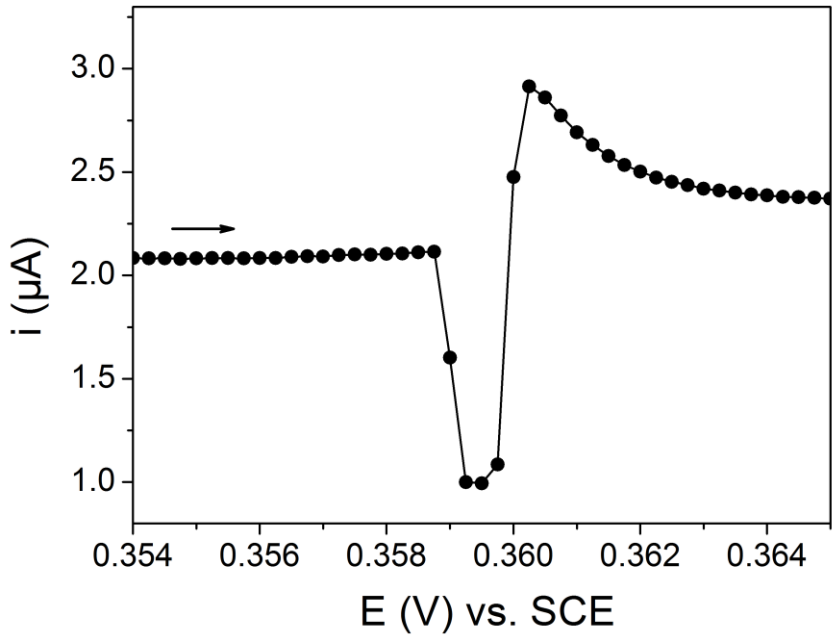

Figure 5.22 – Expanded TPV transient of 1 mV $FcTMA^+$ 0.1 M KNO_3 at 20 W showing individual samples performed at 100 mV s^{-1}.

An inner-sphere redox mediator,[46-48] $Fe(II)SO_4$, was also used with TPV and is shown in Figure 5.23 (a). Inner-sphere mediators are more complicated than outer-sphere mediators as HET with the former is sensitive to the chemical nature of the electrode surface. The peak separation for this couple at ambient conditions is 741 mV, indicative of an electrochemical reaction that is not reversible (slow HET). Investigation of Figure 5.23 reveals several changes as laser power is increased; the forward (oxidation) peak becomes larger and tends towards a more steady state shape, the reverse (reduction) peak is initially reduced in magnitude but then begins to increase again, this peak also shifts towards more positive values. All three aspects (kinetic, thermodynamic, and mass transport) are affected by temperature and it is likely that these three processes will affect the shape the resultant TPV.

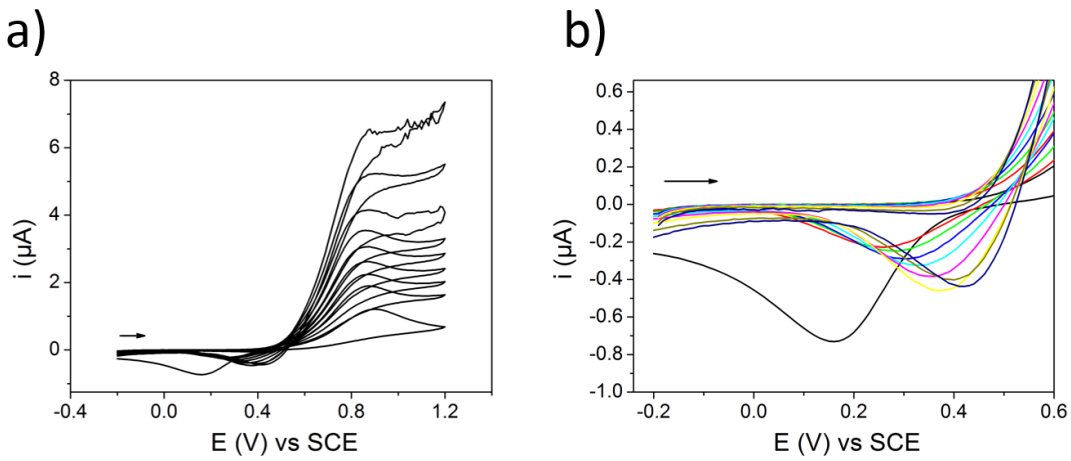

Figure 5.23 – a) TPV of pBDD (sampled data in 1 mM $FeSO_4$, 0.1 M $HClO_4$ at laser powers of; 0 W (smallest curve), to 22.5 W (largest curve) in increments of 2.5 W, b) expanded view of reduction peak shift at same laser powers increasing in the order; black, red, green, blue, cyan, magenta, yellow, dark yellow and navy.

5.3.6 Finite Element Simulations

In addition to experimental measurements, computer simulations using the finite element method were undertaken to assess the temperature of the pBDD electrode during laser heating. Finite element simulations were performed with a Dell Optiplex 9010, Intel Core i7-3770 3.4 GHz computer with 32 GB RAM running Microsoft Windows 7 64-bit edition. The finite element modelling software used was Comsol Multiphysics 4.3b (Comsol AB, Sweden). Simulations utilised approximately 170,000 triangular elements, with the highest resolution at the heated interface (element size of ~ 1 μm).

A 2D model geometry was built that contains a pBDD disk (domain 1) in contact with a body of water (domain 4), mounted onto perspex (domain 2) and held in place by Kapton (domain 3), Figure 5.24 (a) (not to scale). The model is axially symmetric about z = 0 (represented by a dashed line), as this reduces computation time. Each material is defined as a separate domain with its own material properties; specific heat

capacity (C_p), density (ρ), thermal conductivity (κ) and dynamic viscosity (η). Values for water are built into the software that describe these material properties at different temperatures, user added values were implemented for the pBDD disk, Kapton and perspex.

A boundary heat source was used to simulate the laser pulse on the back face of the pBDD disk. The reflectance of the disk was assumed to be negligible so that the optical power of the incident radiation was equal to the heating power applied to the boundary. At time = 0, t_0, a 10 ms heat pulse is applied to the pBDD disk and allowed to propagate through the model geometry as a function of time. The simulation used conjugate heat transfer physics, which contains equations for calculation of heat flux through both solids and fluids involving conductive and convective heat transfer, Table 5.4 and Table 5.5. Heat transfer equations are solved for each element at each time step to model the flow of heat in the system. Simulations are run to model 1 s of time, different laser powers are modelled by changing the boundary heat source power. The outside boundaries of the geometry were set to be thermally insulating, representing a closed system. Gravity, g, has an impact of the flow pattern (convection) of fluids under non-isothermal flow conditions, a volume force (F_v) has been added to the fluid to account for this, Table 4. Indeed, gravity can cause natural convective effects in an electrochemical experiment performed in a static solution at room temperature when long timescales (typically greater than 20 s) are used with a macroscopic electrode.[22]

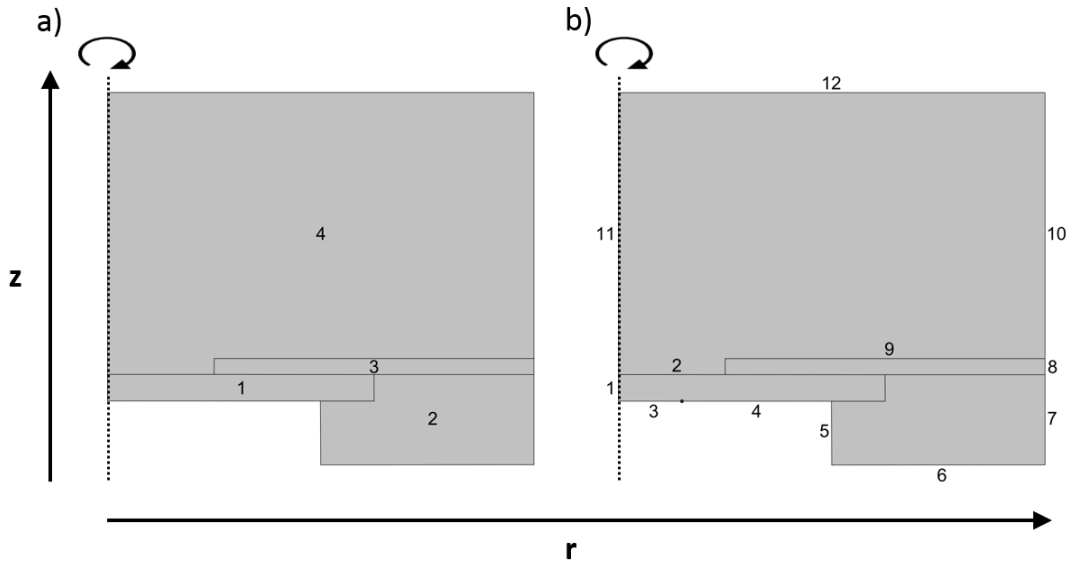

Figure 5.24 – Simulation geometry (not to scale) for a pBDD disk in contact with water; a) different simulation domains and b) different boundary edges.

Domain	Material	Properties	Boundary Conditions
1	Diamond	C_p = (3.2T) – 474 Jkg^{-1}K^{-1} ρ = 3500 kgm^{-3} κ = 600 Wm^{-1}K^{-1}	$\rho C_p \frac{\partial T}{\partial t} - \nabla \cdot (k \nabla T) = 0$
2	Perspex	C_p = 1000 Jkg^{-1}K^{-1} ρ = 1160 kgm^{-3} κ = 50 Wm^{-1}K^{-1}	$\rho C_p \frac{\partial T}{\partial t} - \nabla \cdot (k \nabla T) = 0$
3	Kapton	C_p = 1090 Jkg^{-1}K^{-1} ρ = 1420 kgm^{-3} κ = 0.12 Wm^{-1}K^{-1}	$\rho C_p \frac{\partial T}{\partial t} - \nabla \cdot (k \nabla T) = 0$
4	Water	C_p = 4184 Jkg^{-1}K^{-1} ρ = 1000 kgm^{-3} κ = 0.58 Wm^{-1}K^{-1} η = 6th order polynomial	$\rho C_p \frac{\partial T}{\partial t} + \rho C_p \mathbf{u} \cdot \nabla T - \nabla \cdot (k \nabla T) = 0$ $\rho \frac{\partial \mathbf{u}}{\partial t} + \rho(\mathbf{u} \cdot \nabla)\mathbf{u} = \nabla \cdot$ $\left[-p\mathbf{l} + \mu\left(\nabla \mathbf{u} + (\nabla \mathbf{u})^T\right) - \frac{2}{3}\mu(\nabla \cdot \mathbf{u})\mathbf{l} \right]$ $+ F_v$ $F_v = -\rho g$ in z-dimension $F_v = 0$ in r-dimension

Table 5.4 – Boundary conditions of finite element simulation for a heated pBDD disk in water associated with domains from Figure 5.24 (a).

Physical Representation	Boundary Edge(s)	Boundary Conditions
Axial Symmetry	1, 11	$\mathbf{u} = 0$
Thermal Insulation	1, 3, 4, 5, 6, 7, 8, 10, 11, 12	$-n \cdot (-\kappa \nabla T) = 0$
Boundary Heat Source	3	$-\mathbf{n} \cdot (-\kappa \nabla T) = Q_b$ $Q_b = \frac{P_{b,\text{tot}}}{A}$
No Slip Fluid Boundary	2, 9, 10, 12	$\mathbf{u} = 0$

Table 5.5 - Boundary conditions of finite element simulation for a heated pBDD disk in water associated with boundary edges from Figure 5.24 (b).

The simulation is allowed to reside at an initial temperature of 25 ^{o}C for a short period before t_0, the point at which the boundary heat source is applied; this is true for all domains and boundaries throughout the model. At t_0 heating begins, representing a power input equal to that of the laser used in experiments, values used were 2.5 to 30 W climbing in increments of 2.5 W. Simulations are run to model 10 ms of heating, with an additional 990 ms of cooling time, a total time of 1 s is modelled after t_0. Modelled temperature in the centre of the pBDD disk at the solution interface is plotted against time and is shown in Figure 5.25 (a), the peak temperature attained is plotted against laser power in Figure 5.25 (b), along with values obtained experimentally as described in section 5.3.3. A maximum temperature is reached after 10 ms of heating, after this time the temperature falls rapidly, tending towards the initial system temperature of 25 ^{o}C. A large disparity exists between temperatures calculated experimentally and through simulations, possibly due to the unknown 'sampling volume' of OCP experiments. Another possible cause for the observed disparity is the

adhesive on the Kapton tape, which may have a specific heat capacity and thermal conductivity different from that of the tape itself. This was not included in the model, as it is unlikely to affect the active electrode surface area temperature substantially.

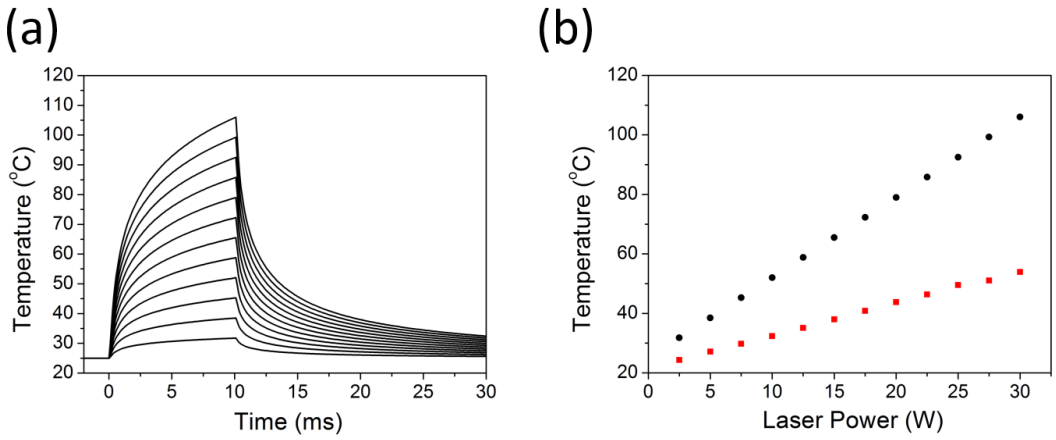

Figure 5.25 – Results of finite element simulations; (a) modelled temperature of centre of pBDD disk at solution interface vs. time and (b) peak temperatures attained at 10 ms; modelled data (black symbols) and experimental data from OCP experiments in section 5.3.3 (red symbols) vs. laser power.

5.4 Conclusion

Electrochemistry at elevated temperatures has been performed with two different methodologies; continuous and pulsed heating, the former an example of an isothermal system and the latter a non-isothermal system. Continuous heating experiments were performed with a simple water bath setup where the entire system was heated (including all electrodes) for both 1 mm diameter disc macroelectrodes and 25 μm diameter UMEs. For the macroelectrodes, mass transport was shown experimentally to be a product of both thermally induced convection and diffusion. In contrast the UMEs, with their higher rates of diffusion, were less affected by thermal convection. Hence mass transport was dominated by diffusion and as such enhancements in current due to a temperature induced higher diffusion coefficient could be calculated and found to be in good agreement with experiment.

TPV experiments, were performed using different redox mediators; $Ru(NH_3)_6^{3+/2+}$, $FcTMA^{+/2+}$, $IrCl_6^{3-/2-}$ and $Fe^{2+/3+}$ at different heating conditions. Higher laser powers and therefore higher electrode temperatures produced an enhanced current response in TPV, resulting in current transients that correspond directly with each laser pulse. The largest enhancement was seen for the $Ru(NH_3)_6^{2+/3+}$ couple by up to a factor of 6 at a laser power of 22.5 W. The enhancement in current for faradaic processes (redox mediator present) was many times larger than that for the case of non-faradaic processes. The choice of mediator also greatly influenced TPV results, with larger values of β producing larger current enhancements near to E_{eq} and also shifting the potential at which peaks occur. The sign of β dictated the direction of current 'enhancement', increasing the recorded current for the forward scan of $Ru(NH_3)_6^{2+/3+}$ and decreasing the this is similar to performing DPV with a pulse amplitude of the

opposite sign of the applied potential staircase. When β is very small any current enhancement, even near to E_{eq}, was mainly a result of an increased diffusion coefficient.

Computer simulation techniques were used as a method to infer the temperature of the electrode surface when heated with a laser pulse. The temperature of the pBDD solution facing surface rose to a maximum temperature of 114 ^{o}C after a 10 ms pulse time, this is common across all mediators studied as water is always used as the solvent.

5.5 References

1. C. G. Ubah and E. Asselin, *ECS Transactions*, 2009, **19**, 3-20.
2. J. Zhang, Z. Xie, J. Zhang, Y. Tang, C. Song, T. Navessin, Z. Shi, D. Song, H. Wang, D. P. Wilkinson, Z.-S. Liu and S. Holdcroft, *J. Power Sources*, 2006, **160**, 872-891.
3. P. Gründler, A. Kirbs and L. Dunsch, *ChemPhysChem*, 2009, **10**, 1722-1746.
4. C. L. Forryan and R. G. Compton, *PCCP*, 2003, **5**, 4226-4230.
5. R. G. Compton and C. E. Banks, *Understanding Voltammetry*, Imperial College Press, London, 2011.
6. J. Wang and P. Gründler, *Electroanalysis*, 2003, **15**, 1756-1761.
7. F. Marken, Y.-C. Tsai, B. A. Coles, S. L. Matthews and R. G. Compton, *New J. Chem.*, 2000, **24**, 653-658.
8. X. Zhang, J. Leddy and A. J. Bard, *J. Am. Chem. Soc.*, 1985, **107**, 3719-3721.
9. A. J. Bard and L. R. Faulkner, *Electrochemical Methods: Fundamentals and Applications*, Wiley, New York, 1980.
10. D. Y. Kim, J. C. Yang, H. W. Kim and G. M. Swain, *Electrochim. Acta*, 2013, **94**, 49-56.
11. S. Fujiwara, S. Kasai, H. Yamauchi, K. Yamada, S. Makino, K. Matsunaga, M. Yoshino, T. Kameda, T. Ogawa, S. Momma and E. Hoashi, *Prog. Nucl. Energy*, 2008, **50**, 422-426.
12. A. Bieberle, L. P. Meier and L. J. Gauckler *J. Electrochem. Soc.*, 2001, **148**, A646-A656.
13. J. Fleig, *Annu. Rev. Mater. Res.*, 2003, **33**, 361-382.
14. W. M. Flarsheim, Y. M. Tsou, I. Trachtenberg, K. P. Johnston and A. J. Bard, *J. Phys. Chem. B*, 1986, **90**, 3857-3862.
15. C.-y. Liu, S. R. Snyder and A. J. Bard, *J. Phys. Chem. B*, 1997, **101**, 1180-1185.
16. T. Zerihun and P. Gründler, *J. Electroanal. Chem.*, 1998, **441**, 57-63.
17. P. Atkins and J. d. Paula, *Atkins' Physical Chemistry*, Oxford University Press, New York, 2002.
18. A. J. deBethune, T. S. Licht and N. Swendeman, *J. Electrochem. Soc.*, 1959, **106**, 616-625.
19. S. R. Jacob, Q. Hong, B. A. Coles and R. G. Compton, *J. Phys. Chem. B*, 1999, **103**, 2963-2969.
20. G. Vijayaraghavan, L. Gao and C. Korzeniewski, *Langmuir*, 2003, **19**, 2333-2337.
21. A. J. de Bethune, H. O. Daley, N. A. S. Loud and G. R. Salvi, *J. Electrochem. Soc.*, 1967, **114**, 578-582.
22. C. M. A. Brett and A. M. O. Brett, *Electrochemistry: Principles, Methods, and Applications*, Oxford University Press, Oxford, 2000.
23. E. P. Parry and R. A. Osteryoung, *Anal. Chem.*, 1965, **37**, 1634-1637.
24. A. Yamakata, T. Uchida, J. Kubota and M. Osawa, *J. Phys. Chem. B*, 2006, **110**, 6423-6427.
25. P. Grundler, A. Kirbs and T. Zerihun, *Analyst*, 1996, **121**, 1805-1810.
26. U. Kumar Sur, F. Marken, N. Rees, B. A. Coles, R. G. Compton and R. Seager, *J. Electroanal. Chem.*, 2004, **573**, 175-182.
27. M. J. Moorcroft, N. S. Lawrence, B. A. Coles, R. G. Compton and L. N. Trevani, *J. Electroanal. Chem.*, 2001, **506**, 28-33.

28. B. Miller, *J. Electrochem. Soc.*, 1983, **130**, 1639-1640.
29. J. F. Smalley, L. Geng, S. W. Feldberg, L. C. Rogers and J. Leddy, *J. Electroanal. Chem.*, 1993, **356**, 181-200.
30. J. L. Valdes and B. Miller, *J. Phys. Chem.*, 1989, **93**, 7275-7280.
31. T. Voß, P. Gründler, A. Kirbs and G.-U. Flechsig, *Electrochem. Commun.*, 1999, **1**, 383-388.
32. P. Gründler, T. Zerihun, A. Möller and A. Kirbs, *J. Electroanal. Chem.*, 1993, **360**, 309-314.
33. www.e6.com.
34. K. Yoshida and H. Morigami, *Microelectron. Rel.*, 2004, **44**, 303-308.
35. P. Bertoncello, J. P. Edgeworth, J. V. Macpherson and P. R. Unwin, *J. Am. Chem. Soc.*, 2007, **129**, 10982-10983.
36. L. Korson, W. Drost-Hansen and F. J. Millero, *J. Phys. Chem.*, 1969, **73**, 34-39.
37. J. T. Edward, *J. Chem. Educ.*, 1970, **47**, 261.
38. I. Dumitrescu, P. R. Unwin, N. R. Wilson and J. V. Macpherson, *Anal. Chem.*, 2008, **80**, 3598-3605.
39. L. N. Trevani, E. Calvo and H. R. Corti, *J. Chem. Soc., Faraday Trans.*, 1997, **93**, 4319-4326.
40. J. Heinze, *Angew. Che. Int. Ed.*, 1993, **32**, 1268-1288.
41. J. F. Smalley, C. V. Krishnan, M. Goldman, S. W. Feldberg and I. Ruzic, *J. Electroanal. Chem. Inter. Electrochem.*, 1988, **248**, 255-282.
42. J. F. Smalley, R. A. MacFarquhar and S. W. Feldberg, *J. Electroanal. Chem. Inter. Electrochem.*, 1988, **256**, 21-32.
43. A. Olivier, E. Merienne, J. P. Chopart and O. Aaboubi, *Electrochim. Acta*, 1992, **37**, 1945-1950.
44. R. Trouillon and D. O'Hare, *Electrochim. Acta*, 2010, **55**, 6586-6595.
45. R. P. Akkermans, M. F. Suárez, S. L. Roberts, Q. Fulian and R. G. Compton, *Electroanalysis*, 1999, **11**, 1191-1202.
46. R. L. McCreery, *Chem. Rev.*, 2008, **108**, 2646-2687.
47. P. Chen, M. A. Fryling and R. L. McCreery, *Anal. Chem.*, 1995, **67**, 3115-3122.
48. M. Hupert, A. Muck, J. Wang, J. Stotter, Z. Cvackova, S. Haymond, Y. Show and G. M. Swain, *Diamond Relat. Mater.*, 2003, **12**, 1940-1949.

6 Heated Stripping Voltammetry at a pBDD Electrode

An all diamond structure was fabricated from sample E, as this was the highest quality material investigated in this thesis. Pulsed laser electrode heating was investigated in Chapter 5, and is used here with DPV to perform heated anodic stripping voltammetry (ASV).

Initial experiments with a glass sealed pBDD in bulk heated solution showed an enhanced Pb stripping signal at elevated temperatures. Pulsed heating was then applied to the all diamond electrode mounted in the high temperature cell during the preconcentration step of ASV, a deposition potential of -1.4 V vs. Ag/AgCl was applied for 300 s. Heating the electrode during deposition in 5 µM Pb^{2+} solution greatly enhanced the stripping signal, a large amount of Pb deposits were seen on the electrode surface with FE-SEM, the particles showed a preference for more conducting regions. A second stripping peak appeared at a more positive potential when electrode heating was employed during deposition in a solution containing 50 µM Pb^{2+}, accompanying this were larger 'flake-like' structures on the electrode surface that were observed during FE-SEM.

Electrode heating performed during the stripping step of ASV showed a shift towards a more negative potential. Continued deposition of Pb during the stripping step, facilitated by electrode heating, produced a larger signal which increased with laser power.

6.1 Introduction

Stripping voltammetry is a widely used class of techniques in electrochemistry,[1, 2] whereby analyte species are deposited onto an electrode during a preconditioning step and subsequently stripped off. Of particular importance is the environmental monitoring of potentially harmful species such as heavy metals,[3] which may contaminate water supplies and have adverse effects on aquatic organisms and even humans.[4] BDD is an obvious candidate for monitoring of heavy metals due to its low background currents, lack of chemical reactivity, biocompatibility and resistance to fouling.[5, 6] Both bare and nanoparticle modified[7] BDD electrodes have been successfully utilised for heavy metal analysis using stripping voltammetry,[8-10]. The detection of non-metal species using stripping voltammetry has also been performed with BDD, where electroactive molecules such as rutin[11] and aniline[12] are first electrodeposited and then stripped from the BDD surface.

The preconditioning step in ASV is achieved by applying a negative potential to the working electrode for a defined period, where metal species dissolved in solution are reduced and deposited onto the electrode. The amount of metal 'collected' during deposition depends on both the flux of species to the electrode during deposition and the metal electrodeposition electron transfer kinetics, and hence is influenced by factors such as; electrode size, electrode geometry, preconditioning time, metal concentration. During electrodeposition, mass transport can be enhanced by introducing forced convection into the system, with examples including; RDE,[13, 14] impinging jet,[15, 16] and ultrasound.[17, 18] By increasing the flux of species towards the electrode surface more material is deposited and subsequently stripped off, increasing the resultant signal and improving detection limits.

Mass transport may also be enhanced by introducing thermal convection into the system by means of electrode[19, 20] and solution[21] heating (isothermal). A temperature gradient is established between the electrode and bulk solution, resulting in forced convection. Many different electrode materials have been utilised in this field including graphite,[22] carbon paste,[23] bismuth[24] and mercury.[25, 26] It was found that much higher signal intensities (4-34 times larger for nucleic acids)[23] could be achieved at elevated temperatures, which was attributed to the enhanced rate of flux of species towards the working electrode.

BDD has been also used in conjunction with high temperature ASV, Prado *et al*[27] showed that isothermal solution heating could be used to facilitate lead deposition and improve detection limits, the stripping signal is found to increase by a factor of 10. It was found from chronoamperometric experiments that both the rates of mass transport and particle nucleation are increased upon heating, AFM analysis revealed larger but not notably more lead particles, however a distribution in particle size is observed indicating a progressive nucleation and growth mechanism. Additionally, both deposition and stripping potentials of lead were found to be shifted towards more positive potentials under heated conditions. Furthermore, by utilising microwave heating close to the electrode, Compton *et al*[28] found that the ASV of palladium on BDD could also be improved, a large shift from -0.4 V to +0.1 V in deposition potential was observed for this metal, the stripping peak height was increased by a factor of 3.

From the literature it is known that there are great benefits to performing ASV at elevated temperatures, most notably a large increase in analytical signal. Experiments involving both bulk solution heating and electrode heating have been performed, with the latter affording more control. There have been relatively few studies of this type

on BDD, despite the potential of this material due to its singular properties for use in electroanalysis. In particular, the high thermal conductivity of BDD (600 $Wm^{-1}K^{-1}$) permits fast changes in electrode temperature with external heating. A laser was chosen as this external stimulus as heat can be applied in a fast a controlled way, whereby the laser is focussed onto the back face of the BDD and heat propagates through to the electrode/solution interface.

6.2 Room Temperature Studies

6.2.1 Glass Sealed pBDD Electrode

Preliminary CVs were recorded with a glass sealed pBDD electrode fabricated as described in section 2.2.1 (sample E) to establish the potential of lead deposition, in a solution containing 100 µM Pb^{2+} at a scan rate of 50 $mVs^{-1;}$ a typical CV is shown in Figure 6.1. For all studies described herein the supporting electrolyte concentration was 0.1 M KNO_3. As can be seen at around -0.75 V the current starts to rise due to Pb electrodeposition and increases as the potential is scanned more negative (larger overpotential). On the return scan current crossover is seen indicating the presence of a nucleation and growth mechanism,[29, 30] where the first lead deposits assist further deposition increasing the rate and producing a larger current.

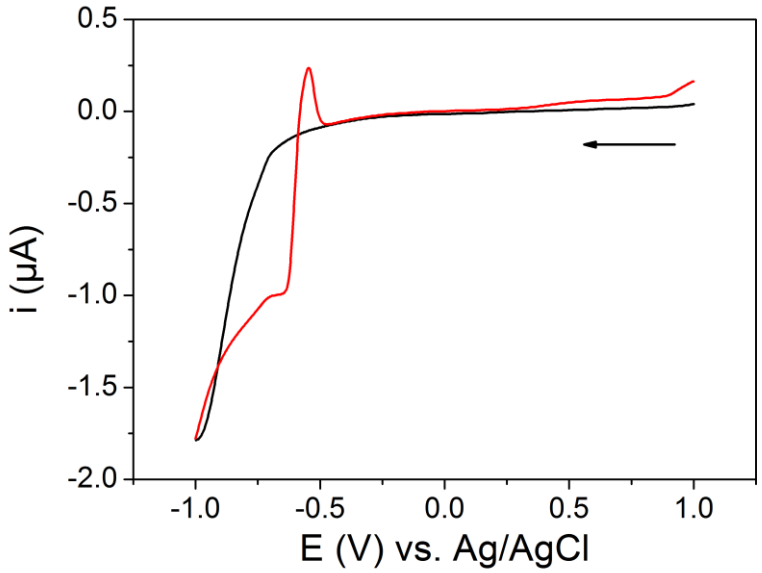

Figure 6.1 – CV of glass sealed pBDD electrode in 100 µM Pb^{2+} at a scan rate of 50 mVs^{-1}, forward and return scans are coloured black and red respectively.

All DPV experiments in this chapter employed the same preconcentration step, which consisted of applying -1.4 V to the working electrode for a time of 300 s. Initial DPV

experiments were conducted at room temperature (24 ± 2 ^{o}C) over a range of different lead concentrations (1 – 100 µM), Figure 6.2. Parameters for the stripping step were as follows: pulse width, 50 ms; pulse period, 200 ms; pulse amplitude 50 mV; step size, 2 mV, as these have previously been established to provide reproducible results with pBDD.[15] The largest signal is attributed to the highest concentration of Pb^{2+}, this signal diminishes with lower concentrations as expected. A clearly defined peak is seen at between -0.62 to -0.72 V vs. Ag/AgCl and is due to the stripping of deposited lead back into solution. This shift towards more negative values at lower concentrations suggests a particle size dependent effect on stripping potential, as is seen for Ag nanoparticles.[31] At the highest concentration (100 µM) an additional, smaller peak is seen at ca. -0.43 V vs. Ag/AgCl, this feature appears to be present at lower concentrations though not as a defined peak. It has been shown previously by Hutton *et al*, that the morphology of lead deposits on pBDD affect the potential at which Pb is stripped from the surface.[15] The authors attribute the first peak to the stripping of lead nanoparticles and the emergence of the second peak (at more positive potentials) to a film-like deposit that occurs at higher concentrations. It has been shown by numerical simulations that the stripping behaviour of deposited metal is affected by morphology,[32] whereby hemispherical particles with a relatively small surface interaction area are stripped off at lower overpotentials than that of film like morphologies with smaller particle sizes.

Peak currents and peak areas are plotted in Figure 6.3 (a) and (b) respectively; a linear trend is observed in (b) at lower concentrations but not for (a). This is because measurement of peak area takes into consideration all features attributed to the stripping of lead which peak height does not. At higher concentrations a linear trend

it not observed for peak area, most likely due to the incomplete removal of lead deposits during stripping.

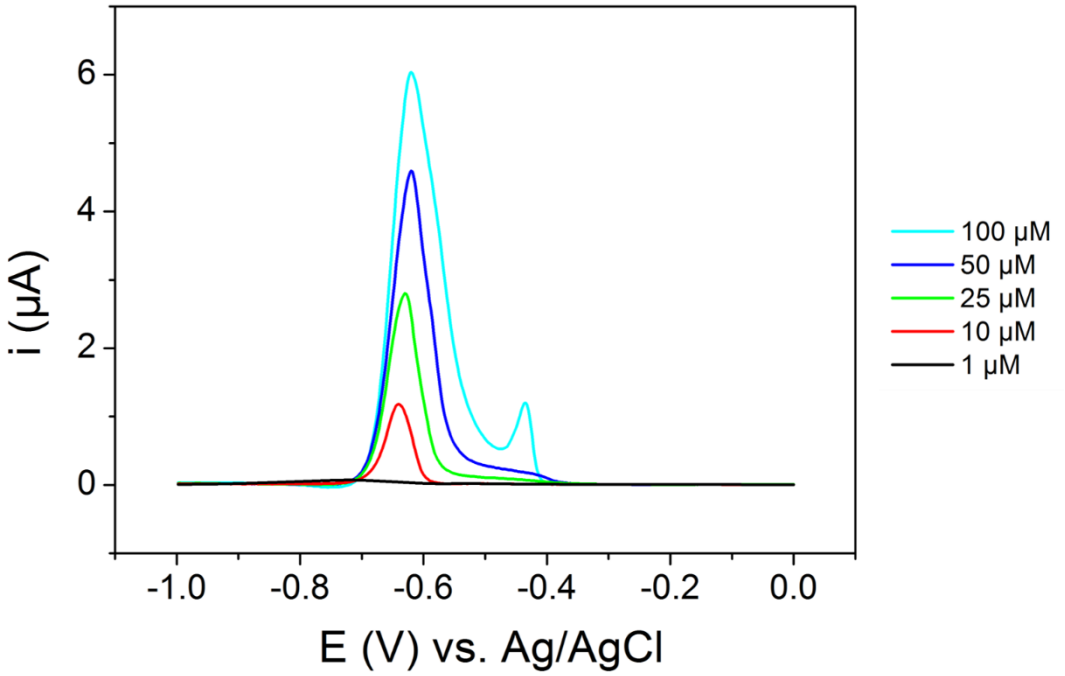

Figure 6.2 – DPV of 1 mm pBDD (sample E) with varying concentrations of Pb^{2+} in 0.1 M KNO_3. Experimental conditions; pulse width, 50 ms; pulse period, 200 ms; pulse amplitude 50 mV; step size, 2 mV and deposition time 300 s.

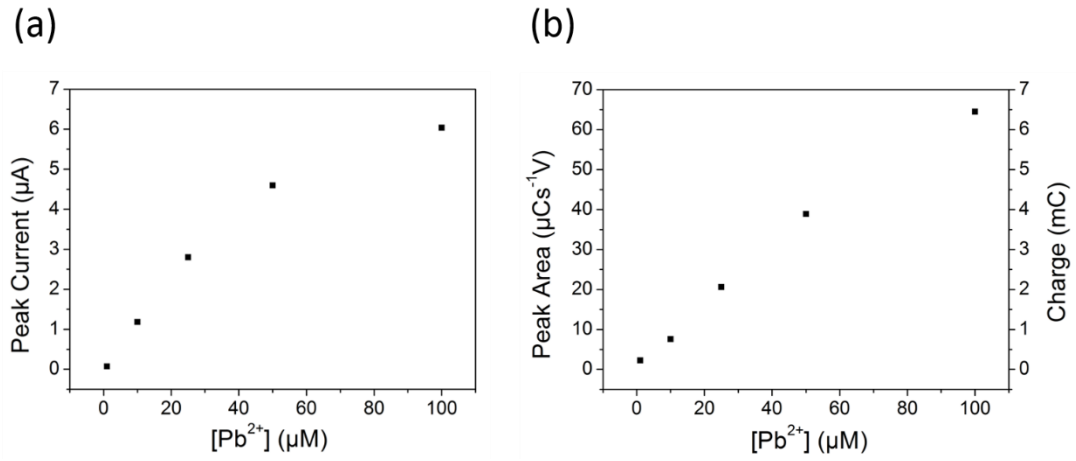

Figure 6.3 – Measured (a) peak currents and (b) peak areas with associated charges of DPV data from Figure 6.2.

6.3 Isothermal Studies

Isothermal experiments were performed using the water bath setup described in section 2.5.1, the effects of continuous heating were tested with a glass sealed pBDD (sample E). Deposition and stripping parameters were the same as before, with the exception that the pulse width was reduced to 10 ms, thus allowing synchronisation with pulse heating in later experiments (section 6.4). Under these heated conditions, both deposition and subsequent stripping occur at elevated temperatures due to the inability of being able to change solution temperature with this methodology. DPV was performed as described above at different temperatures and is shown in Figure 6.4 for a lead concentration of 5 μM.

It can clearly be seen that solution heating has a substantial effect on the resultant stripping peak. As the temperature increases the charge associated stripping increases, as shown in Figure 6.5. This is indicative of either or both, an increased amount of lead deposited on the electrode surface or an improvement in the stripping efficiency of the deposits.

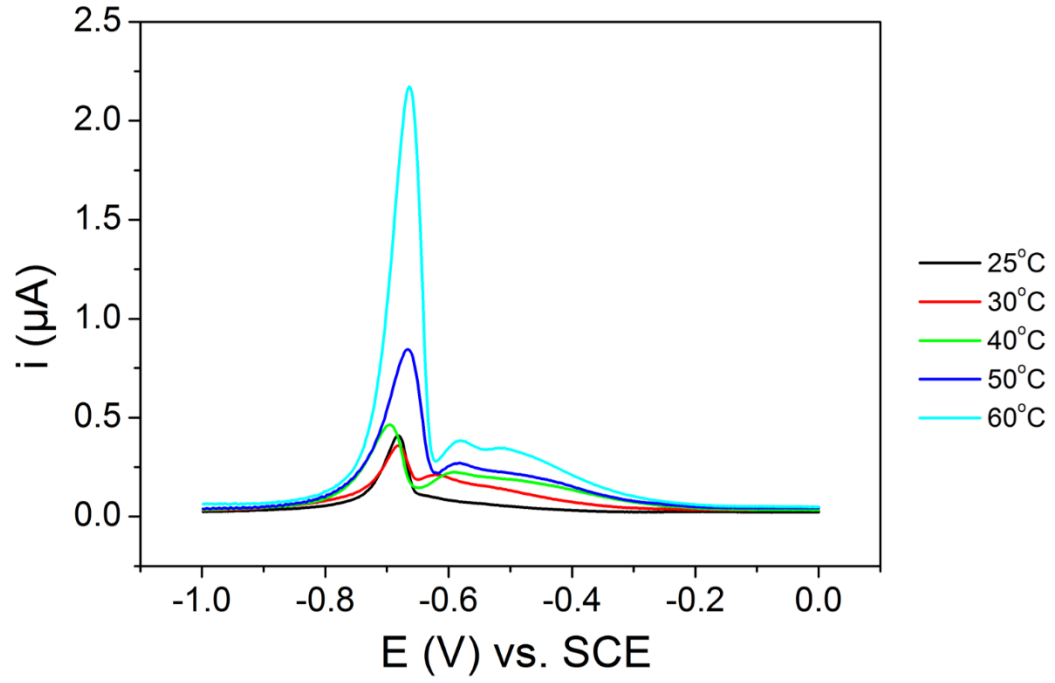

Figure 6.4 – DPV stripping of glass sealed electrode in 5 μM Pb^{2+} at various temperatures, heating is performed isothermally with a water bath apparatus.

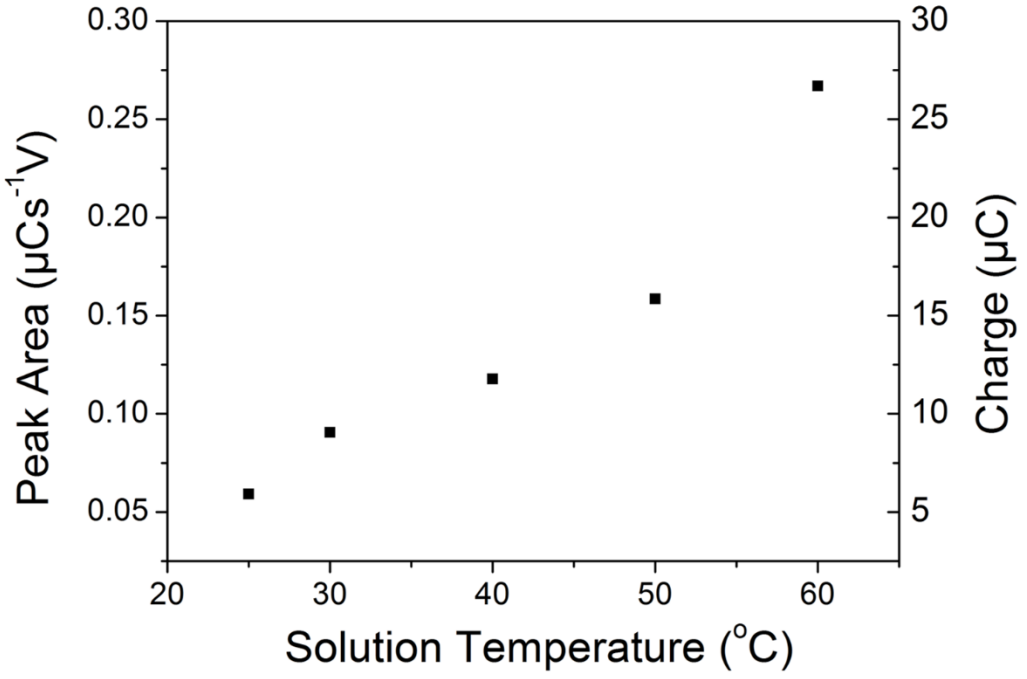

Figure 6.5 – Peak areas and associated charges of DPV in a solution of 5 μM Pb^{2+}at various temperatures.

6.4 Non-Isothermal Studies

6.4.1 All-Diamond Macroelectrode Sample Characterisation

A robust electrode was required for lead stripping experiments, as the frequent cleaning procedures required to obtain a clean, lead free surface after lead deposition (anodic polarisation of 2 V for 600 s) were found to degrade the quality of the insulating Kapton tape used for electrode construction. All-diamond macroelectrodes were thus produced by Element Six in conjunction with Warwick using the following procedure. A circular piece of high quality pBDD (4 mm diameter, sample E) was laser machined to leave a protruding (~ 70 μm) disc of approximately 1 mm diameter in the centre. This was then acid cleaned as described in section 2.2.1 and returned to the supplier (Element Six Ltd.) for overgrowth. An etch was first performed with an oxygen plasma to further clean the surface and intrinsic diamond was then grown over the laser machined structure and lapped back to reveal a 1 mm BDD disc, as depicted in Figure 6.6. This all-diamond electrode was mounted into the high temperature cell described in section 2.2.3. Araldite (Rapid Electronics Ltd., U.K.) was used to seal the diamond into the perspex window.

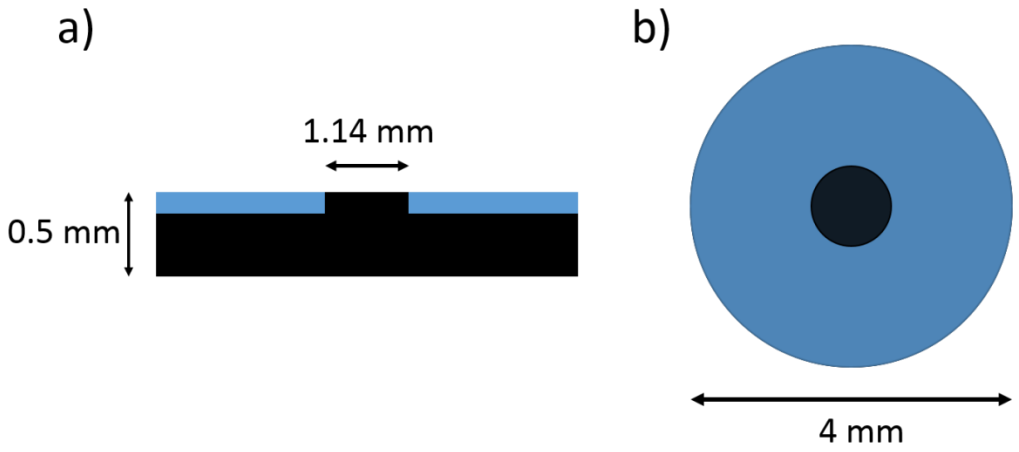

Figure 6.6 – Schematic depiction of all diamond structure (a) side view and (b) top down view; intrinsic and boron doped regions are represented with blue and black respectively.

Electrochemistry, FE-SEM and Raman spectroscopy were used to assess the viability of this structure as an electrode, despite the quality of the original pBDD (sample E) it was unknown whether the intrinsic diamond would provide suitable insulation. CV was performed with the high temperature cell, which was filled with a solution containing the $Ru(NH_3)_6^{2+/3+}$ couple and is shown below in Figure 6.7, ΔEp is 66 mV in accordance with previous CV experiments performed with sample E in section 3.2.3. Crucially, the measured peak current is as expected (Randles-Sevcik equation) for the experimental parameters employed, which is ~ 2.3 µA is assuming a diffusion coefficient of 8.8×10^{-6} cm^2s^{-1}. Hence the overgrown layer of intrinsic diamond serves as a suitable co-planar insulating layer to define a BDD electrode of diameter ~ 1 mm.

Measurements in supporting electrolyte revealed a capacitance of ~ 11.6 µF cm^{-2}, which is almost twice as high as that measured for sample E. Raman spectroscopy of the all diamond structure in both the intrinsic and BDD areas of the surface showed familiar features, as shown in Figure 6.8 including a peak at around 1332 cm^{-1} which is diminished and shifted to lower wavenumbers at high levels of boron doping.[33] Importantly no evidence of sp^2 carbon was observed which could contribute to an

increased capacitance. Hence, the exact origin of this disparity is unknown, though could possibly be manifested from pinholes in the intrinsic layer allowing charge to build up.[34]

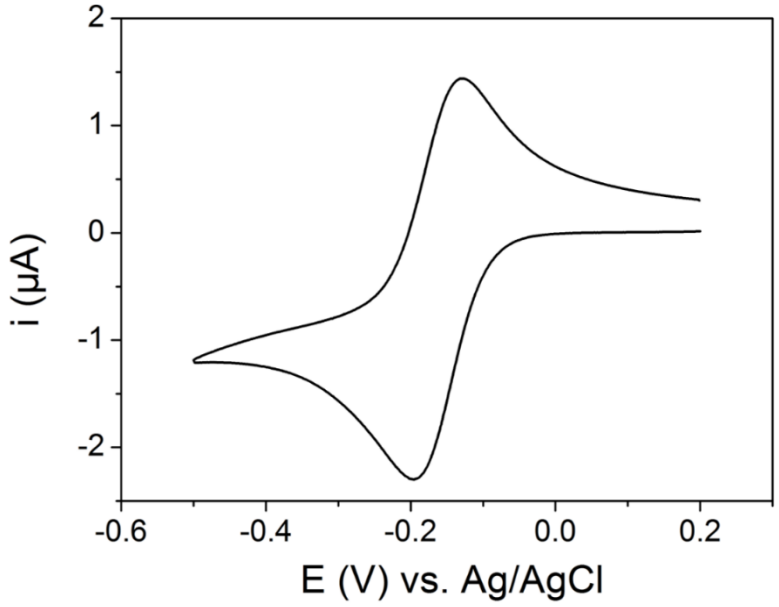

Figure 6.7 – CV of all diamond structure in 0.88 mM $Ru(NH_3)_6$, 0.1 M KNO_3 at 100 mVs^{-1}

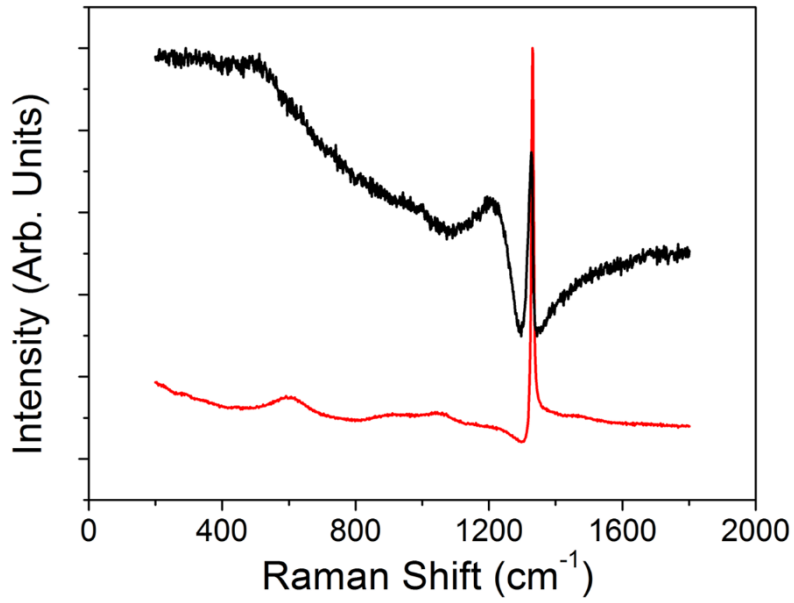

Figure 6.8 – Raman spectrum of relatively higher (black line) and lower (red line) boron doped regions of the all diamond structure.

From SEM, the same grain structure observed in sample E was also present for the all diamond structure, Figure 6.9. Additionally, no regions displayed greater rates of charging during FE-SEM over the entire exposed BDD surface, suggesting that all intrinsic diamond covering the ~ 1 mm BDD disc structure had been removed during lapping.

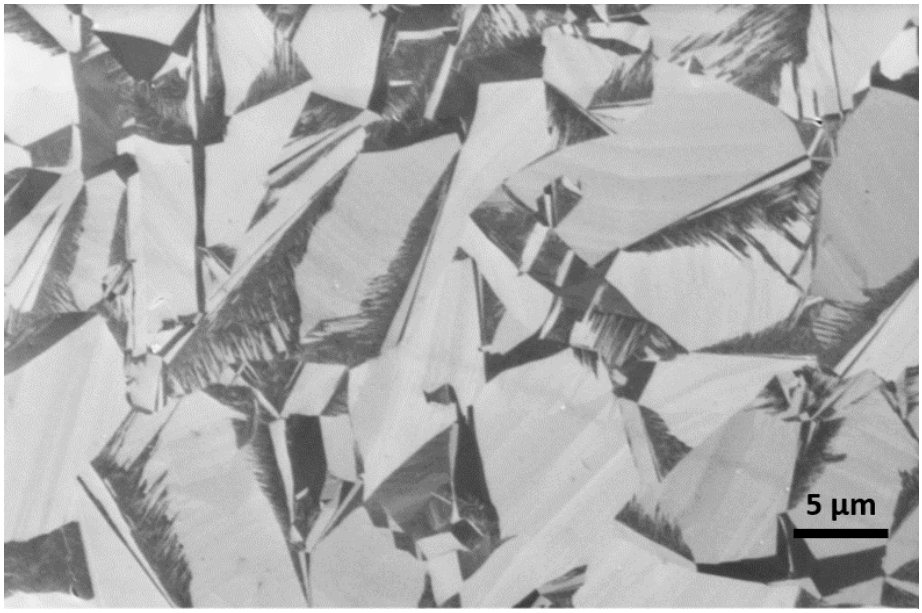

Figure 6.9 – In-lens SEM of all diamond structure.

The temperature of the solution near to the electrode was measured implicitly as before in section 5.3.3, the measured OCPs and associated temperature rises are shown below in Figure 6.10. The temperature profiles of this all-diamond electrode are different from those of electrode H used in section 5.3.3, where the response of the all-diamond electrode is much slower than electrode H. This is thought to be due to the thickness of the all diamond structure (~ 500 µm), compared to 200 µm, increasing the time taken for heat to travel to the electrode/solution interface. TPV experiments were performed as before in section 5.3.5 with $Ru(NH_3)_6^{2+/3+}$ to assess the all diamond structure, Figure 6.11, where raw data is sampled to produce a TPV representing the

hottest part of each temperature pulse. The resultant TPV is dissimilar to examples seen before with the thinner diamond electrode H.

Figure 6.10 shows that the thicker electrode displays a sluggish time response for both temperature rise and decay, as compared to Figure 5.11 (Chapter 5), for the thinner electrode, maximum temperature rises are listed in Table 6.1. As the heat lingers in the system between pulses, the transients do not decay back down to the original temperature, instead tending towards a steady state. The largest ΔT is seen for the highest laser power i.e. 18.4 ^{o} C (at the peak of the transient) for 27.5 W which is less than 31 ^{o}C for the thin electrode at the same laser power. The corresponding TPVs for the different laser powers are shown in Figure 6.8, data is sampled as described in section 5.3 In contrast to the data in Figure 5.14 (Chapter 5), the TPVs tend more towards a steady-state again likely to be due to the sluggish temperature-decay profiles of the pulse.

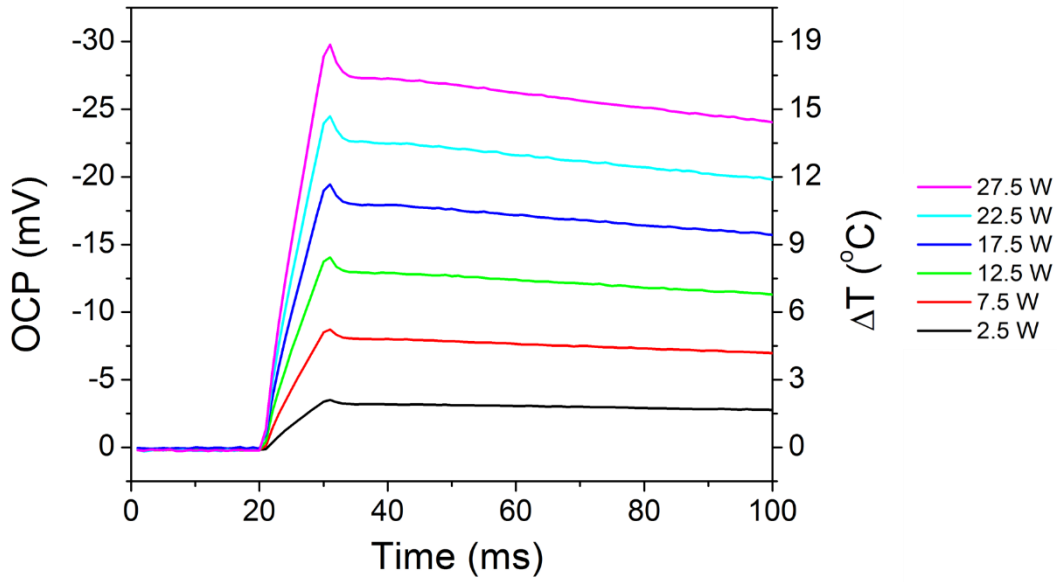

Figure 6.10 – Measured OCP between a non-heated and laser-heated pBDD electrode as a function of time at different laser powers in an equimolar solution of 0.5 mM $K_3[Fe(CN)_6]$ + $K_4[Fe(CN)_6]$ in 0.1 M KNO_3. The associated temperature rise is shown on the right hand axis using β = 1.62 mVK^{-1}.

Laser Power (W)	OCP (mV)	ΔT (°C)
2.5	3.5	2.2
5	6.3	3.9
7.5	8.7	5.4
10	11.3	7.0
12.5	14.1	8.7
15	16.8	10.4
17.5	19.5	12.0
20	22.1	13.6
22.5	24.5	15.1
25	27.2	16.8
27.5	29.8	18.4

Table 6.1 - Measured OCP values with associated temperature rises after 10 ms of laser heating at different laser powers in an equimolar solution of 0.5 mM $K_3[Fe(CN)_6]$ + $K_4[Fe(CN)_6]$ in 0.1 M KNO_3.

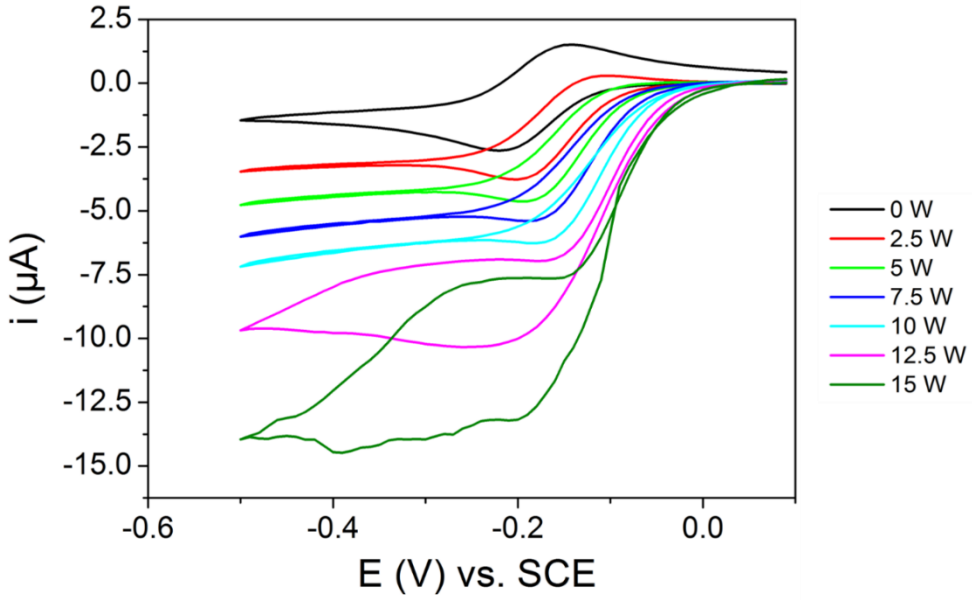

Figure 6.11 - TPV (sampled data) of all diamond structure in 1 mM $Ru(NH_3)_6^{2+/3+}$ 0.1 M KNO_3 at various laser powers.

6.4.2 Pulse Heated Deposition

Two concentrations of Pb^{2+} (5 µM and 50 µM) were chosen to show the effects of electrode heating on metal deposition and subsequent stripping. These two concentrations are an order of magnitude apart, the lower of which is close to the

detection limit found with this electrode at ambient conditions for a deposition time of 300 s. DPV is conducted in the normal manner, with pulsed laser heating being applied to the electrode during the deposition step. Heating is performed at 10 W with a 20 ms laser pulse with a pulse period of 200 ms, this is applied for the entire preconcentration step during which the bulk solution temperature may rise by ~ 5 ^{o}C as measured by a thermocouple.

A DPV of metal stripping from a solution of 5 µM Pb^{2+} at ambient and heated (10 W) deposition conditions is shown in Figure 6.12. It can be seen that employing pulsed heating during metal deposition greatly enhances the subsequent stripping peak, where a slight peak shift towards a more positive potential is also observed. This is especially impressive as the thickness means the maximum temperature rises at the electrode/electrolyte interface are not as significant as for a thinner electrode. The stripping peak area under heated deposition conditions is larger by a factor of 43 than that obtained under ambient conditions (7.5×10^{-9} and 3.2×10^{-7} $Cs^{-1}V$). The presence of a larger stripping peak must be due to an increased amount of lead deposited onto the electrode surface during preconcentration, which thus requires a larger driving force (greater overpotential) for removal.

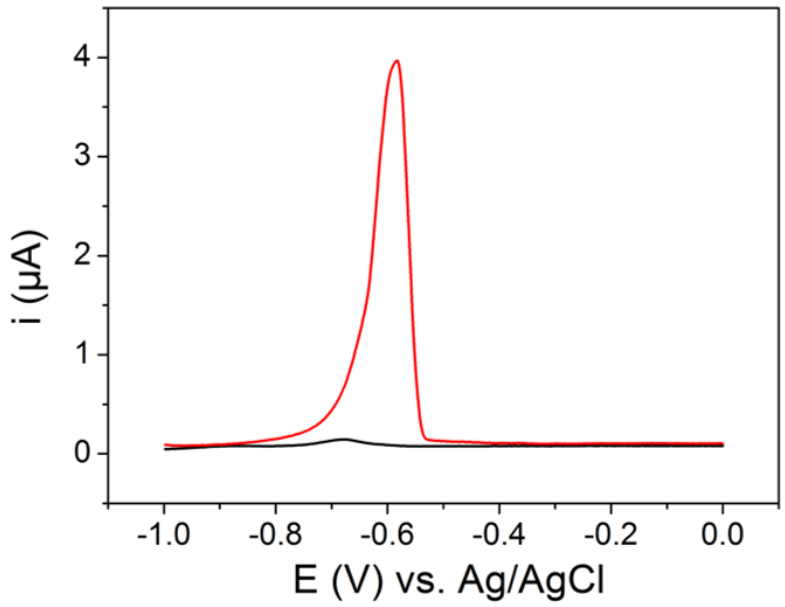

Figure 6.12 – DPV stripping of all diamond structure in 5 μM Pb^{2+} at ambient (black line) and 10 W heated (red line) deposition conditions.

FE-SEM was utilised as a means of assessing lead deposited under ambient and heated conditions, enabling visualisation of the lead deposits. The same deposition procedure was followed as for Figure 6.12 except no stripping took place. The window of the high temperature cell was then removed and the electrode gently rinsed with ultra-pure water to avoid the precipitation of KNO_3 salt crystals. Very few particles were expected for the deposition of lead at ambient conditions in 5 μM Pb^{2+} solution (black line in Figure 6.12), as observed with SEM, with Figure 6.13 revealing a clean surface. However we cannot rule out the possibility that some particles are removed during rinsing.

A much larger stripping peak is seen when pulse heated deposition is employed due more lead being deposited, this is thought to occur due to an enhanced flux towards the electrode caused by thermal gradients (convection) and an increased diffusion coefficient of Pb^{2+}. This was observed microscopically as shown in Figure 6.14, where many particles are now observed on the pBDD surface. Interestingly, there is a

preference for particles to be deposited in the higher doped regions, which appear as darker areas when using the in-lens detector of SEM.[35] From the FE-SEM there appears to be no evidence of deposition within the lighter doped areas (which are still above the metallic threshold), although for absolute confirmation the use of higher resolution techniques such as AFM would be required. Although the applied potential is significantly more negative than the potential at which Pb starts to deposit on the surface (~ -0.75 V), it must not be great enough to overcome the differences in local resistance of the surface due to different boron doping levels.[36] To test this, a larger effective overpotential can be used, which drives the deposition process more. Despite achieving a near reversible CV in $Ru(NH_3)_6$ with this electrode (ΔE_p of 66 mV at a scan rate of 100 mV s^{-1}), it is possible that the electrical contact to the pBDD may have not been ohmic. If the contact became diodic in nature at a value around the lead deposition potential (– 0.7 V vs. SCE), it could account for the observation that lead is preferentially deposited on higher doped (more conducting) regions of the pBDD surface where any poor contact effects would be less pronounced.

Using the same deposition conditions at ambient temperatures but using a different metal, one which has a less negative deposition potential (+0.1 V vs. Ag/AgCl), here silver, the FE-SEM image as shown in Figure 6.15 is observed. Electrodeposition of silver was performed in a solution containing 1 mM Ag^+. Silver deposition can be seen to occur indiscriminately over the entire pBDD electrode, irrespective of boron dopant density, suggesting changes in boron dopant density can be overcome. The effect of preferential deposition of metals on pBDD has been observed by Colley *et al*[37] for silver but using an applied potential of -0.2 V vs. Ag/AgCl and Compton *et al* depositing nickel nanoparticles.[38]

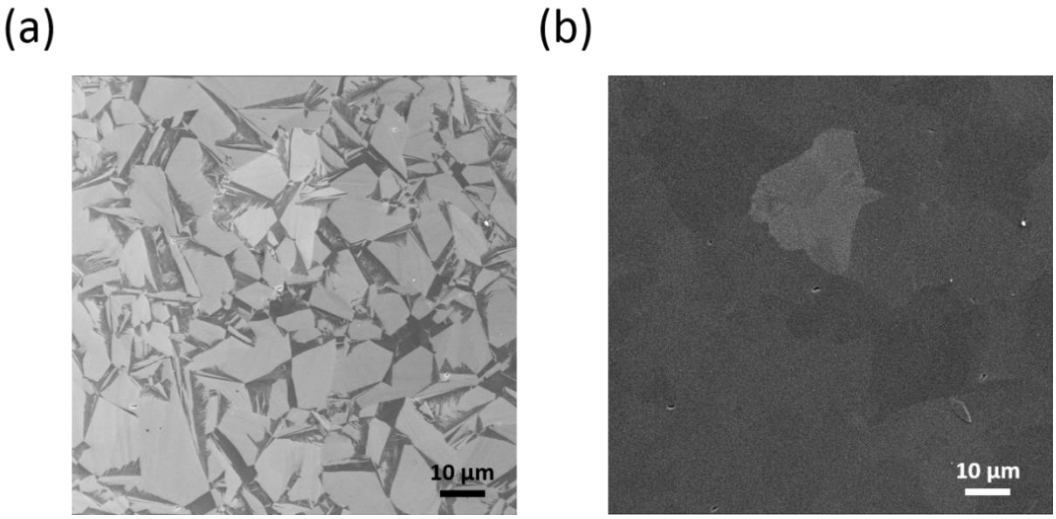

Figure 6.13 - (a) in-lens and (b) secondary electron SEM of all diamond structure after deposition in 5 µM Pb^{2+}at ambient conditions.

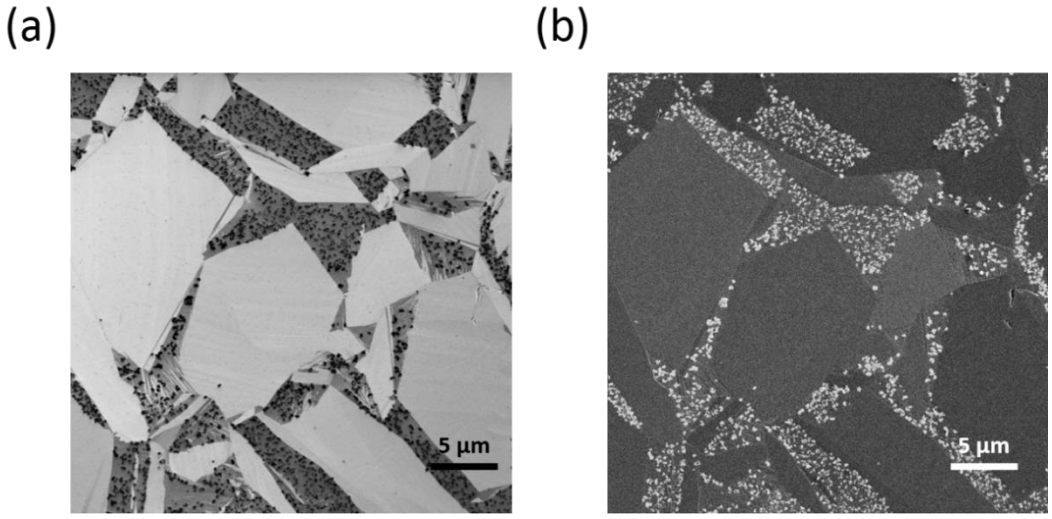

Figure 6.14 – (a) in-lens and (b) secondary electron SEM of all diamond structure after 10 W heated deposition in 5 µM Pb^{2+}.

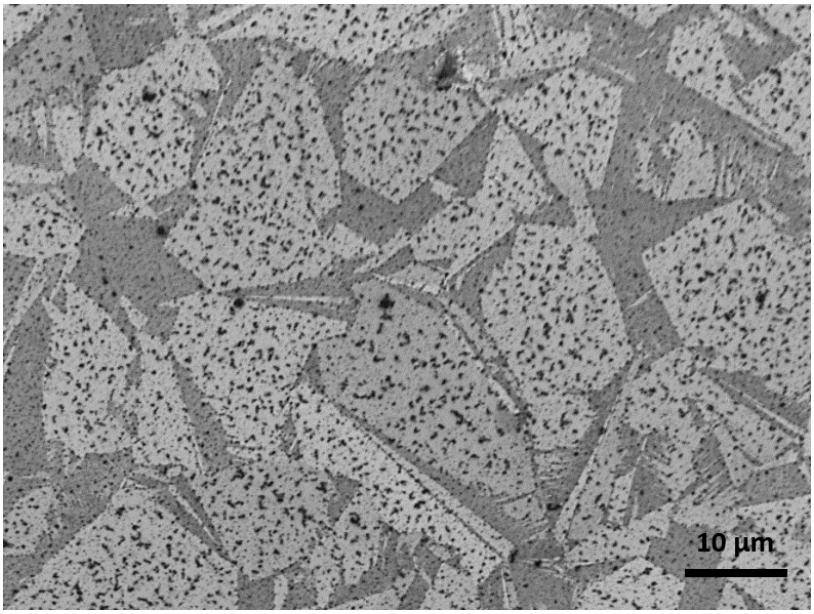

Figure 6.15 – In-lens SEM of all diamond structure after ambient deposition in 1 mM Ag^{+}.

A DPV experiment investigating ambient and heated deposition (DPV stripping under ambient conditions) was also conducted in a solution containing 50 µM Pb^{2+} under the same conditions for 5 µM Pb^{2+} is shown in Figure 6.16. The same effect of electrode heating during deposition is seen at this higher concentration, namely an increased stripping peak area with heating at a potential of -1.4 V vs. Ag/AgCl. Interestingly, a second, larger peak is also seen appearing at more positive potential of -0.48 V vs. Ag/AgCl, most likely indicating a different morphology of deposited lead.

The integrated area for the DPV under heated deposition conditions is 7.5 times larger than for ambient deposition (2.3×10^{-7}, 1.8×10^{-6} $Cs^{-1}V$), smaller than the previous enhancement at 5 µM Pb^{2+} possibly due to incomplete removal of all lead deposits. FE-SEM after deposition under ambient conditions (50 µM Pb^{2+}) reveals Pb particles, deposited in regions of the pBDD containing more boron. These are similar to those seen in Figure 6.14 albeit with a lower density. FE-SEM conducted after heated deposition in 50 µM Pb^{2+} solution, is shown in Figure 6.18 and Figure 6.19, revealing significant deposition on the all diamond structure; these deposits were so extensive

that they were visible to the naked eye. Observation of Figure 6.18 shows two distinct types of deposit; small particles (~ 250 nm) and large 'flakes' (longest dimension ~ 2 µm), but again both showing a preference for areas containing more boron. A higher magnification secondary electron image is presented in Figure 6.19, which clearly shows the difference in size and shape of these two types of lead deposit. The appearance of the peak at -0.48 V vs. Ag/AgCl is thus tentatively ascribed to the larger flake type deposits, as it was only observed when these deposits were witnessed in FE-SEM. Occurrence at a more positive potential suggests dissolution from the flaked structures is not as energetically favourable as from the sub-micron sized particles.

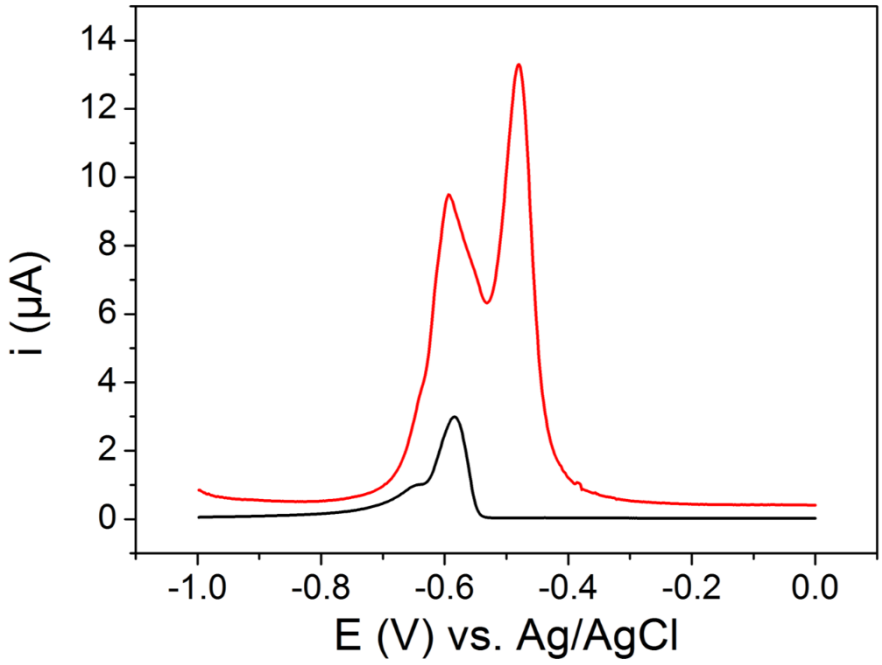

Figure 6.16 - DPV stripping of all diamond structure in 50 µM Pb^{2+} at ambient (black line) and 10 W heated (red line) deposition conditions.

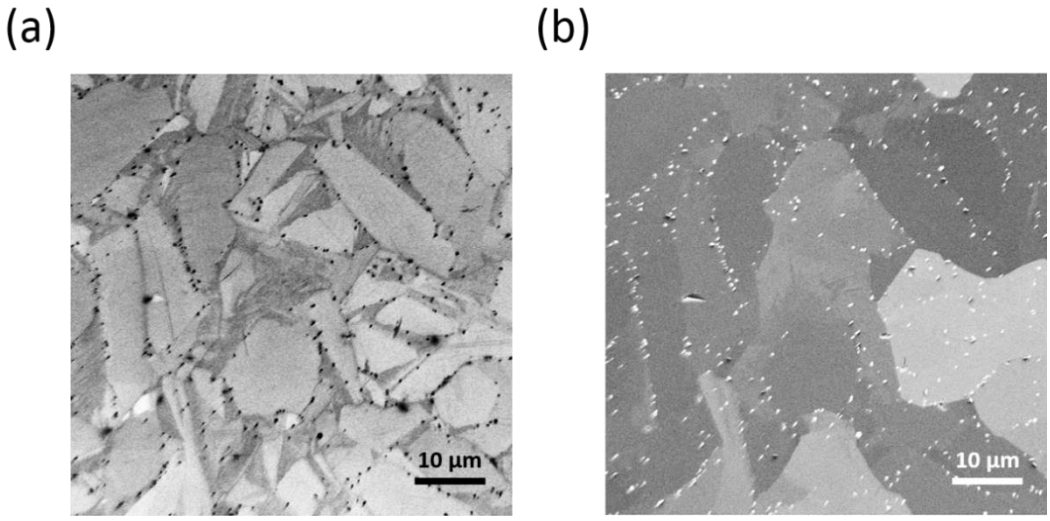

Figure 6.17 - (a) in-lens and (b) secondary electron SEM of all diamond structure after deposition in 50 µM Pb^{2+}at ambient temperature.

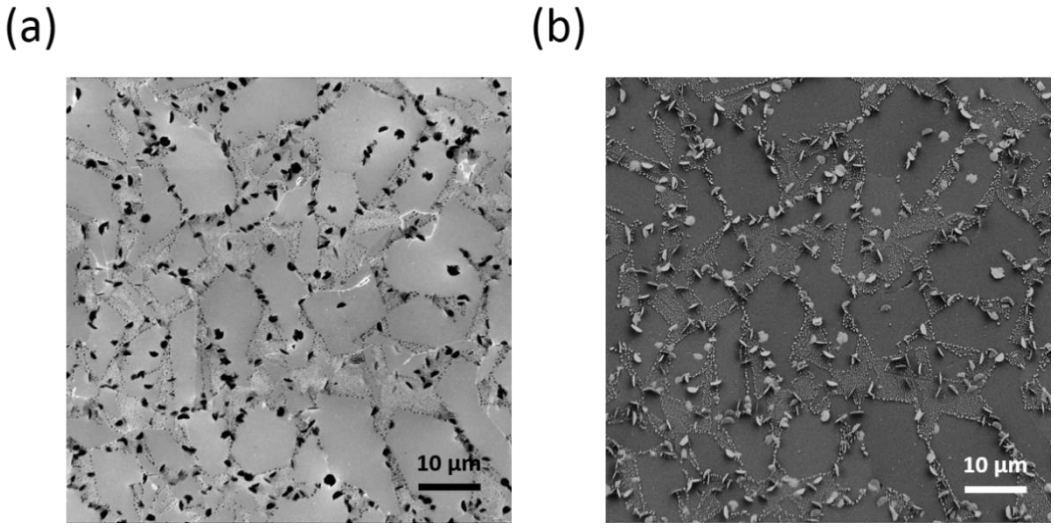

Figure 6.18 - (a) in-lens and (b) secondary electron SEM of all diamond structure after 10 W heated deposition in 50 µM Pb^{2+}.

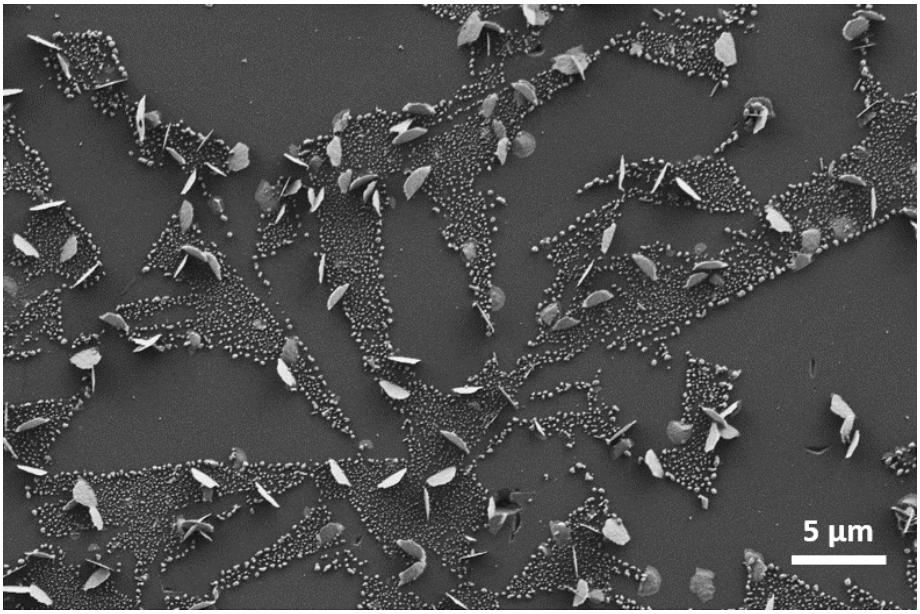

Figure 6.19 - Secondary electron SEM of all diamond structure after 10 W heated deposition in 50 µM Pb^{2+}.

6.4.3 Pulse Heated Stripping

The effect of electrode heating on the stripping step of ASV was also investigated with DTPV, where the all diamond structure is subjected to pulsed laser heating after electrodeposition under ambient conditions. This is shown schematically in Figure 6.20 where laser pulses are synchronised with potential pulses in the DPV waveform. DTPV parameters used throughout this section are as follows; pulse width, 10 ms; pulse period, 200 ms; pulse amplitude 50 mV; step size, 2 mV.

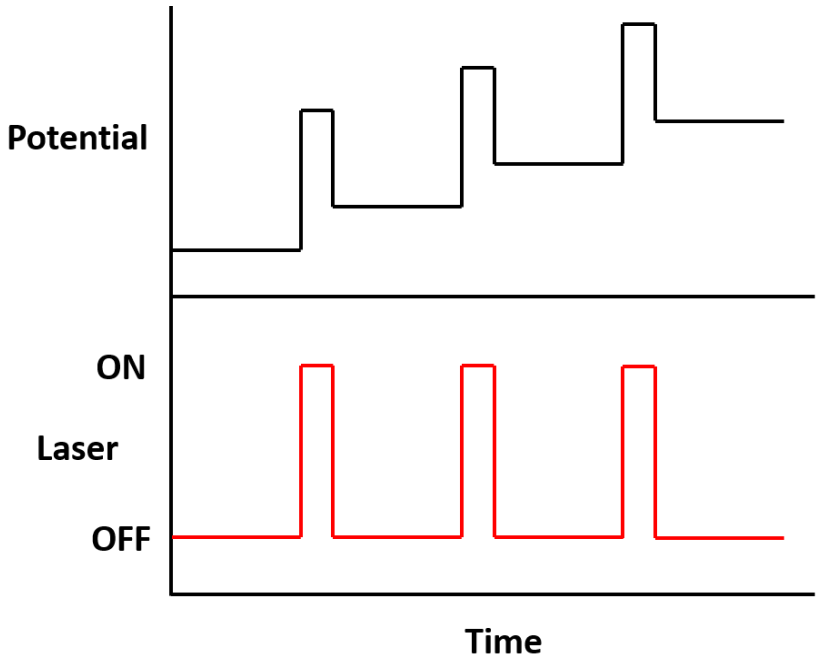

Figure 6.20 – Schematic of DPV experiment performed in *parallel with pulsed electrode heating.*

Two solutions containing Pb^{2+} at a concentration of 5 µM and 50 µM were used to perform these heated stripping experiments, mirroring experiments in section 6.4.2. The result of stripping at ambient (black line) and heated (red line) conditions for a 5 µM solution of lead is shown in Figure 6.21. No apparent enhancement in stripping peak is seen when pulsed heating is employed, though a higher background current manifests which may mask any possibly increased signal. At this low concentration, and from FE-SEM in section 6.4.2, it is known that very little lead is deposited under ambient conditions, which is likely to be stripped off with little difficulty. Any potential benefit in stripping efficiency due to heating is therefore negligible at this concentration; indeed heating actually appears to increase the background current.

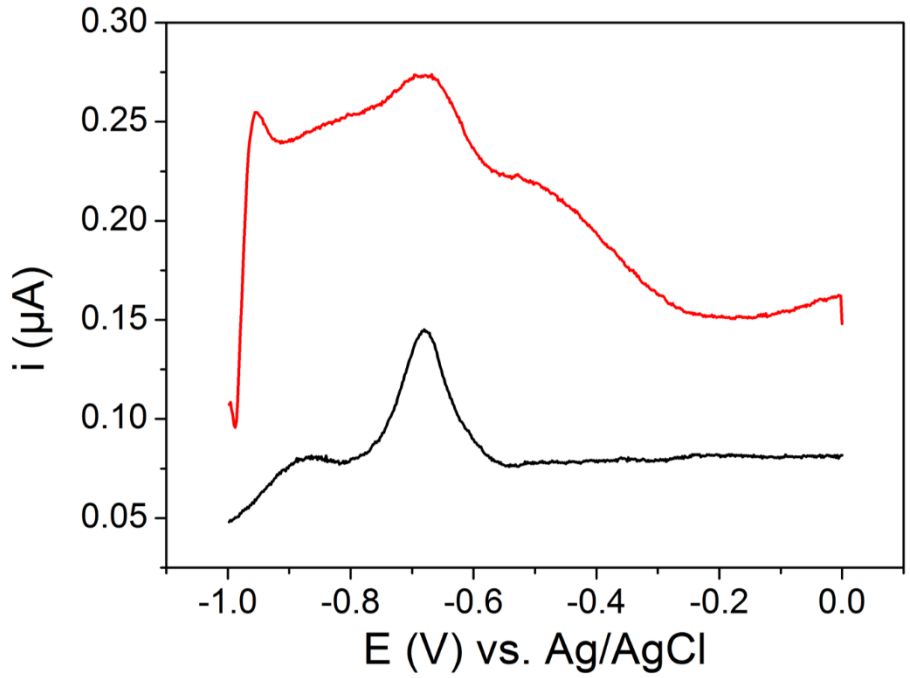

Figure 6.21 - DTPV stripping of all diamond structure in 5 µM Pb^{2+} at ambient (black line) and 10 W heated (red line) stripping conditions.

Data for the 50 µM Pb^{2+} solution are shown in Figure 6.22 for ambient, 10 W heated and 20 W heated stripping conditions; black, red and green lines respectively. A familiar peak is seen at around -0.6 V vs. Ag/AgCl when stripping is conducted at ambient conditions, upon 10 W heating however this peak shifts to a more negative potential at approximately -0.65 V vs. Ag/AgCl thus requiring a lower overpotential for stripping. This may suggest that the act of heating the electrode aids the oxidation of lead solid back into solution. The height of this peak (red line) is very similar to that of stripping at ambient conditions (black line), though the former exhibits a larger area and hence charge so it may be assumed that more lead is being stripped off. Careful observation of the red line in Figure 6.22 at the starting potential of -1 V reveals an initial negative current suggesting that lead is still being deposited at the beginning of the so called 'stripping step'. This seems reasonable based on experiments in section 6.4.2, where it was found that heating greatly increases the

deposition of lead. It follows that this continues under heated stripping conditions when the potential is more negative than the deposition potential of lead.

A higher laser power of 20 W was used to intensify this effect, shown as the green line in Figure 6.22. Once again the peak occurs at a potential more negative than under ambient stripping conditions, however both the peak height and area are now larger than for the ambient and 10 W heated stripping conditions. A negative current of a greater magnitude than for 10 W is seen at the starting potential of -1 V again suggesting the continued deposition of lead, the stripping peak at this power is therefore larger as expected.

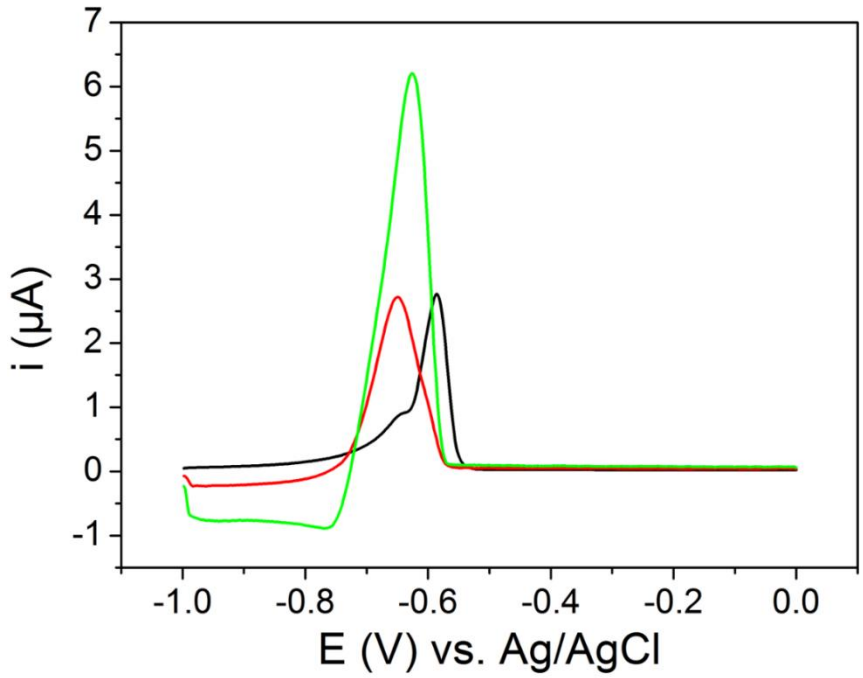

Figure 6.22 - DTPV stripping of all diamond structure in 50 μM Pb^{2+} at ambient (black line), 10 W heated (red line) and 20 W heated (green line) stripping conditions.

6.5 Conclusion

ASV of lead has been conducted on pBDD with DPV under both ambient and heated conditions. Preliminary experiments were performed in a continuously heated solution at different temperatures, utilising a water bath apparatus and glass sealed pBDD. It was shown that the stripping peak become larger at elevated temperatures, with bigger peak areas (i.e. charge) at higher temperatures. This suggests that heating acts to increase the amount of lead deposited on the surface, due to either (or both) an increased flux of species (thermal convection) and/or higher efficiency of the subsequent stripping step.

A pulse heated electrode methodology was employed as described in Chapter 5, using a laser as a fast controllable heat source. An all diamond electrode was fabricated for these studies due to the rigour with which cleaning is required for lead removal. An anodic cleaning step of +2 V for 300 s was used between experiments. Experiments with this setup were divided into two sections; heating during deposition and heating during stripping. For both, a deposition potential of -1.4 V vs. Ag/AgCl was applied for 300 s, a laser pulse width of 20 ms was used for the former, whereas for the latter is was 10 ms.

At a Pb^{2+} concentration of 5 µM a small stripping peak was observed at -0.68 V versus Ag/AgCl, the height and area of which became much larger upon heating, 43 times for the latter. FE-SEM observed a large increase in particle density with heated deposition, occurring preferentially at areas on the pBDD surface possessing a higher concentration of boron. An increase in peak height and area was also seen for ASV with a solution containing 50 µM of Pb^{2+}, although the enhancement is not as large at this concentration. A second stripping peak at -0.48 V vs. Ag/AgCl occurs when

heated deposition is employed at this concentration, FE-SEM images show the presence of a different type of deposit, which are much larger and possess a 'flake-like' structure. The stripping of these larger deposits have been attributed to the second peak at more positive potentials as each are only observed when the other is present.

Experiments utilising electrode heating on the stripping step also show an effect of increased temperature. A shift towards a more positive potential for the stripping peak occurs upon pulse heating, probably due to the temperature coefficient of Pb^{2+} manifesting as a potential shift. The area of the heated stripping peak is larger than that obtained under ambient conditions because deposition continues to occur at an appreciable rate during the initial part of the stripping step. At a higher laser power of 20 W this effect is intensified, causing a larger stripping peak. Any improvement in signal therefore seems to be largely due to an enhanced deposition step, rather than an improved stripping efficiency, though the latter could become more significant at high metal concentrations.

Further experiments for this work would investigate the benefits of pulsed electrode heating on the limit of detection for a pBDD of this size, it is expected that lower concentrations of lead could be detected and quantified with carefully controlled heating conditions. Other metals besides lead could also be detected with this method, of interest would be the effect of heat on the detection of solutions containing more than one metal species, for example lead and cadmium. The potential benefit of heating during stripping could also be explored, by testing much higher concentrations of metal that are not completely removed under normal stripping conditions.

6.6 References

1. K. Z. Brainina, N. A. Malakhova and N. Y. Stojko, *Fresenius J. Anal. Chem.*, 2000, **368**, 307-325.
2. G. Hanrahan, D. G. Patil and J. Wang, *J. Environ. Monit.*, 2004, **6**, 657-664.
3. M. L. Tercier and J. Buffle, *Electroanalysis*, 1993, **5**, 187-200.
4. L. Järup, *British Medical Bulletin*, 2003, **68**, 167-182.
5. D. Luo, L. Wu and J. Zhi, *ACS Nano*, 2009, **3**, 2121-2128.
6. Y. V. Pelskov, A. Y. Sakharova, M. D. Krotova, L. L. Bouilov and B. V. Spitsyn, *J. Electroanal. Chem. Inter. Electrochem.*, 1987, **228**, 19-27.
7. K. E. Toghill, L. Xiao, G. G. Wildgoose and R. G. Compton, *Electroanalysis*, 2009, **21**, 1113-1118.
8. C. Prado, S. J. Wilkins, F. Marken and R. G. Compton, *Electroanalysis*, 2002, **14**, 262-272.
9. C. E. Banks, M. E. Hyde, P. Tomčík, R. Jacobs and R. G. Compton, *Talanta*, 2004, **62**, 279-286.
10. D. Dragoe, N. Spătaru, R. Kawasaki, A. Manivannan, T. Spătaru, D. A. Tryk and A. Fujishima, *Electrochim. Acta*, 2006, **51**, 2437-2441.
11. P. Pınar, Y. Yardım and Z. Şentürk, *Cent.Eur.J.Chem.*, 2013, **11**, 1674-1681.
12. T. Spătaru, N. Spătaru and A. Fujishima, *Talanta*, 2007, **73**, 404-406.
13. C. Brihaye and G. Duyckaerts, *Anal. Chim. Acta*, 1983, **146**, 37-43.
14. R. W. Andrews, J. H. Larochelle and D. C. Johnson, *Anal. Chem.*, 1976, **48**, 212-214.
15. L. A. Hutton, M. E. Newton, P. R. Unwin and J. V. Macpherson, *Anal. Chem.*, 2011, **83**, 735-745.
16. W. J. Albery and C. M. A. Brett, *J. Electroanal. Chem. Inter. Electrochem.*, 1983, **148**, 211-220.
17. F. Marken, T. O. Rebbitt, J. Booth and R. G. Compton, *Electroanalysis*, 1997, **9**, 19-22.
18. F.-M. Matysik, S. Matysik, A. M. O. Brett and C. M. A. Brett, *Anal. Chem.*, 1997, **69**, 1651-1656.
19. S.-H. Wu, J.-J. Sun, Z.-B. Lin, A.-H. Wu, Y.-M. Zeng, L. Guo, D.-F. Zhang, H.-M. Dai and G.-N. Chen, *Electroanalysis*, 2007, **19**, 2251-2257.
20. P. Gründler and G. U. Flechsig, *Electrochim. Acta*, 1998, **43**, 3451-3458.
21. S. B. Hočevar, B. Ogorevc, J. Wang and B. Pihlar, *Electroanalysis*, 2002, **14**, 1707-1712.
22. J.-J. Sun, L. Guo, D.-F. Zhang, W.-H. Yin and G.-N. Chen, *Electrochem. Commun.*, 2007, **9**, 283-288.
23. J. Wang, P. Gründler, G.-U. Flechsig, M. Jasinski, G. Rivas, E. Sahlin and J. L. Lopez Paz, *Anal. Chem.*, 2000, **72**, 3752-3756.
24. G.-U. Flechsig, O. Korbout, S. B. Hocevar, S. Thongngamdee, B. Ogorevc, P. Gründler and J. Wang, *Electroanalysis*, 2002, **14**, 192-196.
25. M. Jasinski, A. Kirbs, M. Schmehl and P. Gründler, *Electrochem. Commun.*, 1999, **1**, 26-28.
26. M. Jasinski, P. Gründler, G.-U. Flechsig and J. Wang, *Electroanalysis*, 2001, **13**, 34-36.
27. C. Prado, S. J. Wilkins, P. Grundler, F. Marken and R. G. Compton, *Electroanalysis*, 2003, **15**, 1011-1016.

28. Y. C. Tsai, B. A. Coles, K. Holt, J. S. Foord, F. Marken and R. G. Compton, *Electroanalysis*, 2001, **13**, 831-835.
29. S. Fletcher, C. S. Halliday, D. Gates, M. Westcott, T. Lwin and G. Nelson, *J. Electroanal. Chem. Inter. Electrochem.*, 1983, **159**, 267-285.
30. A. J. Saterlay, D. F. Tibbetts and R. G. Compton, *Anal. Sci.*, 2000, **16**, 1055-1060.
31. O. S. Ivanova and F. P. Zamborini, *J. Am. Chem. Soc.*, 2009, **132**, 70-72.
32. S. E. W. Jones, K. E. Toghill, S. H. Zheng, S. Morin and R. G. Compton, *J. Phys. Chem. C*, 2009, **113**, 2846-2854.
33. M. Bernard, A. Deneuville and P. Muret, *Diamond Relat. Mater.*, 2004, **13**, 282-286.
34. B. P. Chaplin, D. K. Hubler and J. Farrell, *Electrochim. Acta*, 2013, **89**, 122-131.
35. J. B. Miller and G. R. Brandes, *J. Appl. Phys.*, 1997, **82**, 4538-4545.
36. N. R. Wilson, S. L. Clewes, M. E. Newton, P. R. Unwin and J. V. Macpherson, *J. Phys. Chem. B.*, 2006, **110**, 5639-5646.
37. A. L. Colley, C. G. Williams, U. D'Haenens Johansson, M. E. Newton, P. R. Unwin, N. R. Wilson and J. V. Macpherson, *Anal. Chem.*, 2006, **78**, 2539-2548.
38. N. R. Stradiotto, K. E. Toghill, L. Xiao, A. Moshar and R. G. Compton, *Electroanalysis*, 2009, **21**, 2627-2633.

7 Conclusions

Diamond grown by the CVD method is an extraordinary material, worthy of exhaustive study. Many BDD samples (A-H) were used in this thesis, grown by different suppliers and displaying a variety of characteristics such as boron concentration and electrical conductivity. BDD has emerged as an extremely useful tool for electrochemists, boasting properties unmatched by other electrode materials. Lower background currents can be obtained with pBDD owing to its low capacitance and lack of reactivity towards many chemical species, this is advantageous for electroanalysis where limits of detection and sensitivity are of great importance. pBDD also possesses a wide potential window in aqueous solvent, allowing electrochemistry to be performed on species not available to other electrodes due to the early onset of water reduction and oxidation. Additionally, pBDD is exceedingly hard and resistant to chemical attack, permitting the construction of electrodes that do not succumb to hostile environments such as acidic and basic media. Fast temperature changes can be achieved with pBDD as it possesses a very high thermal conductivity, higher even than copper. This high thermal conductivity can be exploited electrochemically, where pBDD can be rapidly heated and cooled whilst in contact with solution. Two different surface terminations may exist on diamond, which can affect the electrochemistry of BDD, as-grown samples are hydrogen terminated though an oxidation termination can be formed by various treatments.

The aims of this thesis were to characterise a series of different pBDD samples displaying different properties for use in electroanalysis and exploit the thermal conductivity of pBDD for high temperature electrochemical applications.

SIMs was used to measure the average boron concentration of these samples, which ranged from $9.2 \times 10^{16} – 1.6 \times 10^{21}$ boron atoms cm^{-3}, the amount of boron strongly, though not exclusively, affects the electrical conductivity of diamond which ranged from ~ 41000 to 0.05 Ωcm of the freestanding samples that could be measured. The roughness of lapped samples (A-E and H) was less than 5 nm as determined by AFM, samples present on a niobium substrate (F and G) could not be lapped and consequently had much higher surface roughnesses of 1.85 and 9.3 µm.

In Chapter 3, FE-SEM was used to assess the grain structure of pBDD samples, thinner samples contained much smaller grains and thicker samples much larger grains, this structure is due to the way in which grains grow outwards during CVD growth. Grain sizes varied from 2 – 880 µm for the thinnest and thickest of the freestanding samples respectively. The contrast obtained in FE-SEM using the in-lens secondary detector showed areas of different conductivities in pBDD, which are indicative of boron concentration, this has been shown previously with conducting AFM (C-AFM).[1] The heterogeneity of pBDD was further investigated in Chapter 4 with Raman mapping, two samples of similar dopant density (metallic) were used in this study. Areas of the diamond peak (~1332 cm^{-1}) and non-diamond carbon feature (~ 1500 cm^{-1}) were recorded for many spectra and plotted as an image. For the sample that contained non-diamond carbon, it was found that these phases correlated with areas of higher boron doping. The resistivities of moderately (A – C) and heavily doped (E and F) samples were investigated at various temperatures, samples A-C showed a large temperature dependent resistivity. The heavily doped samples (E and F) showed a very small variation of resistivity with temperature, and were deemed effectively metallic.

The electrochemical response of pBDD samples varied considerably, with samples containing less boron resulting in resistance effects, lower currents and slower

kinetics. Although samples with lower boron concentrations produce wider solvent windows and lower capacitances, they are not suitable for electroanalysis. The effect of low boron concentration on kinetics is more pronounced at redox mediators that oxidise and reduce at more negative potentials vs. a reference electrode, due to the p-type nature of semiconducting BDD. In order to be useful as an electroanalytical tool BDD must be around the metallic threshold (2-3 × 10^{20} cm^{-3}), much higher levels of boron doping serve to decrease the available solvent window, increase capacitance and make the incorporation of non-diamond carbon during growth more probable.

Non-diamond carbon is detrimental to the electrochemical response of pBDD, the presence of which can be detected in Raman spectroscopy as a feature around 1500 cm^{-1}. Samples that suffered from incorporation of non-diamond carbon displayed larger capacitances and a narrower solvent window. It is essential therefore that a pBDD electrode must demonstrate metal like conductivity, contain negligible amounts of non-diamond impurities and not be doped with too much boron if it is to be used for electroanalysis. Optimal results were achieved with sample E, which contained an average boron concentration of 3 × 10^{20} cm^{-3} and negligible non-diamond phases.

Surface termination is important when performing electrochemical studies with BDD. A hydrogen termination provides a surface conductivity, allowing semiconducting samples to perform reasonably well, though this is not stable and performance diminishes with subsequent potentials scans. An oxygen termination is far more stable and should be applied to BDD prior to electrochemical studies. The method to produce an oxygen terminated surface drastically affected the electrochemistry of surface sensitive redox mediators; near reversible HET (highest reported to date for oxygen-terminated pBDD) was observed for the $Fe(CN)_6^{4-/3-}$ couple after alumina polishing of sample E. Conversely, anodic polarisation reduced the rate of HET for sample E with

the same redox mediator. The reverse effect (yet less pronounced) was observed for the $Fe^{2+/3+}$ couple, where anodic polarisation of sample E yielded faster HET than with an alumina polish treatment.

XPS studies indicated a larger amount of carbonyl and carboxyl groups on the pBDD surface treated with an anodic polarisation, in addition to more alcohol groups. Alumina polishing was found to be a viable means of producing a clean, reproducible diamond surface, as shown by XPS conducted at different temperatures which showed no evidence of aluminium indicating complete removal of alumina particles.

In Chapter 5, electrochemical experiments involving isothermal solution heating were conducted and showed an enhanced current response for the $Ru(NH_3)_6^{2+/3+}$ couple, this was attributed mainly to an enhanced rate of mass transport towards the electrode. Under heated conditions, CVs tended towards a steady state like response as temperature is increased, though fluctuations become apparent in the current trace for the slower scan rates at higher temperatures. Peak currents are calculated and were found to deviate from those measured experimentally, this disparity increases at slower scan rates suggesting that convection contributes significantly to the overall mass transport. Diffusion coefficients are calculated at different solution temperatures and found to agree with those found experimentally with a Pt UME, where the effects of convection are less pronounced.

Non-isothermal experiments employed the use of a thin (200 μm) pBDD, a pulsed heated methodology was used for rapid heating and cooling of the pBDD electrode. OCP experiments implied that a temperature rise of around ~ 34 ^oC could be achieved in solution close to the electrode surface with a 10 ms laser pulse at 30 W, whereas finite element simulations suggested that the electrode surface itself may rise by ~ 86 ^oC when subjected to the same laser pulse. The bulk solution temperature was largely

unaffected ($\Delta T < 1$ °C) for the duration of experiments conducted in the non-isothermal regime (< 30 s).

TPV experiments showed a very large increase in current for $Ru(NH_3)_6^{2+/3+}$ (~ 6 times for 22.5 W), in addition to a drastic change in shape as compared to a CV at non-heated conditions. The emergence of a 'double cathodic' peak occurs due to the intrinsic temperature coefficient of $Ru(NH_3)_6^{2+/3+}$ which causes a shift to more positive potentials at higher temperatures.[2, 3] This is analogous to performing DPV with a potential pulse of opposite polarity to the potential staircase. This effect was also seen to varying degrees for other redox mediators, the magnitude and sign of current enhancement is dependent upon the temperature coefficient of the studied species.

In Chapter 6, ASV was conducted with a glass sealed pBDD electrode (sample E) at different solution temperatures, using the same water bath apparatus as Chapter 5. The area of the DPV stripping peak for this metal increased, up to a factor of ~ 4.5, when the solution was raised to 60 °C, indicating a greater amount of lead on the electrode surface.

An all diamond structure was constructed (from sample E material) and employed in heated ASV experiments for the deposition and stripping of lead. Pulsed laser heating during the preconcentration step, and subsequent stripping step was performed separately in 5 µM Pb^{2+} solution. The former greatly enhanced the amount of deposited lead, as evidenced by FE-SEM, where deposition showed preferential nucleation in regions containing more boron. At a concentration of 50 µM Pb^{2+}, laser heating produced 'flake' type structures approximately 2 µm long. A second peak was observed in DPV and was attributed to these flakes.

When pulsed laser heating was applied only during the stripping step, a shift in peak potential towards more positive values was seen, accompanied by a slight increase in peak area. This effect was exaggerated at a higher laser power of 20 W, though the increase in peak area is thought to occur simply due to an enhanced rate of metal deposition during the initial part of the stripping step.

7.1 References

1. N. R. Wilson, S. L. Clewes, M. E. Newton, P. R. Unwin and J. V. Macpherson, *J. Phys. Chem. B.*, 2006, **110**, 5639-5646.
2. T. Voß, P. Gründler, A. Kirbs and G.-U. Flechsig, *Electrochem. Commun.*, 1999, **1**, 383-388.
3. R. P. Akkermans, M. F. Suárez, S. L. Roberts, Q. Fulian and R. G. Compton, *Electroanalysis*, 1999, **11**, 1191-1202.